Chemical Imaging Methods for Cultural Heritage

Advanced Data Acquisition and Processing

by

Luis Manuel de Almeida Nieto

CHEMICAL IMAGING METHODS FOR CULTURAL HERITAGE

ADVANCED DATA ACQUISITION AND PROCESSING

CHEMICAL IMAGING METHODS FOR CULTURAL HERITAGE

ADVANCED DATA ACQUISITION AND PROCESSING

Dissertation

for the purpose of obtaining the degree of doctor
at Delft University of Technology
by the authority of the Rector Magnificus,
Prof. dr. ir. H. Bijl,
chair of the Board for Doctorates
to be defended publicly on
Wednesday 6, May 2026, 10:00

by

Luís Manuel DE ALMEIDA NIETO

This dissertation has been approved by the (co)promotors.

Composition of the doctoral committee:

Rector Magnificus,	chairperson
Prof. dr. J. Dik,	Delft University of Technology, *promotor*
Dr. ing. R. Van de Plas,	Delft University of Technology, *promotor*
Dr. M.W.E.M. Alfeld,	Delft University of Technology, *copromotor*
Independent members:	
Prof. dr. ir. C. Vuik,	Delft University of Technology
Prof. dr. S.C. Pont,	Delft University of Technology
Prof. dr. R.G. Erdmann,	University of Amsterdam
Dr. L. van Eijck,	Delft University of Technology
Dr. ir. M.H.F. Sluiter,	Delft University of Technology, *reserve member*

Keywords: Cultural Heritage Science, Spectral Imaging, Macro X-ray Fluorescence, Reflectance Imaging Spectroscopy, Machine Learning

Printed by: Ridderprint | www.ridderprint.nl

Cover by: Design by Luís Manuel de Almeida Nieto, Calligraphy by Aura T. Okkels, Miniature by Milou de Lange.

ISBN 978-94-6518-308-4

An electronic copy of this dissertation is available at
https://repository.tudelft.nl/.

For my friend and mentor, Dr. Francesca Gabrieli, without whom this work would not have been possible.

CONTENTS

Summary xi

Samenvatting xiii

1. Introduction 1
- 1.1. What is cultural heritage and why do we study it? . . . 2
- 1.2. How do we study cultural heritage? . . . 3
- 1.3. Imaging of cultural heritage . . . 5
  - 1.3.1. MA-XRF . . . 10
  - 1.3.2. RIS . . . 16
- 1.4. Data evaluation . . . 21
  - 1.4.1. Machine learning . . . 21

2. Comparison of macro X-ray fluorescence spectroscopy (MA-XRF) and reflectance imaging spectroscopy (RIS) for the analysis of pigments 43
- 2.1. Introduction . . . 44
- 2.2. Materials and methods . . . 45
  - 2.2.1. Test samples . . . 45
  - 2.2.2. Data acquisition and processing . . . 48
- 2.3. Results . . . 51
  - 2.3.1. Paint samples . . . 51
  - 2.3.2. Application to a painting . . . 54
- 2.4. Discussion . . . 56
- 2.5. Conclusion . . . 59

3. Advanced analysis of historical manuscripts through interpretable machine learning of reflectance imaging spectroscopy 67
- 3.1. Introduction . . . 68
- 3.2. Results . . . 70
  - 3.2.1. Case study 1 . . . 70
  - 3.2.2. Case study 2 . . . 73
- 3.3. Discussion . . . 76
- 3.4. Methods . . . 77
  - 3.4.1. Datasets . . . 77
  - 3.4.2. Supervised ML workflow . . . 77
  - 3.4.3. Interpretation of ML model . . . 80
  - 3.4.4. Improved training . . . 81

4. On the Design of flexible MA-XRF scanners for methodological optimization 87
4.1. Introduction . . . 88
4.2. Design requirements . . . 88
4.3. BLB Mark I . . . 89
4.3.1. Scanner . . . 89
4.3.2. Housing . . . 92
4.3.3. Performance evaluation . . . 96
4.3.4. Shortcomings . . . 99
4.4. BLB Mark II . . . 100
4.4.1. Scanner . . . 100
4.4.2. Housing . . . 101

5. Accelerating MA-XRF Through Advanced Scanning Strategies 107
5.1. Introduction . . . 108
5.2. MA-XRF scanning strategies . . . 109
5.2.1. Fast Autonomous Scanning Toolkit (FAST) . . . 110
5.2.2. Chopp algorithm . . . 112
5.3. Methodology . . . 114
5.4. Results . . . 115
5.4.1. Fast Autonomous Scanning Toolkit (FAST) hyperparameters . . . 115
5.4.2. Chopp hyperparameters . . . 117
5.4.3. Real measurements . . . 117
5.5. Conclusion . . . 120

6. Conclusion 125
6.1. Advanced RIS data processing . . . 125
6.2. Advanced MA-XRF data acquisition . . . 126
6.3. Multi-modal MA-XRF/RIS data processing and acquisition . . . 128

A. Appendix A: Supplementary information for chapter 2 135
A.1. Sample pigment characterization . . . 136
A.2. Sample support material characterization . . . 139
A.3. Mixture samples densities . . . 141
A.4. Layer samples densities . . . 143
A.5. Mixture samples MA-XRF maps . . . 146
A.6. Layer samples MA-XRF maps . . . 148
A.7. Pigment attenuation and transmission values . . . 150
A.8. Sample painting distribution maps . . . 151

B. Appendix B: Supplementary information for chapter 3 155
B.1. XGBoost Settings . . . 156
B.2. Classifier Metrics . . . 157
B.3. Leiden Riddle Areas of Interest . . . 158
B.4. Leiden Riddle Sampling Masks . . . 159
B.5. Leiden Riddle Local SHAP Maps . . . 166
B.6. Locke Constitution Sampling Masks . . . 168

B.7. Locke Constitution Local SHAP Maps 175
B.8. Locke Constitution SHAP Spectra 177

C. Appendix C: Supplementary information for chapter 5 **179**
C.1. MA-XRF Simulation maps 180
C.2. FAST Simulation parameters 186
C.3. Chopp Simulation parameters 187
C.4. Accelerated MA-XRF maps 189

Acknowledgements **195**

Curriculum Vitæ **199**

List of Publications **201**

SUMMARY

Imaging spectroscopy methods are becoming increasingly relevant in the field of cultural heritage science. The datacubes output by these methods represent some of the most significant challenges related to their application, namely how to make sense of complex multi-dimensional datasets. As the selection of imaging spectroscopy methods and the complexity of the resulting datasets continue to grow, the time required to conduct all these measurements and process all of the data also increases. This research focuses on addressing both the problem of extended data acquisition times and the challenge of processing the complex datacubes.

Firstly, chapter 1 introduces the basic concepts of cultural heritage and the field of cultural heritage science. It also provides an overview of some of the scientific methods used for the study of cultural heritage objects, with a focus on imaging methods, and particularly imaging spectroscopy methods. The two primary methods considered in this work, macro X-ray fluorescence spectroscopy (MA-XRF) and reflectance imaging spectroscopy (RIS), are described in greater detail and an overview of the state-of-the-art in equipment and data processing methods is provided.

Beginning with the issue of data processing, chapter 2 discusses a novel method for the use of short-wave infrared (SWIR) (1000–2500 nm) RIS for semi-quantitative analysis of historical paintings. The method consists of the isolation and deconvolution of characteristic absorption features of target pigments. The concept is proven on two pigments, lead white and blue verditer. The method is tested on a set of specially prepared paint samples as well as a 16th century painting. The method is compared to MA-XRF on its ability to selectively map pigments as well as its ability to provide quantitative information on the pigment concentrations. A novel data visualization method, able to visualize chemical relevance of individual pixels whilst also highlighting larger spatial patterns, is also presented.

Chapter 3 continues on the topic of data processing, presenting a novel approach for the analysis of damaged historical manuscripts through the use of visible and near-infrared (VNIR) (400–1000 nm) RIS combined with supervised machine learning methods and machine learning explainability methods. The approach uses manually labeled VNIR RIS data acquired from historical manuscripts to train an XGBoost classification model, followed by the application of Shapley additive explanations (SHAP) to analyse the behaviour of the classification model. The calculated SHAP values are then used to calculate a SHAP-weighted intensity map (SWIM), which is found to improve the legibility of the analysed manuscripts. An adaptive colour scheme is also proposed as a method of easing the evaluation by paleographists of the resulting images. The approach is tested on two texts, the Leiden Riddle, a 9-10th century Northumbrian text, and the 1669 First Set of the Fundamental Constitutions of Carolina, the earliest text attributed to political philosopher John Locke.

Shifting to the issue of data acquisition, chapter 4 documents the design and testing of two MA-XRF scanners. These scanners, the big lead box (BLB) Mark I and Mark II, are designed to be flexible measurement platforms that allow for the testing of alternate scanning strategies and multi-modal acquisitions. Highlighted are the safety features implemented into the design of the scanners with the goal of minimizing potential radiation exposure to users and bystanders.

Following the development of the MA-XRF scanners, chapter 5 discusses two methods for the acceleration of MA-XRF measurements through the use of smart scanning strategies. The first method, the Fast Autonomous Scanning Toolkit (FAST), uses machine learning models to dynamically select which pixels to scan whilst trying to reduce the estimated distortion between the reconstructed data set and the underlying ground truth. The second method, the Chopp algorithm, uses a double scan approach, where a first fast initial scan is used to estimate the optimal scan time per pixel for a second scan with a specified total scan time. The two methods are evaluated on their scan times and the achieved data quality compared to each other and a traditional raster scan.

Lastly, chapter 6 provides some concluding remarks on the themes covered during this work and highlights potential future developments.

SAMENVATTING

Beeldvormende spectroscopiemethoden worden steeds relevanter in het vakgebied van de erfgoedwetenschap. De datacubes die door deze methoden worden gegenereerd, vertegenwoordigen enkele van de grootste uitdagingen met betrekking tot hun toepassing, namelijk hoe complexe multidimensionale datasets geïnterpreteerd dienen te worden. Naarmate de selectie van beeldvormende spectroscopiemethoden en de complexiteit van de resulterende datasets blijven toenemen, neemt ook de tijd toe die nodig is om al deze metingen uit te voeren en alle gegevens te verwerken. Dit onderzoek richt zich op het aanpakken van zowel het probleem van lange data-acquisitietijden als de uitdaging van het verwerken van de complexe datacubes.

Hoofdstuk 1 introduceert allereerst de basisconcepten van cultureel erfgoed en het vakgebied van de erfgoedwetenschap. Het geeft ook een overzicht van enkele wetenschappelijke methoden die worden gebruikt voor het onderzoeken van cultureel erfgoed, met de nadruk op beeldvormende methoden, en in het bijzonder beeldvormende spectroscopiemethoden. De twee belangrijkste methoden die in dit werk worden behandeld, macro-röntgenfluorescentiespectroscopie (MA-XRF) en reflectiebeeldvormende spectroscopie (RIS), worden gedetailleerder beschreven en er wordt een overzicht gegeven van de state-of-the-art op het gebied van apparatuur en dataverwerkingsmethoden.

Hoofdstuk 2 begint met het bespreken van de gegevensverwerking en introduceert een nieuwe methode voor het gebruik van kortgolvige infrarood (SWIR) (1000–2500 nm) RIS voor semi-kwantitatieve analyse van historische schilderijen. De methode bestaat uit het isoleren en deconvolueren van karakteristieke absorptiepieken van de doelpigmenten. Het concept wordt bewezen aan de hand van twee pigmenten: loodwit en synthetische azuriet. De methode wordt getest op een reeks speciaal geprepareerde verfmonsters en op een schilderij uit de 16e eeuw. De methode wordt vergeleken met MA-XRF wat betreft het vermogen om pigmenten selectief in kaart te brengen en kwantitatieve informatie te verschaffen over de pigmentconcentraties. Er wordt ook een nieuwe datavisualisatiemethode gepresenteerd, waarmee de chemische relevantie van individuele pixels kan worden gevisualiseerd en tegelijkertijd grotere ruimtelijke patronen kunnen worden benadrukt.

Hoofdstuk 3 gaat verder in op het onderwerp dataverwerking en presenteert een nieuwe benadering voor de analyse van beschadigde historische manuscripten door gebruik te maken van zichtbaar en nabij-infrarood (VNIR) (400–1000 nm) RIS in combinatie met methoden voor supervised machine learning en methoden voor het verklaren van machine learning-resultaten. De benadering maakt gebruik van handmatig gelabelde VNIR RIS-gegevens, verkregen uit historische manuscripten, om een XGBoost-classificatiemodel te trainen, gevolgd door de toepassing van Shapley additive explanations (SHAP) om het gedrag van het classificatiemodel te analyseren. De berekende SHAP-waarden worden vervolgens gebruikt om een SHAP-gewogen intensiteitskaart (SWIM) te berekenen, die

de leesbaarheid van de geanalyseerde manuscripten verbetert. Er wordt ook een adaptief kleurenschema voorgesteld als methode om de evaluatie van de resulterende afbeeldingen door paleografen te vergemakkelijken. De aanpak is getest op twee teksten: het Leiden Riddle, een tekst uit de 9e-10e eeuw uit Northumbrië, en de First Set of the Fundamental Constitutions of Carolina uit 1669, de vroegste tekst die wordt toegeschreven aan de politieke filosoof John Locke.

Wat betreft de data-acquisitie, beschrijft hoofdstuk 4 het ontwerp en het testen van twee MA-XRF-scanners. Deze scanners, de BLB Mark I en Mark II, zijn ontworpen als flexibele meetplatformen die het testen van alternatieve scanstrategieën en multimodale acquisities mogelijk maken. De veiligheidsvoorzieningen die in het ontwerp van de scanners zijn geïmplementeerd, met als doel de potentiële blootstelling aan straling voor gebruikers en omstanders te minimaliseren, worden benadrukt.

Na de ontwikkeling van de MA-XRF-scanners bespreekt hoofdstuk 5 twee methoden voor het versnellen van MA-XRF-metingen door middel van slimme scanstrategieën. De eerste methode, de Fast Autonomous Scanning Toolkit (FAST), gebruikt machine learning-modellen om dynamisch te selecteren welke pixels gescand moeten worden, waarbij geprobeerd wordt de geschatte vervorming tussen de gereconstrueerde dataset en de onderliggende grondwaarheid te minimaliseren. De tweede methode, het Chopp-algoritme, gebruikt een dubbele scanbenadering, waarbij een eerste snelle initiële scan wordt gebruikt om de optimale scantijd per pixel te schatten voor een tweede scan met een gespecificeerde totale scantijd. De twee methoden worden geëvalueerd op hun scantijden en de behaalde datakwaliteit, waarna ze worden vergeleken met elkaar en met een traditionele rasterscan.

Tot slot bevat hoofdstuk 6 enkele afsluitende opmerkingen over de thema's die in dit werk aan bod zijn gekomen en belicht het mogelijke toekomstige ontwikkelingen.

Acronyms

ANN	artificial neural network
AOTF	acousto-optic tunable filter
BLB	big lead box
CCD	charge-coupled device
CL	computed laminography
CMOS	complementary metal-oxide-semiconductor
CNC	computer numerical control
CNN	convolutional neural network
CT	computed tomography
DA	dynamic analysis
DNN	deep neural network
EMCCD	electron-multiplying charge-coupled device
ER-FTIR	external reflectance Fourier transform infrared spectroscopy
ERD	expected reduction in distortion
ERR	energy resolved radiography
FAST	Fast Autonomous Scanning Toolkit
FFF	fused filament fabrication
FORS	fibre optic reflectance spectroscopy
FWHM	full width at half maximum
GC-MS	gas chromatography–mass spectrometry
GEM	gas electron multiplier
GS	gamma spectroscopy
HSI	hyperspectral imaging
ICA	independent component analysis
IR	infrared
IRR	infrared reflectography
KM	Kubelka-Munk
L-LS	linear least-squares
LightGBM	light gradient-boosting machine
LIS	luminescence imaging spectroscopy
LOD	limit of detection
MA-XRF	macro X-ray fluorescence spectroscopy
MA-XRPD	macro X-ray powder diffraction spectroscopy
MC	Monte Carlo
MCT	mercury cadmium telluride
MIR	Mid infrared
ML	machine learning

MNF	minimum noise fraction
MSE	mean squared error
MSI	multispectral imaging
NI	neutron imaging
NIR	near-infrared
NL-LS	non-linear least-squares
NMF	non-negative matrix factorization
NN	neural network
NN-LS	non-negative least-squares
NT	neutron tomography
OCT	optical coherence tomography
PCA	principal component analysis
RD	reduction in distortion
RIS	reflectance imaging spectroscopy
RMSE	root mean square error
ROI	region of interest
SAM	spectral angle mapping
SDD	silicon drift detector
SEM	scanning electron microscopy
SHAP	Shapley additive explanations
SIFT	scale-invariant feature transform
SiVM	simplex volume maximization
SLADS	Supervised Learning Approach for Dynamic Sampling
SLADS-Net	deep neural network-based Supervised Learning Approach for Dynamic Sampling
SNIP	Statistics-sensitive Non-linear Iterative Peak-clipping
SNR	signal-to-noise ratio
SOM	self-organizing map
SSIM	structural similarity index measure
SVD	singular value decomposition
SWIM	SHAP-weighted intensity map
SWIR	short-wave infrared
t-SNE	t-distributed stochastic neighbour embedding
THz	terahertz
UL-LS	unrestricted linear least-squares
UMAP	uniform manifold approximation and projection
UV	ultraviolet
UVIFL	UV-induced fluorescence photography
VNIR	visible and near-infrared
XGBoost	extreme gradient boosting
XRF	X-ray fluorescence spectroscopy
XRPD	X-ray powder diffraction spectroscopy
XRR	X-ray radiography

1

INTRODUCTION

Cultural heritage is a broad and complex subject. Cultural heritage science seeks to use scientific methods to aid in the study of cultural heritage objects. There is a very wide selection of methods that are used, which fall under increasingly specific categories. Non-invasive imaging methods are the focus of this dissertation. Two methods in particular, MA-XRF and RIS, are discussed in greater detail, highlighting the current state-of-the-art in equipment and data processing.

1

1.1. WHAT IS CULTURAL HERITAGE AND WHY DO WE STUDY IT?

Cultural heritage is a somewhat broad and nebulous term. The United Nations Educational, Scientific and Cultural Organization (UNESCO) defined the cultural heritage of a people in the Mexico City Declaration on Cultural Policies[1] as including "the works of its artists, architects, musicians, writers and scientists and also the work of anonymous artists; expressions of the people's spirituality, and the body of values which give meaning to life. It includes both tangible and intangible works through which the creativity of that people finds expression: languages, rites, beliefs, historic places and monuments, literature, works of art, archives and libraries." However, in later documents, like the 2009 UNESCO Framework for Cultural Statistics,[2] cultural heritage is defined as one of 6 cultural domains encompassing "artefacts, monuments, and groups of buildings and sites that have a diversity of values including symbolic, historic, artistic, aesthetic, ethnological or anthropological, scientific and social significance." Notably, in this framework, intangible cultural heritage (ICH) is defined as a separate transversal cultural domain, and therefore cultural heritage is understood to encompass only tangible cultural works and the intangible aspects embedded into these tangible cultural works. Luckily, both these definitions are appropriate, as this work focuses on tangible cultural heritage, and it is not necessary to delve into the intricacies of these discussions.

Cultural heritage artefacts are the primary interest of this dissertation, and are here understood to be the material goods inherited by a society "which carry and transmit the cultural features of a society".[3] This includes paintings, sculptures, books, among many other types of objects. These artefacts can be viewed and studied from different angles. Art historians may view a painting based on its composition, historical context and subject. Linguists may view an old manuscript from a syntactic or morphological angle. The field of cultural heritage science, which this work is a part of, primarily focuses on viewing these artefacts from a material point of view, understanding what these objects are made of, how they are made and how they have aged. Understanding these material aspects doesn't only unlock large amounts of historical information, it also helps conserve these objects for future generations, making sure they remain part of the world's cultural heritage.

The ongoing restoration of Hubert and Jan van Eyck's *Ghent Altarpiece* presents a very suitable example of the nature and value of cultural heritage science research.[4] The altarpiece was painted in the 15th century and has since undergone significant modifications, including many restoration campaigns, looting by the French army of Napoleon Bonaparte, and being sawn in half by overzealous curators. So the altarpiece was decidedly not in the same state as it was when the van Eycks painted it, but not all of the changes were recorded, and thus it was difficult to know what parts of the altarpiece were still in their original state. During a previous restoration campaign in the 1950s (documented in French[5]), it was noted that several areas showed signs of overpainting. An area which became of particular interest during the latest restoration campaign was the face of the Lamb of God, shown in figure

1.1. Van der Snickt et al.[6] used modern analytical techniques to study the Lamb, and were able to better identify the extent of overpainting which helped guide conservators in the restoration of the altarpiece to what is currently believed to be closer to its original composition. And thus, the restoration campaign has made the object better reflect the culture and symbolism of the time in which it was made.

Having set out what cultural heritage is, how cultural heritage science interacts with the artefacts that comprise cultural heritage, and the value its studies have, the next question would be, how are these studies conducted? What tools are used and how are their results interpreted?

1.2. How do we study cultural heritage?

Cultural heritage Science research is extremely broad. Any analytical method that provides material information can (and often is or has been) used for the analysis of cultural heritage objects. X-ray radiography (XRR), optical coherence tomography (OCT), scanning electron microscopy (SEM), among many other methods, are routinely used in the study of heritage objects, each providing unique insight into the material reality of these objects.

How these methods are applied, however, can often be different to how they are used in more traditional scientific research. The strict uniqueness and scarcity of the objects being analysed introduces very specific requirements for the methods used. Destructive methods are uncommon (though not inexistent[8]), whilst non-destructive methods are further differentiated into invasive and non-invasive methods. Invasive methods, like SEM or gas chromatography–mass spectrometry (GC-MS), require taking a microsample from the object being studied. This has been a very common practice for as long as the field has existed, and remains very widespread, but has been decreasing in popularity as non-invasive methods have become more prominent. Non-invasive methods, like XRR or infrared reflectography (IRR), do not require taking microsamples, leaving the analyzed object completely unaffected by the measurement (at least theoretically). Invasive and non-invasive methods provide highly complementary information and are often used together, with non-invasive methods helping guide researchers on where and how invasive methods should be used. Whilst some of the methods discussed in this work could be applied to both invasive and non-invasive methods, they are primarily developed with non-invasive methods in mind and the rest of this dissertation will only discuss non-invasive methods.

Non-invasive methods have a long and storied history in heritage science. Only a few months after the discovery of X-rays, Walter König and August Töpler used X-rays to analyze paintings, and the practice has remained common since the 1920s.[9] As new analytical methods were developed, it would not take very long for them to be applied to the study of cultural heritage objects. Within non-invasive methods, there are two other subclasses: point-based methods and imaging methods. Point-based methods, as their name would suggest, measure individual points. These are methods like fibre optic reflectance spectroscopy (FORS), X-ray fluorescence spectroscopy (XRF), and external reflectance Fourier transform infrared

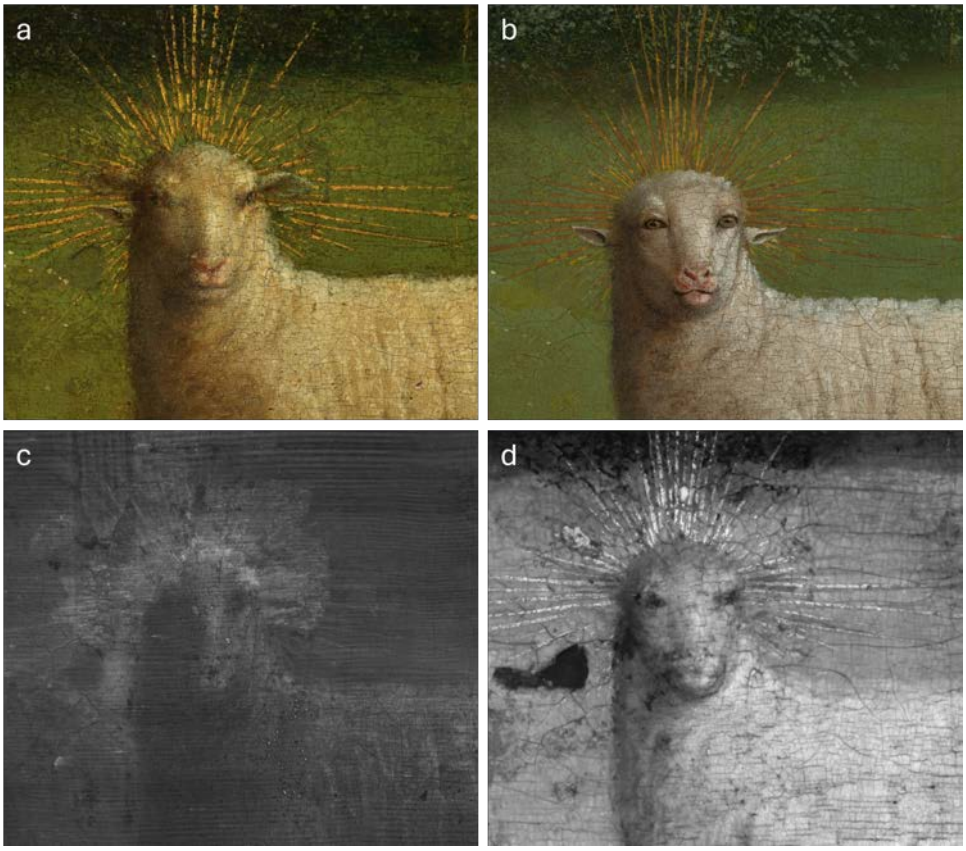

Figure 1.1.: Hubert and Jan van Eyck, *Ghent Altarpiece*, 1432, oil on panel, h 375 cm x w 520 cm, Saint Bavo's Cathedral, Ghent. Close up of the Adoration of the Mystic Lamb.[7] (a) Visible light photograph before restoration. (b) Visible light photograph after restoration. (c) XRR before restoration showing potential changes on and around the lamb's face. (d) IRR before restoration showing areas of paint loss and parts of the underlying original face of the lamb. Modified from [4].

spectroscopy (ER-FTIR). In contrast, imaging methods measure large areas within a single measurement, gathering data from a collection of points to form a full image. Technical photography, XRR and IRR are examples of imaging methods. In many cases, an imaging method has a point-based analogue, like MA-XRF and traditional point-based XRF. This work focuses primarily on imaging methods, so a selection of them will be covered in more detail.

1.3. IMAGING OF CULTURAL HERITAGE

Most imaging methods are based on interactions of electromagnetic radiation with the measured objects and are classified by the part of the electromagnetic spectrum considered and the nature of the interaction being measured. An overview of this can be seen in figure 1.2.

Beginning with X-rays ($10^{-11} - 10^{-10}$ m), the longest standing method is the previously mentioned XRR, which consists of emitting X-rays onto an object and using a film or a sensor to measure the X-rays that are transmitted through the object.[10] Since the X-ray absorption of an object depends on its thickness and composition, XRR can give insight into the structure and rough composition of an object. Whilst XRR by itself can only provide limited information, there are several variations of its base concept that can provide further insight. Computed tomography (CT), and the related computed laminography (CL), use computational methods to combine a collection of radiographs acquired at different angles to form a virtual 3D reconstruction of the object and its X-ray transmission, providing even further insight into the objects structure.[11] Another variation of XRR is energy resolved radiography (ERR), which measures not only the amount of photons transmitted through the object, but also measures their energy. How these energies are measured varies, with the most common approach being dichromography, where a series of radiographs are acquired using monochromatic X-ray beams of different energies. These radiographs can then be compared to each other to achieve the desired energy resolution. If the compared radiographs are acquired using energies above and below the absorption edge of an element, the difference between the two form a distribution image of the target element, a process more commonly known as K-edge imaging.[12] Figure 1.3 shows an example of XRR and ERR applied to an easel painting.[1]

[1] A Note on the Imaging of Lead White and Vermilion Paint Layers by Synchrotron Radiation-based, Simultaneous Dual Energy K-edge Absorption Radiography, Arie Wallert, Alberto Bravin, Liisa Porra, et al, Journal of the American Institute for Conservation, copyright 2013, reprinted by permission of Informa UK Limited, trading as Taylor & Francis Group, https://www.tandfonline.com

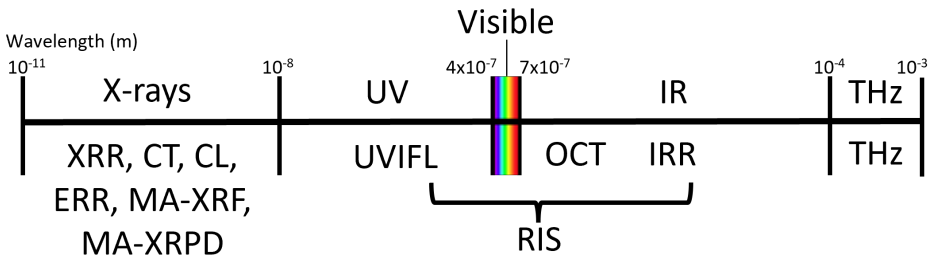

Figure 1.2.: Overview of the imaging methods based on electromagnetic radiation interactions.

X-rays are also used for spectral imaging methods. MA-XRF is a method that uses an X-ray beam to excite the atoms in the object of interest.[14] The excited atoms will then emit secondary X-rays, which are measured using a detector. These secondary X-rays have an energy characteristic to the elements present in the sample, giving insight into its elemental composition. MA-XRF is usually a scanning method, as each pixel in the image is measured individually, resulting in a full datacube with two spatial dimensions and one spectral dimension. MA-XRF is one of the primary focuses of this dissertation and will be discussed in greater detail in section 1.3.1. Macro X-ray powder diffraction spectroscopy (MA-XRPD) is similarly a scanning

Figure 1.3.: Carel Fabritius, *Abraham de Potter (1592-1650). Amsterdam Silk Merchant*, 1649, oil on canvas, h 68.5 cm x w 57 cm, Rijksmuseum, Amsterdam (inventory nr. SK-A-1591).[13] (a) Visible light photograph. (b) Conventional XRR, showing the difference in X-ray absorption between the paints as well as the wooden stretcher. (c) K-edge absorption image for Pb (low energy 87.3 keV, high energy 88.7 keV) showing the lead white distribution. (d) K-edge absorption image for Hg (low energy 82.4 keV, high energy 83.8 keV) showing the vermilion distribution. Modified from [12].

method which takes advantage of how X-rays are scattered by crystalline structures to create diffraction patterns. The resulting diffraction patterns are characteristic of the crystal structures within the sample, providing molecular information. MA-XRPD has the drawback of only being useful for the characterisation of crystalline materials. MA-XRPD is a very novel method within cultural heritage science and is not very wide spread as a result, but it has already proved its value in the analysis of paintings.[15] Figure 1.4 shows an example of MA-XRF and MA-XRPD.

Further along the electromagnetic spectrum, the ultraviolet (UV) range ($10^{-8} - 4 \times 10^{-7}$ m) is primarily used for UV-induced fluorescence photography (UVIFL), in which UV light is used to induce visible fluorescence which can be measured using a normal visible light camera.[17] This method can be useful for identifying areas of restoration as well as studying components which are invisible to other methods, like the varnish layers on a painting.[18, 19]

The visible range ($4 \times 10^{-7} - 7 \times 10^{-7}$ m) is used extensively for the analysis of cultural heritage artefacts. The most obvious application of it is visible light photography, which is so routine a method that it is sometimes forgotten in the discussion of heritage science practices. Whilst the method provides very limited chemical information, it can provide significant spatial information and is fundamental in guiding the application and interpretation of other methods. Continuous improvement of photography equipment has made possible higher spatial resolution photographs. The most significant current example is the 5 µm resolution photograph of Rembrandt's *Night Watch*, which is composed of 717 gigapixels and allows for the visualization of individual pigment particles.[20] Visible light microscopy is also used to achieve even higher spatial resolution images, with the most prominent example being the imaging campaign of Vermeer's *Girl with a Pearl Earring* which produced a full 4.4 µm resolution scan of the painting, as well as some detail scans with resolutions up to 0.22 µm. However, such high resolution photographs and microscopy scans require specialized imaging platforms and significant amounts of time in both acquisition and processing, significantly limiting their use, though there are initiatives to make these methods more affordable and user-friendly.[21]

In terms of spectral imaging, the visible range is most used with RIS (also known as hyperspectral imaging (HSI)), and the related multispectral imaging (MSI), both of which measure the light reflected by the target object in a series of spectral channels. Figure 1.5 shows an example of RIS. The two methods use different approaches to measure the same effect, but the most significant practical difference is the number of spectral channels considered, with MSI typically measuring dozens of channels and RIS measuring hundreds.[22] MSI uses either narrow-band illumination or filters, combined with an appropriately sensitive camera, whilst RIS uses broad-band illumination and specialized cameras equipped with a dispersive element or an interferometer that allows collection of very narrow spectral bands. Both RIS and MSI often also incorporate (or focus exclusively on) parts of the infrared (IR) range ($7 \times 10^{-7} - 10^{-4}$ m).[23] RIS is one of the primary focuses of this dissertation and will be covered in more detail in section 1.3.2. RIS equipment can also be used to acquire luminescence imaging spectroscopy (LIS) measurements by using narrow

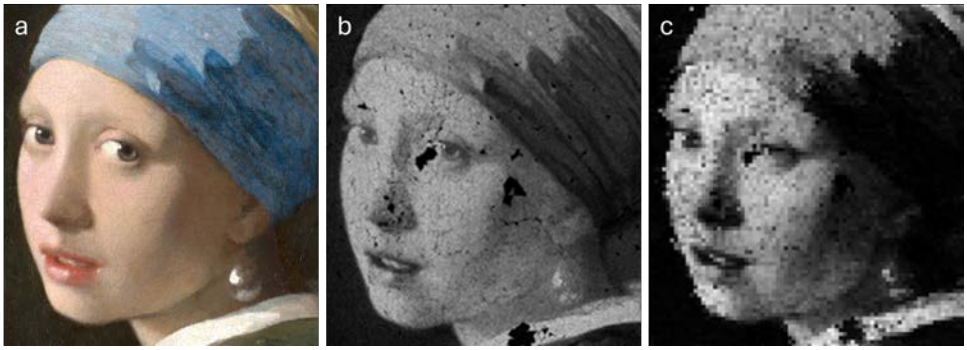

Figure 1.4.: Johannes Vermeer, *Girl with a Pearl Earring*, c. 1665, oil on canvas, h 44.5 cm x w 39 cm, Mauritshuis, The Hague (inventory nr. 670). Close up with the girl's face.[16] (a) Visible light photograph. (b) MA-XRF distribution map for Pb-M, showing surface presence of Pb throughout the face. (c) MA-XRPD distribution map for hydrocerussite, showing selective use of hydrocerussite-rich lead white on the brighter side of the face. Modified from [15] under the CC BY-NC 4.0 license (https://creativecommons.org/licenses/by-nc/4.0/).

band light sources, like lasers, to induce photoluminescence in the target object. Radpour et al.[24] produced such LIS measurements using a full-field hyperspectral camera combined with filters on the light source, to limit the emission source, and on the camera, to block the reflected excitation light. Moreau et al.[25] instead used a combination of scanning VNIR and SWIR FORS spectrometers with multiple lasers and broadband light sources to acquire both the RIS and LIS cubes.

Entering the IR range, OCT is a method that uses the interference of a reference beam and a beam reflected from the surface of the target object to produce an interference signal.[28] This signal can be processed to form a digital cross-section of the target sample, where the interface between different component layers are visible. These digital cross-section are then combined to form a 3D tomogram of the sample. OCT is limited by the opacity of the target to the light being used, which currently means it is often limited to analyse transparent and semi-transparent superficial layers like glazes and varnishes.

IR-photography and IRR are routinely used to visualize restorations and IR absorbing subsurface features, like underdrawings.[29] These methods are longstanding in the field and see widespread use, with the main difference between the two being the spectral ranges measured, usually up to 1.1×10^{-6} m for IR-photography and up to 1.7×10^{-6} m or 2.5×10^{-6} m for IRR, depending on the detector used. RIS in the IR range also provides this information, but is a much more recent and expensive development, and often has worse spatial resolution than IRR.[22]

In the terahertz (THz) range ($10^{-4} - 10^{-3}$ m), THz imaging and THz imaging spectroscopy are methods that are not very common in cultural heritage science,

Figure 1.5.: Johannes Vermeer, *The Milkmaid*, c. 1660, oil on canvas, h 45.5 cm x w 41 cm, Rijksmuseum, Amsterdam (inventory nr. SK-A-2344)[26] (a) Visible light photograph. Credit to Carola van Wijk, Rijksmuseum. (b) False colour image made using SWIR-RIS data (channels R: 1000 nm, G: 1500 nm, B: 2250 nm), showing compositional changes in the background. Credit to Dr. Francesca Gabrieli, Rijksmuseum.[27]

but previous research has proven the methods' ability to provide insight into the composition and stratigraphy of painted works of art.[30–32]

An imaging method that is not based on electromagnetic radiation interactions is neutron imaging (NI).[33] This method is conceptually similar to XRR, but measures the transmission of neutrons rather than X-rays to form the images. Neutrons are able to penetrate more deeply into heavier elements, like metals, whilst also showing high sensitivity to lighter elements, specially hydrogen. This makes NI a very useful method for the analysis of metal and organic materials. NI can also be used to conduct neutron tomography (NT), which provides similar structural information to CT. NT has also been combined with gamma spectroscopy (GS) to provide both structural and compositional information[2].[34]

Now, the two primary methods considered in this work, MA-XRF and RIS, are discussed in greater detail.

[2]Whilst gamma radiation ($<10^{-11}$ m) is certainly part of the electromagnetic spectrum, GS is not based on the interaction of electromagnetic radiation with the measured object, but on the emission of electromagnetic radiation as a result of other events, and is thus here considered as a method not based on electromagnetic radiation interactions.

1

1.3.1. MA-XRF

As mentioned in the previous section, MA-XRF uses the principle of secondary X-ray emissions of ionized atoms, shown in figure 1.6. An X-ray source, usually an X-ray tube or a synchrotron, is used to ionize the atoms in the target object by causing the ejection of electrons from the atomic orbitals of the sample atoms. If the electron is ejected from one of the lower atomic orbitals, electrons from higher atomic orbitals may fall to fill the hole in the lower orbitals. The difference in energy between the higher and lower atomic orbitals is emitted as a photon. As the energy of the atomic orbitals of an element is characteristic, the energy difference between different orbitals is also characteristic. Thus, if the energy of the photons emitted by a sample are measured, the resulting emission or "fluorescence" spectra can be used to characterize the elemental composition of the target object. MA-XRF uses an XRF spectrometer attached to a positioning system to perform many XRF measurements across the surface of the target object to form elemental distribution maps.

MA-XRF is a method designed primarily for use in cultural heritage science and was initially developed in the early 2010's, following successful early experiments at synchrotron sources.[29] Since then, the method has become widespread across cultural heritage institutions, with custom scanners developed by research groups, as well as commercially available scanners. Section 1.3.1 provides an overview of the most relevant MA-XRF devices currently in use.

Regarding the processing of MA-XRF data, the method benefits from the long history and well-described physics of traditional point-based XRF. However, MA-XRF data processing did face a major challenge when compared to XRF data processing, which was the amount of data that would have to be processed. Applying traditional XRF data processing methods to MA-XRF data was prohibitively computationally expensive with the computer hardware available in the early 2010's and therefore methods had to be adapted to be practically feasible. Since then, several MA-XRF data processing methods have been developed. An overview of currently relevant methods is presented in section 1.3.1.

MA-XRF has some significant limitations for its application to cultural heritage science. Firstly, the output information is limited to elemental data and thus cannot be used to distinguish between chemical compounds which share an elemental footprint, like the pigments azurite ($Cu_3(CO_3)_2(OH)_2$) and malachite ($Cu_2CO_3(OH)_2$). The results are also limited in what elements can be identified. They are considered to be practically limited to elements with atomic numbers above 11 (Na),[35] but the specific sensitivity for each element depends on what specific setup is used.[36] Because of this, MA-XRF is usually considered unsuitable for the analysis of many compounds, like organic pigments, which lack any elements identifiable by this method. Beyond this, measurement times are also an issue, ranging from hours to months.[37]

EQUIPMENT

MA-XRF scanners generally consist of 4 main components: the X-ray source, the beam defining optic, the X-ray detector, and the positioning system. A diagram of how these are usually laid out is shown in figure 1.7. The selection of each of these

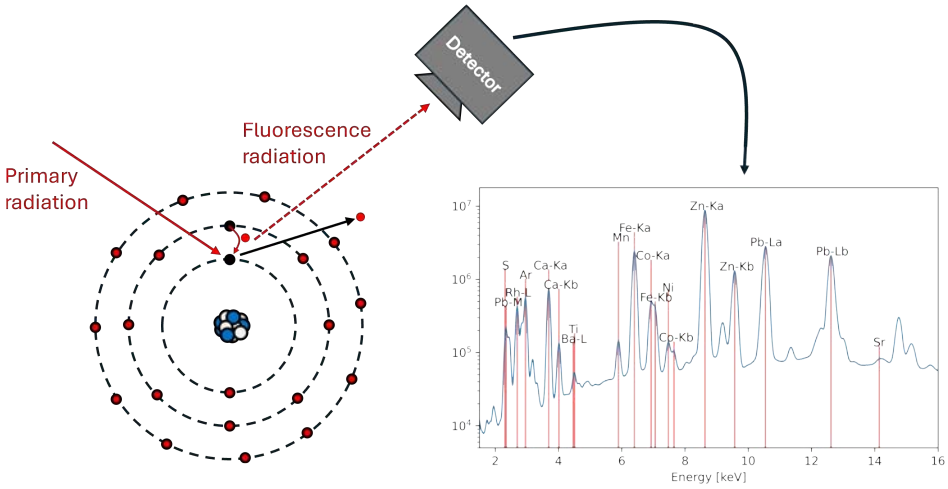

Figure 1.6.: Diagram showing the fundamental concepts of MA-XRF.

4 components thus defines the nature of the MA-XRF scanner.

In terms of X-ray sources, MA-XRF as a term tends to be primarily used for devices based on X-ray tubes, with synchrotron-based setups more commonly referred to as SR-XRF. However, the principle is the same and synchrotron-based setups are often included in discussions about MA-XRF scanning, as the high brilliance and monochromatic nature of the X-rays produced by synchrotrons provide analytical opportunities not possible with X-ray tubes. Beyond these two types of sources, no other alternative source has been documented, though a source based on Inverse Compton Scattering for cultural heritage research is in active development within the Smart*Light 2.0 project.[38]

The other 3 components of MA-XRF scanners theoretically hold a greater range of possible solutions, but in practice most devices tend to use the same basic design. Most scanners use either pinhole collimators or policapillary lenses as their beam defining optics and the great majority have some variation of a Cartesian coordinate robot as their positioning system (though alternatives have been proposed[39]). The choice of X-ray detector, their amount and their layout show a greater amount of variation, though most use one or two silicon drift detectors (SDDs).

The first documented examples of MA-XRF scanning measurements on cultural heritage objects come in the early 1990s, from an experimental scanner developed by Mantler et al.[40] This scanner was based on a Cartesian coordinate robot (1000 mm x 800 mm) fitted with a 2.8 kW/60 kV Siemens AG60 W-target X-ray tube with a 1 mm collimator and a Tracor-Northern Si(Li) detector. Later on, INTAX GmbH released the ArtTAX mobile XRF spectrometer,[41] which is based on a Cartesian coordinate robot (50 mm x 50 mm) fitted with a 30 W/50 kV metal-ceramic-type MCBM 50 X-ray tube with a polycapillary lens and a XFlash 5 mm^2 SDD. This device, whilst capable of producing area scans, is usually not considered an MA-XRF scanner, as the 50 mm x

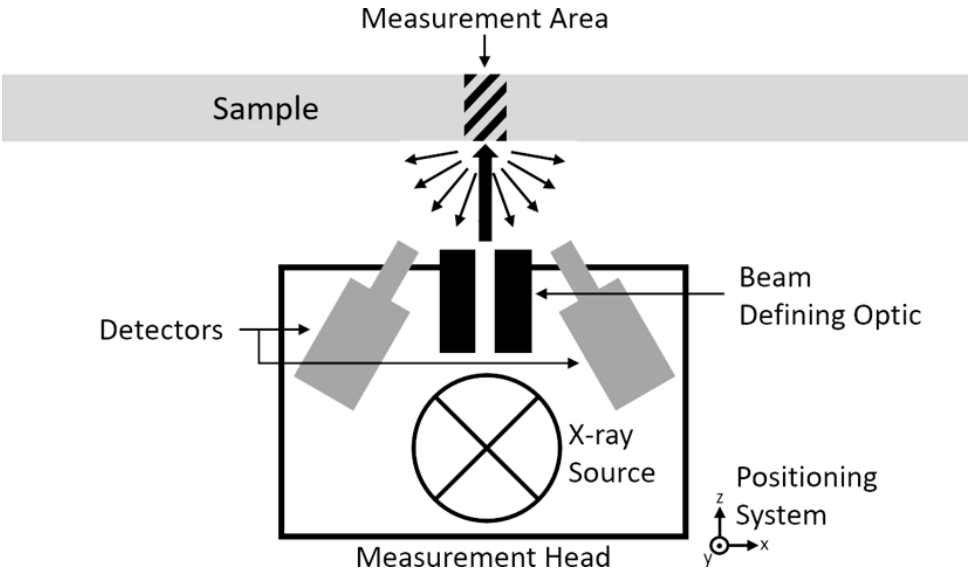

Figure 1.7.: Diagram of a MA-XRF scanner, showing its most relevant components: X-ray source, beam defining optic, X-ray detector, and positioning system.

50 mm robot is significantly smaller than the scanners prevalent when the term was coined, and as the ArtTAX scanner was not widely used for area scans. Both of these early MA-XRF scanners required long measurement times, with the earlier scanner documented as requiring over a minute per pixel, and with the ArtTAX requiring around at least a second per pixel, which significantly limited their applicability for large area scanning.

The first MA-XRF scanners considered practical were developed by Alfeld et al.[14] They developed 3 experimental scanners sequentially, with the final one, *Instrument C* consisting of a 50 W XOS X-Beam Powerflux Mo-target X-ray tube with a polycapillary lens, four Vortex EX 50 mm^2 SDDs and a 600 mm x 250 mm Cartesian coordinate robot. Following these first 3 prototypes, a collaboration with Bruker Nano GmbH resulted on what is now the most widespread MA-XRF scanner, the Bruker M6 Jetstream,[36] shown in figure 1.8, which was the first commercially available MA-XRF scanner. Many institutions make use of this scanner and it has been involved in many research projects.[37, 42–46] The M6 uses a 30 W (50 kV, 600 µA) Rh-target X-ray tube with a polycapillary lens and a 800 mm x 600 mm Cartesian coordinate robot. It can be outfitted with either one or two 60 mm^2 SDDs and can be used for vertical or horizontal scans. Bruker also offers another commercial MA-XRF scanner, the CRONO[47] (originally developed by XGLab S.R.L.), which uses a 10 W (50 kV, 200 µA) Rh-target X-ray tube with an exchangeable pinhole collimator (0.5, 1, 2 mm diameters), a 50 mm^2 SDD, and a 600 mm x 450 mm Cartesian coordinate robot, capable of both horizontal and vertical scans. Bruker also

recently revealed their new IRIS scanner,[48, 49] which is a combined MA-XRF/RIS scanner, but its MA-XRF components are the same as those in the CRONO.

Ravaud et al.[50, 51] developed an MA-XRF scanner which uses a 30 W (50 kV, 600 µA) ROENTEC X1 Mo-target X-ray tube with an exchangeable pinhole collimator (0.65, 1 mm diameter), an Amptek X123 50 mm^2 Fast SDD, and a 500 mm x 600 mm Cartesian coordinate robot. This scanner would later be improved further by Moreau et al.,[25, 52] not only to include also parallel RIS and LIS scanning, but also by exchanging the X-ray source for a more powerful 35 W (50 kV, 700 µA) iMOXS HELMUT-FISCHER Rh-target X-ray tube and the beam defining optic for an exchangeable optic using a pinhole collimator (0.2 – 0.8 mm diameter) or a polycapillary mini-lens.

Pouyet et al.[53] developed an MA-XRF scanner which uses a 12 W (60 kV, 200 µA) Moxtec Rh-target X-ray tube with a polycapillary lens which can be exchanged for a pinhole collimator if desired, a Bruker 50 mm^2 SDD, and a 840 mm x 840 mm Cartesian coordinate robot.

Delaney et al.[54, 55] developed a combined MA-XRF/RIS scanner which uses a 37.5 W XOS Rh-target X-ray tube with a polycapillary lens and a Vortex-90EX SDD. Whilst the positioning system used for this scanner is also a Cartesian coordinate robot, its implementation is unique in that the part that moves is actually the object rather than the measurement head. Its impressive 1700 mm x 1400 mm scan area also makes it the largest MA-XRF scanner described so far.

Romano et al.[56, 57] developed an MA-XRF scanner which uses a 30 W Rh-target X-ray tube with a polycapillary lens, six 40 mm^2 SDDs, and a 1200 mm x 900 mm x 200 mm Cartesian coordinate robot. The system is capable of horizontal (1200 mm x 200 mm) or vertical (1200 mm x 900 mm) scanning and the distance from the scan surface can be dynamically corrected during scanning using a laser sensor on the scan head. The large amount of detectors combined with the dynamic distance correction and a very small focal spot size (50 µm) makes the system capable of conducting very fast and very sharp MA-XRF scans, making the system one of the most advanced scanners in current operation.

A very promising recent development is the scanner developed by Wang et al.[58] This is a unique design based around the use of a six-axis robotic arm as a positioning system, which provides a scanning radius of over 900 mm, with an accuracy of less than 30 µm.[59] The scanner uses a Mo-target X-ray tube, a polycapillary lens capable of achieving a focal spot size of 42.2 µm, and an SDD. The scan head also has a depth camera used to determine the surface contour of the measured object, allowing not only dynamic distance correction, but also dynamic angle correction to ensure the incident X-ray beam is always perpendicular to the object surface. This allows for high quality scanning of complex curved surfaces.

A very unique system is that developed by Łach et al.[60] Unlike all the other systems described, this is a full-field XRF spectrometer, so it captures a full area in one measurement, rather than combining many small measurements. The system uses a 100 mm x 100 mm gas electron multiplier (GEM) detector in a pinhole camera capturing a 100 mm x 100 mm area illuminated by two 50 W (50 kV, 1 mA) Varian VF-50J Mo-target X-ray tubes. The scan head is mounted onto a robotic

Figure 1.8.: The most widely adopted MA-XRF is the Bruker M6 Jetstream. Highlighted are (1) the scan head which includes the X-ray source, polycapillary lens and two SDD X-ray detectors; and (2) the Cartesian coordinate robot positioning system.

arm for positioning, but it does not move during acquisition. The documented measurements use a readout pitch of 800 µm resulting in 128 readout channels in each spatial direction and an image spatial resolution of 110 µm. This system allows for the measurement of complex three-dimensional artworks, albeit as a two-dimensional projection and not a three-dimensional surface.[61] This novel kind of MA-XRF is very promising but has significant shortcomings. The energy resolution of the resulting measurements is quite poor compared to SDD-based scanners, with 1.1 keV full width at half maximum (FWHM) at 5.9 keV, compared to 122 eV FWHM at the same energy with an Amptek X123 50 mm^2 Fast SDD.[62] And whilst measurement times are comparatively quite fast, at around 20 to 30 minutes per frame, the measurements require significant initial setup, including the stabilisation of the gas amplification factor with respect to the polarisation effects of the GEM foil, with respect to the output of the X-ray source and with respect to the fluorescence of the object, which is documented to take around 11 hours. This does not have to be repeated between immediately subsequent measurements, and thus this approach could be faster than traditional raster scans when dealing with large

measurement campaigns, be them a singular large object or many small objects measured subsequently.

Overall, from a mechanical point of view, Cartesian MA-XRF scanners have become widespread, mature systems, and have reached their practical limit in development. The development of alternative positioning systems is promising but still presents significant challenges for their practical implementation, primarily in their movement pathing. X-ray tubes and SDD detectors also seem to be mature technologies that will continue being used in MA-XRF scanners, and their development is expected to be incremental rather than revolutionary. The only exception being the significant potential of full-field MA-XRF devices, which could revolutionize the field if their practical limitations are addressed. Beyond that, the development of multi-modal scanners is a prominent research avenue.

DATA PROCESSING

The processing of MA-XRF data is traditionally based on the deconvolution of the different fluorescence peaks present in the measured spectra. The first and still most prominent tool for the evaluation of MA-XRF spectra is PyMCA,[63] which is based on the procedures described by Van Espen.[64] PyMCA uses a linear least-squares (L-LS) fitting approach, optimized to account for a priori information like peak position and element line groups. This approach, whilst accurate, proved too time consuming for increasingly large MA-XRF scans, leading to the development of the Datamuncher software.[65] Datamuncher makes use of dynamic analysis (DA)[66] to perform unrestricted linear least-squares (UL-LS) by means of the matrix multiplication:

$$A = \Gamma S \tag{1.1}$$

where A is a vector comprised of the intensity of all the fluorescence peaks, S is the full spectrum and Γ is the so called DA matrix. The DA matrix is a collection of elemental profiles which contribute to the spectrum. This matrix is usually determined by performing an initial non-linear least-squares (NL-LS) fit of the sum spectrum of the dataset using PyMCA. Datamuncher became widespread during the early days of MA-XRF scanning and remains a common tool for the processing of MA-XRF data. The DA approach proved successful enough to later be implemented directly into PyMCA as well.

Since those initial days of MA-XRF, significant progress has been made in the field of machine learning (ML), leading to a variety of ML-based methods for the analysis of MA-XRF data. The main concepts of ML are covered in more detail in section 1.4.1, but here we highlight a few of the methods used for MA-XRF data processing.

Preisler et al.[67] recently described a deep learning convolutional neural network (CNN) model trained on purely synthetic data generated by Monte Carlo (MC) simulations. The initial results show great potential, even providing less noisy elemental maps for certain elements than traditional MA-XRF processing methods. The use of synthetic data should make the model scanner-agnostic, but further testing is required to prove systems beyond their in-house built scanners and with more diverse data-sets.

Vermeulen et al.[68] developed the XRFast software package, which uses sparse dictionary learning combined with a non-negativity constrained approximate Singular Value Decomposition (K-SVD). This ultimately results not in elemental distribution maps per se, but something more akin to pigment distribution maps which already include some amount of elemental correlation information.

Kogou et al.[46] described an approach based on self-organizing maps (SOMs). This approach is different than the others discussed here as it does not output concentration maps, but instead produces cluster maps, categorizing each pixel into a specific cluster based on its spectrum. This is a fundamentally different approach, but one that can provide significant insight into the spatial distribution of the measurement. This approach is also more method-agnostic than those discussed previously, which makes it possible to expand it to include other kinds of information, allowing for multi-modal approaches.

Generally, the processing of MA-XRF data based on deconvolution is considered to be a solved problem, and any developments in this would likely be incremental increases in computation speeds. However, ML methods present a potential revolution to how MA-XRF data is processed, both in how the elemental distribution maps are produced and in how those maps are further evaluated.

1.3.2. RIS

As mentioned previously, RIS is based on measuring the amount of light reflected by a target object along many contiguous spectral channels, as shown in figure 1.9. The spectral ranges most commonly considered are UV, visible, near-infrared (NIR) (700 – 1000 nm), and SWIR (1000 – 2500 nm). The spectral range considered depends on the sensor being used for the acquisition, with the most common being Si charge-coupled device (CCD)/complementary metal-oxide-semiconductor (CMOS) (400 – 1000 nm), InGaAs (900 – 1700 nm), mercury cadmium telluride (MCT) (900 – 2500 nm) and InSb (1000 – 2500 nm).[69] Each of the spectral ranges provide certain kinds of information, with the VNIR range providing electronic transitions, particularly useful when studying semi-conductive materials, and the SWIR range providing information on vibrational modes.

Unlike MA-XRF, RIS is a method that was already commercially developed before its implementation into cultural heritage science. The method had been extensively used in the realm of remote sensing for geology and mining, and thus a variety of equipment and data processing tools were available. However, this does not mean these were particularly well suited for cultural heritage science applications. Since its initial introduction in the 1990s,[70] specialized equipment and processing tools have been developed for heritage science and its use is becoming increasingly prevalent. Given the large variety of RIS systems available, a complete review is not possible within the context of this work, but section 1.3.2 covers some of the more prominent setups.

Also unlike MA-XRF, RIS is based on a physical phenomena that is much less well defined. Geometric and matrix effects play a significant role in the measured signal and these are very difficult to properly characterize and model. This has made RIS data processing a complex issue that has seen constant development. Section 1.3.2

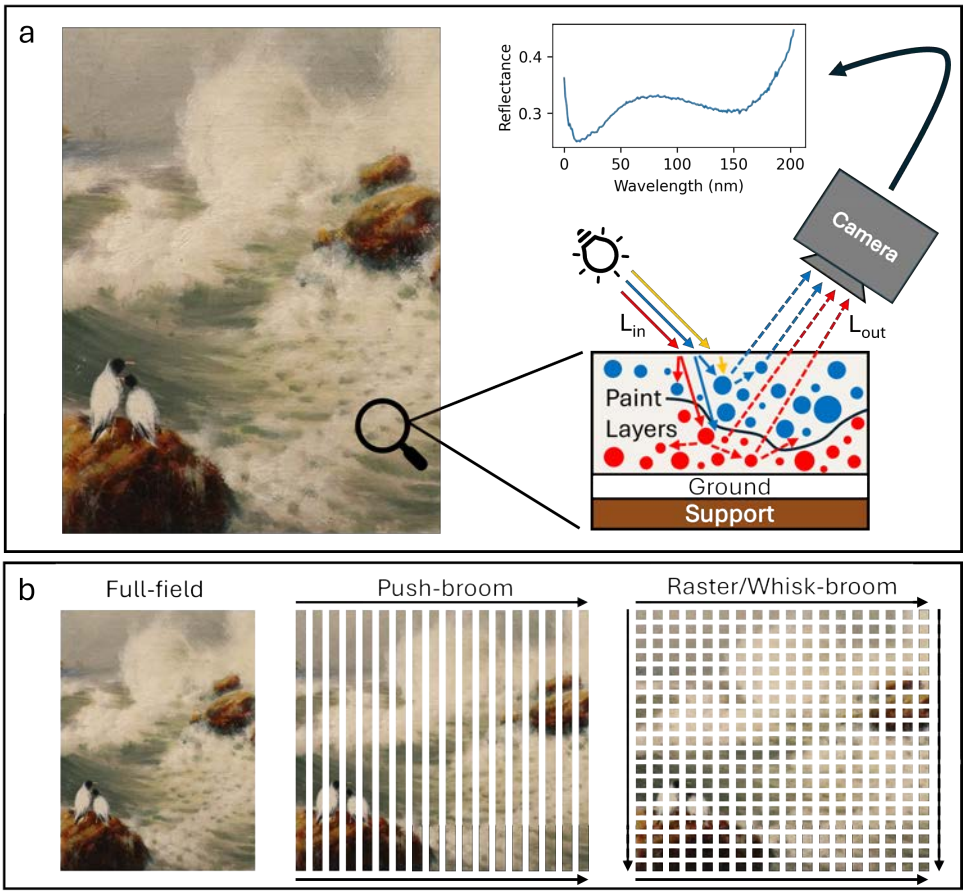

Figure 1.9.: a) Diagram showing the fundamental concepts of RIS. b) Different image acquisition geometries.

provides a brief overview of some of the RIS data processing methods used.

Given the variety of features that are present in the spectral ranges considered by RIS, it is applicable for the analysis of a large variety of chemical compounds. This includes certain organic pigments, like red lake,[71] and inorganic pigments, like goethite (α-FeO(OH)) and azurite.[72] However, the large variety of compounds combined with the complexity of the involved signals can make evaluation very complex and time-consuming, which is currently a significant limitation of the method.

EQUIPMENT

Figure 1.10 shows the basic components of a standard RIS setup. Whilst MA-XRF scanners function exclusively by combining a large set of point-based measurements,

often as a raster scan, RIS cameras have a greater variety of acquisition geometries. RIS setups are usually classified as either whisk-broom scanners (which are conceptually similar to raster scanners) or push-broom scanners, as shown in figure 1.10b.

Several large institutions now have RIS systems. The National Gallery of Art (Washington D.C., U.S.A.) was an early adopter of RIS and their system has inspired multiple further ones. Their initial system[73] consisted of a Surface Optics Corporation SOC-730VNIR Si CCD camera (417 – 973 nm, 2.25 nm sampling) and a Surface Optics Corporation SOC-720SWIR InGaAs camera (895 – 1749 nm, 10 nm sampling). Both cameras were slit-based systems with an internal mirror for spatial sweeping. The system was later changed,[74] then consisting of an Si electron-multiplying charge-coupled device (EMCCD) VNIR camera (400 – 950 nm, 2.5 nm sampling) and a digital ROIC InSb SWIR camera (1000 – 2450 nm, 2.8 nm sampling). Both the cameras are capable of operating in push-broom mode, by moving the painting in front of the camera, or as a whisk-broom, by using an internal scan mirror.

The Rijksmuseum (Amsterdam, the Netherlands) has a system described by Gabrieli et al.[72] The system consists of a Surface Optics Corporation SOC-710E EMCCD camera (400 – 1000 nm, 2.54 nm sampling) and a Headwall Photonics M640 MCT camera (900 – 2500 nm, 6 nm sampling). The system is usually operated in push-broom mode by using a specialized positioning easel to move the object in front of the camera. However, in the context of *Operation Night Watch,* the cameras were mounted onto a specialized imaging frame which scanned over the large painting, also in push-broom mode.

An RIS camera which has seen some adoption since its release is the Specim IQ.[69, 75, 76] The camera is a compact CMOS camera (400 – 1000 nm, 7 nm sampling) with an internal push-broom scanning mechanism. Its small size makes it highly portable and thus suitable for quick in-situ investigations. Its large focal depth (15 – ∞ cm) makes it suitable for both short and long-distance analysis, though its 512 x 512 pixel output suffers from limited spatial resolution. The relative affordability and ease of use of the system has made it a common choice for cultural heritage applications.

A recent development in RIS was the commercial release of the NIREOS HERA hyperspectral camera.[77, 78] This camera is based on Fourier-Transform spectroscopy and uses a novel birefringent interferometer,[79] combined with a Si CMOS sensor (400 – 1000 nm, 2 – 10 nm wavelength dependent sampling) to provide high spectral and spatial resolution. This system is unique within the ones documented here for its use of the birefringent interferometer to conduct spectral scanning rather than spatial scanning. The system has not yet seen widespread use in cultural heritage, but initial results are promising.

Beyond cameras, there are also RIS raster scanners, which tend to be multimodal devices. The Delaney et al. MA-XRF/RIS scanner[54] is outfitted with a Malvern PANalytical ASD FieldSpec 3 FORS (350 – 2500 nm, 1.4 – 2 nm sampling). The Moreau et al. MA-XRF/RIS/LIS scanner[25] is outfitted with an Ocean Insight QEPRO CCD spectrometer (200 – 1000 nm, 3 nm sampling) and an AVANTES Avaspex NIR-256 2.5 HSC-ECO InGaAs spectrometer (1000 – 2500 nm, 13 nm sampling). The

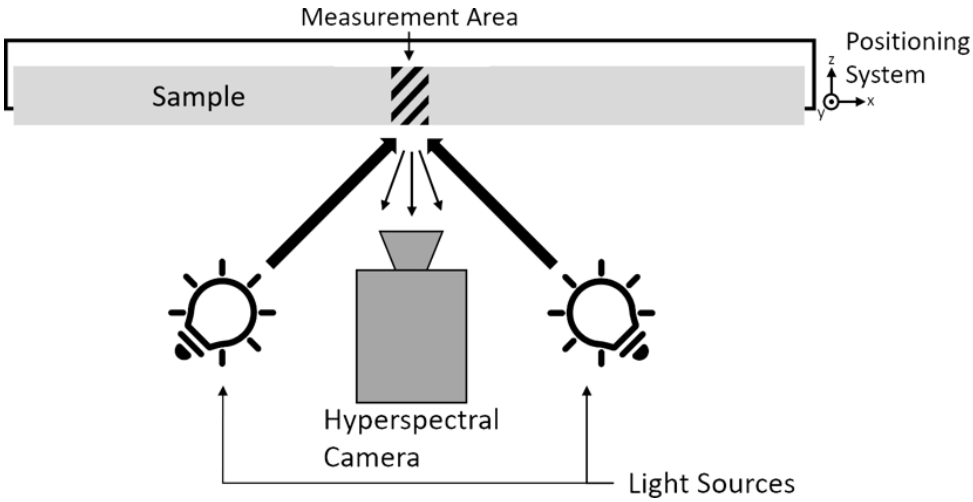

Figure 1.10.: Diagram of a push-broom RIS setup, showing its most relevant components: hyperspectral camera, light sources, and positioning system. Some push-broom systems may have the hyperspectral camera on the positioning system rather than the sample, or may have an internal scanning mechanism within the camera.

commercially available Bruker IRIS MA-XRF/RIS scanner[48, 49] is outfitted with a CMOS spectrometer (350 – 1100 nm, 1.5 nm sampling) and an InGaAs spectrometer (1100 – 2500 nm, 9 nm sampling).

Another different approach has been that of Liang et al.[80], which uses remote imaging systems for multispectral scanning. The multispectral imaging is conducted using either a telescope or traditional lenses, depending on the target distance, combined with a CCD detector with interference filters (400 – 900 nm, 50 nm sampling) and an imaging acousto-optic tunable filter (AOTF) spectrograph and an InGaAs detector (900 – 1700 nm).

Unlike with MA-XRF, RIS are still very varied. The adoption of specific commercial equipment, like the Specim IQ or the NIREOS HERA could potentially lead to greater homogeneity across the field, but that remains to be seen. As noted in section 1.3.1, the development of multi-modal scanners is a prominent current trend.

DATA PROCESSING

For a very long time, diffuse reflectance has been modelled using Kubelka-Munk (KM) theory.[81] This has seen some use in the processing of RIS data,[82–84] especially for quantitative analysis. However, its application requires a significant amount of a priori information that does not make it suitable for the general investigation of cultural heritage objects.

Lacking a reliable model for reflectance, RIS data processing has instead primarily focused on extracting characteristic spectra from the datacubes, which can then

be compared to reference spectra for different potential components. These characteristic spectra are often referred to as "endmembers". These endmembers can then be used to cluster the data according to each pixels relative similarity to a specific endmember. How one goes about determining the endmembers is where most data processing approaches differ, but most methods use some form of ML.

Early applications made use of the "hourglass paradigm" implemented in the ENVI software package.[73] This approach uses a minimum noise fraction (MNF) transform to both de-noise and reduce the dimensionality of the datacube. The reduced data can then be used to find the pixels in the dataset which most closely approximate the reduced components. From this selection of pixels, endmembers can be manually extracted. The clustering is then usually done manually using spectral angle mapping (SAM).

Since then, many novel methods have been described. Alfeld et al.[85] combined independent component analysis (ICA), singular value decomposition (SVD) and simplex volume maximization (SiVM) to describe spectral "archetypes". These are extreme spectra which describe the data rather than the "pure" spectra used as endmembers. A non-negative least-squares (NN-LS) regression is then conducted to form distribution images. This provided better results for the analysis of highly degraded and uneven traces of antique polychromy than could be achieved with the traditional binary clustering used with SAM. Pouyet et al.[86] described using t-distributed stochastic neighbour embedding (t-SNE) to provide a non-linear representation of the datacube, which could then be used to manually or automatically cluster the pixel data. Alfeld et al.[87] also made use of t-SNE, but applied the method to a combined MA-XRF/RIS datacube, providing multi-modal data processing. Vermeulen et al.[88] proposed the use of uniform manifold approximation and projection (UMAP) as an alternative to t-SNE, as it is both faster and provides a better preservation of the global and local structure of the dataset. Rohani et al.[82] described a method using a deep neural network (DNN) to identify constituent pigments followed by KM modelling to conduct non-linear spectral unmixing. Kogou et al.[89] described the use of a mix of unsupervised and supervised SOM for the clustering of large imaging datasets. Pouyet et al.[90] described a DNN-based method for the classification of pigments using SWIR RIS data.

Again unlike MA-XRF, the processing of RIS data is not a solved issue and remains extremely varied. Most methods are based around some sort of ML, and the majority are based around the reduction of the data into representative spectra and clustering. The implementation of ML methods for direct pigment classification is a prominent trend in the field, but their generalizability remains a significant challenge. A point of interest is the lack of approaches based on the targeted use of known reflectance features for the mapping of specific chemical compounds, akin to how MA-XRF data is processed using known elemental fluorescence features.

1.4. DATA EVALUATION

For all imaging techniques, the amount of information that can be derived from the measurements depends on how the data is evaluated. Alfeld et al.[87] describes a framework in which data evaluation is structured into four phases:

- Exploration: identifying the relevant chemical features present in the data.
- Evaluation: the data is reduced to a set of legible representations that contain all relevant chemical features.
- Interpretation: conclusions are drawn from these representations, based on the current research question.
- Presentation: these conclusions are communicated using the relevant representations as arguments.

Given the often highly exploratory nature of heritage science research, it is rare for any investigation to cleanly follow each phase in sequence. Instead, the exploration/evaluation/interpretation phases tend to be iterative, either as the results lead to the research question becoming more specific or as the results are used to guide subsequent measurements. What is usually considered as "data processing" focuses on the exploration and evaluation phases, work done primarily using machines and algorithms. Interpretation and presentation are then seen more as a researcher-driven endeavour, based primarily on knowledge and experience rather than algorithms. This is not completely wrong, but it minimizes the amount of input a researcher has on the exploration and evaluation phases and the effect of algorithms on the interpretation and presentation phases. Knowing how and when to apply any algorithm to address a specific research question will have as much of an effect as what algorithm is used to represent the results in the interpretation and presentation phases. Because of this it is of great importance to be aware of and familiar with a variety of data processing algorithms and approaches.

Sections 1.3.1 and 1.3.2 already document some of the relevant algorithms that have been applied for the analysis of MA-XRF and RIS data. Different ML methods have risen as the most prevalent approach for the analysis of hyperspectral data. The following section will provide a more detailed description of ML and the specific methods most prevalent in heritage science.

1.4.1. MACHINE LEARNING

Machine learning is described by Prof. Stephen Marsland as "making computers modify or adapt their actions so that these actions get more accurate, where accuracy is measured by how well the chosen actions reflect the correct ones."[91] The systems that modify the actions of the computer are the learning algorithms. These algorithms use existing data, referred to as "training data", to guide the required modifications. Machine learning algorithms can be categorized into several types, two of which are of particular interest in the context of this work: unsupervised and supervised methods. These approaches are fundamentally different, and are described in the following subsections.

1

UNSUPERVISED MACHINE LEARNING METHODS

Unsupervised ML methods are those which do not include what the "correct" answer is in the training data. This could be due to there not being a known "correct" answer to the question being asked or because it would be too time consuming to provide the "correct" answers to a sufficiently large amount of training data. Therefore, unsupervised ML algorithms are not meant to answer specific questions, but instead try to identify similarities within the training data.[91] Unsupervised methods are particularly well suited for the processing of chemical imaging data in heritage science, as the research is often exploratory.

Sections 1.3.1 and 1.3.2 already mentioned some unsupervised ML methods, like principal component analysis (PCA) and SOM. Most of the methods are based around the concept of matrix factorization, which is shown in figure 1.11. The problem this seeks to solve is to reduce the measured data matrix V of dimensions $d \times n$ into a product of a matrix W and a matrix H plus a remainder matrix R. In the case of hyperspectral imaging, V is an unfolded version of the datacube into a two-dimensional matrix in which d is the number of spectral channels and n is the number of pixels in the image. W represents the spectral information, with k signal components covering the spectral range of the original datacube, and H represents the spatial information, similarly unfolded into a set of k images of n pixels, with each image related to a signal component. The remainder matrix R is usually ignored, as it contains only measurement noise, but can be a good metric for the quality of the factorization.

$$V_{d\times n} = W_{d\times k} H_{k\times n} + R_{d\times n} \tag{1.2}$$

$$V_{d\times n} \approx W_{d\times k} H_{k\times n} \tag{1.3}$$

Equation 1.3 is similar to equation 1.1, because DA is functionally a matrix factorization method. In DA, W would contain the previously defined elemental fluorescence lines and H would be the distribution maps of each of these fluorescence lines. Unlike in DA, however, in unsupervised ML methods based on matrix factorization the signal components in W are not previously known, and the methods differ primarily in how these are defined.

The most commonly used unsupervised ML method in heritage science is PCA. First described in 1901,[92] PCA has seen widespread use in a plethora of applications.[93] PCA aims to describe the input data in as few meaningful components as possible by projecting the data onto a new coordinate system, along so called "principal components". Each of these principal components are orthogonal to each other and are ranked by the data variance they describe. Thus, the first principal component will be the direction upon which most of the variation in the data is described. The second principal component is the direction orthogonal to the first principal component which describes the second most amount of variation in the data, and so forth. In hyperspectral imaging, PCA is helpful for identifying the most significant signal correlations between the different channels in the datacube, and how they are spatially distributed. However, the only restriction on the components is that they are orthogonal to each other, meaning that they can

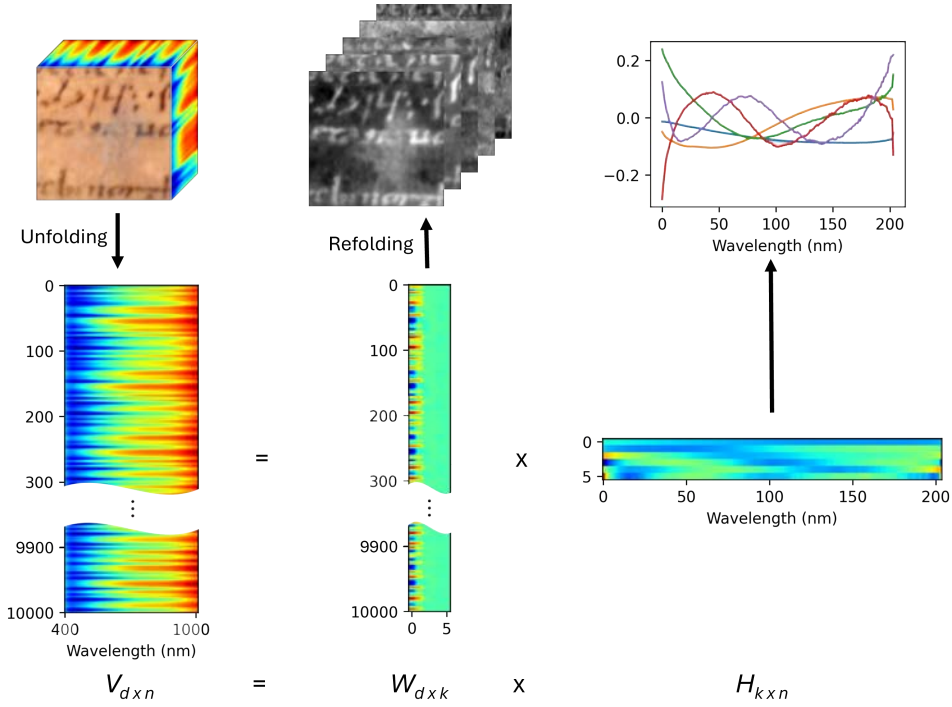

Figure 1.11.: Diagram of how matrix factorization is applied to spectral imaging data.

be positive or negative, which, in cases when the data is inherently non-negative, like MA-XRF and RIS, means that the components may not make physical sense, and thus usually can't be used for chemical characterisation. Figure 1.12 shows an example of PCA applied to an RIS dataset.

Because of this, one may wish to instead restrict all of the matrices to be non-negative, which is the concept behind non-negative matrix factorization (NMF). This approach, first described in its current form by Lee & Seung,[94] is applied much in the same way as PCA is, but the fully positive components may hold more physically significant information. However, unlike in PCA where the choice of k usually does not affect the principal components, as they are intrinsic to the data, the choice of k is crucial to NMF and has a direct effect on the components. Figure 1.13 shows an example of this, with NMF applied to an RIS dataset. Selecting the correct value for k is a non-trivial issue, and there are many methods for this.[95]

If, instead of restricting the components to be non-negative, one restricts the components to be statistically independent from each other, the result is ICA. First described by Jutten & Hérault[96] (initially referring to it as INCA), ICA is an example of blind source separation, where a mixed signal is broken into k original independent components. Much like NMF, the choice of k is a non-trivial issue that significantly affects the resulting components, as shown in figure 1.14

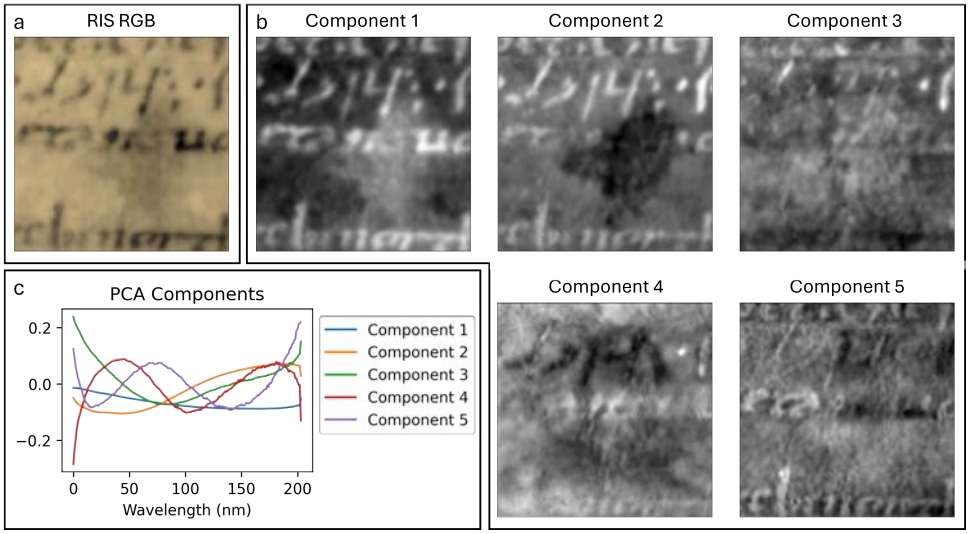

Figure 1.12.: Example of PCA applied to an RIS scan of a historical manuscript. a) RGB reconstruction based on the RIS data. b) Principal component maps 1-5. c) Principal components 1-5.

But not all unsupervised ML methods are based on matrix factorization. A popular such method is t-SNE, developed by van der Maaten & Hinton.[97] This is a method to visualize high-dimensional data by transferring each datapoint onto a new low-dimensional (usually two-dimensional) coordinate system. This new coordinate system does not hold any physical meaning and is determined by minimizing a cost function C. In this case, this function is the Kullback-Leibler divergence (KL) between a probability distributions P and Q, which represent the similarities between the datapoints within the original n-dimensional data x, and the similarities between the datapoints within the new low-dimensional map y as a Student t-distribution space with a single degree of freedom, respectively.

$$C = KL(P\|Q) = \sum_{i \neq j} p_{ij} \log \frac{p_{ij}}{q_{ij}} \tag{1.4}$$

with q_{ij} defined as:

$$q_{ij} = \frac{(1 + \|y_i - y_j\|^2)^{-1}}{\sum_{k \neq l}(1 + \|y_k - y_l\|^2)^{-1}} \tag{1.5}$$

and p_{ij} defined as:

$$p_{ij} = \frac{p_{j|i} + p_{i|j}}{2n} \tag{1.6}$$

where:

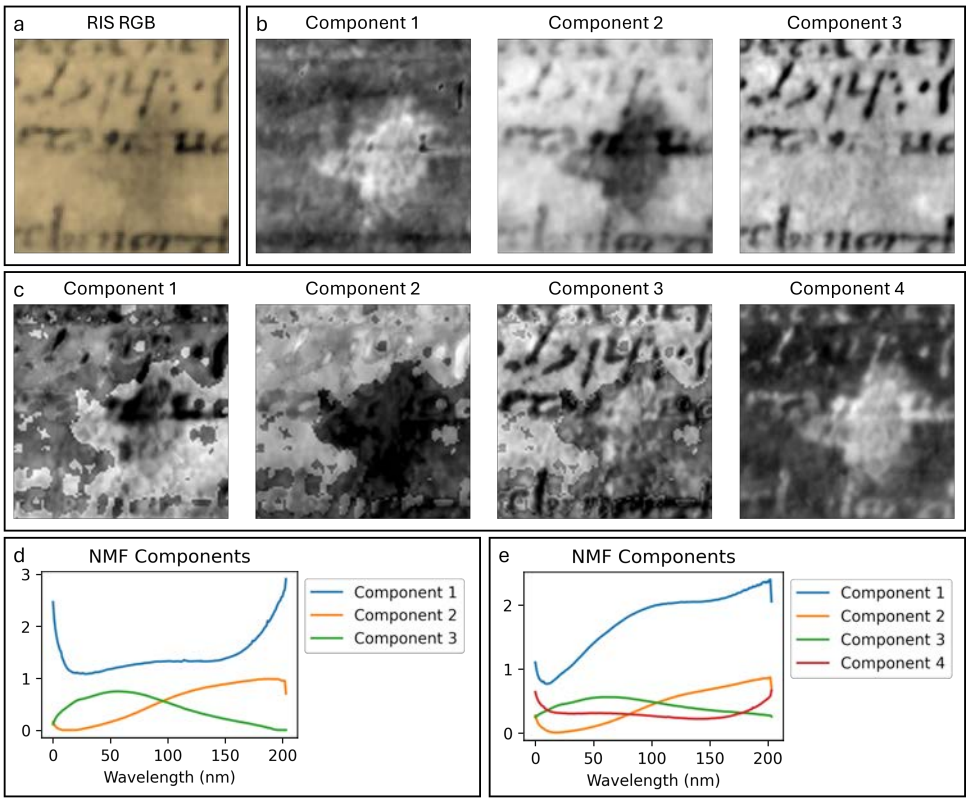

Figure 1.13.: Example of NMF applied to an RIS scan of a historical manuscript. a) RGB reconstruction based on the RIS data. b) NMF maps for k=3. c) NMF maps for k=4. d) NMF components for k=3. e) NMF components for k=4.

$$p_{i|j} = \frac{e^{-\|x_i - x_j\|^2/2\sigma_i^2}}{\sum_{k \neq i} e^{-\|x_i - x_k\|^2/2\sigma_i^2}} \tag{1.7}$$

where σ_i is the variance of the Gaussian function centered on datapoint x_i.

The resulting low-dimensional representation thus represents a measure of similarity between the datapoints within the dataset, which can then be used to cluster the original n-dimensional data, from which chemical information can then be extracted and mapped. An example of t-SNE applied to RIS data is shown in figure 1.15.

When it comes to processing hyperspectral data, one of the shortcomings of t-SNE is that it favours the preservation of local distances over global distances.[88] Thus, the distance between datapoints in the low-dimensional map does not always reflect the real similarity between the n-dimensional datapoints. To address this, McInnes

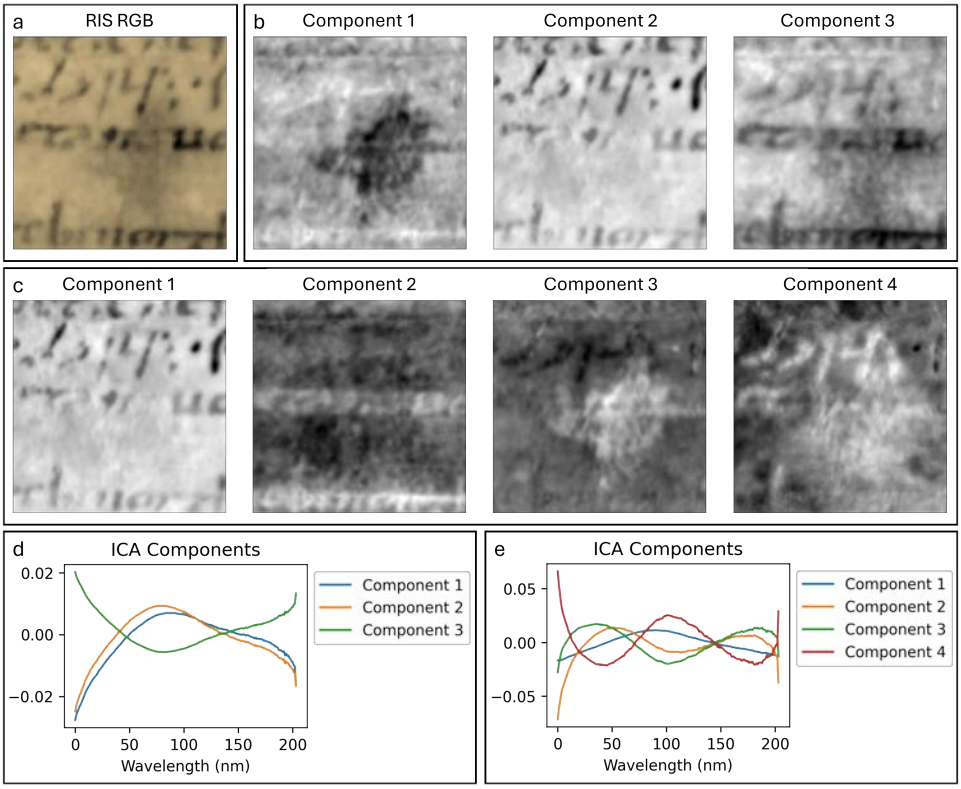

Figure 1.14.: Example of ICA applied to an RIS scan of a historical manuscript. a) RGB reconstruction based on the RIS data. b) ICA maps for k=3. c) ICA maps for k=4. d) ICA components for k=3. e) ICA components for k=4.

et al. developed UMAP,[98] which is conceptually similar to t-SNE, but in which the cost function C_{UMAP} is defined as:

$$C_{UMAP} = \sum_{i \neq j} v_{ij} \log \frac{v_{ij}}{w_{ij}} + (1 - v_{ij}) \log \left(\frac{1 - v_{ij}}{1 - w_{ij}} \right) \tag{1.8}$$

and where w_{ij} is defined as:

$$w_{ij} = (1 + a \| y_i - y_j \|_2^{2b})^{-1} \tag{1.9}$$

in which a and b are user-defined hyperparameters, and where v_{ij} is defined as:

$$v_{ij} = (v_{j|i} + v_{i|j}) - v_{j|i} v_{i|j} \tag{1.10}$$

where $v_{j|i}$ is defined as:

$$v_{j|i} = e^{(-d(x_i, x_j) - \rho_i)/\sigma_i} \tag{1.11}$$

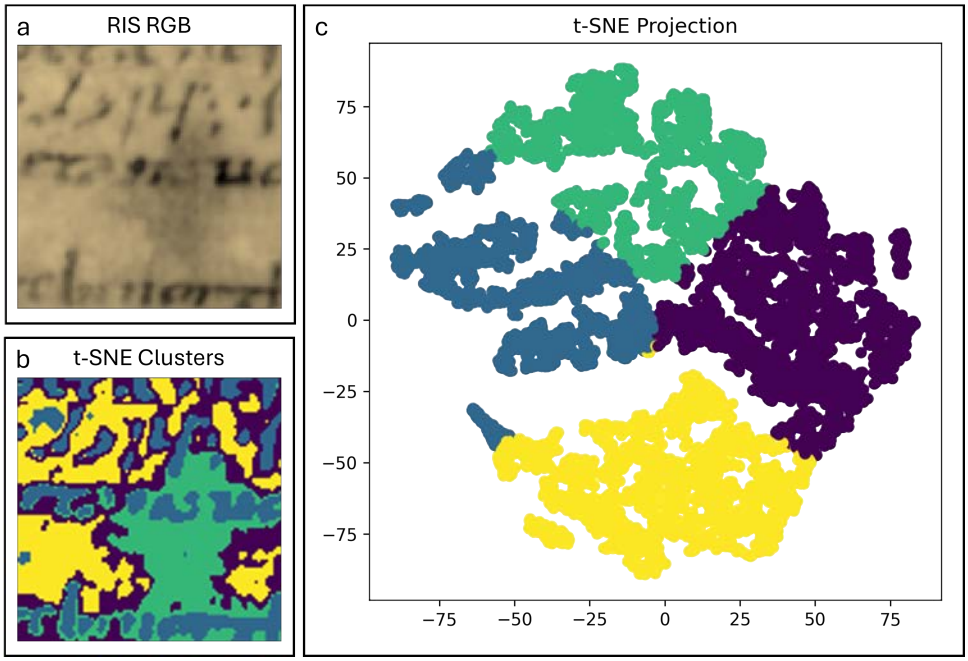

Figure 1.15.: Example of t-SNE applied to an RIS scan of a historical manuscript. a) RGB reconstruction based on the RIS data. b) t-SNE cluster map. c) t-SNE projection of the dataset, with clusters shown.

in which $d(x_i, x_j)$ is the distance between x_i and x_j, ρ_i is the distance between point x_i and its nearest neighbour, and σ_i is a normalizing factor, similar to σ_i in t-SNE but defined in a different way. Figure 1.16 shows an example of UMAP applied to RIS data.

SUPERVISED MACHINE LEARNING METHODS

Supervised ML methods are those which do include what the "correct" answer is in the training data, so the system can focus on determining what parts of the input actually relate to the expected answer, ultimately resulting in a generalizable answer that can be applied to new data.[91]

The most well known approach to supervised ML is artificial neural networks (ANNs), often just referred to as neural networks (NNs). The concept was first described by McCulloch and Pits[99] and first implemented by Rosenblatt in his perceptron.[100] These are systems composed of connected units, called neurons, which relate an input signal to an output signal. Each of the connections between two neurons has a certain weight that determines how the signal propagates. Each of the neurons has some sort of activation function that defines its output based on its input, and the neurons tend to be grouped into layers that share their inputs and have the same kind of activation function. These layers are classified by where

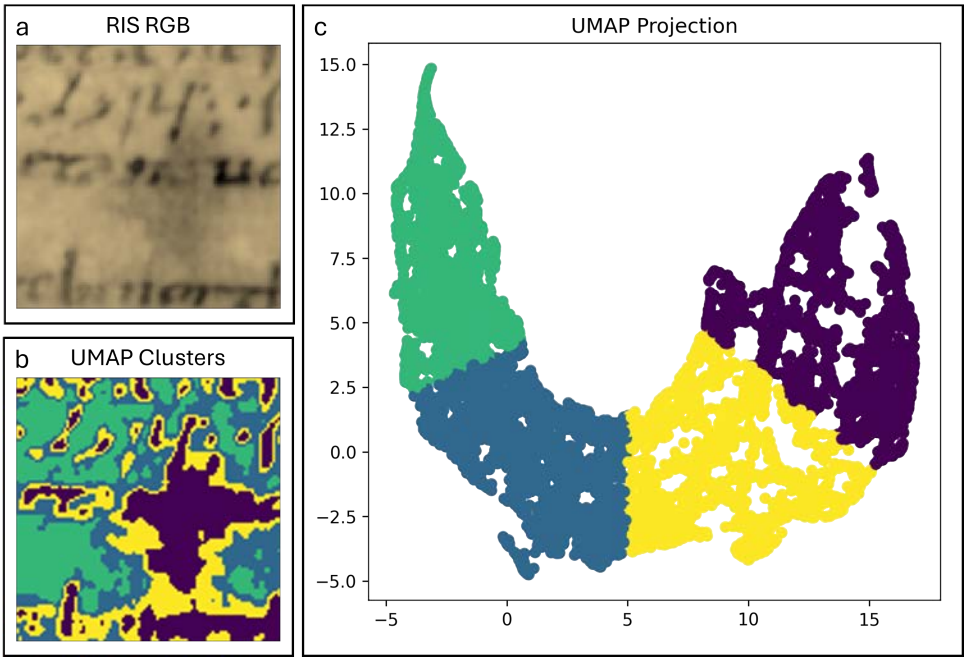

Figure 1.16.: Example of UMAP applied to an RIS scan of a historical manuscript. a) RGB reconstruction based on the RIS data. b) UMAP cluster map. c) UMAP projection of the dataset, with clusters shown.

they are located (input layer, hidden layer or output layer) and by how they connect to their surrounding layers (dense or fully-connected layers, convolutional layer, pooling layer, among others). How these layers are built up is referred to as the architecture of the network, as shown in figure 1.17. There are countless different architectures applied for countless different tasks.[101, 102]

NNs are trained using a variety of training algorithms using the available labelled data, usually referred to as the dataset, divided into a training dataset, which is used to actually train the system, a validation dataset, which is used to evaluate how the training is progressing, and a test dataset, which is used to evaluate the final model.[91] Confusingly, the dataset is sometimes also referred to as the training dataset,[90, 103] but it's important to remember not all the used data actually trains the system. The ratio between training, validation and testing data varies, but common ratios range from 50/25/25 to 80/10/10.[90, 104]

Beyond NNs, another prominent form of supervised ML is decision trees. They basically function by sequentially partitioning the data along one dimension at a time. The value at which the data is split is optimized to best segregate the data according to its labels.[105] Given their limited complexity, decision trees are most often used as parts of an ensemble, which is a set of multiple ML models that are used to produce a joint output. The most common form of this is known as a

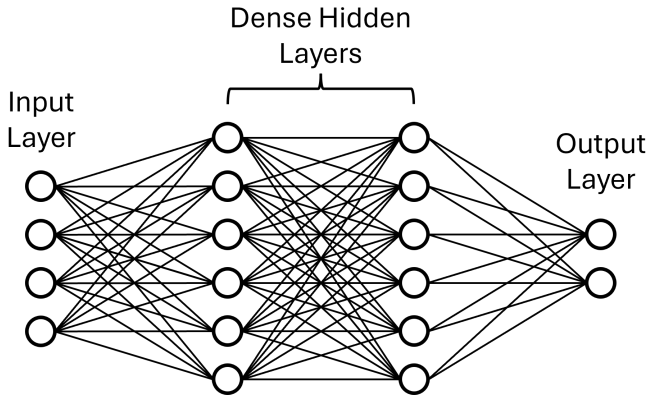

Figure 1.17.: Example of a NN architecture with one input layer, two dense hidden layers and one dense output layer.

random forest, first applied by Ho.[106] A random forest trains a variety of individual trees, each using only a randomly selected subspace of the overall feature space, and then the appropriate output is selected based on all the outputs of the individual trees, as shown in figure 1.18.

A tree ensemble approach that is currently prominent is that of gradient boosted trees. Boosting was first described by Freund & Schapire[107] and further developed into gradient boosting by Friedman et al.[108] Boosting is based on training simple, less accurate models, referred to as weak learners, to build an ensemble that functions as a highly accurate model, referred to as a strong learner.[109] This is conceptually similar to the already explained random forests, the difference being that the models are not trained separately from each other, but are instead trained sequentially. The output of the trained model m is used to weigh the data used to train model $m+1$, giving more weight to data that has been misclassified and less weight to data that has been correctly classified. Thus, each subsequent weak learner becomes better at classifying previously misclassified data, improving the overall performance of the strong learner. Gradient boosting follows the same principle, but adds a differentiable loss function L which the system seeks to minimize based on its gradient across the function space of the learner function $F(x)$. Gradient boosting can be applied to ML models using various types of weak learners, but decision trees are most common.[110] Given the accuracy of gradient boosting models, the method has become very prevalent in recent ML applications and has been implemented in multiple open-source frameworks like XGBoost,[111] which is further discussed in chapter 3, and LightGBM.[112]

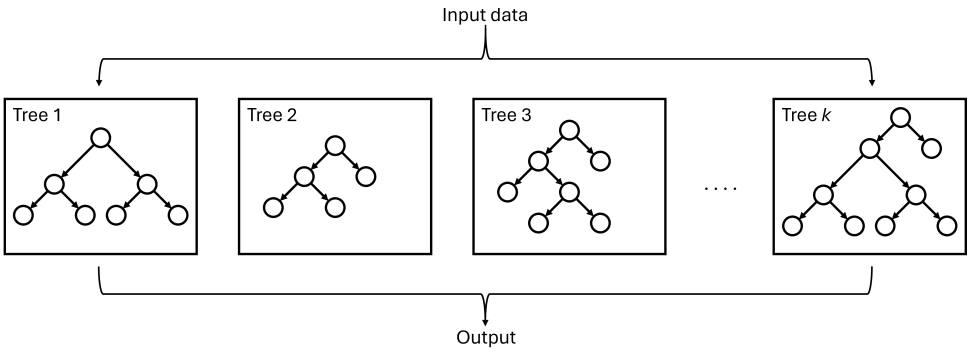

Figure 1.18.: Example of a decision tree ensemble.

BIBLIOGRAPHY

[1] UNESCO. *Mexico City Declaration on Cultural Policies*. Mexico City, 1982. arXiv: arXiv:1011.1669v3.

[2] UNESCO Institute for Statistics. *2009 UNESCO Framework for Cultural Statistics*. Montreal: UNESCO Institute for Statistics, 2009, pp. 1–101. ISBN: 9789291890750.

[3] Harvard University. *What is Cultural Heritage? | Whose Culture?* URL: https://projects.iq.harvard.edu/whoseculture/what-world-heritage.

[4] KIK-IRPA. *Closer to Van Eyck*. 2020. URL: https://closertovaneyck.kikirpa.be/.

[5] P. Coremans. *L'Agneau mystique au Laboratoire: Examen et Traitment*. De Sikkel-Anvers, 1953.

[6] G. van der Snickt, K. A. Dooley, J. Sanyova, H. Dubois, J. K. Delaney, E. Melanie Gifford, S. Legrand, N. Laquiere, and K. Janssens. "Dual mode standoff imaging spectroscopy documents the painting process of the Lamb of God in the Ghent Altarpiece by J. And H. Van Eyck". In: *Science Advances* 6.31 (2020). ISSN: 23752548. DOI: 10.1126/sciadv.abb3379.

[7] J. van Eyck and H. van Eyck. *Ghent Altarpiece*. 1432. URL: https://closertovaneyck.kikirpa.be/.

[8] A. Alvarez-Martin, J. Quanico, T. Scovacricchi, E. A. Clerici, G. Baggerman, and K. Janssens. "Chemical Mapping of the Degradation of Geranium Lake in Paint Cross Sections by MALDI-MSI". In: *Analytical Chemistry* 95 (49 Dec. 2023), pp. 18215–18223. ISSN: 15206882. DOI: 10.1021/acs.analchem.3c03992.

[9] G. Vanpaemel. "X-rays and old masters. The art of the scientific connoisseur". In: *Endeavour* 34 (2 June 2010), pp. 69–74. ISSN: 01609327. DOI: 10.1016/j.endeavour.2010.04.004.

[10] M. Alfeld and J. A. Broekaert. "Mobile depth profiling and sub-surface imaging techniques for historical paintings - A review". In: *Spectrochimica Acta - Part B Atomic Spectroscopy* 88 (Oct. 2013), pp. 211–230. ISSN: 05848547. DOI: 10.1016/j.sab.2013.07.009.

[11] S. Gondrom, J. Zhou, M. Maisl, H. Reiter, M. Kröning, and W. Arnold. "X-ray computed laminography: An approach of computed tomography for applications with limited access". In: *Nuclear Engineering and Design* 190 (1 1999), pp. 141–147. ISSN: 00295493. DOI: 10.1016/S0029-5493(98)00319-7.

[12] A. Wallert, G. Tauber, L. Porra, A. Bravin, K. Krug, and J. Dik. "A NOTE ON THE IMAGING OF LEAD WHITE AND VERMILION PAINT LAYERS BY SYNCHROTRON RADIATION-BASED, SIMULTANEOUS DUAL ENERGY K-EDGE ABSORPTION RADIOGRAPHY". In: *Journal of the American Institute for Conservation* 48 (2 2009), pp. 159–169. ISSN: 01971360. URL: http://www.jstor.org.tudelft.idm.oclc.org/stable/27784661.

[13] C. Fabritius. *Portrait of Abraham de Potter, Amsterdam Silk Merchant*. 1649. URL: https://id.rijksmuseum.nl/20027868.

[14] M. Alfeld, K. Janssens, J. Dik, W. De Nolf, and G. Van Der Snickt. "Optimization of mobile scanning macro-XRF systems for the in situ investigation of historical paintings". In: *Journal of Analytical Atomic Spectrometry* 26.5 (2011), pp. 899–909. ISSN: 02679477. DOI: 10.1039/c0ja00257g.

[15] S. D. Meyer, F. Vanmeert, R. Vertongen, A. V. Loon, V. Gonzalez, J. Delaney, K. Dooley, J. Dik, G. V. der Snickt, A. Vandivere, and K. Janssens. "Macroscopic x-ray powder diffraction imaging reveals Vermeer's discriminating use of lead white pigments in Girl with a Pearl Earring". In: *Science Advances* 5 (8 Aug. 2019). ISSN: 2375-2548. DOI: 10.1126/sciadv.aax1975. URL: https://www.science.org/doi/10.1126/sciadv.aax1975.

[16] J. Vermeer. *Girl with a Pearl Earring*. c. 1665. URL: https://www.mauritshuis.nl/en/our-collection/artworks/670-girl-with-a-pearl-earring.

[17] E. Rie. "Fluorescence of paint and varnish layers (part III)". In: *Studies in Conservation* 27 (Aug. 1982), pp. 102–108. DOI: 10.1179/sic.1982.27.3.102.

[18] N. Ludwig, J. Orsilli, L. Bonizzoni, and M. Gargano. "UV-IR image enhancement for mapping restorations applied on an Egyptian coffin of the XXI Dynasty". In: *Archaeological and Anthropological Sciences* 11 (Nov. 2019), pp. 6841–6850. DOI: 10.1007/s12520-019-00943-z.

[19] C. Invernizzi, G. Fichera, M. Licchelli, and M. Malagodi. "A non-invasive stratigraphic study by reflection FT-IR spectroscopy and UV-induced fluorescence technique: The case of historical violins". In: *Microchemical Journal* 138 (May 2018), pp. 273–281. DOI: 10.1016/j.microc.2018.01.021.

[20] Rijksmuseum. *Ultra high resolution photo*. 2022. URL: https://www.rijksmuseum.nl/en/stories/operation-night-watch/story/ultra-high-resolution-photo.

[21] A. Marrocchesi and R. G. Erdmann. "Empowering Cultural Heritage Photography: A Low-Cost, Automated, Open-Source Approach". In: *AHM Conference 2024: 'Heritage, Memory and Material Culture'* 3 (2024), pp. 89–95.

[22] A. J. Zawacki, K. A. Huskin, H. Davies, T. Kleynhans, D. Messinger, and G. Heyworth. "Fragments under the Lens: A Case Study of Multispectral versus Hyperspectral Imaging for Manuscript Recovery". In: *Digital Philology: Journal of Medieval Cultures* 12.1 (2023), pp. 123–143. ISSN: 21629552. DOI: 10.1353/dph.2023.0004.

[23] J. K. Delaney, M. Thoury, J. G. Zeibel, P. Ricciardi, K. M. Morales, and K. A. Dooley. "Visible and infrared imaging spectroscopy of paintings and improved reflectography". In: *Heritage Science* 4 (1 2016). ISSN: 20507445. DOI: 10.1186/s40494-016-0075-4.

[24] R. Radpour, G. A. Gates, I. Kakoulli, and J. K. Delaney. "Identification and mapping of ancient pigments in a Roman Egyptian funerary portrait by application of reflectance and luminescence imaging spectroscopy". In: *Heritage Science* 10.1 (2022), pp. 1–16. ISSN: 20507445. DOI: 10.1186/s40494-021-00639-5. URL: https://doi.org/10.1186/s40494-021-00639-5.

[25] R. Moreau, T. Calligaro, L. Pichon, B. Moignard, S. Hermon, and I. Reiche. "A multimodal scanner coupling XRF, UV–Vis–NIR photoluminescence and Vis–NIR–SWIR reflectance imaging spectroscopy for cultural heritage studies". In: *X-Ray Spectrometry* 53.4 (2024), pp. 271–281. ISSN: 10974539. DOI: 10.1002/xrs.3364.

[26] J. Vermeer. *The Milkmaid*. c. 1660. URL: https://id.rijksmuseum.nl/200108369.

[27] Rijksmuseum. *Rijksmuseum reveals major discoveries on Vermeer's painting The Milkmaid - Rijksmuseum*. Sept. 2022. URL: https://www.rijksmuseum.nl/en/press/press-releases/rijksmuseum-reveals-major-discoveries-on-vermeer-s-painting-the-milkmaid.

[28] M. Iwanicka, M. Sylwestrzak, and P. Targowski. "Optical Coherence Tomography (OCT) for Examination of Artworks". In: *Advanced Characterization Techniques, Diagnostic Tools and Evaluation Methods in Heritage Science*. Ed. by D. M. Bastidas and E. Cano. 1st ed. Springer International Publishing, 2018, pp. 49–59. DOI: 10.1007/978-3-319-75316-4_4.

[29] M. Alfeld and L. de Viguerie. "Recent developments in spectroscopic imaging techniques for historical paintings - A review". In: *Spectrochimica Acta - Part B Atomic Spectroscopy* 136 (2017), pp. 81–105. ISSN: 05848547. DOI: 10.1016/j.sab.2017.08.003. URL: https://doi.org/10.1016/j.sab.2017.08.003.

[30] C. L. Koch Dandolo, M. Picollo, C. Cucci, and P. U. Jepsen. "Fra Angelico's painting technique revealed by terahertz time-domain imaging (THz-TDI)". In: *Applied Physics A: Materials Science and Processing* 122.10 (2016), pp. 1–8. ISSN: 14320630. DOI: 10.1007/s00339-016-0396-x.

[31] K. Fukunaga. *THz technology applied to cultural heritage*. Springer Japan, 2016. ISBN: 978-4-431-55883-5. DOI: 10.1007/978-4-431-55885-9. URL: https://link.springer.com/content/pdf/10.1007/978-4-431-55885-9.pdf.

[32] E. S. Reyes-Reyes, R. Carriles-Jaimes, E. D'Angelo, S. Nazir, C. L. Koch-Dandolo, F. Kuester, P. U. Jepsen, and E. Castro-Camus. "Terahertz time-domain imaging for the examination of gilded wooden artifacts". In: *Scientific Reports* 14.1 (2024), pp. 1–8. ISSN: 20452322. DOI: 10.1038/s41598-024-56913-6. URL: https://doi.org/10.1038/s41598-024-56913-6.

[33] D. Mannes and E. H. Lehmann. “Neutron Imaging of Cultural Heritage Objects”. In: *Handbook of Cultural Heritage Analysis*. Ed. by S. D’Amico and V. Venuti. Vol. 1. Cham: Springer Nature Switzerland, 2022, pp. 211–237. ISBN: 9783030600167. DOI: 10.1007/978-3-030-60016-7_9.

[34] Y. Li, S. Creange, Z. Zhou, W. Southworth, A. Pappot, and L. van Eijck. “Exploiting activation radiation from neutron tomography reveals the hidden elemental composition of 3D art objects for free”. In: *Scientific Reports* 14.1 (2024), pp. 1–11. ISSN: 20452322. DOI: 10.1038/s41598-024-80047-4.

[35] M. Schreiner, B. Frühmann, D. Jembrih-Simbürger, and R. Linke. “X-rays in art and archaeology: An overview”. In: *Powder Diffraction* 19 (1 2004), pp. 3–11. ISSN: 0885-7156. DOI: 10.1154/1.1649963.

[36] M. Alfeld, J. V. Pedroso, M. V. E. Hommes, G. V. D. Snickt, G. Tauber, J. Blaas, M. Haschke, K. Erler, J. Dik, and K. Janssens. “A mobile instrument for in situ scanning macro-XRF investigation of historical paintings”. In: *Journal of Analytical Atomic Spectrometry* 28 (5 2013), pp. 760–767. ISSN: 13645544. DOI: 10.1039/c3ja30341a.

[37] N. De Keyser, F. T. Broers, F. Vanmeert, A. van Loon, F. Gabrieli, S. De Meyer, A. Gestels, V. Gonzalez, E. Hermens, P. Noble, F. Meirer, K. Janssens, and K. Keune. “Discovery of pararealgar and semi-amorphous pararealgar in Rembrandt’s The Night Watch: analytical study and historical contextualization”. In: *Heritage Science* 12.1 (2024), pp. 1–20. ISSN: 20507445. DOI: 10.1186/s40494-024-01350-x. URL: https://doi.org/10.1186/s40494-024-01350-x.

[38] Interreg Vlanderen-Nederland. *Interreg | About us | Smart*Light 2.0*. 2023. URL: https://interregvlaned.eu/en/smart-light-2-0/over-ons.

[39] M. Alfeld, P. Tempel, and V. van der Wijk. “Cable Robots as Conventional Linear Stage Alternatives for the Investigation of Complex-Shaped Objects via Macroscopic X-ray Fluorescence Imaging”. In: *Quantum Beam Science* 7.4 (2023), pp. 1–10. ISSN: 2412382X. DOI: 10.3390/qubs7040037.

[40] M. Mantler, M. Schreiner, F. Weber, R. Ebner, and F. Mairinger. “An X-Ray Spectrometer for Pixel Analysis of Art Objects”. In: *Advances in X-ray Analysis* 35 (B 1991), pp. 987–993. ISSN: 0376-0308. DOI: DOI:10.1154/S0376030800013215. URL: https://www.cambridge.org/core/product/F336B506AA10F48344BE950A135C2DCF.

[41] H. Bronk, S. Röhrs, A. Bjeoumikhov, N. Langhoff, J. Schmalz, R. Wedell, H.-E. Gorny, A. Herold, and U. Waldschläger. “ArtTAX – a new mobile spectrometer for energy-dispersive micro X-ray fluorescence spectrometry on art and archaeological objects”. In: *Fresenius’ Journal of Analytical Chemistry* 371 (3 2001), pp. 307–316. ISSN: 1432-1130. DOI: 10.1007/s002160100989. URL: https://doi.org/10.1007/s002160100989.

[42] J. K. Delaney, K. A. Dooley, A. van Loon, and A. Vandivere. “Mapping the pigment distribution of Vermeer’s Girl with a Pearl Earring”. In: *Heritage Science* 8.1 (2020), pp. 1–16. ISSN: 20507445. DOI: 10.1186/s40494-019-0348-9. URL: https://doi.org/10.1186/s40494-019-0348-9.

[43] S. Yan, J. J. Huang, N. Daly, C. Higgitt, and P. L. Dragotti. "Revealing hidden drawings in Leonardo's 'The Virgin of the Rocks' from macro X-ray fluorescence scanning data through element line localisation". In: *ICASSP, IEEE International Conference on Acoustics, Speech and Signal Processing - Proceedings* 2020-May.May (2020), pp. 1444–1448. ISSN: 15206149. DOI: 10.1109/ICASSP40776.2020.9054460.

[44] A. Haddad, G. Pastorelli, A. S. Ortiz Miranda, L. Ludvigsen, S. A. Centeno, I. Duvernois, C. Hoover, M. Duffy, A. Aviram, and L. Zycherman. "Exploring the private universe of Henri Matisse in The Red Studio". In: *Heritage Science* 10.1 (2022), pp. 1–27. ISSN: 20507445. DOI: 10.1186/s40494-022-00797-0. URL: https://doi.org/10.1186/s40494-022-00797-0.

[45] P. Ricciardi, K. A. Dooley, D. MacLennan, G. Bertolotti, F. Gabrieli, C. S. Patterson, and J. K. Delaney. "Use of standard analytical tools to detect small amounts of smalt in the presence of ultramarine as observed in 15th-century Venetian illuminated manuscripts". In: *Heritage Science* 10.1 (2022), pp. 1–19. ISSN: 20507445. DOI: 10.1186/s40494-022-00671-z. URL: https://doi.org/10.1186/s40494-022-00671-z.

[46] S. Kogou, L. Lee, G. Shahtahmassebi, and H. Liang. "A new approach to the interpretation of XRF spectral imaging data using neural networks". In: *X-Ray Spectrometry* 50.4 (2021), pp. 310–319. ISSN: 10974539. DOI: 10.1002/xrs.3188.

[47] R. Alberti, T. Frizzi, L. Bombelli, M. Gironda, N. Aresi, F. Rosi, C. Miliani, G. Tranquilli, F. Talarico, and L. Cartechini. "CRONO: a fast and reconfigurable macro X-ray fluorescence scanner for in-situ investigations of polychrome surfaces". In: *X-Ray Spectrometry* 46.5 (2017), pp. 297–302. ISSN: 10974539. DOI: 10.1002/xrs.2741.

[48] E. Catelli, Z. Li, G. Sciutto, P. Oliveri, S. Prati, M. Occhipinti, A. Tocchio, R. Alberti, T. Frizzi, C. Malegori, and R. Mazzeo. "Towards the non-destructive analysis of multilayered samples: A novel XRF-VNIR-SWIR hyperspectral imaging system combined with multiblock data processing". In: *Analytica Chimica Acta* 1239.September 2022 (2023), p. 340710. ISSN: 18734324. DOI: 10.1016/j.aca.2022.340710. URL: https://doi.org/10.1016/j.aca.2022.340710.

[49] M. Occhipinti, R. Alberti, T. Parsani, C. Dicorato, P. Tirelli, M. Gironda, A. Tocchio, and T. Frizzi. "IRIS: A novel integrated instrument for co-registered MA-XRF mapping and VNIR-SWIR hyperspectral imaging". In: *X-Ray Spectrometry* January 2023 (2023), pp. 520–530. ISSN: 10974539. DOI: 10.1002/xrs.3405.

[50] E. Ravaud, L. Pichon, E. Laval, V. Gonzalez, M. Eveno, and T. Calligaro. "Development of a versatile XRF scanner for the elemental imaging of paintworks". In: *Applied Physics A: Materials Science and Processing* 122.1 (2016), pp. 1–7. ISSN: 14320630. DOI: 10.1007/s00339-015-9522-4.

[51] J. Tapia, M. Eveno, T. Calligaro, L. Pichon, E. Laval, E. Ravaud, and I. Reiche. "Efficiency of combined MA-XRF and CXRF to give nondestructive insights about changes of a historical painting". In: *European Physical Journal Plus* 138.1 (2023), pp. 1–12. ISSN: 21905444. DOI: 10.1140/epjp/s13360-022-03596-5.

[52] R. Moreau, L. Brunel -Duverger, L. Pichon, B. Moignard, D. Gourier, and T. Calligaro. "Application of a MA-XRF/RIS/PL scanner to paintwork studies". In: *European Physical Journal Plus* 138.1 (2023). ISSN: 21905444. DOI: 10.1140/epjp/s13360-022-03604-8. URL: https://doi.org/10.1140/epjp/s13360-022-03604-8.

[53] E. Pouyet, N. Barbi, H. Chopp, O. Healy, A. Katsaggelos, S. Moak, R. Mott, M. Vermeulen, and M. Walton. "Development of a highly mobile and versatile large MA-XRF scanner for in situ analyses of painted work of arts". In: *X-Ray Spectrometry* April (2020), pp. 1–9. ISSN: 10974539. DOI: 10.1002/xrs.3173.

[54] J. K. Delaney, D. M. Conover, K. A. Dooley, L. Glinsman, K. Janssens, and M. Loew. "Integrated X-ray fluorescence and diffuse visible-to-near-infrared reflectance scanner for standoff elemental and molecular spectroscopic imaging of paints and works on paper". In: *Heritage Science* 6 (1 2018), pp. 1–12. ISSN: 20507445. DOI: 10.1186/s40494-018-0197-y. URL: https://doi.org/10.1186/s40494-018-0197-y.

[55] K. A. Dooley, D. M. Conover, L. D. Glinsman, and J. K. Delaney. "Complementary standoff chemical imaging to map and identify artist materials in an early italian renaissance panel painting". In: *Angewandte Chemie - International Edition* 53.50 (2014), pp. 13775–13779. ISSN: 15213773. DOI: 10.1002/anie.201407893.

[56] F. P. Romano, E. Puglia, C. Caliri, D. P. Pavone, M. Alessandrelli, A. Busacca, C. G. Fatuzzo, K. J. Fleischer, C. Pernigotti, Z. Preisler, C. Vassallo, G. Verhasselt, C. Miliani, and G. Ranocchia. "Layout of ancient Greek papyri through lead-drawn ruling lines revealed by Macro X-Ray Fluorescence Imaging". In: *Scientific Reports* 13.1 (2023), pp. 1–11. ISSN: 20452322. DOI: 10.1038/s41598-023-33242-8. URL: https://doi.org/10.1038/s41598-023-33242-8.

[57] F. P. Romano, C. Caliri, P. Nicotra, S. Di Martino, L. Pappalardo, F. Rizzo, and H. C. Santos. "Real-time elemental imaging of large dimension paintings with a novel mobile macro X-ray fluorescence (MA-XRF) scanning technique". In: *Journal of Analytical Atomic Spectrometry* 32.4 (2017), pp. 773–781. ISSN: 13645544. DOI: 10.1039/c6ja00439c.

[58] Y. Wang, Q. Xu, Y. Li, C. Wei, and L. Wei. "3-D μXRF Imaging System for Curved Surface". In: *IEEE Transactions on Instrumentation and Measurement* 73 (2024), pp. 1–11. ISSN: 1557-9662. DOI: 10.1109/TIM.2024.3470990.

[59] Q. Xu, Y. Wang, X. Zhou, P. Duan, Y. Liu, J. Gao, L. Wei, C. Wei, and L. Qu. "Applications of surface adaptive micro X-ray fluorescence scanner in cultural relics". In: *npj Heritage Science* 13 (1 2025), p. 365. ISSN: 3059-3220. DOI: 10.1038/s40494-025-01936-z. URL: https://doi.org/10.1038/s40494-025-01936-z.

[60] B. Łach, T. Fiutowski, S. Koperny, P. Krupska-Wolas, M. Lankosz, A. Mendys-Frodyma, B. Mindur, K. Świentek, P. Wiaceką, P. M. Wróbel, and W. Dabrowskią. "Application of factorisation methods to analysis of elemental distribution maps acquired with a full-field XRF imaging spectrometer". In: *Sensors* 21 (23 Dec. 2021). ISSN: 14248220. DOI: 10.3390/s21237965.

[61] B. Łach, T. Fiutowski, J. M. del Hoyo-Meléndez, S. Koperny, P. Krupska-Wolas, B. Mindur, P. Wiącek, P. M. Wróbel, and W. Dąbrowski. "Application of a Full-Field macro-XRF imaging spectrometer to non-invasive investigation of elemental composition in three-dimensional artworks". In: *npj Heritage Science* 13 (1 2025), p. 58. ISSN: 3059-3220. DOI: 10.1038/s40494-025-01646-6. URL: https://doi.org/10.1038/s40494-025-01646-6.

[62] AMPTEK Inc. *FAST SDD® Ultra High Performance Silicon Drift Detector – Amptek – X-Ray Detectors and Electronics*. 2025. URL: https://www.amptek.com/products/x-ray-detectors/fastsdd-x-ray-detectors-for-xrf-eds/fastsdd-silicon-drift-detector (visited on 02/23/2025).

[63] V. A. Solé, E. Papillon, M. Cotte, P. Walter, and J. Susini. "A multiplatform code for the analysis of energy-dispersive X-ray fluorescence spectra". In: *Spectrochimica Acta - Part B Atomic Spectroscopy* 62 (1 2007), pp. 63–68. ISSN: 05848547. DOI: 10.1016/j.sab.2006.12.002.

[64] P. Van Espen. "Spectrum Evaluation". In: *Handbook of X-Ray Spectrometry*. Ed. by R. Van Grieken and A. Markowicz. 2nd. New York, NY: Marcel Dekker, Inc., 2002. Chap. 4, pp. 239–339. ISBN: 0-8247-0600-5.

[65] M. Alfeld and K. Janssens. "Strategies for processing mega-pixel X-ray fluorescence hyperspectral data: A case study on a version of Caravaggio's painting Supper at Emmaus". In: *Journal of Analytical Atomic Spectrometry* 30 (3 2015), pp. 777–789. ISSN: 13645544. DOI: 10.1039/c4ja00387j. URL: http://dx.doi.org/10.1039/C4JA00387J.

[66] C. G. Ryan, D. N. Jamieson, C. L. Churms, and J. V. Pilcher. "A new method for on-line true-elemental imaging using PIXE and the proton microprobe". In: *Nuclear Inst. and Methods in Physics Research, B* 104.1-4 (1995), pp. 157–165. ISSN: 0168583X. DOI: 10.1016/0168-583X(95)00404-1.

[67] Z. Preisler, R. Andolina, A. Busacca, C. Caliri, C. Miliani, and F. P. Romano. "Deep learning for enhanced spectral analysis of MA-XRF datasets of paintings". In: *Science advances* 10.39 (2024), eadp6234. ISSN: 23752548. DOI: 10.1126/sciadv.adp6234.

[68] M. Vermeulen, A. McGeachy, B. Xu, H. Chopp, A. Katsaggelos, R. Meyers, M. Alfeld, and M. Walton. "XRFast a new software package for processing of MA-XRF datasets using machine learning". In: *Journal of Analytical Atomic Spectrometry* 37.10 (2022), pp. 2130–2143. ISSN: 13645544. DOI: 10.1039/d2ja00114d. URL: http://dx.doi.org/10.1039/D2JA00114D.

[69] M. Picollo, C. Cucci, A. Casini, and L. Stefani. "Hyper-spectral imaging technique in the cultural heritage field: New possible scenarios". In: *Sensors* 20 (10 2020). ISSN: 14248220. DOI: 10.3390/s20102843.

[70] C. Fischer and I. Kakoulli. "Multispectral and hyperspectral imaging technologies in conservation: current research and potential applications". In: *Studies in Conservation* 51.sup1 (2006), pp. 3–16. ISSN: 0039-3630. DOI: 10.1179/sic.2006.51.supplement-1.3.

[71] N. D. Keyser, A. van Loon, F. Gabrieli, F. Vanmeert, F. T. Broers, P. Noble, S. D. Meyer, A. Gestels, V. Gonzalez, M. Almasian, I. van der Werf, E. Hermens, K. Janssens, and K. Keune. "Illuminating Rembrandt's Chiaroscuro in The Night Watch: the painting process of Van Ruytenburch's costume". In: *npj Heritage Science* 13 (1 Dec. 2025). ISSN: 30593220. DOI: 10.1038/s40494-025-01874-w.

[72] F. Gabrieli, J. K. Delaney, R. G. Erdmann, V. Gonzalez, A. van Loon, P. Smulders, R. Berkeveld, R. van Langh, and K. Keune. "Reflectance imaging spectroscopy (RIS) for Operation Night Watch: Challenges and achievements of imaging Rembrandt's masterpiece in the glass chamber at the Rijksmuseum". In: *Sensors* 21 (20 2021), pp. 1–18. ISSN: 14248220. DOI: 10.3390/s21206855.

[73] J. K. Delaney, J. G. Zeibel, M. Thoury, R. Littleton, M. Palmer, K. M. Morales, E. R. D. L. Rie, and A. Hoenigswald. "Visible and infrared imaging spectroscopy of picasso's harlequin musician: Mapping and identification of artist materials in situ". In: *Applied Spectroscopy* 64 (6 2010), pp. 584–594. ISSN: 00037028. DOI: 10.1366/000370210791414443.

[74] C. Cucci, J. K. Delaney, and M. Picollo. "Reflectance Hyperspectral Imaging for Investigation of Works of Art: Old Master Paintings and Illuminated Manuscripts". In: *Accounts of Chemical Research* 49 (10 2016), pp. 2070–2079. ISSN: 15204898. DOI: 10.1021/acs.accounts.6b00048.

[75] J. Behmann, K. Acebron, D. Emin, S. Bennertz, S. Matsubara, S. Thomas, D. Bohnenkamp, M. T. Kuska, J. Jussila, H. Salo, A. K. Mahlein, and U. Rascher. "Specim IQ: Evaluation of a new, miniaturized handheld hyperspectral camera and its application for plant phenotyping and disease detection". In: *Sensors (Switzerland)* 18.2 (2018). ISSN: 14248220. DOI: 10.3390/s18020441.

[76] M. Picollo, A. Casini, C. Cucci, J. Jussila, M. Poggesi, and L. Stefani. "A New Compact VNIR Hyperspectral Imaging System for Non-Invasive Analysis in the FineArt and Architecture Fields". In: *Electronic Imaging & the Visual Arts. EVA 2018 Florence*. Ed. by V. Cappellini. Florence: Firenze University Press, 2018, pp. 69–74. DOI: 10.36253/978-88-6453-707-8.16.

[77] F. Preda, A. Perri, and D. Polli. "A New 'Hera' in Hyperspectral Imaging". In: *PhotonicsViews* 18.1 (2021), pp. 45–49. ISSN: 2626-1294. DOI: 10.1002/phvs.202100020.

[78] C. Pelosi, A. Lo Monaco, M. Bernabei, G. Agresti, C. Colantonio, A. Perri, D. Comelli, G. Valentini, and C. Manzoni. "Beyond the visible: The Viterbo Crucifixion panel painting attributed to Michelangelo Buonarroti". In: *Microchemical Journal* 154.January (2020), p. 104636. ISSN: 0026265X. DOI: 10.1016/j.microc.2020.104636. URL: https://doi.org/10.1016/j.microc.2020.104636.

[79] A. Perri, B. E. Nogueira de Faria, D. C. T. Ferreira, D. Comelli, G. Valentini, F. Preda, D. Polli, A. M. de Paula, G. Cerullo, and C. Manzoni. "Hyperspectral imaging with a TWINS birefringent interferometer". In: *Optics Express* 27.11 (2019), p. 15956. ISSN: 10944087. DOI: 10.1364/oe.27.015956.

[80] H. Liang, A. Lucian, R. Lange, C. Cheung, and B. Su. "Remote spectral imaging with simultaneous extraction of 3D topography for historical wall paintings". In: *ISPRS Journal of Photogrammetry and Remote Sensing* 95 (2014), pp. 13–22. ISSN: 09242716. DOI: 10.1016/j.isprsjprs.2014.05.011. URL: http://dx.doi.org/10.1016/j.isprsjprs.2014.05.011.

[81] P. Kubelka and F. Munk. *Ein Beitrag zur Optik der Farbanstriche*. 1931.

[82] N. Rohani, E. Pouyet, M. Walton, O. Cossairt, and A. K. Katsaggelos. "Nonlinear Unmixing of Hyperspectral Datasets for the Study of Painted Works of Art". In: *Angewandte Chemie International Edition* 57 (34 Aug. 2018), pp. 10910–10914. ISSN: 14337851. DOI: 10.1002/anie.201805135. URL: https://onlinelibrary.wiley.com/doi/10.1002/anie.201805135.

[83] F. Pottier, M. Gerardin, A. Michelin, M. Hébert, and C. Andraud. "Simulating the composition and structuration of coloring layers in historical painting from non-invasive spectral reflectance measurements". In: *Comptes Rendus Physique* 19 (7 2018), pp. 599–611. ISSN: 16310705. DOI: 10.1016/j.crhy.2018.09.007. URL: https://doi.org/10.1016/j.crhy.2018.09.007.

[84] G. Dupuis and M. Menu. "Quantitative characterisation of pigment mixtures used in art by fibre-optics diffuse-reflectance spectroscopy". In: *Applied Physics A: Materials Science and Processing* 83.4 (2006), pp. 469–474. ISSN: 09478396. DOI: 10.1007/s00339-006-3522-3.

[85] M. Alfeld, M. Mulliez, J. Devogelaere, L. de Viguerie, P. Jockey, and P. Walter. "MA-XRF and hyperspectral reflectance imaging for visualizing traces of antique polychromy on the Frieze of the Siphnian Treasury". In: *Microchemical Journal* 141.April (2018), pp. 395–403. ISSN: 0026265X. DOI: 10.1016/j.microc.2018.05.050. URL: https://doi.org/10.1016/j.microc.2018.05.050.

[86] E. Pouyet, N. Rohani, A. K. Katsaggelos, O. Cossairt, and M. Walton. "Innovative data reduction and visualization strategy for hyperspectral imaging datasets using t-SNE approach". In: *Pure and Applied Chemistry* 90 (3 2018), pp. 493–506. ISSN: 13653075. DOI: 10.1515/pac-2017-0907.

[87] M. Alfeld, S. Pedetti, P. Martinez, and P. Walter. "Joint data treatment for Vis–NIR reflectance imaging spectroscopy and XRF imaging acquired in the Theban Necropolis in Egypt by data fusion and t-SNE". In: *Comptes Rendus Physique* 19 (7 2018), pp. 625–635. ISSN: 16310705. DOI: 10.1016/j.crhy.2018.08.004. URL: https://doi.org/10.1016/j.crhy.2018.08.004.

[88] M. Vermeulen, K. Smith, K. Eremin, G. Rayner, and M. Walton. "Application of Uniform Manifold Approximation and Projection (UMAP) in spectral imaging of artworks". In: *Spectrochimica Acta - Part A: Molecular and Biomolecular Spectroscopy* 252 (2021), p. 119547. ISSN: 13861425. DOI: 10.1016/j.saa.2021.119547. URL: https://doi.org/10.1016/j.saa.2021.119547.

[89] S. Kogou, G. Shahtahmassebi, A. Lucian, H. Liang, B. Shui, W. Zhang, B. Su, and S. van Schaik. "From remote sensing and machine learning to the history of the Silk Road: large scale material identification on wall paintings". In: *Scientific Reports* 10.1 (2020), pp. 1–14. ISSN: 20452322. DOI: 10.1038/s41598-020-76457-9. URL: https://doi.org/10.1038/s41598-020-76457-9.

[90] E. Pouyet, T. Miteva, N. Rohani, and L. de Viguerie. "Artificial intelligence for pigment classification task in the short-wave infrared range". In: *Sensors* 21 (18 2021). ISSN: 14248220. DOI: 10.3390/s21186150.

[91] S. Marsland. *Machine Learning : an algorithmic perspective*. Second edition. CRC Press, 2015. ISBN: 9781466583337; 1466583339; 9781466583368; 1466583363; 9781466583283; 1466583282. URL: http://www.crcnetbase.com/isbn/9781466583337.

[92] K. Pearson. "LIII. On lines and planes of closest fit to systems of points in space". In: *The London, Edinburgh, and Dublin Philosophical Magazine and Journal of Science* 2 (11 Nov. 1901), pp. 559–572. ISSN: 1941-5982. DOI: 10.1080/14786440109462720.

[93] J. Shlens. *A Tutorial on Principal Component Analysis*. 2014. arXiv: 1404.1100 [cs.LG]. URL: https://arxiv.org/abs/1404.1100.

[94] D. D. Lee and H. S. Seung. "Learning the parts of objects by non-negative matrix factorization". In: *Nature* 401 (6755 1999), pp. 788–791. ISSN: 1476-4687. DOI: 10.1038/44565. URL: https://doi.org/10.1038/44565.

[95] J. M. Maisog, A. T. Demarco, K. Devarajan, S. Young, P. Fogel, and G. Luta. "Assessing methods for evaluating the number of components in non-negative matrix factorization". In: *Mathematics* 9 (22 Nov. 2021). ISSN: 22277390. DOI: 10.3390/math9222840.

[96] C. Jutten and J. Herault. "Blind separation of sources, part I: An adaptive algorithm based on neuromimetic architecture". In: *Signal Processing* 24 (1 1991), pp. 1–10. ISSN: 0165-1684. DOI: https://doi.org/10.1016/0165-1684(91)90079-X. URL: https://www.sciencedirect.com/science/article/pii/016516849190079X.

[97] L. van der Maaten and G. Hinton. "Visualizing data using t-SNE". In: *Journal of Machine Learning Research* 9 (Nov. 2008), pp. 2579–2605.

[98] L. McInnes, J. Healy, and J. Melville. *UMAP: Uniform Manifold Approximation and Projection for Dimension Reduction*. 2020. arXiv: 1802.03426 [stat.ML]. URL: https://arxiv.org/abs/1802.03426.

[99] W. S. McCulloch and W. Pitts. "A logical calculus of the ideas immanent in nervous activity". In: *The bulletin of mathematical biophysics* 5 (4 1943), pp. 115–133. ISSN: 1522-9602. DOI: 10.1007/BF02478259. URL: https://doi.org/10.1007/BF02478259.

[100] F. Rosenblatt. "Perceptron Simulation Experiments". In: *Proceedings of the IRE* 48 (3 1960), pp. 301–309. ISSN: 2162-6634. DOI: 10.1109/JRPROC.1960.287598.

[101] A. Khan, A. Sohail, U. Zahoora, and A. S. Qureshi. "A survey of the recent architectures of deep convolutional neural networks". In: *Artificial Intelligence Review* 53 (8 2020), pp. 5455–5516. ISSN: 1573-7462. DOI: 10.1007/s10462-020-09825-6. URL: https://doi.org/10.1007/s10462-020-09825-6.

[102] I. D. Mienye and T. G. Swart. "A Comprehensive Review of Deep Learning: Architectures, Recent Advances, and Applications". In: *Information (Switzerland)* 15 (12 Dec. 2024). ISSN: 20782489. DOI: 10.3390/info15120755.

[103] T. Kleynhans, C. M. S. Patterson, K. A. Dooley, D. W. Messinger, and J. K. Delaney. "An alternative approach to mapping pigments in paintings with hyperspectral reflectance image cubes using artificial intelligence". In: *Heritage Science* 8 (1 2020), pp. 1–16. ISSN: 20507445. DOI: 10.1186/s40494-020-00427-7. URL: https://doi.org/10.1186/s40494-020-00427-7.

[104] S. Kovačević, M. K. Banjac, and S. Podunavac-Kuzmanović. "Artificial Intelligence and Experimental Design: The Flywheel of Innovating Food Processing Engineering". In: *Processes* 13 (3 Mar. 2025). ISSN: 22279717. DOI: 10.3390/pr13030846.

[105] T. Hastie, R. Tibshirani, and J. Friedman. "Additive Models, Trees, and Related Methods". In: *The Elements of Statistical Learning*. 2nd ed. Springer New York, 2009, pp. 295–336. DOI: 10.1007/b94608_9. URL: hastie.su.domains/ElemStatLearn.

[106] T. K. Ho. "Random decision forests". In: *Proceedings of 3rd International Conference on Document Analysis and Recognition*. Vol. 1. 1995, 278–282 vol.1. DOI: 10.1109/ICDAR.1995.598994.

[107] Y. Freund and R. E. Schapire. "A Short Introduction to Boosting". In: *Journal of Japanese Society for Artificial Intelligence* 14 (5 1999), pp. 771–780. URL: www.research.att.com/fyoav,.

[108] J. Friedman, T. Hastie, and R. Tibshirani. "Additive logistic regression: a statistical view of boosting". In: *The Annals of Statistics* 28 (2 Apr. 2000), pp. 337–407. DOI: 10.1214/aos/1016218223. URL: https://doi.org/10.1214/aos/1016218223.

[109] T. Hastie, R. Tibshirani, and J. Friedman. “Boosting and Additive Trees”. In: *The Elements of Statistical Learning*. 2nd ed. Springer New York, 2009, pp. 337–387. DOI: 10.1007/b94608_10. URL: hastie.su.domains/ElemStatLearn.

[110] C. Bentéjac, A. Csörgő, and G. Martínez-Muñoz. “A comparative analysis of gradient boosting algorithms”. In: *Artificial Intelligence Review* 54 (3 2021), pp. 1937–1967. ISSN: 1573-7462. DOI: 10.1007/s10462-020-09896-5. URL: https://doi.org/10.1007/s10462-020-09896-5.

[111] T. Chen and C. Guestrin. “XGBoost: A scalable tree boosting system”. In: *Proceedings of the ACM SIGKDD International Conference on Knowledge Discovery and Data Mining* 13-17-Augu (2016), pp. 785–794. DOI: 10.1145/2939672.2939785. arXiv: 1603.02754.

[112] G. Ke, Q. Meng, T. Finley, T. Wang, W. Chen, W. Ma, Q. Ye, and T.-Y. Liu. “LightGBM: A Highly Efficient Gradient Boosting Decision Tree”. In: *Advances in Neural Information Processing Systems*. Ed. by I. Guyon, U. V. Luxburg, S. Bengio, H. Wallach, R. Fergus, S. Vishwanathan, and R. Garnett. Vol. 30. Curran Associates, Inc., 2017. URL: https://proceedings.neurips.cc/paper_files/paper/2017/file/6449f44a102fde848669bdd9eb6b76fa-Paper.pdf.

2

COMPARISON OF MA-XRF AND RIS FOR THE ANALYSIS OF PIGMENTS

Macro X-ray fluorescence spectroscopy (MA-XRF) and reflectance imaging spectroscopy (RIS) are important tools in the analysis of cultural heritage objects, both for conservation and art historical research purposes. The elemental and molecular distributions provided by MA-XRF and RIS respectively, are particularly useful for the identification and mapping of pigments in easel paintings. While MA-XRF has relatively established data processing methods based on modelling of the underlying physics, RIS data cannot be modelled with sufficient precision and its processing has considerable room for improvements. This work seeks to improve RIS data processing workflows in the short-wave infrared (SWIR) range ($1000-2500\,\mathrm{nm}$*) with a novel method that fits profiles to pigment-specific absorption features, and we compare its performance to MA-XRF for the task of semi-quantitative pigment mapping, evaluating their limits of detection (LODs) and the matrix effects that affect their signals. Two pigments are considered in this work, lead white and blue verditer, which are mapped in SWIR RIS using the first overtone of −OH stretching of their primary compounds, hydrocerussite (*$Pb_3(CO_3)_2(OH)_2$*) and azurite (*$Cu_3(CO_3)_2(OH)_2$*), at 1447 and* $1497\,\mathrm{nm}$ *respectively, and in MA-XRF using the Pb-L and Cu-K fluorescence signals. The methods are evaluated using two sets of custom-prepared paint samples, as well as a 16th-century painting, discussing the identification, mapping, and semi-quantitative analysis of the considered pigments. SWIR RIS was found to be a pigment-specific method with a longer linear range but inferior LODs and penetration depth when compared to MA-XRF, the latter is often not capable of discriminating between different pigments with identical elemental markers.*

Parts of this chapter have been published in X-Ray Spectrom 2024, 53 (6): 438-451.[1]

2.1. INTRODUCTION

PAINTINGS are, from a material point of view, highly heterogeneous systems consisting of many unevenly distributed paint layers. Each paint layer consists of a heterogeneous mixture of pigments that have the strongest contribution to the perceived color, a binder that holds the paint together; and potentially any other additives that modify other characteristics of the paint, such as its viscosity or drying speed. The combined heterogeneity of paintings mandates the use of techniques that provide spatially resolved chemical information. In recent years, two such imaging techniques, macro X-ray fluorescence spectroscopy (MA-XRF) and reflectance imaging spectroscopy (RIS) have become routine tools for the analysis of historical paintings and other cultural heritage objects. They contribute to conservation and art historical research by identifying pigments and visualizing their distribution.[2–10]

MA-XRF reveals distributions in samples by recording characteristic radiation emitted during inner shell electronic transitions upon stimulation by a primary x-ray beam. The underlying physics of XRF are well understood and modelled, such that element-specific distribution images can be readily obtained.[11] However, its limitation to elemental information prevents it from delivering conclusive pigment identification, as distinct pigments can share an elemental footprint. Examples are azurite ($Cu_3(CO_3)_2(OH)_2$) and malachite ($Cu_2CO_3(OH)_2$) whose single elemental marker is Cu.

In the visible and infrared spectral ranges, RIS measures the light reflected or scattered by a sample, supplying information on the molecules present in the material, and delivering insight complementary to information provided by MA-XRF. RIS in the visible range (commonly the visible to near-infrared range in commercial cameras, VNIR, from 350 to 1000 nm) may provide information on the electronic transitions of molecules occurring in that spectral range, which can provide insight as to the visible colour of some compounds. RIS in the short-wave infrared (1000 – 2500 nm), which is the focus of this research, provides information on the distribution of many chemical species using characteristic frequencies related to vibrational modes of certain functional groups, like O – H.[12] However, modelling of the reflectance response of complex material matrices, like paint layers, in the SWIR spectral range is challenging,[13, 14] making the extraction of chemical distribution maps from SWIR RIS data more difficult than for MA-XRF. Novel methods have also been described for RIS in certain sections of the Mid infrared (MIR) (2500 – 25 000 nm), like 2500 = 3750 nm in [15] and 8064 – 13 158 nm in [16], which provides access to even further vibrational modes, such as C – H and C – O, respectively. However, these have not yet seen widespread use.

Currently, most RIS data processing methods used in cultural heritage science revolve primarily around dimensionality reduction methods, such as PCA, UMAP[17, 18] or t-SNE[19] followed by manual endmember selection and a mapping approach, such as spectral angle mapping (SAM).[20, 21] While these methods are commonly used in the analysis of RIS datasets (in particular for the VNIR range, presenting less sharp spectral features), their unsupervised machine-learning nature makes the results often dataset-specific, and the manual user intervention

steps tend to be rather labour–intensive and difficult to reproduce. Recently, more automated approaches based on artificial neural networks and other spectral matching algorithms have been successfully demonstrated[22–25] but have not yet seen widespread use in the routine analysis of RIS data from paintings.

This paper describes an approach for SWIR RIS data processing that enables the spatial mapping and semi-quantitative evaluation of pigments, namely a confirmation of pigment presence and an estimation of the pigment's areal density, through the vibrational spectral features they present in the SWIR spectral range.

We demonstrate our data workflow and focus our study on two specific pigments: lead white (abbreviated as LW) (typically a mixture of lead carbonates, hydrocerussite $Pb_3(CO_3)_2(OH)_2$, and cerussite $PbCO_3$[26]), and blue verditer (abbreviated as BV) (a hydrated copper carbonate $Cu_3(CO_3)_2(OH)_2$, the synthetic equivalent of azurite[27]). These two pigments were chosen due to their widespread use in historical paintings and their useful absorption features in the SWIR range. Our proposed method consists of fitting a Gaussian profile in the RIS spectrum onto the characteristic absorption features of the two pigments. For lead white, we use the first overtone of –OH stretching of hydrocerussite, which is centred around 1447 nm.[28] For blue verditer, we use the first overtone of –OH stretching of azurite centred around 1497 nm.[29] The SWIR RIS spectra of both pigments and their corresponding absorbance features can be seen in figure 2.1. A similar method was employed by De Meyer et al.[28] for the analysis of SWIR RIS data but was limited to the qualitative mapping of hydrocerussite.

MA-XRF and the Gaussian fitting approach to SWIR RIS features (shown in figure 2.2) are evaluated for their potential for semi-quantitative pigment-specific mapping. The evaluation entails the pigment analysis of three objects: two sets of custom-made paint mock-ups (mixture and layered systems), which allow for the evaluation with regards to both pigment identification and semi-quantitative analysis, and a 16th-century panel painting, which provides a practical example for pigment identification. The potential for semi-quantitative pigment analysis is benchmarked by comparing the intensity of each pigment's characteristic signals in each method (i.e., for blue verditer, Cu-Kα for MA-XRF, and azurite for SWIR RIS) to the pigment areal density of each sample. Whilst MA-XRF and RIS do not always directly measure the pigments themselves, but rather components thereof (elements for MA-XRF and chemical species for RIS), and given that the measured response for each modality reports a different property and covers a different dynamic range, all quantitative results are translated into pigment areal density values that enable direct comparison between the two methods in terms of quantitation.

2.2. MATERIALS AND METHODS

2.2.1. TEST SAMPLES

Two sets of paint mock-ups were prepared to evaluate and compare the methods for different paint layer compositions and structures. These two sets were both made using three pigments: lead white (LW), blue verditer (BV), and yellow ochre (YO). All pigments were sourced from Rublev Colors (Willits, CA, U.S.A.) (Full pigment

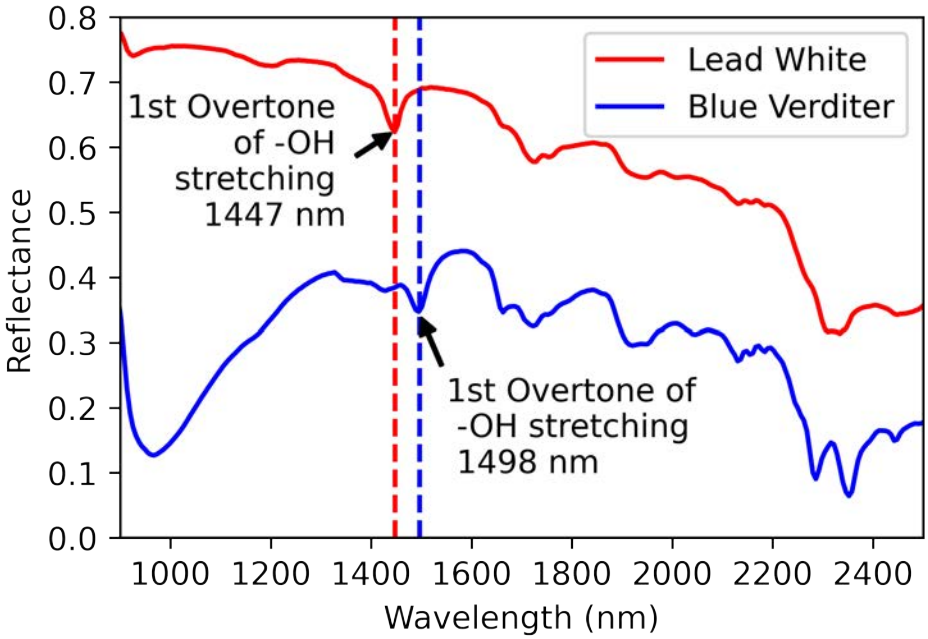

Figure 2.1.: SWIR reflectance spectra for lead white (LW) and blue verditer (BV) taken from their respective 150 µm single-pigment samples, and the fitting reflectance feature of each.

analysis available in appendix A.1). These pigments were selected due to their distinct elemental footprints and characteristic absorption features. In MA-XRF, blue verditer can be detected by means of the Cu-K fluorescence lines, and in SWIR RIS by the first overtone of $-$OH stretching (1497 nm), combination $\nu+\delta$ (stretching and bending) of $-$OH (2285 nm) and second overtone of $-CO_3{}^{-2}$ stretching (2352 nm) of azurite[29] (spectra shown in figure 2.1). Lead white, which in this case is a mixture of 98% hydrocerussite and 2% cerussite, can be detected through MA-XRF by observing the Pb-L and Pb-M fluorescence lines, and in SWIR RIS by the first overtone of $-$OH stretching (1447 nm) and combination $\nu+\delta$ of $-$OH and second overtone of $-CO_3{}^{-2}$ stretching (2325 nm) of hydrocerussite[28, 30] (spectra shown in figure 2.1). Only the features in the 1400$-$1500 nm range were used in this research, as this is the range in which the binder (linseed oil) is least likely to present strong absorption features. While the yellow ochre pigment used in these experiments can be detected through SWIR RIS due to the presence of kaolinite ($Al_2(OH)_4Si_2O_5$) as a secondary component through two absorption bands of the first overtone of $-$OH stretching (1396 nm and 1415 nm),[31] the main colouring component, goethite (α-FeO(OH)), lacks characteristic absorption features in the SWIR spectral range and consequently the pigment is not regarded in the subsequent text.

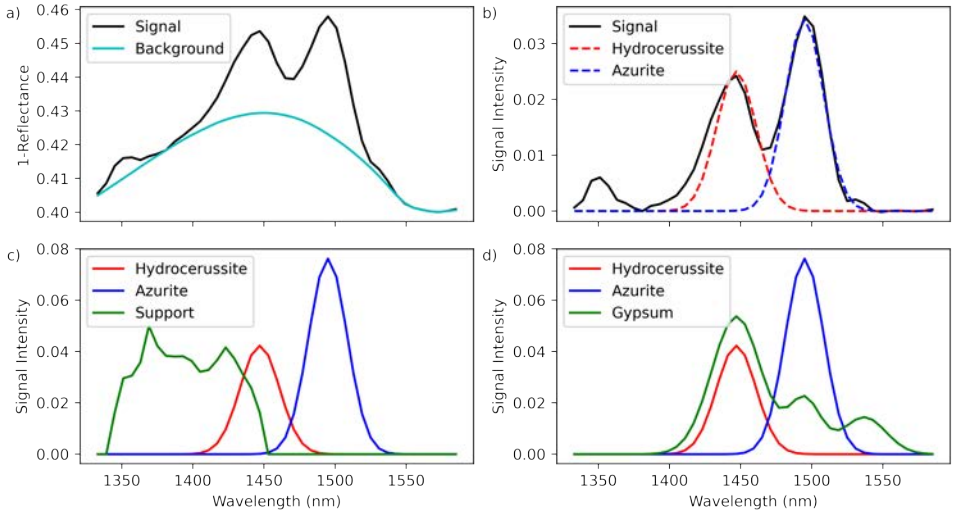

Figure 2.2.: (a) Inverted reflectance spectra from a 50/50 BV/LW 150 µm paint sample and the calculated background. (b) Processed RIS signal and two Gaussian profiles fit onto the absorbance features. (c) Fitting components used for the fitting of the paint mock-ups. (d) Fitting components used for the fitting of the test painting.

All paints were ground by hand with a muller on a glass plate, using raw linseed oil (Kremer Pigments Inc., New York, NY, U.S.A.) as a binder at oil mass ratios of 14%, 22%, and 29%, respectively for lead white, blue verditer, and yellow ochre. The paints were applied on 50 µm Melinex film using a metal 4-sided Bird-type film applicator. After drying, the samples were attached to a 3 mm plexiglass sheet for rigidity. The reflectance spectrum and XRF signals of the support material are provided in appendix A.2.

The first set of paint mock-ups is a collection of single-layer samples, hereafter referred to as the mixture samples (figure 2.4a). Each of these samples was put down as a single paint layer, where the used paint was a mixture of two single-pigment paints at a specific mass ratio. The ratios examined were 5:95, 20:80, 50:50, 80:20, and 95:5 and each paint ratio was applied in three different nominal layer thicknesses (50, 100, and 150 µm). The second mock-up set is a collection of double-layered samples, hereafter referred to as the layer samples (figure 2.5a). Each of these samples was made by first applying a layer of paint of one type of pigment, letting it dry for a week, and then applying another layer of different single-pigment paint. The samples were applied in three thickness combinations: 50 µm over 100 µm (L1), 100 µm over 50 µm (L2), and 50 µm over 50 µm (L3). The paint layers were applied such that for both the top and bottom layers an area of no overlap was present, leaving single-layer areas accessible with three thicknesses (50, 100, and 150 µm). These thicknesses of single paint layers were achieved as in the absence of a second

layer the single layer thickness is the sum of the nominal thicknesses of both layers (e.g., 100 µm for the L3 samples). Figure 2.3 provides a visual diagram of the paint layer build-up. Each sample on both sets has an area of roughly 2 cm × 3 cm. All samples were allowed to dry for a month before measurements started. A full description of the sample compositions is available in appendices A.3 and A.4.

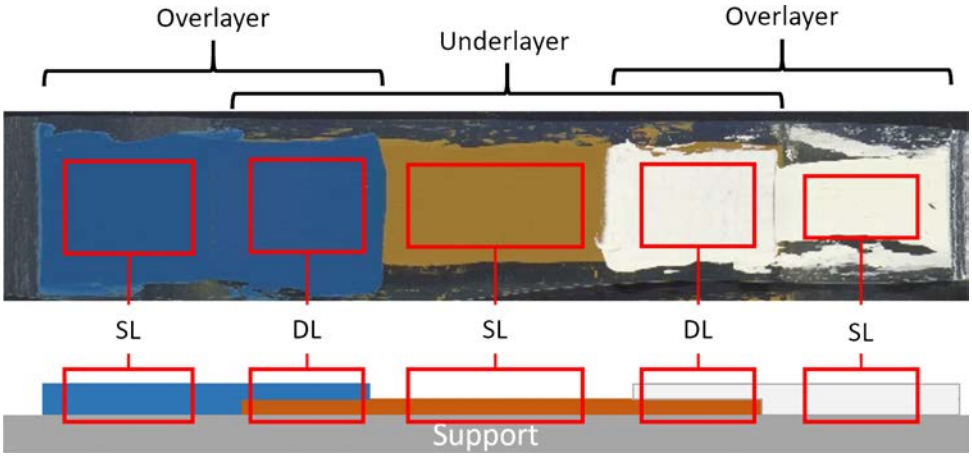

Figure 2.3.: Cross-section diagram of the paint layer build-up of the layer samples. SL are singlelayer samples and DL are doublelayer samples.

MA-XRF and SWIR RIS were also applied to the analysis of Jacob Cornelisz van Oostsanen's *Portrait of Jan Gerritsz van Egmond van de Nijenburg* (oil on panel, h 42.4 cm × w 32.8 cm, c. 1518), from the Rijksmuseum Collection (SK-A-3838) (figure 2.7a). Given the painting's shape and non-removable frame, only a section of the painting was scanned with MA-XRF to avoid potential collisions between the frame and the MA-XRF measurement head. This painting was analysed in relation to conservation work in preparation for an upcoming exhibition. The analysis confirmed the presence of both azurite and lead white, making it the perfect test case for our novel mapping method.

2.2.2. DATA ACQUISITION AND PROCESSING

MA-XRF

MA-XRF data were acquired using an M6 Jetstream MA-XRF scanner equipped with two 60 mm^2 SDD detectors (Bruker Nano GmbH, Berlin, Germany).[32] The Rhodium x-ray tube was operated at 50 kV and 200 µA, and the scan was conducted with a dwell time of 400 ms and a step size of 500 µm for the paint mock-ups and a dwell time of 70 ms and a step size of 450 µm for the painting. This resulted in data sets of 342 × 892 pixels for the mixture samples, 372 × 1232 pixels for the layer samples, and 485 × 374 pixels for the painting. The spectral data were processed using DataMuncher[33] and PyMCA[34] to produce elemental signal intensity maps.

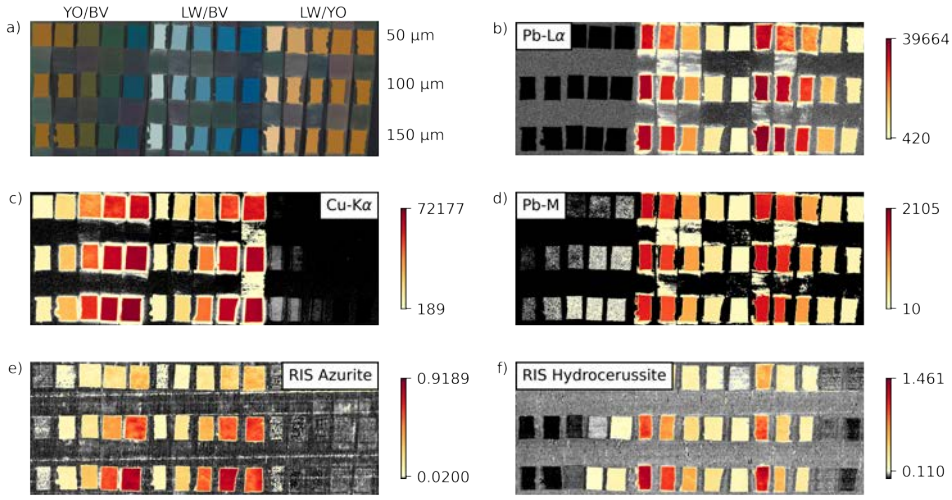

Figure 2.4.: Mixture samples of lead white (LW), blue verditer (BV), and yellow ochre (YO). (a) Visible photograph. The three different mixtures are marked. Each mixture includes five mixture ratios (5%, 20%, 50%, 80%, and 95%). All samples in each row have the same layer thickness, marked on the left. (b) MA-XRF Pb-Lα map. (c) MA-XRF Cu-Kα map. (d) MA-XRF Pb-M map. (e) RIS azurite map. (f) RIS hydrocerussite map. All maps are displayed with the signals below the LODs in greyscale, and the signals above the LODs in a yellow-red heatmap.

To evaluate the potential for semi-quantitative analysis, the arithmetic means of signal intensities of each paint sample were taken and compared to the known pigment areal density of each sample. To determine the LODs, the critical signal value y_c was calculated using equation 1, where $\overline{y}_{BL}$ is the average blank signal and s_{BL} is the standard deviation of the blank signal.[35] The blank signal was taken from areas of the data set where each considered pigment is not present.

$$y_c = \overline{y}_{BL} + 3s_{BL} \tag{2.1}$$

For these datasets, it was observed that the relationships between signal intensity and areal density for the single layer 50 µm samples of both pigments were approximately linear. This happens since the samples are thin enough for matrix effects to not play a very prominent role in signal intensity. A linear fit of these 50 µm samples was used to describe these relations and the areal density value at which this linear fit crosses y_c was taken as the LOD. An alternative, more traditional method of calculating the LODs for MA-XRF compares the intensity of a fluorescence signal to its spectral background[32] using:

$$LOD = 3\frac{\sqrt{N_{back}}}{N_{signal}}c\sqrt{t} \tag{2.2}$$

where N_{back} and N_{signal} are the background and peak intensities, respectively, c is the elemental concentration and t is the measurement time. However, in the context of this paper, we prefer the first method since it can also be applied to SWIR RIS, and therefore can yield a more direct comparison.[32]

SWIR RIS

SWIR RIS data was acquired using a Micro-Hyperspec SWIR 640 hyperspectral camera (Headwall Photonics, Boston, MA, U.S.A.), covering a spectral range from 900 to 2500 nm, with a spectral resolution of 6 nm (267 channels) and a custom-built motorized easel (LG Motion, Basingstoke, United Kingdom). The samples were illuminated by two Gulliver 30 lamps (Ianiro LED, New Taipei City, Taiwan, China) with 150 W halogen 3000 K bulbs set at 50° of the surface normal. The camera was operated using an integration time of 120 ms per line. The datasets were calibrated using a Spectralon 99% diffuse white reflectance standard (Labsphere, North Sutton, NH, U.S.A.). The mixture samples were too large to be acquired in a single scan, and thus two scans were taken and later stitched together using DataHandlerP.[36] The datasets were scaled to match the resolution of the MA-XRF scans, resulting in datasets of 342 × 892 pixels for the mixture samples and 357 × 1232 pixels for the layer samples, with a pixel size of approximately 500 µm. The painting was also too large for a single scan acquisition, and instead four scans were stitched together, resulting in a dataset of 3250 × 2170 pixels with a pixel size of ~168 µm.

To be able to fit the reflectance features, the data needed to be pre-processed. First, the data set was cropped to the desired spectral range (1333 – 1591 nm). Then, a 5-pixel special median filter perpendicular to the scanning direction was used to get rid of single-pixel measurement artifacts, followed by a Savitzky–Golay filter (window length of 5 and polynomial degree of 2) in the spectral direction to reduce noise and smooth the SWIR spectral profile. The flat-field normalized reflectance signal (R) was then inverted (1-R). Afterward, the specific features were isolated from the background absorption using a variant of the Statistics-sensitive Non-linear Iterative Peak-clipping (SNIP) filter,[37] as shown in figure 2.2a. The initial half-window size for the SNIP filter depends on the width of the absorbance features being studied and is traditionally set as approximately half the width of the target feature. Following this, a half-window size of six was used for this research and was found to provide reliable feature isolation. After the pre-processing, the fitting of features is done using the SciPy NN-LS function provided through DataHandlerP. The Gaussian profiles used for the fitting of spectral features are derived from the 150 µm single-pigment samples. Spectra from these samples were pre-processed as described above, and then the width and height of the Gaussian profiles were calculated using the SciPy *curve_fit()* function.[38] These profiles are shown in figure 2.2b. Gaussian profiles were initially chosen due to their simplicity and were found to provide satisfying fits to the considered absorption features, as the background removal forces the peaks to have very short tails. Since the support material used

for the paint mock-ups also has a broad absorption feature slightly overlapping with the hydrocerussite feature, it was required to include a third component during the fitting (figure 2.2c). This component was taken directly from the processed data. A similar issue occurred with the painting, where the presence of gypsum ($CaSO_4 \cdot 2H_2O$) in areas of restoration caused problems during the fitting due to its triple absorption features at 1445, 1490, and 1535 nm.[20] The first two features overlap directly with those of hydrocerussite and azurite, respectively, and thus cause significant issues with the identification. To account for that, a third component was added for gypsum (figure 2.2d). The component was derived using a method similar to that used for the other components but using a function consisting of 3 Gaussian profiles of which the height and width are calculated using the *curve_fit* function on a sample spectrum extracted from the painting's data set.

For the semi-quantitative analysis and calculation of SWIR LODs, an approach similar to that used for MA-XRF signals was utilized on the SWIR signals, with the mean signal intensities of each paint sample being compared to the pigment's areal density.

To clearly show which areas of an elemental or chemical map are above or below its corresponding limit of detection we devised a non-standard colour scheme in that signals above the LOD are shown in a red-orange heat map and signals below in a greyscale. The signals depicted in the red-orange colourmap can be labelled as detected. While signals that fall below a conservatively set LOD (with the LOD only considering spectral information and not spatial information) cannot be labelled as reliably detected, their distribution often still reports genuine pigment distribution traces and thus still allows for low-abundant pigment distributions to be discerned. The combined colour scale allows for a clear visual distinction between reliably detected and sub-LOD signals, but also still yields a way for spatial pigment distributions to be discerned regardless of whether the LOD threshold is met in all pixel locations.

2.3. RESULTS

2.3.1. PAINT SAMPLES

MA-XRF

For the paint mock-ups, the elemental distribution maps for Cu-Kα (8.0 keV), Pb-Lα (10.6 keV), and Pb-M (0.6 –3.7 keV) are used (All other MA-XRF maps are presented in appendices A.5 and A.6). These specific lines are chosen as they are the most intense of their respective electron shells. For the single-layer samples, the MA-XRF maps (figure 2.4b–d) reliably confirm the elemental presence of the considered pigments. In the case of the layer samples (figure 2.5b–d), the presence of overlying layers does affect the elemental signal intensity from underlying layers, but the extent of this effect depends mostly on both the fluorescence energy of the underlying layer and how strongly absorbing the overlying layer is with regards to that fluorescence energy. For example, comparing the signal intensity (I) of an uncovered 100 µm blue verditer layer to the signal intensity of such a layer covered by an overlying 50 µm yellow ochre layer it is found that the covered Cu-Kα signal is only 69.7%

(= $I_{covered}/I_{uncovered}$) of the intensity of the uncovered signal. For an overlying 50 µm lead white layer, the Cu-Kα signal is reduced to 3.3% of the uncovered signal intensity.

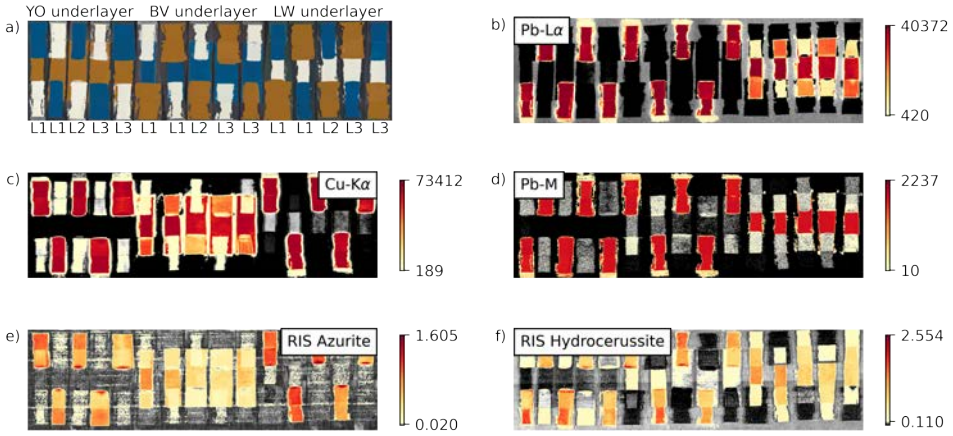

Figure 2.5.: Layer samples of lead white (LW), blue verditer (BV), and yellow ochre (YO). (a) Visible photograph. Three different layer sample configurations are marked: L1 (50 µm over 100 µm), L2 (100 µm over 50 µm), and L3 (50 µm over 50 µm). (b) MA-XRF Pb-Lα map. (c) MA-XRF Cu-Kα map. (d) MA-XRF Pb-M map. (e) RIS azurite map. (f) RIS hydrocerussite map. All maps are displayed with the signals below the LODs in greyscale, and the signals above the LODs in a yellow-red heatmap.

As for semi-quantitative analysis, in figure 2.6a,b the average sample signal intensities of the considered fluorescence lines are plotted against the areal density of the corresponding pigments. The results suggest a discernible relationship between signal intensity and pigment areal density. However, as expected, this relationship varies significantly in function of several factors such as the overall pigment concentration, the presence of other pigments, and their mass absorption coefficients, which influences absorption within the sample. All of these are well-documented factors common to quantitative XRF analysis.[11]

One notable exception to this trend is the Pb-M fluorescence lines (figures 2.4d and 2.5d), a group of low energy (0.6 –3.7 keV) and low intensity (~50 times less than Pb-Lα) fluorescence lines, which are very strongly absorbed by the samples, and are therefore only related to superficial Pb presence. Since the signal from these fluorescence lines is only related to a very thin section of the surface, matrix effects play much less of a role in the investigated samples, and the signal is therefore much more strongly correlated to Pb concentration at the surface of the paint layer, as can be seen in figure 2.6c. Any material beyond the first 13 µm of a lead white paint layer is not expected to contribute significantly to the Pb-M signal, as only around 0.5% of the radiation at 2.3 keV, the energy of the strongest Pb-M line, is able to escape (as shown in appendix A.7).

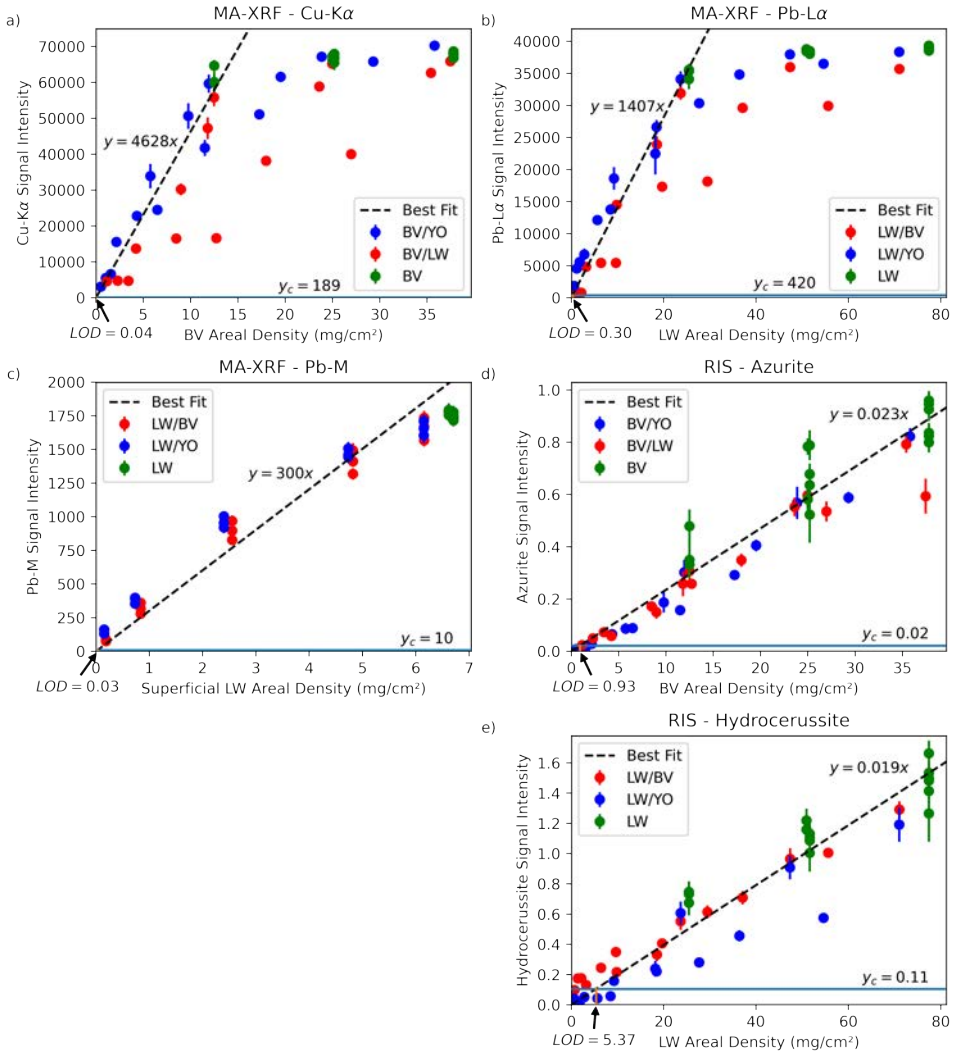

Figure 2.6.: Relationship between signal intensities and pigment areal densities and calculated limits of detection for (a) MA-XRF Cu-Kα, (b) MA-XRF Pb-Lα, (c) MA-XRF Pb-M, (d) RIS azurite, (e) RIS hydrocerussite. Error bars represent the standard deviation of the related signal intensities across each paint sample.

The calculated LODs (using the Cu-K and Pb-L lines) are of 0.04 mg/cm^2 for blue verditer and 0.30 mg/cm^2 for lead white, which are equivalent to 0.02 mg/cm^2 of Cu and 0.24 mg/cm^2 of Pb, respectively. Using the Pb-M lines, the surface-specific LODs are 0.03 mg/cm^2 for lead white, which is equivalent to 0.02 mg/cm^2 of Pb. Using

equation 2, the LODs for the 100 µm 50% blue verditer/50% lead white sample were calculated as 0.04 and 0.01 mg/cm^2 for Cu and Pb, respectively. These results are in good agreement with those reported by Alfeld et al.,[32] which reported 90 ppm of Cu for a NIST SRM 610 (density: 2.5 g/cm^3, thickness: 1 mm), which is equivalent to 0.03 mg/cm^2 of Cu.

SWIR RIS

The method manages to produce fairly accurate pigment distribution maps, shown in Figures 2.4e,f and 2.5e,f, but it sometimes struggles with identifying the compounds when they are minor components (<20 mass%) of a mixture. In the layer samples (figure 2.5e,f), it is seen that the signals from underlying layers tend to be attenuated by overlying layers, the extent of which again depends on the nature of the overlying layer. For example, using the same comparison method as during the MA-XRF analysis, a 100 µm blue verditer layer has its signal attenuated to 29% of the uncovered signal intensity by an overlying 50 µm yellow ochre layer and to 46% by an overlying 50 µm lead white layer. Again, the difference between blue verditer and lead white reappears with the method being able to identify blue verditer in all layer configurations, but not lead white. In both datasets, areas with large concentrations of azurite present a hydrocerussite signal, which means the method is more reliable for the identification of blue verditer than for lead white.

Regarding semi-quantification, figure 2.6d,e shows the average sample signal intensity plotted against the areal density of the corresponding pigments. The relationship between the SWIR RIS signal intensity and the pigment areal density in the single-layer samples is much better described by a linear fit than for MA-XRF. The azurite results show a closer correlation than the hydrocerussite results, but this could be due to the previously mentioned azurite misidentifications or due to the overlap between the support and kaolinite features and the hydrocerussite feature.

The calculated LODs are 0.93 mg/cm^2 for blue verditer and 5.37 mg/cm^2 for lead white, which are equivalent to 0.93 mg/cm^2 of azurite and 5.26 mg/cm^2 of hydrocerussite, respectively.

2.3.2. APPLICATION TO A PAINTING

In the selected painting by Jacob Cornelisz van Oostsanen, the Pb-L map (figure 2.7b) reports the presence of Pb over the entire painting, except for small areas of restoration, implying the use of a lead white priming layer. As mentioned before, the Pb-M map (figure 2.7c) is surface-specific and therefore shows the presence of Pb also on the surface paint layers throughout most of the painting, but most predominantly in the sky in the background and in the skin of the figure. Cu (figure 2.7d) was identified in the landscape background, most intensely in the water and rearmost section of trees, and less intensely in the clothing of the figure. Other MA-XRF maps of the painting are presented in appendix A.8.

The azurite signal (figure 2.7e) is identified in amounts above the LOD in the background in the water, the sky, and the rearmost section of trees. Other areas show azurite signals below the LOD, but they are not highly spatially correlated,

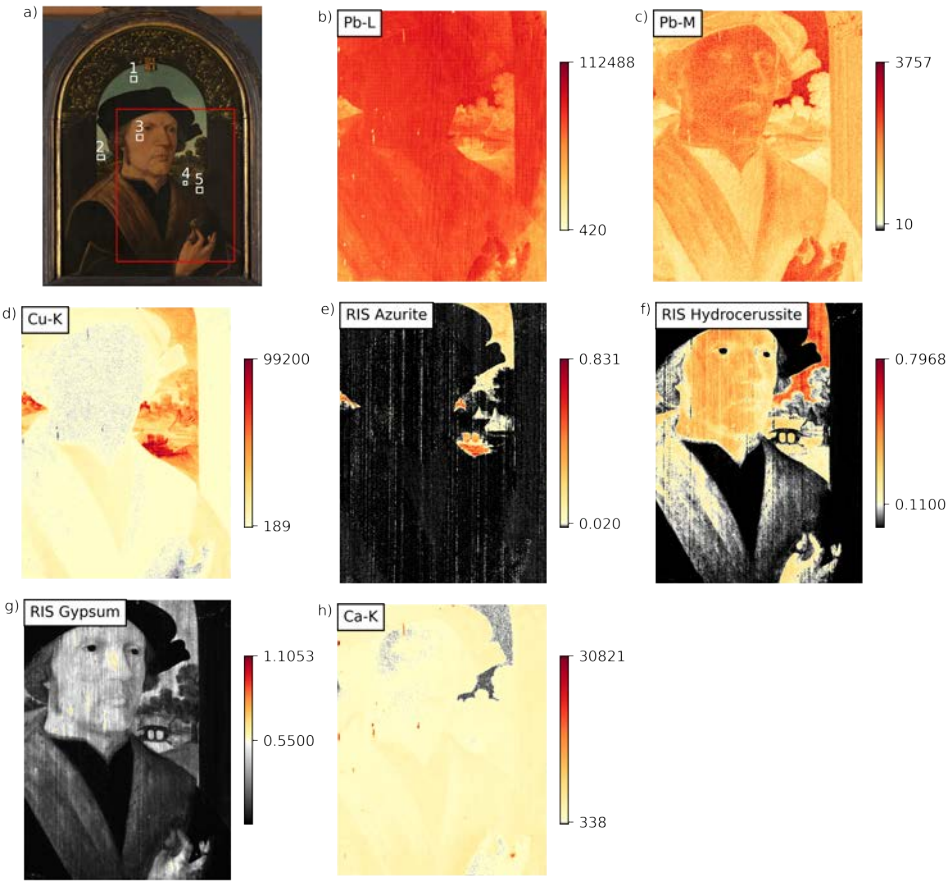

Figure 2.7.: Jacob Cornelisz van Oostsanen, *Portrait of Jan Gerritsz van Egmond van de Nijenburg*, c. 1518, oil on panel, h 42.4 cm x w 32.8 cm, Rijksmuseum (SK-A-3838) (a) Visible light photograph with the MA-XRF scanned area marked in red and areas used for SWIR RIS calculations in white. (b) MA-XRF Pb-L map. (c) MA-XRF Pb-M map. (d) MA-XRF Cu-K map. (e) RIS azurite map. (f) RIS hydrocerussite map. (g) RIS gypsum map. (h) MA-XRF Ca-K map. All maps are displayed with the signals below the LODs in greyscale, and the signals above the LODs in a yellow-red heatmap. RIS maps are cropped to show only the area scanned with MA-XRF, full maps are available in appendix A.8.

implying they are likely due to measurement noise. A hydrocerussite signal (figure 2.7f) above the LOD is present in the open sky in the background and the skin of the figure, whilst signals below the LOD appear in the other sections of the outdoor background, a section of the background arch and the fur vest of the figure.

Since a component for gypsum was included in the fitting, a map for this feature

could be produced as well (figure 2.7g). This gypsum signal is present most intensely in areas of restoration, where it was used to fill the long cracks which formed along the direction of the wood grain of the supporting panel, a common practice in the restoration of panel paintings. The signal is also mapped in other areas of the painting, with a strong correlation to the areas with a hydrocerussite signal. The Ca-K maps produced with MA-XRF (figure 2.7h) show the presence of Ca in similar areas of restoration, but a low-intensity Ca-K signal is also present in the clothing of the figure and darker areas of the background. Lacking a reference sample, which could be used to determine the LODs for gypsum and Ca, an area of the painting was used to determine the blank signal. The area used was the small area of open sky between the figure's face and the trees on the right, as this was the area with the lowest Ca-K signal.

2.4. DISCUSSION

Regarding pigment identification, SWIR RIS yields mixed results. It mostly compares well with the results achieved with MA-XRF, but notable differences are apparent. In the mixture samples (figure 2.4), SWIR RIS method struggles to identify either azurite or hydrocerussite (figure 2.4e,f) when they are present in amounts close to the LODs, the values of which are poor (higher LOD values) compared to those achievable with MA-XRF (figure 2.4b–d). This can be seen in several of the samples including 5% of either blue verditer or lead white which are not correctly mapped. However, in the samples with larger blue verditer (>50 mg/cm^2) and lead white (>25 mg/cm^2) areal densities, MA-XRF fails to clearly differentiate between samples of different thickness, as the samples approach infinite thickness from the point of the discussed XRF lines, as can be seen in figure 2.6a,b. The SWIR RIS method does manage to differentiate between these samples, showing a greater information depth, which is the depth that provides 99.5% of the measured signal in an infinitely thick sample. However, the exact information depth cannot be accurately determined as it seems to exceed the maximum tested layer thickness of 150 µm.

For reference, paint layers are often between 10 and 100 µm,[39] which, assuming similar oil ratios as those recommended by modern suppliers, would equate to between 2.5 and 25 mg/cm^2 for a pure blue verditer paint and between 5.1 and 51 mg/cm^2 for a pure lead white paint. Given that these pigments are often used in mixtures, common areal density values are expected to be lower. However, lead white is commonly used as a ground, often resulting in much thicker layers[40] and therefore higher areal densities.

The layer samples (figure 2.5) mostly support prior observations, as not only does the method differentiate between the different layer thicknesses, but also the areas where the film applicator pooled the paint into thicker layers have much stronger SWIR RIS signals than the rest of the samples (figure 2.5e,f). MA-XRF signals do not exhibit significant variation after a certain thickness as they become infinitely thick from the point of the discussed XRF line (figure 2.5b–d). For both hydrocerussite and azurite, the SWIR RIS signals show a substantial improvement in penetration of overlying paint layers when compared to the corresponding MA-XRF fluorescence

lines (Values for paint layer escape depth for MA-XRF presented in figure A.12). The SWIR RIS signals are attenuated, but not as strongly as the MA-XRF signals, although the level of attenuation depends on the nature of the overlying layer, as yellow ochre layers seem to block more of the signal than the other two paints.

As previously mentioned, there is an issue where SWIR RIS misidentifies higher densities of azurite as low amounts of hydrocerussite. In the case of pure blue verditer samples, the problem is so pronounced that the hydrocerussite signal they present falls slightly above the calculated LOD, as can be seen in the central and right areas of figure 2.5f. Figure 2.8 shows a spectral example of this issue. The cause seems to be a small peak around 1420 nm which is fit as a combination of the support and hydrocerussite components. This peak is likely a contribution of the support material and only causes issues with azurite samples as the other two pigments have features that either fully or partially cover it.

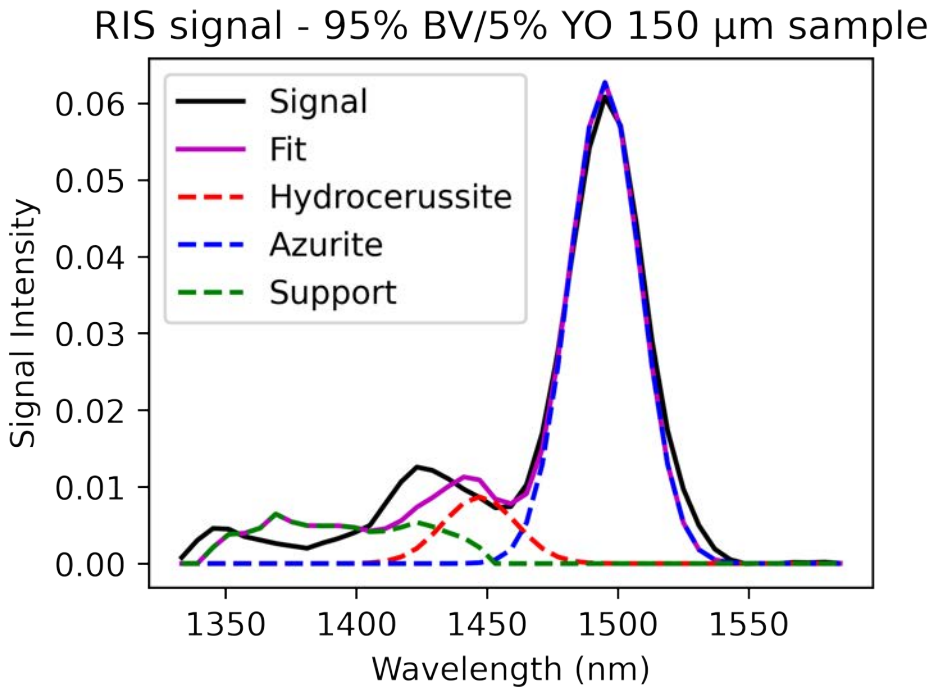

Figure 2.8.: Spectra example showing the fitting of a small hydrocerussite signal in a sample without hydrocerussite (Mixture sample, 95% blue verditer/5% yellow ochre, 150 µm).

Regarding the semi-quantitative analysis, when directly comparing the relationships between the signals of both methods and the associated pigment areal densities (figure 2.6), it can be seen that the SWIR RIS signals exhibit a much larger linear range than the MA-XRF ones. However, certain MA-XRF lines, like Pb-M,

exhibit a strong linear correlation to pigment areal density, but these are limited to surface-specific information (roughly top 13 µm). Their usefulness for the quantification of multi-layer paint systems is therefore limited, especially as overlying varnish layers can further dampen the signal. The relatively poor LODs for SWIR RIS show that it is less suitable for quantification of the pigments when present in low amounts. However, in these regions, the MA-XRF signal still exhibits a roughly linear relation with pigment areal density, and therefore the two methods can be used complementarily to achieve a broader quantification range.

In the test of the painting (figure 2.7), significant differences can be seen between the MA-XRF and SWIR RIS signals. The maps of hydrocerussite (figure 2.7f) and Pb-M (figure 2.7c) have some differences, namely the black clothing and pupils of the figure, and some background elements, like the window wall and the bridge, all of which exhibit a Pb-M signal, but no hydrocerussite signal, implying either the presence of Pb in a form different from hydrocerussite or the presence of a strongly IR absorbing compound which is masking the hydrocerussite signal. Certain areas in the background exhibit a hydrocerussite and Pb-L signal (figure 2.7b), but no significant Pb-M signal. This indicates that a lead white layer is present underneath; the surface paint layer(s) absorb(s) the low energy Pb-M radiation but do(es) not strongly absorb IR radiation. Some of these areas also exhibit a Cu-K signal and have a dark green colour, which would imply the presence of a Cu-based pigment layer on top of an underlying lead white layer, most likely malachite or verdigris, given the lack of an azurite signal. The spatial correlation of the hydrocerussite signals below the LOD shows that how LODs are currently described may not be entirely appropriate for this kind of (spatial) data, as the calculations ignore the spatial components and neighbourhood relationships within the data. Defining a new limit that considers both spatial and spectral data, a limit of detection for imaging, would be perhaps more appropriate.

Comparing the Cu-K (figure 2.7d) and azurite (figure 2.7e) maps yields similar deviations. Whilst Cu-K signals are present throughout the outdoor background as well as the figure clothing, the azurite is only present in the sky, water, and rearmost trees, which are the bluer areas of the background. The differences in the background can be attributed to the use of another (green) Cu-based pigment. The difference in the clothing could be attributed to the use of a Cu-based pigment mixed in with the primary black pigment, or the use of a Cu-based dryer, like verdigris, to reduce the long drying times common to black paints.

The gypsum signal (figure 2.7g) is also of interest due to its strong correlation with the hydrocerussite signal. This could be due to a misfitting of the two features, as the most prominent of the gypsum features is the one that directly overlaps the hydrocerussite –OH feature. However, it is known from cross-section samples that there is gypsum present in the ground layer of the painting. What could be happening is more a negative correlation with the darker areas of the painting. In these areas, the more strongly IR-absorbing paints block the ground layer gypsum signal, which is mostly unobstructed in the brighter areas of the painting, which happens to be where lead white is most prominently used.

Using the relations between RIS signal intensity and pigment areal densities

derived from the paint samples, the average pigment areal densities of certain areas of the painting are calculated. Based on the paints prepared for the mock-up samples, these areal densities can also be converted to the equivalent layer thickness of a single pigment paint layer, to facilitate direct comparison to the paint mock-ups, but they are not actual measurements of the layer thickness in the painting. The target areas are marked in figure 2.7a. For lead white, the sky (area 1) has a pigment areal density of 21.4 mg/cm^2 (the equivalent of a 36 µm layer of pure lead white paint), the face (area 3) has 19.7 mg/cm^2 (33 µm), the background water (area 4) has 10.28 mg/cm^2 (17 µm), and the grass (area 5) has 8.16 mg/cm^2 (14 µm). For azurite, the sky (area 1) has a pigment areal density of 16.1 mg/cm^2 (the equivalent of a 50 µm layer of pure blue verditer paint), the background trees (area 2) have 12.4 mg/cm^2 (38 µm), and the background water (area 4) has 20.1 mg/cm^2 (62 µm). All these areas present the considered pigments in either mixture with other pigments or as underlayers and have average areal densities above the LODs and values within the common areal density values described earlier.

The achieved results of the novel SWIR RIS data processing method in both specially prepared samples and historical samples show promise in the general applicability of the method for mapping the considered pigments. The production of reasonable chemical distribution maps using standard fitting features based on reference materials provides an improvement in both reproducibility and automation over the highly dataset-specific methods currently used for RIS data processing. However, it is also clear that the method suffers when dealing with reflectance features with a strong overlap, like hydrocerussite and gypsum.

2.5. CONCLUSION

The results achieved using MA-XRF and the proposed SWIR RIS data processing method, focusing on characteristic absorption features in specific spectral regions, have shown their potential for both pigment identification and semi-quantitative mapping in a more automated and easily reproducible fashion than the more commonly used endmember-based RIS data processing methods. If properly streamlined, the process can be reduced to roughly 15 – 20 min of computational time, which does not require user intervention. The application of the SWIR RIS method on the prepared paint mock-ups shows an ability to identify the considered pigments more conclusively than with only MA-XRF, albeit with comparatively poor LODs. However, the ability of the SWIR RIS method to differentiate between samples with high pigment concentration and layer thickness shows a greater information depth than that achieved with MA-XRF.

The strong correlation between the SWIR RIS signal intensity and pigment areal density shows great potential for semi-quantitative analysis, but the relatively poor LODs mean it is less suitable for low pigment areal densities. The exploration of the relationship between signal intensity and pigment areal density is limited by the fact that the pigment areal density values used were assumptions based on the amounts mixed during the preparation of the paints, and not directly measured from the prepared sample. The analysis of the samples using X-ray

powder diffraction spectroscopy (XRPD), which provides relatively robust quantitative analysis of inorganic compounds, could provide more accurate pigment densities with which to better define their relationship to SWIR RIS signal intensities. However, the complex absorption effects that happen within a paint layer in the SWIR range make full quantification very difficult and remain a major limitation of the method.

The application of the method on the three objects studied highlights a few issues that must be overcome before the method can be considered sufficiently reliable, the primary being the possibility of overlapping features from different compounds. Some of these issues might be overcome by the inclusion of a greater number of characteristic RIS features in the fitting procedure. For example, azurite presents two other absorption features in the SWIR range at 2245 and 2351 nm. Expanding the method to fit those features as well would make the azurite maps more reliable.

Moreover, some of these shortcomings could also be addressed with a combined MA-XRF and RIS approach. Whilst MA-XRF is very reliable at identifying the elemental presence, there is only so much information that can be extracted from these results, in particular when dealing with different pigments that have the same elemental footprint. And while this RIS method can fail if several compounds with overlapping features are present, these pigments are likely to have different elemental footprints, as is the case between gypsum and azurite. Moreover, absorption effects are much better understood for XRF, which could help increase the reliability for quantitative analysis. The difference in information depth alongside differences in calculated areal densities between the two methods could also provide valuable insight into paint layer stratigraphy, assisting in the identification of areas of interest for further analysis. Further development and refinement of such a multi-modal method would be very beneficial to the reliability and repeatability of pigment identification procedures.

Another possible area of development is the use of the Gaussian fitting method for the analysis of RIS data in other spectral ranges. While pigments often lack reflectance features in VNIR (400 – 1000 nm) that could be fit with this method, the MIR (2500 – 25 000 nm) is rich in these kinds of features.[41] MIR RIS is not currently a commonly used method in the analysis of cultural heritage objects, but as advances in MIR spectrometers make their use more practical in museum contexts, the method is likely to become more relevant and the development of data processing methods well-suited for the analysis of artist's pigments will be of great interest.

However, whilst the method shows promise for its applicability for the identification of other pigments based on prominent and characteristic reflectance features, it is inherently limited to pigments that exhibit such prominent features, and it must be tailored to these specific features. This method should not be seen as a universal solution for the question of RIS data processing, but as an automation tool for specific common questions often addressed using RIS. A practical implementation of this method would allow non-expert users to produce specific pigment distribution maps with a comparable or lower amount of effort than that required for the acquisition of MA-XRF maps. This would be a significant improvement in both speed and reproducibility over the highly labour-intensive methods in use currently.

BIBLIOGRAPHY

[1] L. M. de Almeida Nieto, F. Gabrieli, A. van Loon, V. Gonzalez, J. Dik, R. Van de Plas, and M. Alfeld. "Comparison of macro x-ray fluorescence and reflectance imaging spectroscopy for the semi-quantitative analysis of pigments in easel paintings: A study on lead white and blue verditer". In: *X-Ray Spectrometry* August (2023). ISSN: 10974539. DOI: 10.1002/xrs.3394.

[2] M. Alfeld and L. de Viguerie. "Recent developments in spectroscopic imaging techniques for historical paintings - A review". In: *Spectrochimica Acta - Part B Atomic Spectroscopy* 136 (2017), pp. 81–105. ISSN: 05848547. DOI: 10.1016/j.sab.2017.08.003. URL: https://doi.org/10.1016/j.sab.2017.08.003.

[3] J. K. Delaney, K. A. Dooley, A. van Loon, and A. Vandivere. "Mapping the pigment distribution of Vermeer's Girl with a Pearl Earring". In: *Heritage Science* 8 (1 2020), pp. 1–16. ISSN: 20507445. DOI: 10.1186/s40494-019-0348-9. URL: https://doi.org/10.1186/s40494-019-0348-9.

[4] F. Gabrieli, J. K. Delaney, R. G. Erdmann, V. Gonzalez, A. van Loon, P. Smulders, R. Berkeveld, R. van Langh, and K. Keune. "Reflectance imaging spectroscopy (RIS) for Operation Night Watch: Challenges and achievements of imaging Rembrandt's masterpiece in the glass chamber at the Rijksmuseum". In: *Sensors* 21 (20 2021), pp. 1–18. ISSN: 14248220. DOI: 10.3390/s21206855.

[5] J. K. Delaney, D. M. Conover, K. A. Dooley, L. Glinsman, K. Janssens, and M. Loew. "Integrated X-ray fluorescence and diffuse visible-to-near-infrared reflectance scanner for standoff elemental and molecular spectroscopic imaging of paints and works on paper". In: *Heritage Science* 6 (1 2018), pp. 1–12. ISSN: 20507445. DOI: 10.1186/s40494-018-0197-y. URL: https://doi.org/10.1186/s40494-018-0197-y.

[6] E. Herens, C. Defeyt, P. Walter, and D. Strivay. "Discovery of a woman portrait behind La Violoniste by Kees van Dongen through hyperspectral imaging". In: *Heritage Science* 5 (1 2017), pp. 1–8. ISSN: 20507445. DOI: 10.1186/s40494-017-0127-4.

[7] P. A. Favero, J. Mass, J. K. Delaney, A. R. Woll, A. M. Hull, K. A. Dooley, and A. C. Finnefrock. "Reflectance imaging spectroscopy and synchrotron radiation X-ray fluorescence mapping used in a technical study of The Blue Room by Pablo Picasso". In: *Heritage Science* 5 (1 2017), pp. 1–18. ISSN: 20507445. DOI: 10.1186/s40494-017-0126-5.

[8] M. L. Clarke, F. Gabrieli, K. L. Rowberg, A. Hare, J. Ueda, B. McCarthy, and J. K. Delaney. "Imaging spectroscopies to characterize a 13th century Japanese handscroll, The Miraculous Interventions of Jizō Bosatsu". In: *Heritage Science* 9 (1 2021), pp. 1–10. ISSN: 20507445. DOI: 10.1186/s40494-021-00497-1. URL: https://doi.org/10.1186/s40494-021-00497-1.

[9] K. A. Dooley, D. M. Conover, L. D. Glinsman, and J. K. Delaney. "Complementary standoff chemical imaging to map and identify artist materials in an early italian renaissance panel painting". In: *Angewandte Chemie - International Edition* 53 (50 2014), pp. 13775–13779. ISSN: 15213773. DOI: 10.1002/anie.201407893.

[10] N. D. Keyser, F. Broers, F. Vanmeert, S. D. Meyer, F. Gabrieli, E. Hermens, G. V. der Snickt, K. Janssens, and K. Keune. "Reviving degraded colors of yellow flowers in 17th century still life paintings with macro- and microscale chemical imaging". In: *Science Advances* 8 (23 2022). ISSN: 23752548. DOI: 10.1126/sciadv.abn6344.

[11] R. V. Grieken and A. Markowicz. *Handbook of X-Ray Spectrometry*. Second. Marcel Dekker,Inc., 2002. ISBN: 9780824706005. DOI: 10.1201/9780203908709.

[12] C. Cucci, E. K. Webb, A. Casini, M. Ginanni, E. Prandi, L. Stefani, T. Vitorino, and M. Picollo. "Short-wave infrared reflectance hyperspectral imaging for painting investigations: A methodological study". In: *Journal of the American Institute for Conservation* 58 (1-2 2019), pp. 16–36. ISSN: 19452330. DOI: 10.1080/01971360.2018.1543102. URL: https://doi.org/10.1080/01971360.2018.1543102.

[13] F. Pottier, M. Gerardin, A. Michelin, M. Hébert, and C. Andraud. "Simulating the composition and structuration of coloring layers in historical painting from non-invasive spectral reflectance measurements". In: *Comptes Rendus Physique* 19 (7 2018), pp. 599–611. ISSN: 16310705. DOI: 10.1016/j.crhy.2018.09.007. URL: https://doi.org/10.1016/j.crhy.2018.09.007.

[14] S. Ramsey, T. Mayo, and S. G. Lambrakos. "A parametric model of NIR and SWIR reflectance spectra for dyed fabrics". In: *Journal of Electromagnetic Waves and Applications* 31 (15 2017), pp. 1508–1519. ISSN: 15693937. DOI: 10.1080/09205071.2017.1352541. URL: http://doi.org/10.1080/09205071.2017.1352541.

[15] A. Polak, T. Kelman, P. Murray, S. Marshall, D. J. M. Stothard, N. Eastaugh, and F. Eastaugh. "Use of infrared hyperspectral imaging as an aid for paint identification". In: *Journal of Spectral Imaging* 5 (July 2016), pp. 1–10. ISSN: 20404565. DOI: 10.1255/jsi.2016.a2.

[16] F. Gabrieli, K. A. Dooley, M. Facini, and J. K. Delaney. "Near-UV to mid-IR reflectance imaging spectroscopy of paintings on the macroscale". In: *Science Advances* 5 (8 2019). ISSN: 23752548. DOI: 10.1126/sciadv.aaw7794.

[17] M. Picollo, C. Cucci, A. Casini, and L. Stefani. "Hyper-spectral imaging technique in the cultural heritage field: New possible scenarios". In: *Sensors* 20 (10 2020). ISSN: 14248220. DOI: 10.3390/s20102843.

[18] M. Vermeulen, K. Smith, K. Eremin, G. Rayner, and M. Walton. “Application of Uniform Manifold Approximation and Projection (UMAP) in spectral imaging of artworks”. In: *Spectrochimica Acta - Part A: Molecular and Biomolecular Spectroscopy* 252 (2021), p. 119547. ISSN: 13861425. DOI: 10.1016/j.saa.2021.119547. URL: https://doi.org/10.1016/j.saa.2021.119547.

[19] E. Pouyet, N. Rohani, A. K. Katsaggelos, O. Cossairt, and M. Walton. “Innovative data reduction and visualization strategy for hyperspectral imaging datasets using t-SNE approach”. In: *Pure and Applied Chemistry* 90 (3 2018), pp. 493–506. ISSN: 13653075. DOI: 10.1515/pac-2017-0907.

[20] C. Cucci, J. K. Delaney, and M. Picollo. “Reflectance Hyperspectral Imaging for Investigation of Works of Art: Old Master Paintings and Illuminated Manuscripts”. In: *Accounts of Chemical Research* 49 (10 2016), pp. 2070–2079. ISSN: 15204898. DOI: 10.1021/acs.accounts.6b00048.

[21] J. K. Delaney, J. G. Zeibel, M. Thoury, R. Littleton, M. Palmer, K. M. Morales, E. R. D. L. Rie, and A. Hoenigswald. “Visible and infrared imaging spectroscopy of picasso’s harlequin musician: Mapping and identification of artist materials in situ”. In: *Applied Spectroscopy* 64 (6 2010), pp. 584–594. ISSN: 00037028. DOI: 10.1366/000370210791414443.

[22] E. Pouyet, T. Miteva, N. Rohani, and L. de Viguerie. “Artificial intelligence for pigment classification task in the short-wave infrared range”. In: *Sensors* 21 (18 2021). ISSN: 14248220. DOI: 10.3390/s21186150.

[23] N. Rohani, E. Pouyet, M. Walton, O. Cossairt, and A. K. Katsaggelos. “Nonlinear Unmixing of Hyperspectral Datasets for the Study of Painted Works of Art”. In: *Angewandte Chemie International Edition* 57 (34 Aug. 2018), pp. 10910–10914. ISSN: 14337851. DOI: 10.1002/anie.201805135. URL: https://onlinelibrary.wiley.com/doi/10.1002/anie.201805135.

[24] T. Kleynhans, C. M. S. Patterson, K. A. Dooley, D. W. Messinger, and J. K. Delaney. “An alternative approach to mapping pigments in paintings with hyperspectral reflectance image cubes using artificial intelligence”. In: *Heritage Science* 8 (1 2020), pp. 1–16. ISSN: 20507445. DOI: 10.1186/s40494-020-00427-7. URL: https://doi.org/10.1186/s40494-020-00427-7.

[25] T. Kleynhans, D. W. Messinger, and J. K. Delaney. “Towards automatic classification of diffuse reflectance image cubes from paintings collected with hyperspectral cameras”. In: *Microchemical Journal* 157 (August 2019 2020), p. 104934. ISSN: 0026265X. DOI: 10.1016/j.microc.2020.104934. URL: https://doi.org/10.1016/j.microc.2020.104934.

[26] R. J. Gettens, H. Kühn, and W. T. Chase. “Lead White”. In: *Studies in Conservation* 12 (4 1967), pp. 125–139. ISSN: 20470584. DOI: 10.1179/sic.1967.013.

[27] N. Eastaugh, V. Walsh, T. Chaplin, and R. Siddall. *The Pigment Compendium*. Elsevier Butterworth-Heineman, 2004. ISBN: 0 7506 57499.

[28] S. D. Meyer, F. Vanmeert, R. Vertongen, A. V. Loon, V. Gonzalez, J. Delaney, K. Dooley, J. Dik, G. V. der Snickt, A. Vandivere, and K. Janssens. "Macroscopic x-ray powder diffraction imaging reveals Vermeer's discriminating use of lead white pigments in Girl with a Pearl Earring". In: *Science Advances* 5 (8 Aug. 2019). ISSN: 2375-2548. DOI: 10.1126/sciadv.aax1975. URL: https://www.science.org/doi/10.1126/sciadv.aax1975.

[29] K. A. Dooley, S. Lomax, J. G. Zeibel, C. Miliani, P. Ricciardi, A. Hoenigswald, M. Loew, and J. K. Delaney. "Mapping of egg yolk and animal skin glue paint binders in Early Renaissance paintings using near infrared reflectance imaging spectroscopy". In: *Analyst* 138 (17 2013), pp. 4838–4848. ISSN: 13645528. DOI: 10.1039/c3an00926b.

[30] C. Miliani, F. Rosi, A. Daveri, and B. G. Brunetti. "Reflection infrared spectroscopy for the non-invasive in situ study of artists' pigments". In: *Applied Physics A: Materials Science and Processing* 106 (2 2012), pp. 295–307. ISSN: 09478396. DOI: 10.1007/s00339-011-6708-2.

[31] R. Frost, É. Makó, J. Kristóf, and J. Kloprogge. "Modification of kaolinite surfaces through mechanochemical treatment—a mid-IR and near-IR spectroscopic study". In: *Spectrochimica Acta Part A: Molecular and Biomolecular Spectroscopy* 58.13 (2002), pp. 2849–2859. ISSN: 1386-1425. DOI: https://doi.org/10.1016/S1386-1425(02)00033-1. URL: https://www.sciencedirect.com/science/article/pii/S1386142502000331.

[32] M. Alfeld, J. V. Pedroso, M. V. E. Hommes, G. V. D. Snickt, G. Tauber, J. Blaas, M. Haschke, K. Erler, J. Dik, and K. Janssens. "A mobile instrument for in situ scanning macro-XRF investigation of historical paintings". In: *Journal of Analytical Atomic Spectrometry* 28 (5 2013), pp. 760–767. ISSN: 13645544. DOI: 10.1039/c3ja30341a.

[33] M. Alfeld and K. Janssens. "Strategies for processing mega-pixel X-ray fluorescence hyperspectral data: A case study on a version of Caravaggio's painting Supper at Emmaus". In: *Journal of Analytical Atomic Spectrometry* 30 (3 2015), pp. 777–789. ISSN: 13645544. DOI: 10.1039/c4ja00387j. URL: http://dx.doi.org/10.1039/C4JA00387J.

[34] V. A. Solé, E. Papillon, M. Cotte, P. Walter, and J. Susini. "A multiplatform code for the analysis of energy-dispersive X-ray fluorescence spectra". In: *Spectrochimica Acta - Part B Atomic Spectroscopy* 62 (1 2007), pp. 63–68. ISSN: 05848547. DOI: 10.1016/j.sab.2006.12.002.

[35] K. Danzer. *Analytical Chemistry: Theoretical and Metrological Fundamentals*. 1st ed. Springer Berlin Heidelberg, 2007. ISBN: 978-3-540-35990-6. DOI: https://doi.org/10.1007/978-3-540-35990-6. URL: https://www.researchgate.net/publication/269107473_What_is_governance/link/548173090cf22525dcb61443/download%0Ahttp://www.econ.upf.edu/~reynal/Civil%20wars_12December2010.pdf%0Ahttps://think-asia.org/handle/11540/8282%0Ahttps://www.jstor.org/stable/41857625.

[36] M. Alfeld, S. Pedetti, P. Martinez, and P. Walter. “Joint data treatment for Vis–NIR reflectance imaging spectroscopy and XRF imaging acquired in the Theban Necropolis in Egypt by data fusion and t-SNE”. In: *Comptes Rendus Physique* 19 (7 2018), pp. 625–635. ISSN: 16310705. DOI: 10.1016/j.crhy.2018.08.004. URL: https://doi.org/10.1016/j.crhy.2018.08.004.

[37] C. G. Ryan, E. Clayton, W. L. Griffin, S. H. Sie, and D. R. Cousens. “SNIP, a statistics-sensitive background treatment for the quantitative analysis of PIXE spectra in geoscience applications”. In: *Nuclear Inst. and Methods in Physics Research, B* 34 (3 1988), pp. 396–402. ISSN: 0168583X. DOI: 10.1016/0168-583X(88)90063-8.

[38] G. V. der Snickt, S. Legrand, I. Slama, E. V. Zuien, G. Gruber, K. V. der Stighelen, L. Klaassen, E. Oberthaler, and K. Janssens. “In situ macro X-ray fluorescence (MA-XRF) scanning as a non-invasive tool to probe for subsurface modifications in paintings by P.P. Rubens”. In: *Microchemical Journal* 138 (2018 2018), pp. 238–245. ISSN: 0026265X. DOI: 10.1016/j.microc.2018.01.019. URL: https://doi.org/10.1016/j.microc.2018.01.019.

[39] N. Salvadó, S. Butí, M. A. G. Aranda, and T. Pradell. “New insights on blue pigments used in 15th century paintings by synchrotron radiation-based micro-FTIR and XRD”. In: *Analytical Methods* 6 (11 2014), pp. 3610–3621. ISSN: 17599679. DOI: 10.1039/c4ay00424h.

[40] V. Gonzalez, A. V. Loon, S. W. Price, P. Noble, and K. Keune. “Synchrotron micro-XRD and micro-XRD-CT reveal newly formed lead-sulfur compounds in Old Master paintings”. In: *Journal of Analytical Atomic Spectrometry* 35 (10 2020), pp. 2267–2273. ISSN: 13645544. DOI: 10.1039/d0ja00169d.

[41] F. Gabrieli, K. A. Dooley, J. G. Zeibel, J. D. Howe, and J. K. Delaney. “Standoff Mid-Infrared Emissive Imaging Spectroscopy for Identification and Mapping of Materials in Polychrome Objects”. In: *Angewandte Chemie - International Edition* 57 (25 June 2017), pp. 7341–7345. ISSN: 15213773. DOI: 10.1002/anie.201710192.

3

ADVANCED ANALYSIS OF HISTORICAL MANUSCRIPTS THROUGH INTERPRETABLE MACHINE LEARNING OF REFLECTANCE IMAGING SPECTROSCOPY

Historical manuscripts are treasure troves of historical and linguistic information. However, their analysis is often hindered by the degradation and damage accumulated during their history. RIS is a promising, information-rich method that allows non-invasive analysis of historical manuscripts, yet offers the analytical specificity to discern content from damage. However, the most prevalent data processing methods for RIS data, e.g. unsupervised ML methods, are not necessarily optimal for all applications. Supervised ML methods tend to be better suited for tailored recognition tasks, but the black-box nature of these models often limits understanding of the underlying decision process and hamper interpretation. This work addresses this challenge by expanding supervised ML for RIS with concepts from interpretable ML, namely SHAP. We develop two novel methodological advances for analysis of historical manuscripts, SHAP pseudo-spectra and SWIM, and apply them to two manuscript case studies. The Leiden Riddle, a 9-10th century text, is one of few surviving examples of the Northumbrian dialect of Old English, and the 1669 First Set of the Fundamental Constitutions of Carolina is the earliest text attributed to political philosopher John Locke. Our methods are able to provide advanced insight into the spatial and chemical differentiation of inks from other manuscript features, such as damage areas, facilitating greater historical understanding of these manuscripts.

3.1. INTRODUCTION

Historical manuscripts are carriers of a wealth of information. Not only do they include literary information through the text, but they also carry linguistic information in how the text is written, and a variety of historical information in the materiality of the object itself, such as the writing materials available to the authors.[1] This variety of information is, ultimately, carried by the object and is therefore at risk of becoming unavailable to the reader as the object experiences material changes, purposeful or otherwise. These changes can include passive chemical or mechanical degradation, purposeful edits by authors or later editors, and accidental damage caused by overzealous conservators.[2–5]

The study of historical manuscripts plays a major role in the centuries-old field of paleography. Given its long history, the analytical methods used in paleography have varied greatly alongside technological developments. Early research included careful visual analysis under specific conditions, like early morning sunlight,[6] or the more invasive use of chemical reagents to temporarily increase ink contrast.[2] As novel imaging methods developed, like photography in the visible and non-visible spectral ranges, paleography incorporated them.[7] The proliferation of multi-spectral imaging methods would provide researchers with more detailed chemical information on historical objects, but also presented a challenge in terms of the sheer amount of data produced.[8] Whilst paleographers could reasonably be expected to analyse three or four different spectral images of a text, having to analyse 10 to 15, as well as their relations to each other, without introducing human bias, is a non-trivial task. To account for this dimensionality issue, computational methods were introduced to handle these increasingly complex datasets. While methods such as ICA[9] and NMF[10, 11] have been used, PCA[12] has been the most widely adopted for reconstruction of damaged texts.[13–16]

As RIS, also known as hyperspectral imaging, started seeing wider use in cultural heritage science, it has been increasingly applied to the analysis of manuscripts as well. While not a universal improvement over multi-spectral imaging (e.g., the loss of spatial resolution is a common drawback[17]) RIS application to the study of damaged historical manuscripts has been successful.[4] However, in cases there the (chemical) variation that reports a manuscript feature of interest is not one of the more dominant trends present in the data, unsupervised methods such as PCA might not be able to retrieve (and amplify) that signal. For such cases, supervised ML methods can be a solution. The externally applied labelling that makes these methods supervised can be used to focus on a particular recognition task that is tailored so answer a specific question. Unlike unsupervised methods, in which data is processed with relatively little user input, supervised ML methods require user input in the form of data labels that accompany the measurements and a relatively large amount of training data. Early works by Easton et al.[13] use supervised methods on multi-spectral imaging datasets for specific problems, such as differentiating between original inks and later inks, with reasonable success. The labour intensive nature of generating labels for supervised ML and the quality and speed with which, for example, PCA results can be obtained, means that the choice of whether a supervised or unsupervised approach is optimal depends on whether

an unsupervised method is able to pick up on a signal of interest and on what the application demands. Specifically in manuscript analysis, however, often a majority of a manuscript's surface area does not tend to carry ink, while the writing of interest usually takes up a relatively small amount of of the surface area. As a result, signals of interest are sometimes hard to discern and more focused supervised methods hold particular promise to advance this field.

This work continues to push supervised ML methods for analysis of historical manuscripts forward. It addresses particular challenges that emerge in more high-dimensional measurement types, such as RIS. When dealing with manuscripts, the goal is often to amplify the signal of a particular ink class in a manuscript. This can be focused on boosting its spatial specificity such that it can be differentiated more clearly in the spatial domain from other inks, blotches, or background classes. This spatial-centric application is often focused on increasing intelligibility of the text and unlocking literary and linguistic information. Better differentiation of ink can also be focused on boosting its chemical specificity such that one develops a better understanding of how it differs chemically from other classes in the manuscript. This chemistry-centric application is often aimed more at accessing the material information and history that lies latent in the object. In either case, training a (supervised) classification model to learn to discern the ink of interest from everything else that is measured in the manuscript can be powerful driver for recognizing the class of interest with greater sensitivity and specificity than a human interpreter could achieve. In this work, we use XGBoost[18] models to build such classifiers that can distinguish between target and non-target classes (e.g., original ink vs. damage). However, the black-box nature of classifiers is a recurring issue in supervised ML approaches. Whilst a user can interpret the output predictions delivered by a classification model (namely predicted label maps indicating where the computer estimates the target ink is found on the basis of the input RIS measurements), it is not necessarily possible to understand the decision process that lead to these predicted labels if one starts from the chemical inputs described by the RIS measurements. If we could identify which chemical information or features along the pixels spectral domain drive the differentiation of our ink class of interest, this information could be used both to amplify spatial discernment of writing and to answer questions on the materiality of the object (e.g., if genuinely different inks were used in the manuscript, and how they differ). Therefore, elucidating the functioning of this black box is essential, and has led directly to the methodological advances described in this work. Specifically, use of SHAP,[19] an interpretable ML approach for extracting from supervised ML classifiers which input features are more relevant to deciding whether a new observation is predicted to be a member of the target or non-target class, i.e. which chemical/spectral features are related to the ink of interest. Here, SHAP results are used in two novel ways. Firstly, SHAP pseudo-spectra are used to evaluate the relative importance of each spectral channel for the class differentiation, which provides information on the spectral differences between the classes. Secondly, a new synthetic image type, referred to as a SWIM, combines the input RIS data and the calculated SHAP pseudo-spectra to amplify target-related variation and attenuate non-target-related variation, providing

a higher-legibility segmentation of the target class. Beyond this, SHAP maps[20] are used to guide the iterative improvement of training data, offering a new means of improving supervised ML models in an environment of low target class training example numbers or class imbalance

The potential of these methods is evaluated using two case studies, for which unsupervised methods proved insufficient. First, the Leiden Riddle, a 9th-10th century manuscript, is one of very few examples of the Northumbrian dialect of Old English. It is damaged by abrasion and chemical stains but its rarity makes any additional intelligibility that can be extracted from this text a substantial advance in the historical understanding of this dialect. Then, the 1669 Fundamental Constitutions for the Government of Carolina, the earliest text attributed to political philosopher John Locke, forms a second case study. This manuscript was edited extensively during or after its writing, documenting the early ideological evolution of one of the Enlightenment's most influential thinkers. The two case studies present different types of damage and different challenges in their analysis, allowing us to demonstrate both the spatial domain and spectral domain improvements that can be pursued using the methods we introduce.

3.2. RESULTS

3.2.1. CASE STUDY 1

The Leiden Riddle (Leiden, Bibliotheek der Rijksuniversiteit, Codex Vossanius Latinus 4° 106, 25v) (figure 3.1a) is a section of a 9th or 10th century copy of Aldhelm's *Enigmata* (Riddles), a section of his *Epistola ad Acircium* (The Letter to Acircius), a well-documented Latin text from 8th century England.[6, 21] What sets the Leiden Riddle apart from the rest of the text and from other copies of Aldhelm's treatise is that it is not written in the original Latin but is a translation of one of the riddles (Number 33, *Lorica*) to the Northumbrian dialect of Old English, a dialect and language very different from Modern English.

If the Leiden Riddle is viewed through the frames of reference discussed in the introduction, the materiality of the Leiden Riddle is fairly well understood, as it is iron gall ink on parchment, the predominant form of written records in medieval Europe.[23] The literary content is mostly also well understood, as it is a translation from an existing Latin text, albeit not a direct translation. The linguistic content is decidedly where the most can be gained from further analysis of the text. Written examples of Old Northumbrian are very rare,[24] so any small piece of text can provide significant insight into the practice of this dialect, and therefore, to the evolution of the Anglic languages. The Leiden Riddle also has the benefit of having a similar translation in the *Exeter Book*,[21] which provides some ground for comparison, albeit in West Saxon, a different dialect of Old English. This linguistic value has not gone unnoticed, and the text has been the focus of research for quite some time. Several transcriptions have been made of the text since 1861.[6, 7] However, these transcriptions are not in full agreement with one another. Between the transcriptions, there are 27 areas of disagreement, which are the focus of this research (appendix B.3), three of which are used as examples (figure 3.1b-d).

Figure 3.1.: a) Photograph of the Leiden Riddle, with the three interest areas marked. b-d) Detail photograph of the three interest areas. e-g) RGB derived from the RIS data, produced using the XYZ method in DataHandlerP.[22] h-j) Probability maps output by the classifier shown in a special manuscript colourmap for the Riddle Ink class. k-m) SWIM for the Riddle Ink class shown in a special manuscript colourmap.

One of the reasons for these disagreements is the degraded state of the ink. The exact degradation mechanism of iron gall ink is not very well understood, but the primary result of the degradation is the fading of the ink, ultimately making it illegible.[25–28] The fading seems to have already been a problem back in 1861, as only a few years later, in 1864, chemical reagents were applied to try to make certain parts of the text more legible, but ultimately damaging the text. Gerritsen states that the reagent used is ammonium sulphide (sometimes referred to as volatile liver of sulphur), based on unpublished documentation made by Pluygers, the conservator who applied the reagent.[7] However, some of the damage also matches the kind of blue residue more closely related to the use of Giobert tincture,[2] so it is believed both reagents may have been used. The reagents were used in a relatively sparing manner, being only applied in specific locations. The three areas chosen show different kinds of degradation present in the text. Area 1 has a blue stain, area 2 has a dark stain and area 3 does not seem stained, but the text is faded.

For this case, the ML classifier was trained to distinguish between the ink used in the Northumbrian text and all other components. The output of the classifier for the three target areas are shown in figure 3.1h-j, in the form of probability maps. For area 1, the classifier succeeds in recognizing a set of characters obfuscated by the blue stain. For area 2, the classifier identifies roughly the area where text is present, but is unable to distinguish clearly between the ink and the dark stain. For area 3, the classifier is able to identify the characters that are still visible, but does not find anything in the blank space in between these characters. This could be due to there not having been any characters in this space or due to the ink being degraded or abraded past the point where it is identifiable with this method. The SWIMs (figure 3.1k-m) provide some more useful spatial information than the output probability maps. For area 1 and 3, it does not provide any further information, but for area 2 it provides a significant improvement in legibility of the stained area, significantly suppressing the contribution of the dark stain.

As for the SHAP spectrum (figure 3.2), it shows a strong negative cluster at 750 −850 nm, a weaker negative cluster around 590 nm, and a weak positive cluster around 950 nm. This means that these spectral areas are the most relevant for the classification task. The NIR region (700 −1400 nm) is not usually used for the study of iron gall ink because of the ink's increased transparency in this range compared to other historical inks, like carbon-based inks,[29–31] so the high SHAP values in this range are an initially unexpected result. However, the NIR region usually being considered less relevant is likely due to the most common question during the analysis of manuscripts being differentiating iron gall ink, carbon-based inks and the parchment supports. But in this case, where iron gall ink is being distinguished from other non-ink components, the NIR region seems to provide useful information.

The classifier outputs also show there is a consistent spectral difference between the Northumbrian text ink and the Latin text ink, as they can be consistently distinguished by the system. This would support Parkes'[6] hypothesis that the two texts were written with different inks, giving further credence to their hypothesis that the Northumbrian text was a later addition by a different scribe.

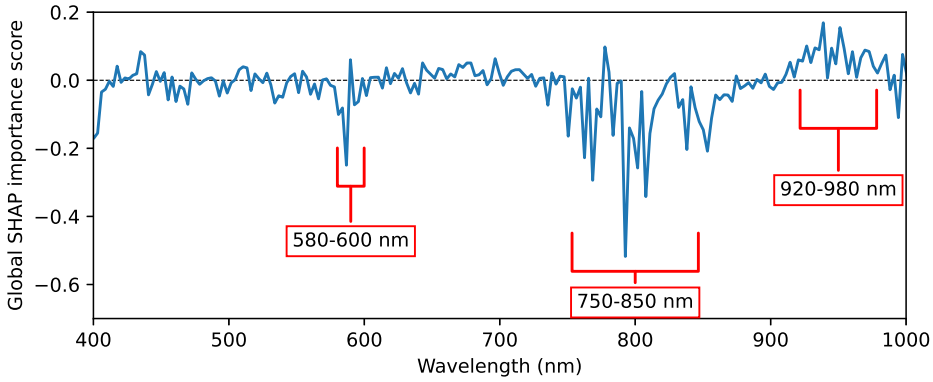

Figure 3.2.: SHAP pseudo-spectrum for the Leiden Riddle classifier.

3.2.2. CASE STUDY 2

The 1669 Fundamental Constitutions for the Government of Carolina, preserved in the manuscript PRO 30/24/47/3 at the UK National Archives (figure 3.3a), holds profound historical significance as one of the earliest frameworks for colonial governance. Written in the hand of philosopher John Locke, then secretary to Anthony Ashley Cooper (later known as the 1st Earl of Shaftesbury), the manuscript outlines a hierarchical structure for the governance of the Carolina colony. Its importance lies not only in its role as a precursor to constitutional governance in America but also in the light it sheds on Locke's political thought. However, the manuscript presents a significant challenge to researchers, as large portions of the texts have been obscured by erasure and overwriting, in a variety of inks (figure 3.3b-c), making certain sections unreadable and complicating scholarly efforts to fully interpret what may be Locke's original contribution.[32, 33]

To overcome these challenges, reflectance imaging spectroscopy and its ability to detect subtle differences in ink colours was seen as a method of choice to differentiate the various inks and retrieve the original text. By using this technique, we aim to recover these illegible sections, offering access to Locke's unaltered draft and providing new insights into Locke's evolving constitutional ideas and contributing to a deeper understanding of the document's broader historical context. However, unsupervised ML methods were unable to provide significant insight, likely because the spectral difference between different types of ink is very small in comparison to the broader spectral difference present in the dataset. Therefore, supervised ML methods are used.

The area scanned includes two pages of the text, both containing edits. The left page has more prominent edits and is the primary area of interest. The main edit is a full paragraph of text which was covered with a looping pattern and a large X. The right page has a small area which was edited by having the text crossed out using a horizontal line and a small note added on the left margin. The ink used

Figure 3.3.: a) Photograph of the Locke Constitution (PRO 30/24/47/3), with the two example areas marked. b-c) Detail photograph of the two example areas. d-e) RGB derived from the RIS data, produced using the XYZ method in DataHandlerP.[22] f-g) Probability maps output by the classifier shown in a special manuscript colourmap for the Text Ink class. h-i) SWIM for the Text Ink class shown in a special manuscript colourmap.

for these edits visually resembles that used for the large X on the left page, having a darker colour, whilst the ink used for the looping pattern in the left page has a lighter colour.

To isolate the original text, the system was built to distinguish between the inks used in the original text and those used for the edits. The output of the classifier for two example areas are shown in figure 3.3f-g. In both areas, the system does not provide significant improvements in legibility. Whilst it partially suppresses some of the edits, like the large X on the left page or the left most annotation in the right page, it also partially suppresses areas of original text. The SWIMs (figure 3.3h-i) provide mixed results. In the left area, some parts of the looping edits are suppressed, but not in a consistent manner, whilst the large X edit is not suppressed. For the right area, the edits on the left margin are not significantly suppressed, but the horizontal editing lines are somewhat suppressed. Both of these results may be more related to the limited spatial resolution and focus of the measurement (visible in figure 3.3d-e), with the SWIM being weighed more strongly to channels with poor sharpness, resulting in an effect similar to a Gaussian blur, which reduces the prominence of smaller spatial features, like thin ink lines.

The system uses two separate classifiers, an ink vs non-ink classifier and an original ink vs. edit ink classifier, and therefore, there are two SHAP spectra (figure 3.4). For the ink vs non-ink classifier, only the 600 −650 nm and 960 −1000 nm ranges seem to have any significant effect, both positive. For the original ink vs. edit ink classifier, only the 800 −900 nm and 950 −1000 nm ranges have any noticeable effect, but have absolute values four orders of magnitude lower than the other two classifiers shown, meaning that the effect on the output is much lower. This is likely due to the similarity of the different ink classes (visible in appendix B.6). These results show the same surprising outcome as those present in case study 1, with the commonly disregarded NIR region providing what is seemingly useful insight to the classifier. This is again likely due to the task in question, differentiating between two inks of the same type, not being a common one.

The inconsistent suppression of the different edit inks implies that these may be spectrally different from each other, which could mean they are different inks, potentially applied at different times or by different people. To better understand the specific differences between the edit inks, it was decided to also train different classifiers to distinguish between the different edit ink classes. All considered metrics (accuracy, balanced accuracy, recall, precision and F1-score) show a fairly reliable differentiation between the three edit ink classes (~0.8 for all metrics), better than that between the original ink and edit ink super classes(~0.7 for all metrics). This would imply the three edit inks are spectrally different, and therefore likely different inks. A different set of classifiers were also trained to distinguish between each of the ink classes and the original ink super class, of which the Edit Ink 2 vs. Original Ink classifier had the worst performance (~0.6-0.7). This would imply that Edit Ink 2 is the most spectrally similar to the original ink from all the edit ink classes, although the difference in performance is not significant enough to draw any meaningful conclusions. Further insight can be gained from looking into the SHAP spectra of each of the classifiers (visible in appendix B.8), which show variations on the SHAP

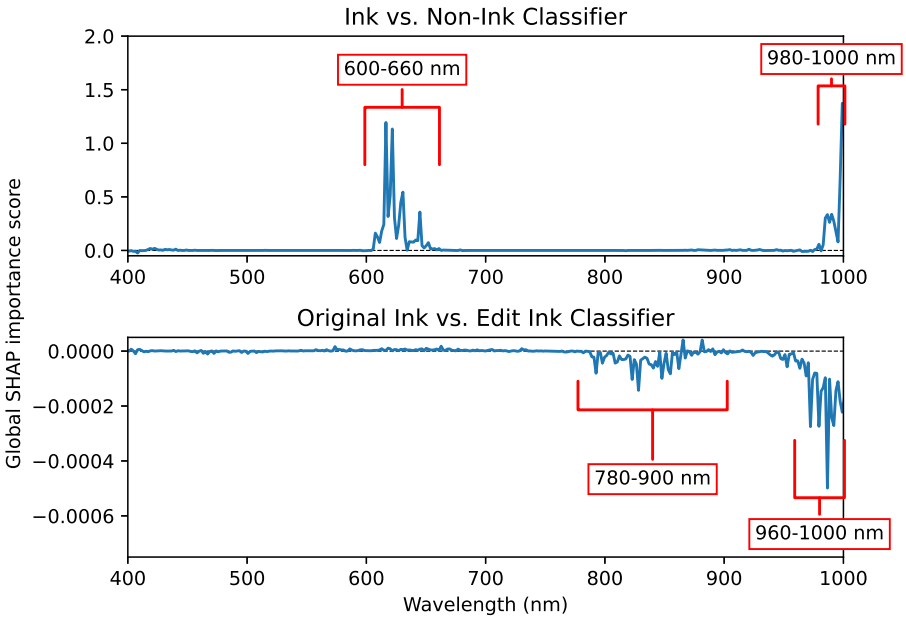

Figure 3.4.: SHAP importance spectra for the two classifiers used for the Locke Manuscript, the Ink vs. Non-classifier and the Original Ink vs. Edit Ink classifier.

importance of each spectral feature for the different classifiers. The SHAP spectra show that for all the classifiers the most important spectral regions are 450 −650 nm and 800 −1000 nm, with almost no contribution for the areas outside these ranges. The SHAP spectra also show that the individual classifiers may focus on specific parts of the ranges, like the Edit Ink 2 vs. Edit Ink 1 classifier showing greater SHAP values in the 450 −520 nm range, whilst the Edit Ink X vs. Edit Ink 1 classifier shows greater values in the 520 −600 nm range. This further supports the hypothesis that all three edit inks are different inks, which vary in their materiality and, consequently, their reflectance.

3.3. DISCUSSION

The two case studies show the potential of this method for the analysis of historical manuscripts. SHAP pseudo-spectra are able to provide insight into the spectral differences between different classes in RIS datasets. For both case studies, the output of the classifiers and the SHAP pseudo-spectra provide insight into the differences between ink classes from which historical information can be extracted. In both cases, the SHAP pseudo-spectra provided surprising results highlighting the

commonly disregarded NIR spectral range as one of interest when analyzing iron gall ink manuscripts.

SWIMs present a method for direct contrast enhancement for target classes. Case study 1 shows that SWIMs can provide improvements in legibility when dealing with some types of accidental damage, like chemical staining. Other types of damage, like passive/mechanical degradation, are not very likely to be addressable with these methods, as their sensitivity to the degraded traces of inks are not high enough. In such cases, methods with higher sensitivities for the minor metallic components of inks that can remain after any visible traces of the ink are gone, like MA-XRF scanning, may prove more successful.[34–36] Case study 2 shows that purposeful edits present different difficulties in undoing, as the spectral differences may be less prominent.

In both cases, the limited spatial resolution of the hyperspectral cameras used proved a significant limitation for the legibility of the resulting maps. The use of cameras with a higher spatial resolution would not only provide a general improvement in legibility, but also make it much easier to make the initial sample masks, as well as providing more examples for each class.

3.4. METHODS

3.4.1. DATASETS

The two case studies covered in this article were measured using different RIS setups.

Case study 1 (Leiden Riddle) was conducted using a Specim IQ hyperspectral camera (Specim, Spectral Imaging Ltd., Oulu, Finland),[37] measuring the VNIR spectral range (400 – 1000 nm) over 204 channels. The RIS data were acquired with an integration time of 10 ms and the camera positioned at around 12 cm from the object. Two ARRILITE 70 Plus 240 V/800 W halogen lamps (ARRI AG., Munich, Germany) positioned at around 1 m were used as light sources and an in frame 99% barium sulfate white reference was used to flat-field the data. Four scans were taken and stitched together using DataHandlerP.[22, 38] The resulting dataset consisted of 403 260 (858 x 470) spectra with 204 spectral channels.

Case study 2 (Locke Constitution) was conducted using a MV.C VNIR hyperspectral camera (Headwall Photonics, Bolton, MA, USA), measuring the VNIR spectral range (400 – 1000 nm) over 342 channels, with an integration time of 10 ms. A perClass Mira Stage with integrated Quartz Tungsten Halogen (QTH) illumination was used, positioning the item at around 30 cm from the camera. White balance and flat-fielding were recorded using an integrated 99% barium sulfate white reference. The resulting dataset consisted of 730 000 (1000 x 730) spectra with 342 spectral channels.

3.4.2. SUPERVISED ML WORKFLOW

Our workflow is described in figure 3.5. It is based on using the XGBoost software library[18] to train a machine learning model consisting of an assembly of decision trees on manual data masks.

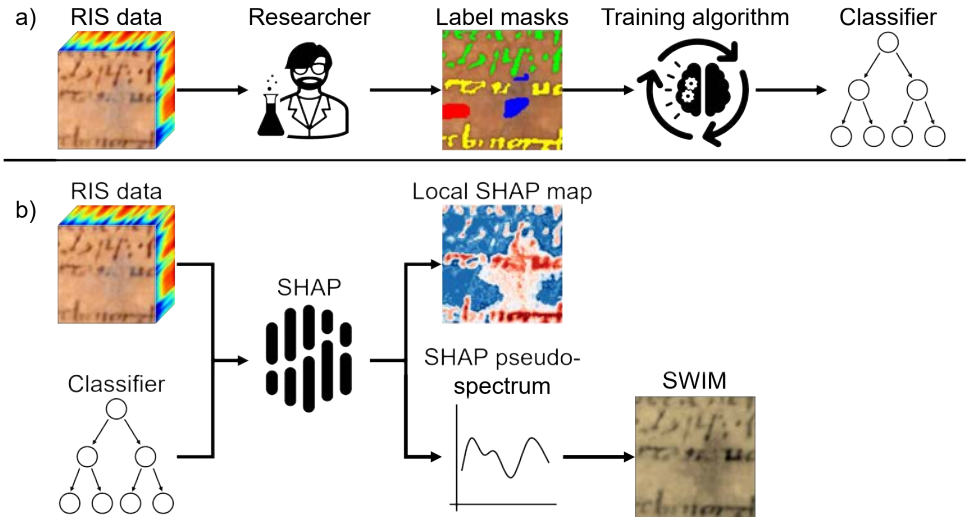

Figure 3.5.: Diagram of the workflow. a) Training of the classifier based on manually labeled data. b) Using SHAP to explain the trained classifiers and evaluating the local and global importance of each of the input features of the RIS data. This information is then used to produce a SWIM with the aim of improving contrast between the target class and other classes.

The exact ML model structure used for each case study varies slightly and the specific differences of each are discussed below. However, many of the settings are shared between the two case studies. All classifiers are trained as binary classifiers to distinguish between a target class and all other classes. Given the deviations possible during ML training, all the ML model outputs presented are an average over 10 different models initiated with different random seeds. The full settings of the XGBoost trainers are available in appendix B.1.

As mentioned in section 3.2.1, the primary goal for case study 1 was to distinguish the ink used in the Northumbrian text from the other components of the manuscript in the hopes of recovering damaged text as well as determining if the ink used for the Northumbrian sections of the text can be distinguished from the ink used for the Latin sections of the text. For this, class labels were manually assigned to the dataset using the classes detailed in in table 3.1. The XGBoost classifier was trained as a binary classifier to distinguish between the Riddle Ink class and all other classes.

As mentioned in section 3.2.2, case study 2 sought to distinguish the ink used in the original text from the ink used in later edits, as well other components in the manuscript. For this, class labels were manually assigned to the dataset using the classes detailed in in table 3.2. Due to the complexity of the dataset, the system was built up of two separate XGBoost classifiers. The first classifier is trained to distinguish between ink and non-ink pixels, and the second one to distinguish between the “Original Ink” and “Edit Inks” superclasses. The output of the first

Table 3.1.: Description of the classes and their sample amounts for the mask for the analysis of the Leiden Riddle.

Class	Samples	Description
Riddle Ink	25396	Ink related to Northumbrian text
Other Ink	7602	Ink related to Latin text
Dark Stain	7897	Dark stains on parchment
Blue Stain	7519	Blue stains on parchment
Parchment	81111	Undamaged/unstained parchment

classifier is used to mask the data that goes into the second classifier.

Table 3.2.: Description of the classes and their sample amounts for the mask for the analysis of the Leiden Riddle.

Super Class	Class	Samples	Description
Original Ink	Text Ink	2328	Ink related to the text underlying the edits on the left page
	Other Ink	7377	Ink related to the text outside of the edited area on the left page
	Overlap Ink	7897	Overlap between the original text ink and the ink used for edits on the left page
Edit Inks	Edit Ink 1	2458	Ink used for the looping pattern of the edit on the left page
	Edit Ink 2	1072	Ink related to the edits on the right page
	Edit Ink X	508	Ink related to the large X on the left page
Non-Ink	Red Stamp	1141	Red archival stamp on the left page
	Paper	60174	Bare paper support
	Weight	91758	Weights used to flatten the manuscript

3.4.3. INTERPRETATION OF ML MODEL

SHAP[19] is used to explain the classifiers and evaluate the importance of each input feature to the classifiers, which in this case are the different spectral bins. The SHAP values are calculated by selectively adding each feature into the classifier, and measuring the effect this has on the output, which is positive if it makes the classifier more likely to classify the input as the target class, and negative if it makes it less likely. Since the order in which features are added into the classifier change the effect that each individual feature has on the output, the SHAP value is an average over all the possible feature orderings (See [20] for a more detailed explanation on the application of SHAP on hyperspectral imaging data). Since calculating all possible orderings of features is prohibitively computationally expensive, SHAP values tend to be approximations in practical applications. However, the choice of ML model allows us to use the TreeExplainer python library[39] to calculate exact SHAP values by exploiting the structure of decision-tree based ML models. A SHAP value is calculated for every feature of every pixel spectrum and this information can be used in different ways. The primary way it is used in this research is by calculating the average of all the SHAP values of each feature. This results in a global importance pseudo-spectrum, which shows the relative importance of each input feature for the overall output of the system. For RIS, this can provide insight into the spectral ranges in which differentiating reflectance features are present and how relatively important these features may be for the specific classification task. As values are calculated for each channel and each pixel, it is also possible to form SHAP maps for each channel. These can be used to better understand the relationship between the SHAP values and the classes, by comparing the spatial distribution of the SHAP values with the spatial distributions of the classes. The final use for the SHAP values is to compute what are here referred to as a SWIM, a novel way of combining the input data and the SHAP results which serve to increase the visible contrast between the target class and other classes by increasing the effect of the spectral channels which SHAP has identified as the most relevant for the target class and decreasing the effect of the spectral channels identified as less important. SWIMs are defined in one of two ways:

$$\sum_{i=0}^{n} \Phi_i r_i \tag{3.1}$$

or

$$\sum_{i=0}^{n} \Phi_i \left(\frac{1}{r_i}\right) \tag{3.2}$$

Where n is the total number of channels, Φ_i is the average SHAP value of channel i, and r_i is the reflectance image of channel i. Equation 3.1 uses reflectance values and equation 3.2 uses pseudo-absorbance values. The choice of which one to use is related to the overall reflectance value of the target class. If the target class has low reflectance values (like ink), using pseudo-absorbance can provide better contrast.

As 10 different ML classifiers were trained for each system, the SHAP values presented are an average over these 10 different models.

3.4.4. IMPROVED TRAINING

Since the amount of data available for training is fairly limited, the label masks must be carefully made to use as much of the data as possible. However, because the actual areas of interest are inherently difficult to label, the training data tends to be skewed towards those areas that are already easier to read. To address this, the data masks are iterated upon based on the outputs of the trained classifiers and existing a priori knowledge of the object, like the alignment of the lines of text and the location of damaged areas. For this, SHAP maps[20] and the output probability maps provide useful insight, highlighting spatial correlations in the challenge areas. This allows beginning with a fairly conservative approach to the labelling of data and progressively add more data particularly targeted to address the classification task at hand.

Regarding the case studies considered in this research, seven iterations of the sampling mask were made for each dataset, available in appendices B.4 and B.6.

BIBLIOGRAPHY

[1] S. P. Johns, C. A. Maule, L. Angelova, M. Vermeulen, C. Day, M. Muñoz-Alegre, M. J. Collins, and M. Roffet-Salque. "Minimally Invasive Vacuum-Aided Extraction Technique for the Lipid Analysis of Historic Parchment". In: *Analytical Chemistry* August (2024). ISSN: 15206882. DOI: 10.1021/acs.analchem.4c01395.

[2] F. Albrecht. "Between boon and bane: the use of chemical reagents in palimpsest research in the nineteenth century". In: *Care and conservation of manuscripts* 13.April 2001 (2012), pp. 147–165.

[3] L. O'Connor. *Science in the library: observing historic manuscripts, part 1*. Nov. 2017. URL: https://www.nli.ie/news-stories/stories/science-library-observing-historic-manuscripts-part-1.

[4] L. Pereira Pardo, P. Dryburgh, E. Biggs, M. Vermeulen, P. Crooks, A. Gibson, M. Fort, C. Vlachou-Mogire, M. Bertasa, J. R. Gilchrist, and J. Danskin. "Advanced imaging to recover illegible text in historic documents. The challenge of past chemical treatments for ink enhancement". In: *Journal of Cultural Heritage* 68 (2024), pp. 342–353. ISSN: 12962074. DOI: 10.1016/j.culher.2024.06.013.

[5] G. Cardinali. "The problem of 'Extinguished letters' and the use of chemical reagents on manuscripts (1551-1553)". In: *Notes and Records* 76 (2 2022), pp. 273–286. ISSN: 17430178. DOI: 10.1098/rsnr.2021.0027.

[6] M. B. Parkes. "The manuscript of the Leiden Riddle". In: *Anglo-Saxon England* 1.September 2008 (1972), pp. 207–217. ISSN: 14740532. DOI: 10.1017/S0263675100000168.

[7] J. Gerritsen. "The text of the Leiden Riddle". In: *English Studies* 50.1-6 (1969), pp. 529–544. ISSN: 17444217. DOI: 10.1080/00138386908597348.

[8] J. Gippert. "The Application of Multispectral Imaging in the Study of Caucasian Palimpsests". In: *Bulletin of the Georgian National Academy of Sciences* 175 (2007), pp. 168–179.

[9] A. Tonazzini, L. Bedini, and E. Salerno. "Independent component analysis for document restoration". In: *International Journal on Document Analysis and Recognition* 7 (1 Mar. 2004), pp. 17–27. ISSN: 14332833. DOI: 10.1007/s10032-004-0121-8.

[10] A. Di Benedetto, L. M. de Almieda Nieto, A. Candeo, G. Valentini, D. Comelli, and M. Alfeld. "Multivariate analysis on fused hyperspectral datasets within Cultural Heritage field". In: *EPJ Web of Conferences* 309 (2024), pp. 1–2. ISSN: 2100014X. DOI: 10.1051/epjconf/202430914007.

[11] A. D. Benedetto, L. M. de Almieda Nieto, D. Marsh, J. Zwetsloot, R. Janssen, A. T. Popkema, H. de Vries, D. Comelli, and M. Alfeld. "Unveiling hidden text in Frisian historic manuscripts by fused reflectance and transmittance imaging spectroscopy". In: *npj Heritage Science* 13 (1 Dec. 2025). ISSN: 30593220. DOI: 10.1038/s40494-025-02001-5.

[12] I. T. Jolliffe. *Principal Component Analysis*. 2nd ed. Springer New York, NY, 2002. ISBN: 978-0-387-95442-4. DOI: https://doi.org/10.1007/b98835.

[13] R. L. Easton, W. A. Christens-Barry, and K. T. Knox. "Spectral image processing and analysis of the Archimedes Palimpsest". In: *European Signal Processing Conference*. December. 2011, pp. 1440–1444.

[14] R. L. Easton, K. T. Knox, W. A. Christens-Barry, and K. Boydston. *Spectral imaging methods applied to the syriac Galen palimpsest*. 2018. DOI: 10.1353/mns.2018.0003.

[15] A. Buncic, C. Albers-Morris, and G. Heyworth. "Multispectral imaging to recover lost text in the Sarajevo Haggadah". In: *Journal of Cultural Heritage* 67 (2024), pp. 284–289. ISSN: 12962074. DOI: 10.1016/j.culher.2024.03.015. URL: https://doi.org/10.1016/j.culher.2024.03.015.

[16] K. A. Huskin, A. J. Zawacki, and G. Heyworth. *Multispectral recovery of a fragment of Richard FitzRalph's Summa de Questionibus Armenorum from University of Rochester, D.460 1000-03*. 2019. DOI: 10.1353/mns.2019.0016.

[17] A. J. Zawacki, K. A. Huskin, H. Davies, T. Kleynhans, D. Messinger, and G. Heyworth. "Fragments under the Lens: A Case Study of Multispectral versus Hyperspectral Imaging for Manuscript Recovery". In: *Digital Philology: Journal of Medieval Cultures* 12.1 (2023), pp. 123–143. ISSN: 21629552. DOI: 10.1353/dph.2023.0004.

[18] T. Chen and C. Guestrin. "XGBoost: A scalable tree boosting system". In: *Proceedings of the ACM SIGKDD International Conference on Knowledge Discovery and Data Mining* 13-17-Augu (2016), pp. 785–794. DOI: 10.1145/2939672.2939785. arXiv: 1603.02754.

[19] S. M. Lundberg and S. I. Lee. "A unified approach to interpreting model predictions". In: *Advances in Neural Information Processing Systems*. Vol. 2017-Decem. May 2017, pp. 4766–4775. arXiv: 1705.07874. URL: http://arxiv.org/abs/1705.07874.

[20] L. E. Tideman, L. G. Migas, K. V. Djambazova, N. H. Patterson, R. M. Caprioli, J. M. Spraggins, and R. Van de Plas. "Automated biomarker candidate discovery in imaging mass spectrometry data through spatially localized Shapley additive explanations". In: *Analytica Chimica Acta* 1177 (2021), p. 338522. ISSN: 18734324. DOI: 10.1016/j.aca.2021.338522. URL: https://doi.org/10.1016/j.aca.2021.338522.

[21] F. Pantaleoni. "Aldhelm's Lorica , the Leiden Riddle , and Riddle 33 of the Exeter Book". In: *The Medieval Translator* 15 (2013). Ed. by A. Petrina, pp. 163–173. DOI: 10.1484/m.tmt.1.101430.

[22] M. Alfeld. *DataHandlerP*. 2019. URL: https://sourceforge.net/projects/datahandlerp/.

[23] I. Rabin. "Material Studies of Historic Inks: Transition from Carbon to Iron-Gall Inks". In: *Traces of Ink*. Ed. by L. Raggetti. Leiden, The Netherlands: Brill, 2021. Chap. 4, pp. 70–78. ISBN: 9789004444805. DOI: 10.1163/9789004444805_006.

[24] A. H. Smith. *Three Northumbrian poems; Caedmon's Hymn, Bede's Death song and the Leiden riddle*. London, United Kingdom: Methuen & Co. Ltd., 1933. URL: https://archive.org/search.php?query=external-identifier%3A%22urn%3Aoclc%3Arecord%3A1151441849%22.

[25] J. Weber, M. Tsukada, and B. Pretzel. "Treating Brown Inks: Investigation into the Effects of Aqueous Treatment Methods on the Colour Stability of Bister, Sepia, Iron Gall and Logwood Inks". In: *Restaurator* (2024), pp. 1–23. ISSN: 18658431. DOI: 10.1515/res-2023-0024. URL: https://doi.org/10.1515/res-2023-0024.

[26] Y. Liu, T. Fearn, and M. Strlič. "Photodegradation of iron gall ink affected by oxygen, humidity and visible radiation". In: *Dyes and Pigments* 198.August 2021 (2022). ISSN: 18733743. DOI: 10.1016/j.dyepig.2021.109947.

[27] A. Ferretti, F. Sabatini, and I. Degano. "A Model Iron Gall Ink: An In-Depth Study of Ageing Processes Involving Gallic Acid". In: *Molecules* 27 (23 Dec. 2022). ISSN: 14203049. DOI: 10.3390/molecules27238603.

[28] M. J. Melo, V. Otero, P. Nabais, N. Teixeira, F. Pina, C. Casanova, S. Fragoso, and S. O. Sequeira. "Iron-gall inks: a review of their degradation mechanisms and conservation treatments". In: *Heritage Science* 10 (1 Dec. 2022). ISSN: 20507445. DOI: 10.1186/s40494-022-00779-2.

[29] M. Gerken, J. Sander, and C. Krekel. "Visualising iron gall ink underdrawings in sixteenth century paintings in-situ by micro-XRF scanning (MA-XRF) and LED-excited IRR (LEDE-IRR)". In: *Heritage Science* 10 (1 Dec. 2022). ISSN: 20507445. DOI: 10.1186/s40494-022-00696-4.

[30] O. Hahn, U. Golle, C. Wintermann, and D. Laurenza. "Scientific analysis of Leonardo's manuscript with anatomic drawings and notes". In: *Exploring Written Artefacts*. De Gruyter, Nov. 2021, pp. 213–227. ISBN: 9783110753301. DOI: 10.1515/9783110753301-011.

[31] A. Cosentino. *Infrared Reflectography for Palimpsests (1h)*. 2024.

[32] D. Armitage. *John Locke, Carolina, and the Two Treatises of Government*. Oct. 2004. DOI: 10.1177/0090591704267122.

[33] H. Brewer. "Whose Fundamental Constitutions?" In: *Locke Studies* 24 (Oct. 2024), pp. 1–57. ISSN: 2561-925X. DOI: 10.5206/ls.2024.17536. URL: https://ojs.lib.uwo.ca/index.php/locke/article/view/17536.

[34] U. Bergmann. "Archimedes brought to light". In: *Physics World* 20(11) (Nov. 2007). DOI: 10.1088/2058-7058/20/11/39.

[35] U. Bergmann, P. L. Manning, and R. A. Wogelius. “Chemical mapping of paleontological and archeological artifacts with synchrotron X-Rays”. In: *Annual Review of Analytical Chemistry* 5 (July 2012), pp. 361–389. ISSN: 19361327. DOI: 10.1146/annurev-anchem-062011-143019.

[36] A. Michelin, F. Pottier, and C. Andraud. “2D macro-XRF to reveal redacted sections of French queen Marie-Antoinette secret correspondence with Swedish count Axel von Fersen”. In: *Science Advances* 7.40 (2021), pp. 1–9. ISSN: 23752548. DOI: 10.1126/sciadv.abg4266. URL: https://doi.org/10.1126/sciadv.abg4266.

[37] J. Behmann, K. Acebron, D. Emin, S. Bennertz, S. Matsubara, S. Thomas, D. Bohnenkamp, M. T. Kuska, J. Jussila, H. Salo, A. K. Mahlein, and U. Rascher. “Specim IQ: Evaluation of a new, miniaturized handheld hyperspectral camera and its application for plant phenotyping and disease detection”. In: *Sensors (Switzerland)* 18.2 (2018). ISSN: 14248220. DOI: 10.3390/s18020441.

[38] M. Alfeld, S. Pedetti, P. Martinez, and P. Walter. “Joint data treatment for Vis–NIR reflectance imaging spectroscopy and XRF imaging acquired in the Theban Necropolis in Egypt by data fusion and t-SNE”. In: *Comptes Rendus Physique* 19 (7 2018), pp. 625–635. ISSN: 16310705. DOI: 10.1016/j.crhy.2018.08.004. URL: https://doi.org/10.1016/j.crhy.2018.08.004.

[39] S. M. Lundberg, G. Erion, H. Chen, A. DeGrave, J. M. Prutkin, B. Nair, R. Katz, J. Himmelfarb, N. Bansal, and S. I. Lee. “From local explanations to global understanding with explainable AI for trees”. In: *Nature Machine Intelligence* 2.1 (2020), pp. 56–67. ISSN: 25225839. DOI: 10.1038/s42256-019-0138-9. URL: http://dx.doi.org/10.1038/s42256-019-0138-9.

4

On the Design of flexible MA-XRF scanners for methodological optimization

Two MA-XRF scanners were designed, the BLB Mark I and Mark II. The design process, which followed a traditional engineering design approach, is here documented. The BLB Mark I scanner proved to be a valuable research tool providing performance comparable to other research scanners in the field whilst allowing for the testing of novel MA-XRF scanning strategies. However, it also suffered from significant issues regarding its control and thermal characteristics, as well as minor limitations in terms of size and multi-modal capabilities. The BLB Mark II was thus designed to address these issues. It is an evolution of the previous design and does not make any major conceptual changes. The performance of the scanner could not be evaluated due to time constraints.

4.1. Introduction

MA-XRF scanners are increasingly complex devices. Section 1.3.1 already provided a detailed overview of the most prominent MA-XRF scanners and highlighted their differences and similarities. As part of this project, it was planned to try novel alternative MA-XRF scanning strategies, and thus a custom MA-XRF scanner was designed and built. The design process followed a traditional engineering design approach, and thus was separated into background research (section 1.3.1), setting of design requirements (section 4.2), prototype design (sections 4.3.1 and 4.3.2), performance evaluation (sections 4.3.3 and 4.3.4) and improvement (section 4.4).

4.2. Design requirements

After initial discussions and evaluation of other existing MA-XRF scanners, the initial design requirements were set and can be summarized to the following categories:

C1. Radiation Safety

The most important set of requirements is that the system must meet TU Delft Radiation Safety standards. These are based on relevant national regulations regarding the use of ionizing radiation sources, described by the Dutch Nuclear Safety and Radiation Protection Authority (Autoriteit Nucleaire Veiligheid en Stralingsbescherming, ANVS),[1] as well as TU-Delft-specific requirements based on how ionizing radiation sources are handled by the organization. Based on an evaluation of existing MA-XRF scanners and their radiation safety measures, it was concluded that the TU Delft regulations are particularly restrictive, and thus different radiation safety measures would be required for the device than are commonly used in MA-XRF scanners.

C2. Direct Position Control

The main research purpose of the device is to test novel scanning strategies for MA-XRF measurements, and thus, the ability to directly control the position and movement of the scan head is of utmost importance. The system must allow fast, reliable and repeatable positioning of the scan head using a simple and intuitive user interface.

C3. Modular Design

The system also aims to explore possible parallel multi-modal imaging methods, combining MA-XRF with other point-based and full-field measurement methods. To this goal, the system should allow future expansion to accommodate such measurement methods without having to completely replace the scan head. The device should thus follow a modular design, allowing for components of the scan head to quickly and easily be attached or removed. Quickly is here understood to mean a maximum of 30 minutes for the entire procedure.

C4. Vertical and Horizontal Scanning

As certain objects can only be positioned vertically or horizontally, the system should allow for both vertical and horizontal scanning and have the ability to quickly switch between the two modes. Again, quickly is here understood to mean a maximum of 30 minutes to change between the two scanning modes.

C5. Equipment Limitations

The system must make use of some equipment that is already available to the research group, namely:

- Mini X2 X-ray tube (Rh Anode, 50 kV Tube Voltage, 200 µA Tube Current) (Amptek Inc., Bedford, MA, U.S.A.) for an X-ray source.[2]
- X-123 FAST SDD Complete X-ray Spectrometer (70 mm^2 Active Area, 0.5 mm Be window) (Amptek Inc., Bedford, MA, U.S.A.) for an X-ray detector.[3]

Two of the X-ray detectors are available, and the system should be able to use either one or both of the detectors.

4.3. BLB MARK I

The first device was dubbed the big lead box Mark I. The device can be separated into two largely independent sub-systems, the scanner and the housing. Because of this independence between the systems, they are here discussed separately, but both are essential for meeting all the design criteria.

4.3.1. SCANNER

The scanner itself can, like most MA-XRF scanners, be divided into a positioning system and an XRF spectrometer. Out of these two, the positioning system is the most flexible part of the design, as criterion C5 already fixes the most significant design choices available for the XRF spectrometer, namely the choice of X-ray source and X-ray detector. However, criterion C1 does have an effect on the X-ray source. Due to limits on the operating voltage of radiation equipment within current regulations, the X-ray tube firmware is modified to limit the operating voltage to 30 kV, which limits the power of the tube to 6 W.

For the positioning system, the vast majority of existing MA-XRF scanners make use of a Cartesian positioning system based on 3 linear actuators. It was decided to use such a positioning system due to its relative simplicity when it comes to controls and their wide-spread use not only in MA-XRF scanners but also other industrial and consumer devices. This wide-spread availability also makes it possible to use low-cost consumer-oriented ready-made solutions. Such solutions reduce the amount of time required to design and set-up the system and imply a certain ease-of-use common to consumer electronics which would make them ideal for this project. However, the benefits of such ready-made solutions may also come at the cost of flexibility, as the internals of the system can be more difficult to modify.

It was ultimately decided that the ease of design outweighed the potential reduction in flexibility, and thus the system would be based on a consumer-level 3D printer. Two primary Cartesian geometries are used for consumer-level 3D printers, which are differentiated by which axes the print head moves in. The first case has the print head move in the X and Y directions, while the print bed moves in the Z direction. A popular variant of this is the "Core XY" system, which uses a paired belt system for more accurate XY positioning. The second variant, commonly referred to as "bed slingers", use two separate actuators to position the print head in the X and

Z dimensions, whilst a separate actuator moves the print bed in the Y dimension. Of these two, bed slingers most closely resemble most existing MA-XRF scanners, as Core XY geometries are slightly more mechanically complex and can also lead to challenges when wiring and accessing the scan head.

Most consumer-level "bed slinger" 3D printers are designed exclusively for fused filament fabrication (FFF) printing. This presents certain issues as the print heads of FFF printers tend to be quite light, consisting only of a heating nozzle and potentially a small filament extruder. Positioning systems designed for moving such light components may not be able to accurately position heavier components, like the X-ray tube and detectors. It was ultimately decided to use a Snapmaker 2.0 Modular 3-in-1 3D printer[4] (Shenzhen Snapmaker Technologies Co., Ltd., Guangdong, China). This device is designed to function not only as a 3D printer, but also as a simple computer numerical control (CNC) machine for machining materials, like wood, carbon fibre and acrylic. Machining imposes greater loads on the machine head, meaning that the positioning system of the machine must be able to withstand higher loads. After contact with the manufacturer, it was confirmed that the linear actuators used by the machine can withhold up to 8 kg of load, which would comfortably be able to hold the maximum expected weight of the scan head of 5 kg. The modular design of the device is also meant to make it easy to change the machine head between the 3 different functionalities, which ultimately makes it very easy to design and attach new equipment onto the positioning system, simplifying the design and assembly of the MA-XRF scan head.

Figure 4.1.: Snapmaker 2.0 A350 Modular 3-in-1 3D printer.[4]

The Snapmaker 2.0 comes in different models of different sizes. The largest of

these models, the A350, has a nominal work area of 350 mm x 330 mm x 320 mm, which provides a reasonable scan area, regardless of the choice of direction of the scan head.

With the positioning system chosen and the X-ray source and detectors fixed, fulfilling criteria C2 and C5, the next step is attaching these components together. Due to the manufacturing equipment available, the design has to be manufacturable using only 3D printers and laser cutters. The biggest question is initially the exact positioning of the X-ray tube and detectors. Figure 4.2 shows the main components and the dimensions that can be modified. Overall, it is desired to minimize a and b, as reducing the distance to the target sample minimizes the atmospheric absorption. It is also generally desirable to minimize β, as this reduces the matrix absorption, although this effect is very limited in practice. Ultimately, these values are set as a=22 mm, b=9 mm and β=40°.

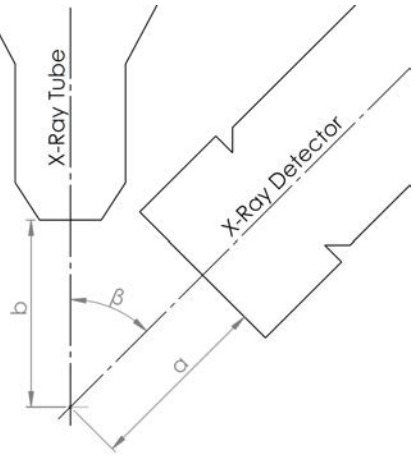

Figure 4.2.: Diagram showing the variables of the scan head geometry of the MA-XRF scanner. Ultimately, these values are set as a=22 mm, b=9 mm and β=40°.

The final design was a simple 3D print and two mirrored laser cut steel plates that would attach the X-ray source and detectors together. This assembly can then be mounted as a single component onto the positioning system. The main piece is designed for horizontal scans, with the scan head moving along the X-axis, whilst the object moves in the Y-axis. However, the scan head was designed so that an extra 3D printed piece could be used to position the scan head for vertical scans, where the scan head moves along both the scanning directions, whilst the object remains static. Thanks to its modular design, the scan head can be switched between the two scanning directions in 15-20 minutes, fulfilling criterion C4. The design also leaves ample space for further devices to be attached onto the scan head, fulfilling criterion C3.

4.3.2. HOUSING

The housing primarily seeks to address criterion C1, but criterion C4 plays a significant role as well.

Radiation safety regulation requires the entire MA-XRF scanner to be completely encased in radiation shielding to prevent any sort of accidental irradiation of users or bystanders. For this, lead panelling will be used. To calculate the required thickness of shielding, the alternate form of Beer-Lambert law can be used:

$$I = I_0 e^{-\frac{\mu}{\rho}\rho l} \tag{4.1}$$

and thus, the energy dependent transmission T can be described as:

$$T(E) = \frac{I}{I_0} = e^{-\frac{\mu(E)}{\rho}\rho l} \tag{4.2}$$

For simplicity, only two E values are considered for the calculation: E_1=20 keV, the most prominent energy emitted by the Rh-target X-ray tube; and E_2=30 keV, the highest energy possible emitted by the X-ray tube. The mass attenuation coefficients $\frac{\mu}{\rho}$ are thus 86.37 cm^2/g and 30.32 cm^2/g (retrieved from xraylib[5] through PyMCA[6]). ρ for metallic lead is 11.34 g/cm^3. The supplier (Salomon's Metalen B.V., Groningen, The Netherlands), offers Pb paneling only in specific thicknesses. Two options were chosen for the calculations, 0.5 and 0.8 mm. For the 0.5 mm panel, the calculated T values are 5.38×10^{-22} for E_1 and 3.42×10^{-8} for E_2. For the 0.8 mm panel, the calculated T values are 9.32×10^{-35} for E_1 and 1.14×10^{-12} for E_2. All of these values are considered sufficient. However, the value considered for radiation safety purposes is the effective dose E, which are a more complicated calculation. 0.5 mm lead-equivalent aprons are documented as shielding 90-99% of potential radiation dose in medical environments.[7, 8] In the Netherlands, there is no specific regulation describing a generally applicable required radiation shielding but is generally determined on a case-by-case basis as per the Directive on radiation protection within the risk inventory and evaluation (NPR 5662:2024).[9] For this device, it was chosen to base the decisions on the closest relevant equivalent, which is radiation protection equipment for medical applications, which are partially regulated by the standard NEN-EN-IEC 61331,[10] part 3 of which defines protective clothing, eyewear and protective patient shields. In this document, a minimum of 0.35 mm lead-equivalent is set for heavy-duty protective aprons, and a minimum of 0.5 mm lead-equivalent is set for heavy-duty protective eyeglasses. The X-ray tube used here operates at a lower voltage than what is typical in medical applications, so these lead-equivalent values are likely more than enough, but as it is unclear in what surroundings the device will be used (i.e. presence of bystanders, distance from the machine, time of use, etc.), and in an abundance of caution, 0.8 mm lead panels were chosen to provide extra protection for users and bystanders.

As the entire system must be fully enclosed in this shielding, the object being investigated itself must also be able to fit within the housing. As this is primarily a test scanner, it is considered reasonable to limit the size of the objects to be scanned to the size of the scan area of the device and therefore the size of the housing is

primarily defined by the size of the scanner. Therefore, the housing must be at least 495 mm x 660 mm x 580 mm to fit the full movement range of the Snapmaker 2.0. Since some other components, like the power source for the Snapmaker 2.0 and later potential equipment additions to the scanner, must also fit within the enclosure, it is best to leave some room for growth within the enclosure by expanding some of its dimensions. In this case, the dimensions have an upper boundary set by the table on which the system will stand. It is ultimately decided to make the housing 580 mm x 980 mm x 660 mm.

The large lead panels that would be needed for this housing would not be able to hold their own weight and thus there must be a load bearing structure onto which the lead panels are attached. For this, a structure is made using standard 40 mm x 40 mm extruded aluminium profiles along the inner edges of the housing volume, which is hereafter referred to as the aluminium skeleton. The lead panels are then bolted onto the outside of this aluminium skeleton. However, even then, this is not enough to fully support the lead panelling as the central parts of the panels are not supported by the skeleton. To address this, the panelling is changed to not be made only of lead panels, but to be made using a sandwich structure, with a lead panel sandwiched between two aluminium panels. These aluminium panels provide rigidity as well as preventing users from coming into direct contact with the lead, which helps avoid potential adverse health effects. A photo of the resulting structure can be seen in figure 4.3.

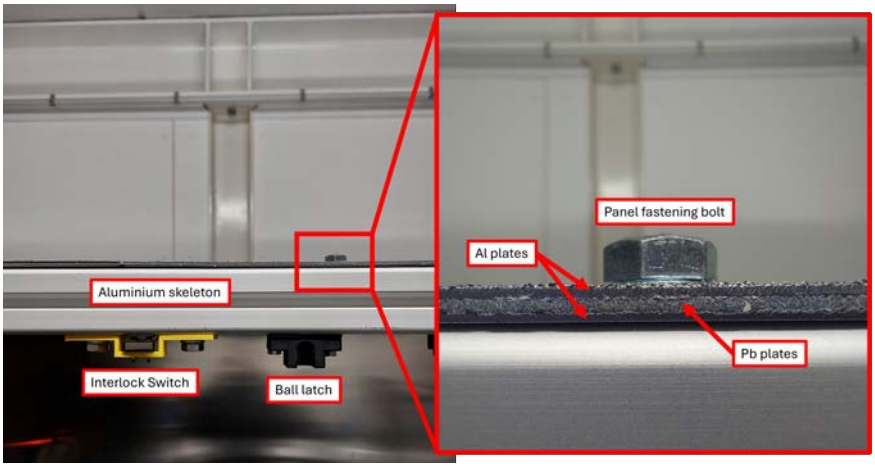

Figure 4.3.: A photo showing the different components of the housing.

With the device now fully enclosed within a big lead box, the required radiation safety measures have been fulfilled. However, the issue now becomes that it is not possible to access the device through the protective housing, which mostly defeats the point of building the device in the first place. To address this prominent shortcoming, doors are added to two sides of the housing. One horizontally swinging door replaces the panel along one of the 580 mm sides, hereafter referred to as door

1, and two horizontally swinging doors replace the panel along one of the 980 mm sides, hereafter referred to as doors 2 and 3, as seen in figure 4.4. These doors are made using the same aluminium/lead sandwich design and thus have the same radiation protection. The doors swivel on three metal hinges and ball latches are used to hold them closed, one ball latch in the centre for door 1, and two ball latches for door 2 and 3, one on the top edge and one on the bottom. Each door is equipped with two safety switches to verify if the doors are closed properly or not. These switches are wired as seen in figure 4.5. The switches are connected to the X-ray tube controller, and to a small red LED on the outside of the housing that turns on when all the doors are properly closed. The controller is set up so that the X-ray tube is not able to turn on unless all of the doors are properly closed. If any of the wires or switches are faulty and disconnect, the X-ray tube will also not be able to turn on.

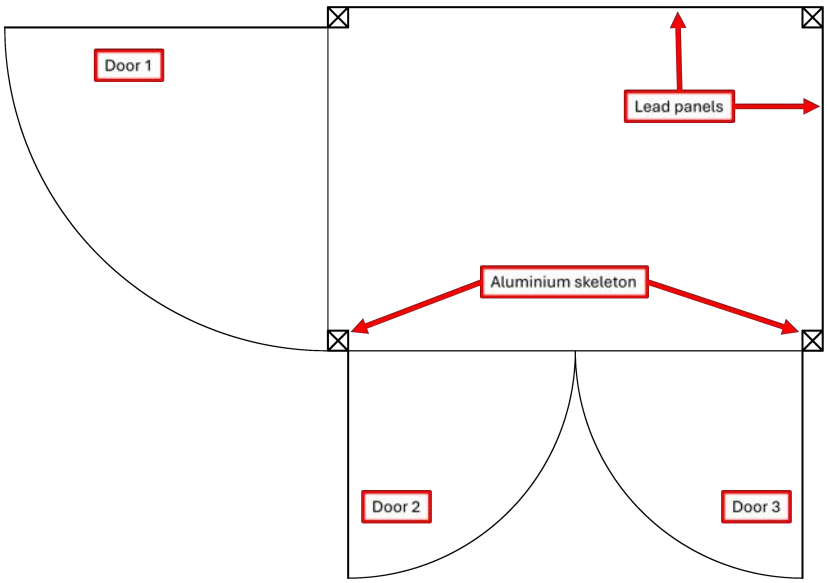

Figure 4.4.: Top view diagram of the BLB Mark I housing.

When the X-ray tube is on, the controller emits a timed beep every few seconds that can be heard from outside the box, to notify the user and bystanders that X-rays are being emitted. Beyond that, a large red safety light is connected to the X-ray tube controller. This light turns on whenever the tube is emitting X-rays. All wiring between the inside and outside of the housing passes through a small channel machined into the top-rear aluminium profile.

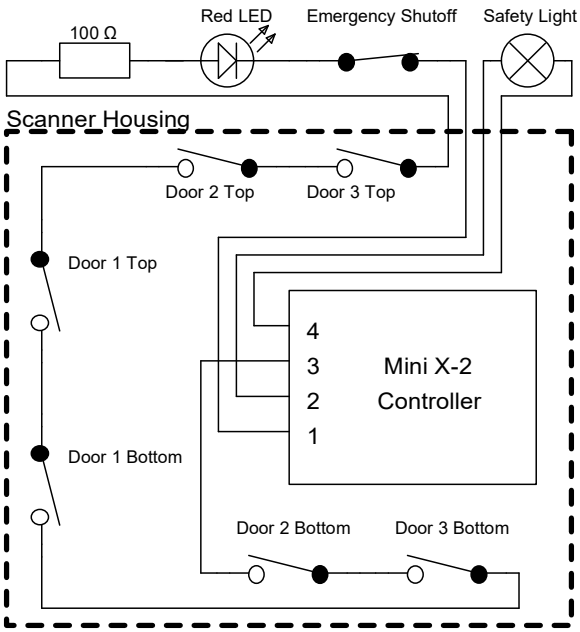

Figure 4.5.: Safety circuit of BLB Mark I housing.

Figure 4.6.: Photo of the BLB Mark I Scanner with the doors closed.

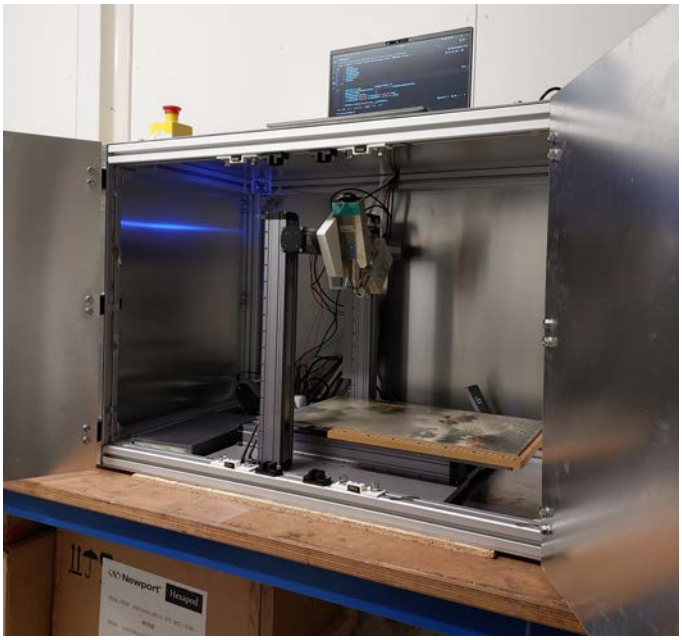

Figure 4.7.: Photo of the BLB Mark I scanner with the doors open.

4.3.3. Performance evaluation

Radiation safety

The device was evaluated by the TU Delft Radiation safety officers. The housing was declared fully safe for use as it provides sufficient shielding of the radiation produced by the X-ray tube. During operation of the X-ray tube, the red warning light turns on, but it is not very bright. This makes it slightly difficult to recognize whether the tube is on when the room is fully lit. The X-ray tube controller emits a beeping noise during operation of the X-ray tube. The combination of these two signals is considered sufficient for the operation of the device by the radiation safety officers.

The emergency stop mechanisms were tested and found to operate properly, shutting down the X-ray tube as soon as any of the doors are opened or the emergency shut off button is pressed.

Scan area size

The scan area size of the device is principally limited by the movement range of the positioning system. However, because of the larger width of the scan head, the limited width of housing is not enough to allow the full range of motion of the scan head, and thus the actual scan range is smaller. For horizontal scanning, this range is 210 mm x 337 mm. For vertical scanning, the range is 249 mm x 337 mm.

BEAM GEOMETRY

The beam characteristics of the X-ray tube were characterized using a sharp razor blade and moving the tube over its edge, for both the X and Y directions. The measurements were done at 7 working distances from the X-ray beam, at approximately 8, 12, 16, 20, 24, 28, 32 mm from the edge of the X-ray tube. The test was repeated at three locations for each working distance, 10 mm from each other. From these measurements, the FWHM was determined and the results are shown in figure 4.8, alongside the respective trend lines. The results present a slightly oblong beam with a divergence of 2.75° in the X direction and 2.79° in the Y direction, with a nominal FWHM at 9 mm (the focal point between the detector and the X-ray tube) of 1.28 mm and 1.36 mm in X and Y, respectively.

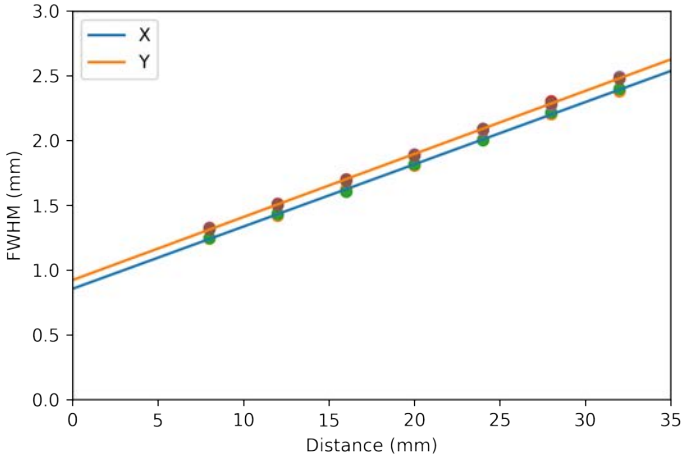

Figure 4.8.: Beam diameter test results, presenting a slightly oblong beam with a divergence of 2.75° in the X direction and 2.79° in the Y direction, with a nominal FWHM at 9 mm of 1.28 mm and 1.36 mm in X and Y, respectively.

DETECTOR TEMPERATURE PERFORMANCE

During operation, the device progressively heats up as scans are conducted. This has an effect on the output signal, primarily through a change of efficiency of the X-ray detector. To evaluate this thermal response, a series of 4 tests were conducted where the scanner is kept static, measuring the same point of a test painting, over a period of 8000 s with dwell time of 0.5 s. During measurement, the X-ray detector does not only provide the X-ray spectra, but also a set of status recordings, which include the detector temperature, board temperature and live time, which can be used to evaluate the state of the detector. Figure 4.9 shows the status values of the tests. The detector and board temperatures increase rapidly during the first 2000 s, after which

the increase slows down significantly. It would be expected for the system to reach a steady state around 265 K detector temperature and 55 °C board temperature, but the test time is not long enough to reach this state. The live time has an inverse relation to the detector temperature, ranging from 420 ms in the initial cool detector state, to 390 ms in the warmer detector state.

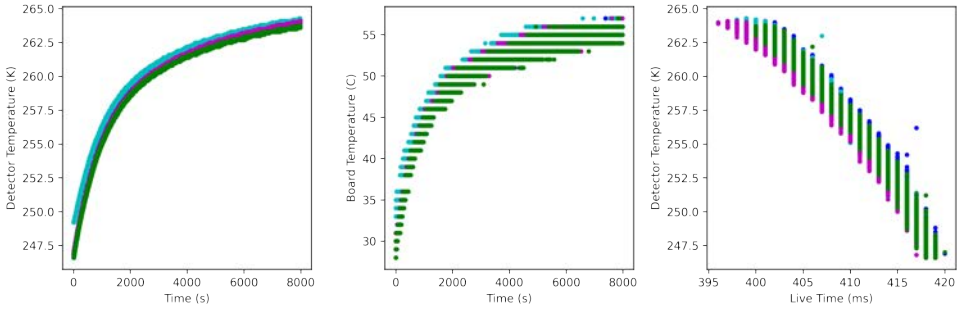

Figure 4.9.: Detector temperature test results showing rapid increases in temperature during the first 2000 s, after which the increase slows down significantly, and an inverse relation of detector temperature to detector live time.

To evaluate how long the detector would take to reach its steady state, a longer 60000 s test was conducted overnight, but with the X-ray tube turned off. The results (figure 4.10) shows the steady state is reached after 20000 s, plateauing at 263 K detector temperature and 55 °C board temperature, with the average live time hovering around 470 ms, which should be understood as the theoretical maximum the detector can achieve under these thermal conditions, as the live time will necessarily go down if the X-ray tube is on.

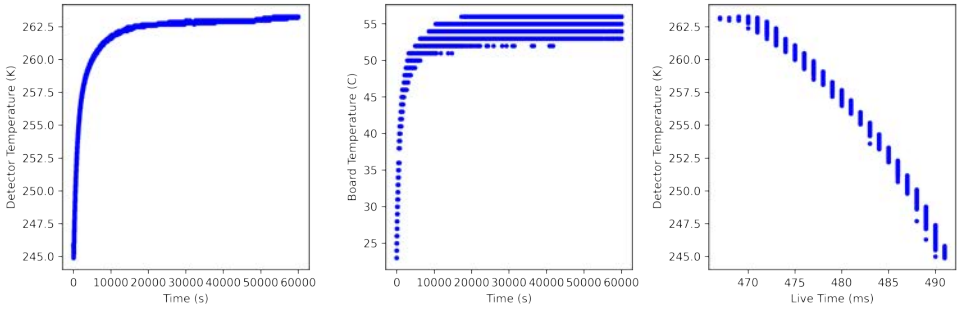

Figure 4.10.: Overnight temperature test results showing temperature plateaus after 20000 s.

The temperature of the detector also affects its energy calibration and resolution. This effect is evaluated using the Pb-Lα emission line (10.55 keV), determining its peak position and width. The results are shown in figure 4.11. The peak position

shifts by around 4 channels, which is equivalent to 0.05 keV. The peak sigma shifts from 6.5 to 7.1 channels, equivalent to a widening of 0.008 keV.

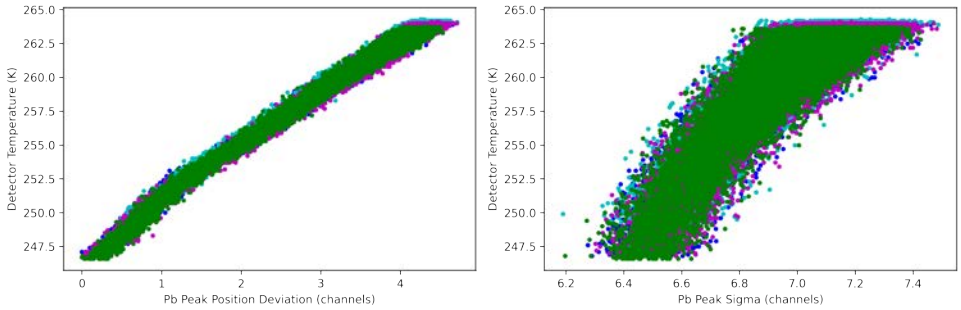

Figure 4.11.: Detector energy calibration and resolution test results show a peak position shift of 4 channels (0.05 keV) and a peak sigma shift of 0.6 channels (0.008 keV).

4.3.4. SHORTCOMINGS

P1. Thermal Issues: During operations, it was found that the temperature inside the safety housing reached up to 35 °C. This is concerning as such temperatures could potentially prove harmful for certain kinds of cultural heritage objects. This increase in temperature is due to the presence of three heat sources within the housing: the power source of the positioning system, the X-ray tube and the X-ray detector. The lack of ventilation between the inside and outside of the housing means that all that heat remains stored within the housing, slowly increasing the internal temperature until plateauing around 38 °C under periods of extended use. This ultimately does not only have a potential effect on the object being studied, but also affects the performance of the device, as documented in section 4.3.3.

P2. Size Issues: Some initial scans highlighted the limitations regarding the size of objects that could be scanned with the device. When operated in horizontal mode, the size of the object to be scanned is limited by the distance between the two vertical motors of the positioning system, which is 340 mm. The other dimensions of the object are limited by the size of the box, to an absolute maximum of 630 mm, but any size beyond 350 mm (the size of the scan bed) require careful positioning. In vertical operation, the size of the object to be scanned is limited by the size of the box, leaving the maximum size at 500 mm x 580 mm, but only a central 249 mm x 337 mm area can be scanned.

P3. Control Issues: The current system has some significant control issues, primarily related to the synchronization of the positioning system and the detectors. Whilst the system has encoders, extracting the readings from these encoders through the existing firmware has proved difficult. The current system has the control computer use the M114 G-code command to retrieve the position information from the scanner. However, this command only retrieves the current target position, not

the actual current position of the system. This means that the timing of the detector must ultimately be done mostly independently from the positioning system. This affects the quality of the results and makes it more susceptible to miscoordination during acquisitions.

P4. Wiring Issues: The wiring channel machined into the aluminium skeleton, whilst being able to handle all the currently needed wires, does not allow for further expansion of the system. The installation of the second XRF detector or any other device would require significant modifications to the housing.

P5. X-ray Tube Control Issues: The X-ray tube is currently controlled separately from the rest of the device, through the Amptek Mini-X2 Controller software. This software is used to turn the tube on and off, as well as controlling the operation parameters, primarily operating voltage and current. This currently means that the X-ray tube can only be turned on and off manually. This is not a major issue but does result in increased energy use and unnecessary radiation of the object.

4.4. BLB Mark II

The design of the BLB Mark II was based on the same design criteria, but now with the added goal of addressing the shortcomings identified in the previous design. The design is not meant to have major conceptual changes but instead be an evolution of the design decisions done previously. As such, the design is documented in the same format as used in section 4.3.

4.4.1. Scanner

As was the case in the previous, the XRF spectrometer design is mostly fixed by C5. Since the design of the scan head was not found to have any significant shortcomings, it was decided to leave that largely unchanged, outside of any required geometrical changes to account for other new components.

However, the positioning system was found to have significant shortcomings, primarily the size issues (P2) and synchronization issues (P3). To address these, a new positioning system was designed. Whilst the use of a commercial 3D printer in the previous design helped reduce the costs significantly, the amount of work necessary to adapt the system to address P3 would have been significant. Instead, it was decided to make use of a set of linear stages that had been made available for the project. These stages were three Thorlabs LTS300C/M 300 mm Linear Translation Stage with Integrated Controller, Stepper Motor[11] (Thorlabs Inc., Newton, NJ, U.S.A.). These three linear stages are combined to form a Cartesian coordinate robot to which the scan head is mounted. In this setup, unlike in the previous design, all movement is done by the scan head, with the object remaining completely static during scanning, which is considered safer for the objects. Whilst this positioning system actually has a slightly smaller nominal work area of 300 mm x 300 mm x 300 mm than the previous design, the fact that the system has only one stage per axis means that the size of the object possible to scan horizontally is no longer limited by the positioning system, which partially addresses P2. However, there is still a limitation on the maximum distance from the edge of the object which can be

scanned, it currently being limited to 300 mm, though this can be partially extended by using a special extension on the scan head.

Regarding the controlling of the system, a system designed by Dr. Matthias Alfeld for a previous Thorlabs scanning system is used.[12] The system was modified to function with the X-ray tube and X-ray detector. This control system is already able to synchronize with the positioning system, addressing P3.

4.4.2. HOUSING

The new housing design is largely based on the previous design. It makes use of the same aluminium profile skeleton covered in aluminium/lead sandwich panelling. The most significant difference is the size. The new housing is 740 mm x 1680 mm x 900 mm, providing a threefold increase in total volume. This, combined with the changes to the positioning system, allows for the scanning of objects of up to 556 mm x 1100 mm in horizontal mode and 1600 mm x 820 mm in vertical mode, which addresses the size issues (P2) of the previous design. This housing, much like the previous one, is bound by the size of the table it sits on. This also turns out to be around the maximum size the author is able to reasonably assemble mostly on their own. [1]

The size increase also forced a change in the design of the doors of the housing. The left side door was removed, and the front doors were changed from two doors to four doors, as a two-door design would require too large doors for safe usage. The four-door design requires the addition of a central pillar on the aluminium skeleton to hold the two centre-most doors. This central pillar is designed to be able to slide side-to-side by only loosening 4 bolts, which allows broader access to the inside of the housing. Due to their size and weight, positioning the new doors is more difficult than in the previous design, and thus a close fit between the doors and the lead panels covering the area where the door hinges connect to the aluminium skeleton is more challenging to achieve, leading to small gaps through which radiation leaks. To address this issue, small, angled lead wedges are positioned on the inside of the door hinges so as to block these gaps. The new layout and features of the housing can be seen in figure 4.12.

The other significant difference is the way the panels are assembled. The new design uses partial overlapping panels on the left, rear and right side of the housing to create gaps that allows the flow of air in and out of the housing and are also used for wiring, as shown in figure 4.13. On each of the relevant sides, two panels, one on the inside and one on the outside of the aluminium skeleton with an overlap of between 70 and 100 mm, provide radiation protection to the users, whilst leaving a 40 mm gap (the width of the aluminium profiles used for the skeleton). In the right and left sides of the housing, eight small 30 mm fans are used to force airflow into and out of the housing, with the air flowing in from the left side and flowing out through the right side. The gap on the rear of the housing is used for all the wiring but also has a large amount of unused space which could be fitted with similar

[1] However, thanks are due to the local Andor representatives who provided some required extra hands when lifting the housing onto its table.

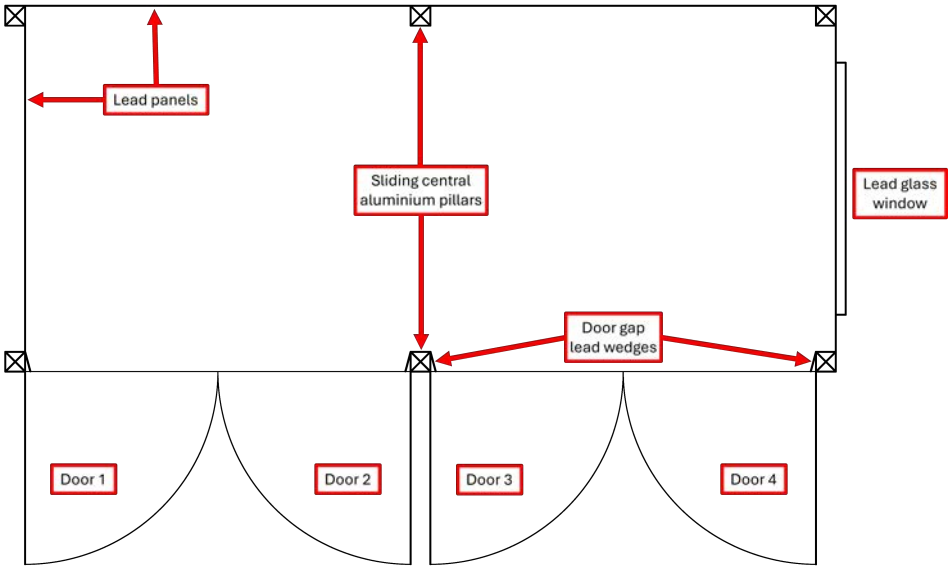

Figure 4.12.: Cross-section top view diagram of the BLB Mark II housing.

small fans if this is found to be necessary. This addresses the thermal (P1) and wiring issues (P4) of the previous design.

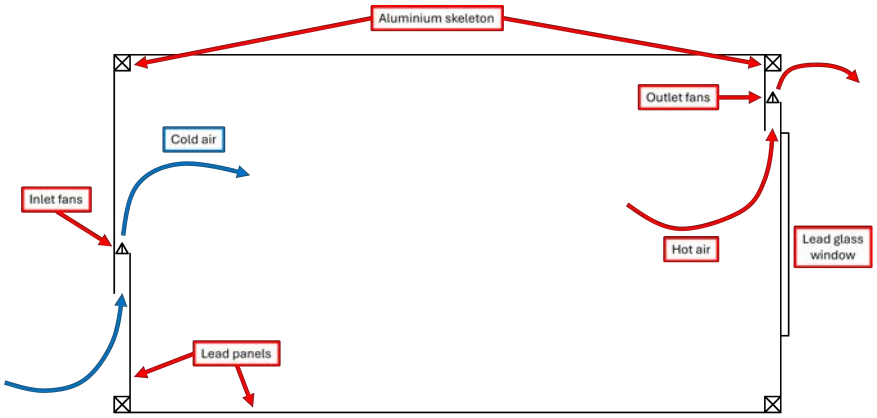

Figure 4.13.: Cross-section side view diagram of the BLB Mark II housing showing the added ventilation gaps.

Whilst not considered a major shortcoming of the previous design, it was inconvenient to have no way of visually checking what was happening within the

housing, and thus a window was added on the right side of the housing. This is a lead glass window salvaged from an old X-ray diffractometer capable of blocking the X-rays emitted by the device during operation. This window is held in place by eight 3D printed parts that are bolted to the right panel.

The safety measures, like the lights and safety switches, remain largely unchanged from the previous design, which simplifies the safety accreditation process, but are updated for the new design. The updated safety circuit is shown in figure 4.14. However, a USB-controlled relay is connected to the safety interlock circuit, which allows the X-ray tube to be turned off through a python command. The command opens the safety interlock circuit which causes the X-ray tube to turn off immediately without having to interface directly with the X-ray tube control software, which addresses the tube control issues (P5).

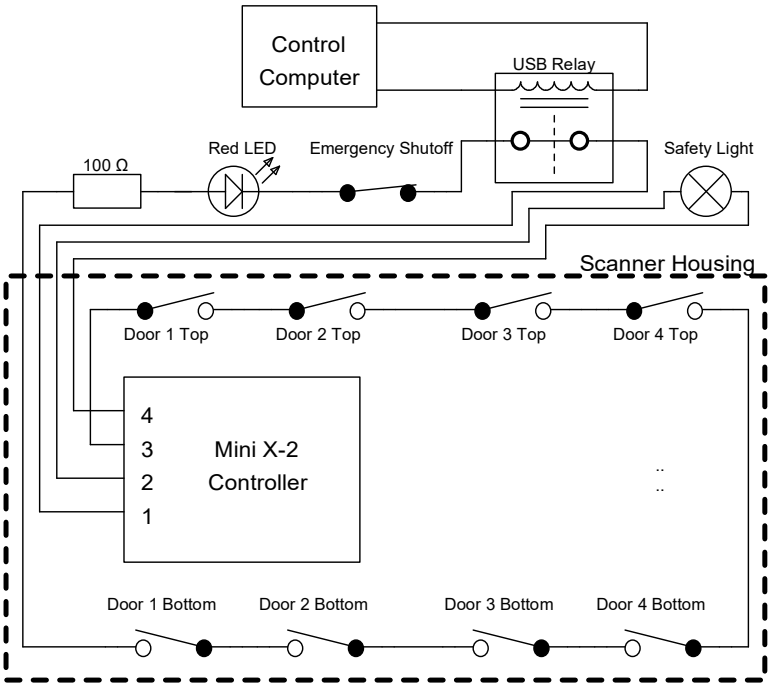

Figure 4.14.: Safety circuit of BLB Mark II housing.

Figure 4.15.: Photo of the BLB Mark II scanner with the doors closed.

BIBLIOGRAPHY

[1] Autoriteit Nucleaire Veiligheid en Stralingsbescherming. *Autoriteit Nucleaire Veiligheid en Stralingsbescherming (ANVS) | Autoriteit NVS*. 2025. URL: https://www.autoriteitnvs.nl/ (visited on 02/23/2025).

[2] AMPTEK Inc. *Mini-X2 X-Ray Tube System for XRF – Amptek – X-Ray Detectors and Electronics*. 2025. URL: https://www.amptek.com/products/mini-x2-x-ray-tube (visited on 02/23/2025).

[3] AMPTEK Inc. *FAST SDD® Ultra High Performance Silicon Drift Detector – Amptek – X-Ray Detectors and Electronics*. 2025. URL: https://www.amptek.com/products/x-ray-detectors/fastsdd-x-ray-detectors-for-xrf-eds/fastsdd-silicon-drift-detector (visited on 02/23/2025).

[4] Snapmaker. *Snapmaker 2.0 | World's Best-selling 3-in-1 3D Printer - Snapmaker*. 2024. URL: https://www.snapmaker.com/en-EU/snapmaker-2.

[5] T. Schoonjans, A. Brunetti, B. Golosio, M. S. del Rio, V. A. Solé, C. Ferrero, and L. Vincze. "The xraylib library for X-ray–matter interactions. Recent developments". In: *Spectrochimica Acta Part B: Atomic Spectroscopy* 66 (11 2011), pp. 776–784. ISSN: 0584-8547. DOI: https://doi.org/10.1016/j.sab.2011.09.011. URL: https://www.sciencedirect.com/science/article/pii/S0584854711001984.

[6] V. A. Solé, E. Papillon, M. Cotte, P. Walter, and J. Susini. "A multiplatform code for the analysis of energy-dispersive X-ray fluorescence spectra". In: *Spectrochimica Acta - Part B Atomic Spectroscopy* 62 (1 2007), pp. 63–68. ISSN: 05848547. DOI: 10.1016/j.sab.2006.12.002.

[7] B. A. Schueler. "Operator shielding: How and why". In: *Techniques in Vascular and Interventional Radiology* 13 (3 Sept. 2010), pp. 167–171. ISSN: 10892516. DOI: 10.1053/j.tvir.2010.03.005.

[8] O. P. Lakhwani, V. Dalal, M. Jindal, and A. Nagala. "Radiation protection and standardization". In: *Journal of Clinical Orthopaedics and Trauma* 10.4 (2019), pp. 738–743. ISSN: 22133445. DOI: 10.1016/j.jcot.2018.08.010. URL: https://doi.org/10.1016/j.jcot.2018.08.010.

[9] NPR 5662:2024. *Directive on radiation protection within the risk inventory and evaluation*. Standard. Stichting Koninklijk Nederlands Normalisatie Instituut, Mar. 2024. URL: https://www.nen.nl/en/npr-5662-2024-nl-315276.

[10] NEN-EN-IEC 61331-1:2014. *Protective devices against diagnostic medical X-radiation - Part 1: Determination of attenuation properties of materials*. Standard. Stichting Koninklijk Nederlands Normalisatie Instituut, Nov. 2014. URL: https://www.nen.nl/en/nen-en-iec-61331-1-2014-en-200717.

[11] Thorlabs Inc. *300 mm Linear Translation Stage with Integrated Controller, Stepper Motor*. 2025. URL: https://www.thorlabs.com/newgrouppage9.cfm?objectgroup_id=7652 (visited on 02/25/2025).

[12] M. Alfeld, S. Pedetti, P. Martinez, and P. Walter. "Joint data treatment for Vis–NIR reflectance imaging spectroscopy and XRF imaging acquired in the Theban Necropolis in Egypt by data fusion and t-SNE". In: *Comptes Rendus Physique* 19 (7 2018), pp. 625–635. ISSN: 16310705. DOI: 10.1016/j.crhy.2018.08.004. URL: https://doi.org/10.1016/j.crhy.2018.08.004.

5

Accelerating MA-XRF Through Advanced Scanning Strategies

MA-XRF is a fairly slow chemical imaging method. Its uniform raster scanning approach is thorough but not optimal. This work explores the use of alternate scanning strategies for optimizing MA-XRF scanning times. Two methods are described, implemented and evaluated, in direct comparison to traditional raster scanning. The first method, FAST, uses machine learning methods to dynamically select pixels for scanning, optimizing to the estimated reduction in distortion between the data and the underlying ground truth. The second approach, the Chopp algorithm, uses a double scan approach, a fast first uniform raster scan to estimate the underlying count rate, which is then used to optimize the scan time of each pixel in a second slower raster scan. The FAST approach outperforms both traditional raster scans and the Chopp algorithm on the considered quality metrics and acquisition time, achieving up to 37% reductions in scanning time compared to traditional raster scans, whilst producing higher quality results.

5.1. INTRODUCTION

MA-XRF has become a prominent method in the analysis of cultural heritage objects[1]. It has been used to cast light on the material history of world famous art pieces like Vermeer's Girl with a Pearl Earring[2] and Da Vinci's Mona Lisa.[3] However, the method suffers from one major practical setback: the long time it takes to do the measurements. While small paintings can realistically be scanned within a day, large paintings can take weeks or even months to fully scan.[4] This has generally limited the use of the method to small or high profile works of art for which such long measurement times are justifiable.

The primary reason for these long scan times is the noise inherent to MA-XRF measurements.[5] This noise leads to a trade-off between acquisition time, spatial quality of the data, and spectral quality of the data. To reduce acquisition time, one can either increase the step size between measurements, which reduces the spatial resolution, or decrease the measurement time per pixel, which reduces the signal-to-noise ratio (SNR) of the resulting spectra.

There has been attempts to improve this trade-off, primarily through the improvement of the hardware of the MA-XRF scanners themselves, such as by increasing the active detection area (i.e. by increasing the number of detectors).[6] This increases the SNR without having to sacrifice the spatial quality or acquisition time. This works well, but is usually prohibitively expensive and is not suitable for users with existing systems.

The main alternative to hardware improvements is to implement advanced signal processing methods which allow producing signals with reasonable SNR from the low acquisition time/low SNR signals. Chopp et al.[5] provided an overview of some image processing-based methods for the acceleration of MA-XRF acquisitions, like denoising,[7, 8] super-resolution,[9] and subsampling methods.[10] These methods are based on exploiting spatial or spectral relations within the data to either improve the quality (spatial or spectral) of a measurement acquired using a standard raster scanning strategy, or to use some sort of a priori information (i.e. an RGB image or a rough fast MA-XRF scan) to define an optimized scanning strategy which reduces acquisition time without sacrificing the quality of the measurement. These two approaches are not exclusive and can be used together, and therefore development of both is useful for accelerating MA-XRF measurements.

Optimizing MA-XRF scanning strategies has been attempted in the past and has shown significant improvements on simulated measurements. However, to the best knowledge of the author, they have never been attempted in practical measurements. Practical implementations of proposed methods present significant challenges, which would affect their efficiency when compared to simulated measurements, as these usually do not account for dynamic aspects (like acceleration and deceleration) of the scan head during measurements.

This paper focuses on the practical implementation and testing of a previously proposed MA-XRF scan optimizer described by Chopp et al.[11] as well as a novel optimization method based on an existing dynamic scanning toolkit, FAST.[12] These methods are compared to the standard raster scanning strategies to evaluate their actual effect on total measurement time, as well as spectral and spatial data quality.

5.2. MA-XRF SCANNING STRATEGIES

First, we mathematically define the MA-XRF measurement process. Let $X \in \mathbb{N}_{H \times W \times C}$ be the ground truth datacube of height H and width W with C spectral channels. X is composed of $n = HW$ individual ground truth XRF spectra $x_i \in \mathbb{N}_C$, here referred to as pixels. The ground truth is here defined as an XRF measurement for which the acquisition time $t_{a,i} \to \infty$. A real MA-XRF measurement will produce a datacube $\tilde{X}$, composed of the individual spectra $\tilde{x}_i$, which when normalized to acquisition time is, hopefully, a good approximation of X. This measurement is conducted by performing a series of individual XRF measurements $\tilde{x}_i$ of acquisition time $0 \leq t_{a,i} \lll \infty$. The total measurement time t_{tot} of a MA-XRF scan can be described as:

$$t_{tot} = \sum_{i}^{n} t_{a,i} + t_{t,i} + t_{c,i} \tag{5.1}$$

with n being the number of individual XRF measurements, $t_{a,i}$ being the active acquisition time (the time during which the system is actively measuring incoming X-rays) for measurement i, $t_{t,i}$ being the travel time between measurement position i and position $i-1$, and $t_{c,i}$ is the calculation time related to measurement i.

Usually, MA-XRF scanners produce their measurements by using a standard raster scanning. In a simplified form, for raster scans $t_{a,i}$ and $t_{t,i}$ can be considered constant for all measurement positions and $t_{c,i} \ll t_{tot}$ and thus can be ignored. Therefore $t_{tot,ras}$ can be considered a linear function of n and the acquisition and travel time per pixel:

$$t_{tot,ras} = (t_a + t_t)n \tag{5.2}$$

However, raster scanning can be conducted in two different ways. "Static" scanning, where the scan head fully stops at every measurement point, conducts the measurement, and then moves to the next measurement point, and "dynamic" (or "on the fly") scanning, where the scan head moves at a constant speed and a timer triggers each measurement based on the speed and pixel size. In dynamic scanning, t_t is theoretically reduced to 0, as there is no down time between measurements, and therefore $t_{tot,ras} = t_a n$. This means dynamic scanning is inherently faster than static scanning, and is therefore the most commonly used method in MA-XRF measurements. However, dynamic scanning introduces some challenges when it comes to the controlling of the device. Accurately triggering the measurements consistently must account for dynamic aspects of the movement of the scan head, as its speed is never perfectly constant, which can lead to hysteresis issues. This is usually accounted for by adding a buffer distance at the beginning and end of each scan line, which falls outside of the measurement area, giving room for the scan head to accelerate and decelerate without affecting the measurement. This adds a certain amount of downtime between measurements, causing t_t to deviate from its theoretical zero value, affecting its efficiency. Usually, this deviation is rather small, often orders of magnitude lower than t_t for static scanning. Thus the objective of this work is to develop a method that minimizes t_{tot}

However, both static and dynamic scanning ultimately have the absolute lower limit of $t_{tot,ras} = t_a n$, and thus the only way to decrease $t_{tot,ras}$ is by decreasing either the number of pixels n, which sacrifices spatial quality, or the acquisition time per pixel t_a, which sacrifices spectral quality. As both spatial and spectral quality are important to MA-XRF scanning, we present two alternative scanning strategies that aim to minimize t_{tot} without sacrificing quality in either domain. The first is FAST, which is based on decreasing the number of pixels measured n through a dynamic sampling process. The second is the Chopp algorithm, which is based on selectively decreasing the acquisition time for each pixel $t_{a,i}$ based on some form of a priori information.

5.2.1. FAST

FAST[12] is a library that combines the deep neural network-based Supervised Learning Approach for Dynamic Sampling (SLADS-Net) algorithm,[13] with a route optimization technique and modular hardware controls. This results in a robust, sample-agnostic tool for dynamic sampling and data reconstruction in scanning imaging methods. SLADS-Net is an implementation of the SLADS framework.[14] This framework is a greedy dynamic sampling approach based on minimizing the distortion between the full dataset $\tilde{X}$ and a reconstructed dataset $\hat{X}_{FA,k}$, which is based on a sub-selection of measured pixels $k < n$. Each pixel in k has a location s and the measured value $\tilde{x}_s$. The measurements are represented as:

$$Y_k = \begin{bmatrix} s_1, \tilde{x}_1 \\ \vdots \\ s_k, \tilde{x}_k \end{bmatrix} \tag{5.3}$$

The problem is then to determine the next pixel location s_{k+1} so that the distortion D between $\tilde{X}$ and $\hat{X}_{FA,k}$ is minimized. The function $D(\tilde{X}, \hat{X}_{FA,k})$ can be any scalar measure of distortion, but for FAST it is described as the L2 norm:

$$D(\tilde{X}, \hat{X}_{FA,k}) = \|\tilde{X} - \hat{X}_{FA,k}\|^2 \tag{5.4}$$

Thus we can define the reduction in distortion (RD) $R_{k,s}$ as:

$$R_{k,s} = D(\tilde{X}, \hat{X}_{FA,k}) - D(\tilde{X}, \hat{X}_{FA,k,s}) \tag{5.5}$$

where $\hat{X}_{FA,k,s}$ is the new reconstructed dataset which includes the new measurement at s. This leaves the goal of SLADS as:

$$s_{k+1} = \arg\max_s R_{k,s} \tag{5.6}$$

Since $\tilde{x}_s$ is unknown during scans, the RD value cannot be known, and thus an expected reduction in distortion (ERD) $\bar{R}_{k,s}$ must be calculated. This is done using a function g so that:

$$\bar{R}_{k,s} = \mathbb{E}[R_{k,s}|Y_k] = g(Y_k) \tag{5.7}$$

In the original SLADS framework, g is a non-linear regression function determined through supervised learning with existing measurement data. Because function g is trained on existing measurement data, the accuracy of the resulting ERD values depends on the similarity between the training data and the current sample, and the use of SLADS with dissimilar images can result in a worse performance than random sampling.[13] To improve upon this, SLADS-Net uses a DNN to calculate the ERD, which provides higher accuracy when trained with dissimilar images. Because of the nature of MA-XRF data in cultural heritage science, where every dataset is quite distinct, this accuracy when measuring dissimilar samples is very important. FAST uses a SLADS-Net trained on the standard cameraman image, which results in generalizable dynamic sampling across different imaging modalities.

Although traditional SLADS selects the next pixel measurement based on a full calculation of the ERD, whether or not this results in reduced measurement times depends on the relation between the measurement time of a single pixel $t_i = t_{a,i} + t_{t,i}$, the measurement time of a group of pixels t_{batch} and the calculation time of the ERD values $t_{c,i}$. In the original description of SLADS, Godaliyadda et al.[14] propose a group-wise SLADS for measurements in which measuring a batch of pixels B in a single burst is faster than measuring all the pixels individually, which is the case in methods where $t_t \gtrsim t_a$, as is the case in MA-XRF. In group-wise SLADS, the ERD values are calculated and the next measurement pixel is selected. However, instead of performing the measurement, the value of the pixel in $\hat{X}_{FA,k}$ is taken as a pseudo-measurement, and a new set of pseudo-ERD values are calculated, which are then used to select the next measurement pixel. The process is repeated until a b number of pixels are selected for measurement, all of which are then measured in one burst. FAST implements group-wise SLADS and uses a route optimization technique based on Google's OR-Tools,[15] which reduces the travel time $t_{t,B}$ between the pixels in group B, and thus the measurement time $t_{batch,B}$, compared to measuring them based on traditional SLADS.

However, all the discussed implementations of SLADS are exclusively used for monospectral imaging datasets. Zhang et al.[16] proposed a modified version of their SLADS-Net for use with energy-dispersive spectroscopy, in which the measured spectra are converted to a scalar value using a classifier. The resulting class values are then used as the monospectral image to which SLADS-Net is applied. This is not suitable for MA-XRF data of cultural heritage objects, as the classification of such spectra is a complex subject and highly sample dependent.[17–20] We propose an alternate approach in which the measured XRF spectra are used to calculate region of interest (ROI) values for a set of pre-selected elemental fluorescence lines. ERD values are then calculated for each of these ROI images and summed together. The pixels with the highest summed ERD values are then selected for measurement. This requires a certain amount of a priori knowledge of the sample and would not be suitable for completely unknown samples. However, in the analysis of paintings, there are certain elements that are more or less relevant depending on the historical background of the painting, and thus it is not considered unreasonable to provide a selection of relevant target elements. Beyond that, even if a specific element is not present in the initial selection, it is likely to have some level of spatial correlation

to a selected element, either through XRF matrix effects or artistic practices, though this is definitely not guaranteed.

In this paper, we have modified FAST to function with our proposed approach to hyperspectral MA-XRF data, as well as to interface with our self-built MA-XRF scanner. Ultimately, with regards to equation 5.1, this method seeks to minimize n, $t_{t,i}$ and $t_{c,i}$, whilst keeping $t_{a,i}$ constant.

5.2.2. CHOPP ALGORITHM

The Chopp algorithm is an algorithm developed specifically for the optimization of MA-XRF measurements.[11] In their formulation, the arrival of a photon to the detector is described with a Poisson process, such that:

$$\tilde{X}_{h,w,c} \sim Poiss(T_{a,h,w} \cdot \Psi_{h,w,c}) \tag{5.8}$$

Where $T_a \in \mathbb{R}^+_{H\times W}$ is an array of the individual acquisition times per pixel $t_{a,h,w}$, and $\Psi \in \mathbb{R}^+_{H\times W\times C}$ is the underlying count rate which linearly relates the unknown Poisson distribution to the sampling time. As Ψ cannot be known there must be a count rate estimation $\Lambda \in \mathbb{R}^+_{H\times W\times C}$ defined as:

$$\Lambda_{h,w,c} = \frac{\tilde{X}_{h,w,c}}{T_{a,h,w}} \tag{5.9}$$

It is desired to minimize the error between Ψ and Λ. This algorithm defines the error as the mean squared error (MSE):

$$\varepsilon_{MSE} = \frac{1}{N}\sum_{h,w,c}(\Psi_{h,w,c} - \Lambda_{h,w,c})^2 \tag{5.10}$$

where $N = HWC = nC$. As Λ is a random variable, then ε_{MSE} is too. Thus the expected error can be shown to be:

$$\mathbb{E}[\varepsilon_{MSE}] = \frac{1}{N}\sum_{h,w,c}\frac{\Psi_{h,w,c}}{T_{a,h,w}} \tag{5.11}$$

The aim is to select T_a as to minimize the expected error, whilst not exceeding a set total acquisition time τ. But since Ψ remains unknown, this approach proposes breaking down the measurement into two scans, a first fast traditional raster scan with dwell time T_{a0} in order to approximate $\Lambda \approx \Psi$, which can then be used to optimize a second scan with a new total acquisition time $\tau^* = \tau - \sum_{h,w} T_{a0,h,w}$. As fast MA-XRF scans can be quite noisy, a fast denoising algorithm is used to provide an improved estimation of Λ, denoted as Λ^*, to better estimate Ψ. The problem can thus be formulated as:

$$T_a^* \approx \underset{\sum_{h,w} T_{h,w}\leq\tau^*}{\operatorname{argmin}} \frac{1}{N}\sum_{h,w,c}\frac{\Lambda^*_{h,w,c}}{T_{a0,h,w} + T_{a,h,w}} = \underset{\sum_{h,w} T_{h,w}\leq\tau^*}{\operatorname{argmin}} \frac{1}{N}\sum_{h,w}\frac{\sum_c \Lambda^*_{h,w,c}}{T_{a0,h,w} + T_{a,h,w}} \tag{5.12}$$

It is also possible to set further constraints on the allowed T_a^*, like a minimum and maximum acquisition time per pixel, $0 \leq T_{a,min} < T_{a,max}$. The way in which the Chopp algorithms approaches this optimization is that of incremental allocation: time is allocated to the pixels in which the error will be reduced the most until $\sum T_a^* = \tau^*$. The greatest reduction in the expected error occurs where the derivative of $\mathbb{E}[\varepsilon_{MSE}]$ with respect to T_a^*:

$$\frac{\partial}{\partial T_{a,h,w}} \mathbb{E}[\varepsilon_{MSE}(T_a)] = \frac{\sum_c \Lambda^*_{h,w,c}}{N(T_{a0,h,w} + T_{a,h,w})^2} \tag{5.13}$$

is the most negative. Since the derivative value of each pixel is independent from all the other pixels, then if $T_{a,h,w}$ is set to 0, the result is functionally a map of which pixels should be prioritized during the optimization. If the pixels are then sorted in a ascending order, we can define p which is the index that corresponds to the p^{th} most negative derivative at the location (h_p, w_p). Then the algorithm allocates time to pixel p until:

$$\frac{\partial}{\partial T_{a,p}} \mathbb{E}[\varepsilon_{MSE}(T_{a,p})] = \frac{\partial}{\partial T_{a,q}} \mathbb{E}[\varepsilon_{MSE}(0)] \tag{5.14}$$

where q is another pixel such that $p < q$. This can be solved for $T_{a,p}$:

$$T_{a,p} = \sqrt{\frac{\sum_c \Lambda^*_{p,c}}{\sum_c \Lambda^*_{q,c}}}\, T_{a0,q} - T_{a0,p} \tag{5.15}$$

This can be extended such that, for any pixel r, the amount of time τ_r that should be allocated to pixels 1,...,$r-1$ becomes:

$$\tau_r = \sum_{p=1}^{r} \left(\sqrt{\frac{\sum_c \Lambda^*_{p,c}}{\sum_c \Lambda^*_{r,c}}}\, T_{a0,r} - T_{a0,p} \right) \tag{5.16}$$

This can be used to find the maximum value of r for which $\tau_r \leq \tau^*$, denoted as r^*. Any pixel $p \leq r^*$ is considered for time allocation. The time can then be allocated by setting 5.16 as an equality with τ^* and solving for $\sum_c \Lambda^*_{r,c}$ and then replacing that value back into equation 5.16, which results in:

$$\tau^* = \sum_{p=1}^{r^*} \left[\frac{\sqrt{\sum_c \Lambda^*_{p,c}}}{\sum_{q=1}^{r^*} \sqrt{\sum_c \Lambda^*_{q,c}}} \left(\tau^* + \sum_{q=1}^{r^*} T_{a0,q} \right) - T_{a0,p} \right] \tag{5.17}$$

This results in the general minimization solution:

$$T^*_{a,p} = \begin{cases} \dfrac{\sqrt{\sum_c \Lambda^*_{p,c}}}{\sum_{q=1}^{r^*} \sqrt{\sum_c \Lambda^*_{q,c}}} \left(\tau^* + \sum_{q=1}^{r^*} T_{a0,q} \right) - T_{a0,p}, & p \leq r^* \\ 0, & p > r^* \end{cases} \tag{5.18}$$

which describes the time allocated to each pixel. If a minimum dwell time per pixel $T_{a,min}$ is set, then the optimization problem changes slightly so that

$$T_{a0} \leftarrow T_{a0} + T_{a,min} \tag{5.19}$$

and

$$\tau^* \leftarrow \tau^* - \sum_{h,w} T_{a,min,h,w} \tag{5.20}$$

After the optimization is conducted, then the optimized acquisition times must be added to the minimum acquisition time:

$$T_a^* \leftarrow T_a^* + T_{a,min} \tag{5.21}$$

If a maximum dwell time per pixel $T_{a,max}$ is set, then the solution requires iterative application of the optimization. The first optimization is the same as if $T_{a,max} = \infty$. Then the next optimization is conducted but with

$$T_{a,min} \leftarrow \min\left(T^*_{a,h,w} + T_{a,min,h,w},\ T_{a,max,h,w}\right) \tag{5.22}$$

If there is no clipping by the maximum dwell time, then the optimization can end. Otherwise, there is time left for allocation and thus a new optimization must take place with

$$\tau^* \leftarrow \tau^* - \sum_{h,w} T_{a,min,h,w} \tag{5.23}$$

Pixels where $T_{a,min,h,w} = T_{a,max,h,w}$ are excluded, since they have already been assigned the maximum acquisition time. this process is repeated until all time has been allocated.

5.3. METHODOLOGY

The two methods, FAST and Chopp, will be evaluated against a traditional static raster scan. To do so, two error metrics will be used: root mean square error (RMSE) (the lower the better) and structural similarity index measure (SSIM) (the higher the better, to a maximum of 1). RMSE provides a decent evaluation of the spectral quality of the resulting data, but does not provide insight into the spatial quality of the data. SSIM provides insight into the spatial quality of the data. These errors are calculated with regards to a dataset acquired as a static raster scan with a dwell time per pixel of 1 s, which is treated as the ground truth X.

Both FAST and Chopp have a variety of hyperparameters which affect how the algorithms perform. To optimize these hyperparameters, simulated measurements are used. Hyperparameters are then corroborated using real measurements on the BLB Mark I MA-XRF scanner, described in chapter 4.3. For FAST, the hyperparameters that will be tested are: sample batch size b (the number of pixels measured per burst), initial sample batch size b_0(the number of pixels measured in the initial random burst), the measurement time per pixel $t_{a,FAST}$, and the element fluorescence lines used for the selection. For Chopp, the hyperparameters that will be tested are: initial scan time T_{a0} (measurement time per pixel in the rough initial

scan), total scan time τ (total acquisition time allocated for the measurement, which does not consider travel time), and the element fluorescence lines used for the selection. From the tested hyperparameters, the top performers are selected and compared to each other and equivalent static raster scans.

The simulated measurements are done using the Poisson function of the PyTorch library[21], treating the 1 s measurement as the underlying count rate $\Psi_{h,w,c}$ as described in equation 5.8. The accuracy of these simulations is evaluated by comparing them to actual measurements. Figure C.6 shows the Zn-K maps for the real measurements and the simulated measurements, as well as their RMSE and SSIM values. The other elemental maps considered are available in appendix C.1. The real 0.1 s measurement has RMSE between 0.15 and 0.16, and SSIM between 0.97 and 0.98. The simulated 0.1 s measurement has RMSE between 0.14 and 0.15 and SSIM of 0.98. The real 0.01 s measurement has RMSE between 0.35 and 0.37, and SSIM values between of 0.84 and 0.85. The simulated 0.01 s measurement has RMSE between 0.34 and 0.38, and SSIM values between of 0.83 and 0.86. All of the RMSE and SSIM values for the simulations fall within a ± 0.02 range of the values of the real measurements and thus it is concluded that the simulations match real measurements in both spatial and spectral quality well enough for the purpose of this research.

5.4. RESULTS

5.4.1. FAST HYPERPARAMETERS

The hyperparameters that are tested are detailed in appendix C.2 As FAST uses the same dwell time for all measured pixels, the acquisition time is a linear function of the amount of pixels measured, and thus will not change between the different simulations. The main aspects affecting the total measurement time are the travel time and the calculation time of the FAST algorithm. The factors which are used to evaluate the efficiency of each set of hyperparameters are the total measurement time, the SSIM and the RMSE.

It can be seen in the results of these simulations (figure 5.2) that the dwell time per pixel t_{a0} is the most significant factor for the total measurement time t_{tot} and the spatial and spectral quality. However, for values above 0.1 s, the minor increase in quality is outweighed by a significant increase in t_{tot}. For $300 \leq b \leq 500$, t_{tot} does not change significantly as the time saved by optimizing the distance travelled, and thus the travel time t_t, during the measurement through the use of larger sample batches is undone by the increase in calculation time t_c required to optimize a path through an increasingly large batch of points. For $b < 300$, t_c is low but t_t is larger, as the total distance covered during the measurement is not well optimized. For $b > 500$, the increased t_c begins to outweigh the reduction in t_t, to the point where planned simulations using larger values for b were ultimately scrapped as t_c were found to be unreasonably long. Ultimately, $b = 400$ was chosen. b_0 was found to play only a very small role in t_{tot} and the quality of the resulting dataset, with larger values slightly increasing the quality at only a very small increase in t_{tot}, so the higher value of $b_0 = 400$ is chosen. The element selection does not play a

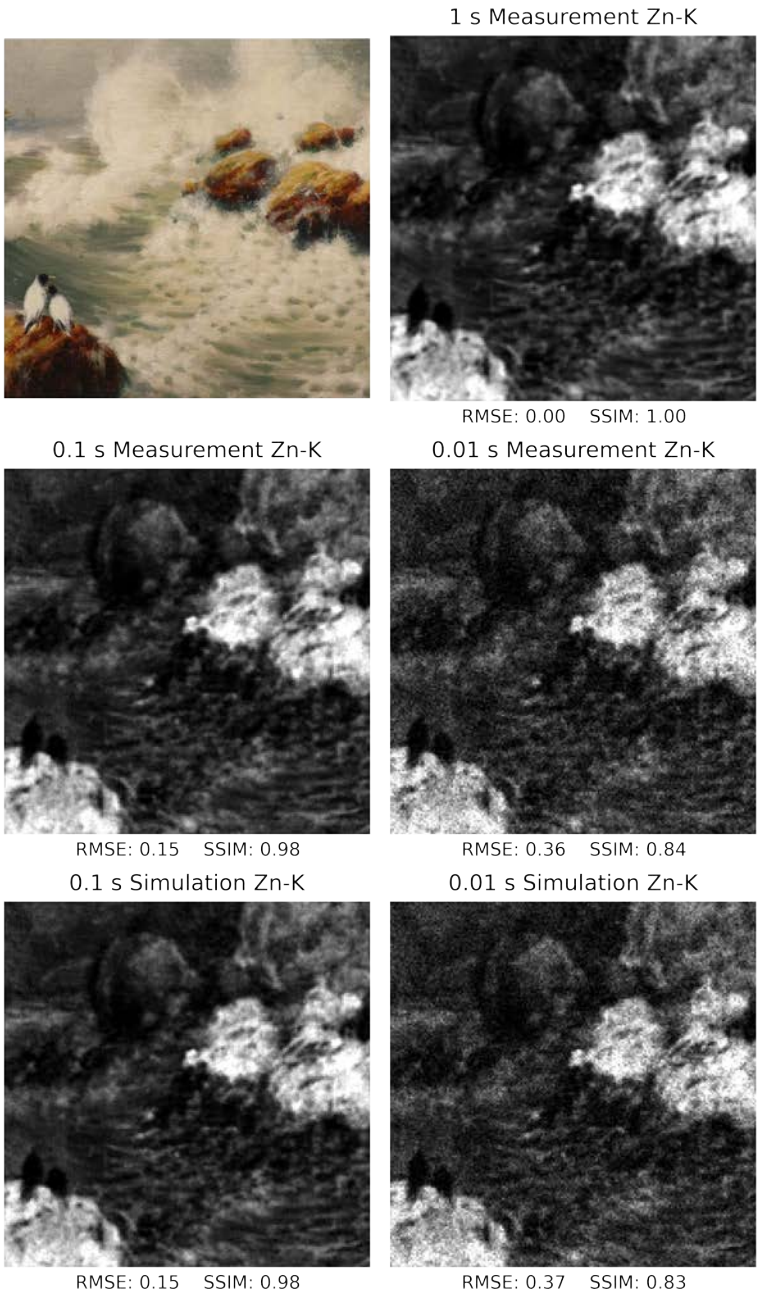

Figure 5.1.: Comparison of Zn-K maps from real MA-XRF scans and simulated MA-XRF scans and the calculated RMSE and SSIM values.

significant role in quality or measurement time. This is likely due to the high level of correlation between the different elements in the tested painting. It was ultimately chosen to use selection 1, considering all of the elements initially selected.

5.4.2. CHOPP HYPERPARAMETERS

The hyperparameters that are tested are detailed in appendix C.3. Unlike FAST, Chopp has a target total measurement time τ for which it optimizes, so the resulting measurement quality is the real measure of the hyperparameters. As can be seen in figure 5.3, initial scan time T_{a0} only plays a minor role in the resulting quality, but is slightly more prominent in lower total scan times τ. For very low values of τ (like 100 s), an increased T_{a0} can have a significant effect. Because of this, T_{a0}=3 ms was chosen, as it also shows a slightly decreased calculation time $t_{c,tot}$. The element selection, much like in FAST, does not play a major role in quality or calculation time, and thus selection 1 is chosen to match the FAST hyperparameters. As τ is the deciding factor in resulting quality, two values of τ are chosen for real tests, 500 s and 1640 s, to verify the results of the simulations and cover both low and high values of τ.

5.4.3. REAL MEASUREMENTS

Based on the selected hyperparameters, 3 real tests were conducted:

- Chopp algorithm using T_{a0} =3 ms, τ =500 s and all considered elements.
- Chopp algorithm using T_{a0} =3 ms, τ =1640 s and all considered elements.
- FAST using $b = 400$, $b_0 = 400$, t_{a0} =0.1 s, all considered elements and a 40% measure ratio.

The error metrics are derived from comparison to the same 1 s raster scan used as a ground truth during the simulations. These results are compared to a t_a =50 ms raster scan, as this uses a comparable acquisition time to the conducted tests. The resulting Zn-K maps can be seen in figure C.12, alongside their error and time metrics. The results for other elemental maps can be seen in appendix C.4. For most of the elemental maps, FAST outperforms both static raster scans and the Chopp algorithm. This is likely due to the reconstruction procedure counteracting some of the inherent Poisson noise that would be present in the unmeasured pixels. The Zn-K maps are a good example of how FAST provides a fairly good approximation of the overall spatial structure of the data, but struggles with small details, like the ripples of the waves in the water.

The Chopp algorithm manages to capture the small details that FAST does not capture, but the error metrics show a greater overall deviation from the ground truth. It also performs very poorly in terms of t_{tot} in comparison to both the static raster scan and FAST. This poor performance is due to the fact that it requires two full raster scans, which means twice the travel time t_t than an equivalent raster scan, and travel time is the most prominent part of t_{tot} in the scanner used. Other tests

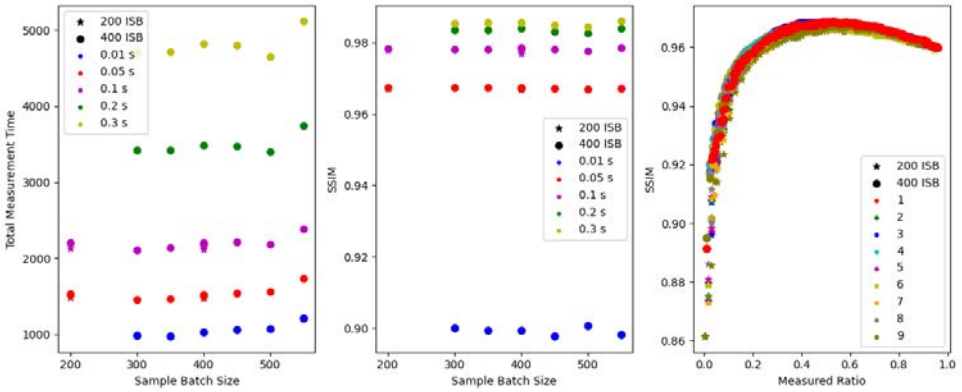

Figure 5.2.: Results of the FAST simulations comparing the SSIM values for the different sets of hyperparameters.

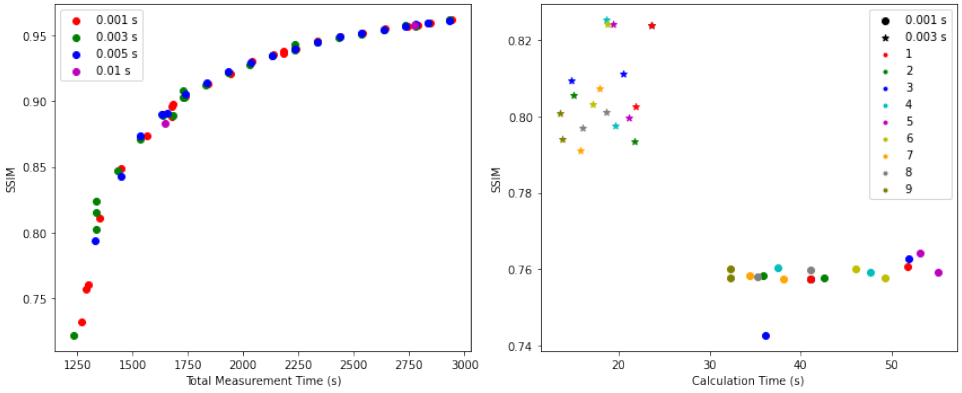

Figure 5.3.: Results of the Chopp simulations comparing the SSIM values for the different sets of hyperparameters.

have found that the minimum value achievable of t_t for a static raster measurement of the test area with this MA-XRF scanner is around 13000 s, meaning that the minimum value of t_{tot} that the Chopp algorithm could achieve in this MA-XRF scanner is around 26000 s, which roughly matches the total measurement time of the 500 s Chopp scan. In these conditions, the Chopp algorithm cannot be fairly compared to the other approaches using t_{tot}. If compared using acquisition time t_a instead, the Chopp algorithm performs more closely to the other scanning strategies, but still does not perform as well as a standard raster scan or a FAST scan. The 500 s Chopp scan shows the potential of the method for optimizing scans in cases where low t_a is preferred.

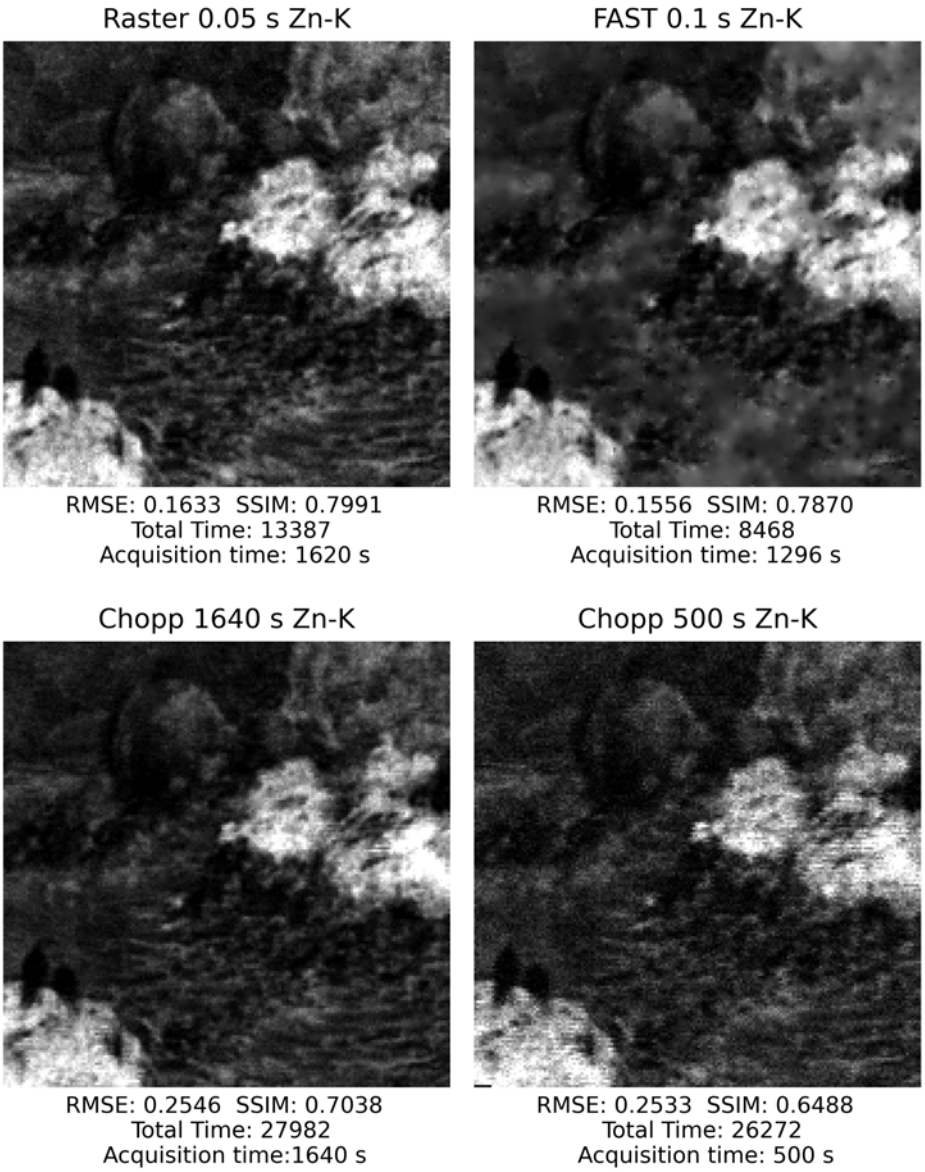

Figure 5.4.: Resulting Zn-K maps of a t_a =50 ms uniform raster scan, a τ =1640 s Chopp scan, a τ =500 s Chopp scan and a FAST scan, and the achieved RMSE and SSIM values for each.

5.5. CONCLUSION

The results show the promise of alternative scanning strategies for accelerating MA-XRF scans. The modified hyperspectral FAST algorithm shows particular promise thanks to its dynamic nature, outperforming comparable static raster scans for both spatial and spectral quality, as well as acquisition and total measurement time. The Chopp algorithm shows promise for optimizing measurements with regards to acquisition time when targeting low acquisition times. However, limitations of the MA-XRF scanner used for the tests and the resulting long travel times for such raster measurements significantly hamper the performance of the algorithm with regards to total measurement time.

The practical implementations of the tested algorithms could be significantly improved through further modifications. Based on the concepts used for dynamic raster scans, it should be possible to optimize FAST to acquire data even during travel time, which would significantly improve the spectral quality of the resulting data. However, this would require significant changes to both the reconstruction procedure currently used by FAST and the way pathing works, as the MA-XRF scanner used would only allow such traveling acquisitions in movements where the timing is consistent (vertical, horizontal and 45° diagonals).

Dynamic raster scans could also be used to improve upon the Chopp algorithm, but would present significant practical challenges, as coordinating between the changing speed of the scan head and the actual acquisition of the detector is not a trivial issue. This could be handled by clustering pixels into bins of acquisition times and then breaking down each raster line into a set of shorter lines acquired using the dynamic method. This would lead to a slight less optimized acquisition time distribution but would provide significant improvements in total times. However, it is clear from the results of the tests that the main limitation of the Chopp algorithm is its requirement of two raster scans. If the first scan that is used to estimate the underlying count rate could be replaced by the use of some other form of a priori information, that would cut the achieved total measurement times in half. Dai et al.[10] showed the promise of using a simple RGB image as an a priori estimator for MA-XRF optimization measurement. Such a system, or one based on other types of imaging data, could provide an initial estimation of the spatial relations that the Chopp algorithm seeks to exploit and could replace the first scan entirely.

BIBLIOGRAPHY

[1] M. Alfeld. "MA-XRF for Historical Paintings: State of the Art and Perspective". In: *Microscopy and Microanalysis* 26.Suppl 2 (2020), pp. 72–75. ISSN: 14358115. DOI: 10.1017/S1431927620013288.

[2] J. K. Delaney, K. A. Dooley, A. van Loon, and A. Vandivere. "Mapping the pigment distribution of Vermeer's Girl with a Pearl Earring". In: *Heritage Science* 8.1 (2020), pp. 1–16. ISSN: 20507445. DOI: 10.1186/s40494-019-0348-9. URL: https://doi.org/10.1186/s40494-019-0348-9.

[3] V. Gonzalez, G. Wallez, E. Ravaud, M. Eveno, I. Fazlic, T. Fabris, A. Nevin, T. Calligaro, M. Menu, V. Delieuvin, and M. Cotte. "X-ray and Infrared Microanalyses of Mona Lisa's Ground Layer and Significance Regarding Leonardo da Vinci's Palette". In: *Journal of the American Chemical Society* 145.42 (2023), pp. 23205–23213. ISSN: 15205126. DOI: 10.1021/jacs.3c07000.

[4] N. De Keyser, F. T. Broers, F. Vanmeert, A. van Loon, F. Gabrieli, S. De Meyer, A. Gestels, V. Gonzalez, E. Hermens, P. Noble, F. Meirer, K. Janssens, and K. Keune. "Discovery of pararealgar and semi-amorphous pararealgar in Rembrandt's The Night Watch: analytical study and historical contextualization". In: *Heritage Science* 12.1 (2024), pp. 1–20. ISSN: 20507445. DOI: 10.1186/s40494-024-01350-x. URL: https://doi.org/10.1186/s40494-024-01350-x.

[5] H. Chopp, A. McGeachy, M. Alfeld, O. Cossairt, M. Walton, and A. Katsaggelos. "Image Processing Perspectives of X-Ray Fluorescence Data in Cultural Heritage Sciences". In: *IEEE BITS the Information Theory Magazine* (2022), pp. 1–12. ISSN: 2692-4080. DOI: 10.1109/mbits.2022.3197100.

[6] F. P. Romano, E. Puglia, C. Caliri, D. P. Pavone, M. Alessandrelli, A. Busacca, C. G. Fatuzzo, K. J. Fleischer, C. Pernigotti, Z. Preisler, C. Vassallo, G. Verhasselt, C. Miliani, and G. Ranocchia. "Layout of ancient Greek papyri through lead-drawn ruling lines revealed by Macro X-Ray Fluorescence Imaging". In: *Scientific Reports* 13.1 (2023), pp. 1–11. ISSN: 20452322. DOI: 10.1038/s41598-023-33242-8. URL: https://doi.org/10.1038/s41598-023-33242-8.

[7] H. Chopp, A. McGeachy, M. Alfeld, O. Cossairt, M. Walton, and A. Katsaggelos. "Denoising Fast X-Ray Fluorescence Raster Scans of Paintings". In: 1 (2022). arXiv: 2206.01740. URL: http://arxiv.org/abs/2206.01740.

[8] B. Vekemans, K. Janssens, L. Vincze, A. Aerts, F. Adams, and J. Hertogen. "Automated Segmentation of μ-XRF Image Sets". In: *X-Ray Spectrometry* 26.6 (1997), pp. 333–346. ISSN: 00498246. DOI: 10.1002/(SICI)1097-4539(199711/12)26:6<333::AID-XRS231>3.0.CO;2-D.

[9] Q. Dai, E. Pouyet, O. Cossairt, M. Walton, and A. K. Katsaggelos. "Spatial-Spectral Representation for X-Ray Fluorescence Image Super-Resolution". In: *IEEE Transactions on Computational Imaging* 3.3 (2017), pp. 432–444. ISSN: 2333-9403. DOI: 10.1109/tci.2017.2703987.

[10] Q. Dai, H. Chopp, E. Pouyet, O. Cossairt, M. Walton, and A. K. Katsaggelos. "Adaptive Image Sampling Using Deep Learning and Its Application on X-Ray Fluorescence Image Reconstruction". In: *IEEE Transactions on Multimedia* (2020). ISSN: 19410077. DOI: 10.1109/TMM.2019.2958760. arXiv: 1812.10836.

[11] H. Chopp, M. Alfeld, O. Cossairt, M. Walton, and A. Katsaggelos. "Optimal scans for X-ray fluorescence imaging of paintings". In preparation.

[12] S. Kandel, T. Zhou, A. V. Babu, Z. Di, X. Li, X. Ma, M. Holt, A. Miceli, C. Phatak, and M. J. Cherukara. "Demonstration of an AI-driven workflow for autonomous high-resolution scanning microscopy". In: *Nature Communications* 14.1 (2023), pp. 1–9. ISSN: 20411723. DOI: 10.1038/s41467-023-40339-1. arXiv: 2301.05286.

[13] Y. Zhang, G. M. Godaliyadda, N. Ferrier, E. B. Gulsoy, C. A. Bouman, and C. Phatak. "SLADS-Net: Supervised learning approach for dynamic sampling using deep neural networks". In: *IS and T International Symposium on Electronic Imaging Science and Technology* (2018). ISSN: 24701173. DOI: 10.2352/ISSN.2470-1173.2018.15.COIMG-131. arXiv: 1803.02972.

[14] G. M. D. P. Godaliyadda, D. H. Ye, M. D. Uchic, M. A. Groeber, G. T. Buzzard, and C. A. Bouman. "A Framework for Dynamic Image Sampling Based on Supervised Learning". In: *IEEE Transactions on Computational Imaging* 4.1 (2017), pp. 1–16. ISSN: 2573-0436. DOI: 10.1109/tci.2017.2777482. arXiv: 1703.04653.

[15] V. Furnon and L. Perron. *OR-Tools Routing Library*. Version v9.11. Google, May 7, 2024. URL: https://developers.google.com/optimization/routing/.

[16] Y. Zhang, G. M. Godaliyadda, N. Ferrier, E. B. Gulsoy, C. A. Bouman, and C. Phatak. "Reduced electron exposure for energy-dispersive spectroscopy using dynamic sampling". In: *Ultramicroscopy* 184 (2018), pp. 90–97. ISSN: 18792723. DOI: 10.1016/j.ultramic.2017.10.015. arXiv: 1707.03848.

[17] C. Jones, N. S. Daly, C. Higgitt, and M. R. Rodrigues. "Neural network-based classification of X-ray fluorescence spectra of artists' pigments: an approach leveraging a synthetic dataset created using the fundamental parameters method". In: *Heritage Science* 10.1 (2022), pp. 1–14. ISSN: 20507445. DOI: 10.1186/s40494-022-00716-3. URL: https://doi.org/10.1186/s40494-022-00716-3.

[18] L. Liu, T. Miteva, G. Delnevo, S. Mirri, P. Walter, L. de Viguerie, and E. Pouyet. "Neural Networks for Hyperspectral Imaging of Historical Paintings: A Practical Review". In: *Sensors* 23.5 (2023). ISSN: 14248220. DOI: 10.3390/s23052419.

[19] B. J. Xu, Y. Wu, P. Hao, M. Vermeulen, A. McGeachy, K. Smith, K. Eremin, G. Rayner, G. Verri, F. Willomitzer, M. Alfeld, J. Tumblin, A. Katsaggelos, and M. Walton. "Can deep learning assist automatic identification of layered pigments from XRF data?" In: *Journal of Analytical Atomic Spectrometry* 37.12 (2022), pp. 2672–2682. ISSN: 13645544. DOI: 10.1039/d2ja00246a. arXiv: 2207.12651.

[20] S. Kogou, L. Lee, G. Shahtahmassebi, and H. Liang. "A new approach to the interpretation of XRF spectral imaging data using neural networks". In: *X-Ray Spectrometry* 50.4 (2021), pp. 310–319. ISSN: 10974539. DOI: 10.1002/xrs.3188.

[21] J. Ansel, E. Yang, H. He, N. Gimelshein, A. Jain, M. Voznesensky, B. Bao, P. Bell, D. Berard, E. Burovski, G. Chauhan, A. Chourdia, W. Constable, A. Desmaison, Z. DeVito, E. Ellison, W. Feng, J. Gong, M. Gschwind, B. Hirsh, S. Huang, K. Kalambarkar, L. Kirsch, M. Lazos, M. Lezcano, Y. Liang, J. Liang, Y. Lu, C. Luk, B. Maher, Y. Pan, C. Puhrsch, M. Reso, M. Saroufim, M. Y. Siraichi, H. Suk, M. Suo, P. Tillet, E. Wang, X. Wang, W. Wen, S. Zhang, X. Zhao, K. Zhou, R. Zou, A. Mathews, G. Chanan, P. Wu, and S. Chintala. "PyTorch 2: Faster Machine Learning Through Dynamic Python Bytecode Transformation and Graph Compilation". In: *29th ACM International Conference on Architectural Support for Programming Languages and Operating Systems, Volume 2 (ASPLOS '24)*. ACM, Apr. 2024. DOI: 10.1145/3620665.3640366. URL: https://pytorch.org/assets/pytorch2-2.pdf.

6

CONCLUSION

In chapter 1, the importance of RIS and MA-XRF for the field of heritage science was highlighted. However, their main limitations were also mentioned. In the case of RIS, the main limitation is the complexity of processing the measurement data, which makes data evaluation a lengthy and labour-intensive process. For MA-XRF, on the other hand, the data processing is widely considered a solved problem, but the long measurement times are considered a significant challenge. This dissertation aimed to address both of these issues, and clear progress has been made on both accounts. Each problem will be evaluated individually before discussing the prospect of multi-modal MA-XRF/RIS imaging, which is yet another potential way of addressing both issues.

6.1. ADVANCED RIS DATA PROCESSING

During the discussion of the state-of-the-art, ML methods were highlighted as the most prominent tools for the analysis of RIS data. Whilst unsupervised ML methods have proven to be very useful, they are not universally applicable to the wide variety of questions that arise during object analysis. In such cases, supervised ML methods are certainly useful, but their application is complex and solutions tend to be similarly non-generalizable. Because of that, it was the lack of non-ML methods that became an early focus of research.

Chapter 2 introduced just such a method. This method, based on feature isolation and deconvolution, presents a novel approach to an automated and semi-quantitative analysis of RIS data, greatly inspired by the way MA-XRF data is processed. The results were very positive on the applied test cases and provided a fast and reliable way of distinguishing between blue verditer/azurite and other copper-based pigments. This method could be further expanded to include more target features and pigments. However, its application is limited to pigments that present prominent reflectance features. In the VNIR-SWIR range, this makes for a relatively small selection of pigments, but it is believed that this method would prove useful in the analysis of MIR-RIS data, especially in the so called “fingerprint region” (7000 −20000 nm), where many compounds present strong and characteristic reflectance features. Whilst MIR-RIS remains a very uncommon method, it is likely to

become increasingly relevant as more reliable and affordable spectrometers continue to be developed. In the meantime, the presented method can definitely be expanded to spectral features beyond those discussed here, which can help identify different pigments or increase the reliability of the identification by incorporating multiple features of the same pigment, like azurite/blue verditer and its absorption features at 2245 nm and 2351 nm.

Some preliminary tests were conducted for the application of this method for the analysis of other types of reflectance data, like FORS and ER-FTIR. In this case, the method was applied for the identification of egg yolk binders through the combination band of –CH of the lipids present in the egg yolk at 2307 nm. Whilst the tests were limited to a single dataset of mock-up samples, results were promising and show the flexibility and further potential of the method. Further research into this is recommended.

However, as mentioned previously, the method is limited to the analysis of compounds which present prominent reflectance features. Where this is not the case, ML methods still seem the most promising. Chapter 3 provides a novel such method through the use of explainable supervised machine learning methods. XGBoost by itself provided limited positive results in the analysis of the tested historical manuscripts, but the models would definitely benefit from more labelled data, either from other similar manuscripts or from reconstruction samples. SHAP as an explainability method not only provided significant insight into the ML system itself, by highlighting the most relevant spectral channels for the characterisation tasks being considered, but also provided a novel method of improving the legibility of the considered manuscripts through the use of SWIMs. Whilst the significant labour required for the creation of the sampling masks is an inherent limitation of the method, it has proven a very useful way of introducing prior information into the analysis of complex datasets. This approach could definitely be expanded to address many other questions within the realm of cultural heritage science. Whilst the ML models output by this approach are not strictly generalizable to other datasets, the insight into the importance of specific spectral regions provided by SHAP could help in the analysis of other objects, as long as the research question is similar enough. Applying this methodology for the analysis of more damaged historical manuscripts and comparing the results of the SHAP analysis is recommended.

The major limitation of the achieved results, namely the poor spatial resolution of the resulting maps, could potentially be addressed through the use of super-resolution methods, or potentially avoided completely through the use of cameras with higher spatial resolutions. The NIREOS HERA[1] is particularly attractive in this regard and its capabilities for the analysis of manuscripts should be further investigated.

6.2. ADVANCED MA-XRF DATA ACQUISITION

One of the initial goals of this research project was the design of an MA-XRF scanner. Ultimately, this was a much more significant challenge than originally assumed, not because of the technical issues, but because of administrative ones. Chapter 4 documents the design process of the two MA-XRF scanners developed during this

project in a way that could give the reader the impression that the process was fairly linear. This was certainly not the case. The BLB Mark I scanner was designed and built within the first two years of the project, followed by a year-and-a-half of no progress, as administrative issues on the use of X-ray equipment were addressed. Because of this, the first MA-XRF scan conducted with this device did not take place until the last six months of the project. These last six months were much more productive, producing the evaluation of the BLB Mark I scanner, as well as the design, production and first tests of the BLB Mark II. Whilst this information is of little scientific value, these facts had a significant effect on the conducted research and presented a valuable lesson on the nature of the real-world challenges faced by researchers. This will certainly not be a surprise to any long-term researcher, as it is a very common lesson, but it is often not directly communicated to early-career researchers, and may at times even be wilfully ignored during project planning. This is not meant as a criticism, as learning the value of flexibility is incredibly important to researchers, and is often something best learned under some stress. Instead, it should be taken as a statement of support for those in similar situations and a friendly warning for those that will experience this in the future.

Ultimately, the two scanners produced during this research are not revolutionary designs that are meant to compete with truly high-end research equipment. They were designed to provide all the necessary flexibility required for the experimental optimizations documented in this dissertation and proved themselves to be useful in that endeavour. One way in which these scanners were quite different from other documented scanners was the extent of the safety measures included in their designs. None of the scanners described in section 1.3.1 were subject to such strict radiation safety measures and instead depend on significant care being taken by the users during the operation of the equipment. In contrast, both the BLB Mark I and Mark II cannot be used in a way that would result in radiation exposure to the user or bystanders without wilful mishandling of the device. This dedication to safety proved very relevant in the dynamic research environment of TU Delft and is a very valuable aspect of both the scanners. As the BLB Mark II was not finished until the end of this project, its performance evaluation is the obvious next step for future research.

Beyond the design of the scanners, the tests for accelerated MA-XRF scanning through the use of alternate scanning strategies described in chapter 5 have already achieved significant improvement over traditional raster scanning. Of the tested methods, the modified version of FAST provided the best results with a 37% decrease in scanning time whilst achieving a better result in both the considered quality metrics, RMSE and SSIM. However, the test conducted was fairly limited in scale and a more diverse selection of samples must be analysed before any general conclusions can be drawn. An interesting feature of this version of FAST is that it could be applied also to other types of hyperspectral scanners. Implementing the method with other equipment, like MA-XRPD scanners and multi-modal MA-XRF/RIS scanners, could provide a more favourable active acquisition time to travel time ratio due to their long dwell times per pixel, which is a significant factor in the efficiency of methods like FAST.

The Chopp algorithm provided mixed results. It performed poorly compared to traditional raster scanning when it comes to real measurement time, but provided reasonably good results when it comes to the total active acquisition time. The main drawback of this method is not to do with the algorithm itself, but how the outputs of the algorithm are practically implemented for a real scanner. Again, the relation between active acquisition time and travel time is a significant factor to how efficient this approach can be. Finding a way to estimate the underlying count rate without having to take a full traditional raster scan would significantly benefit the performance of this method.

For both the FAST and Chopp approach, the implementation of acquisition during travel, as is the case for dynamic raster scanning, would provide significant improvements to measurement times. Implementing this would present different challenges for each of the methods. For FAST, how the systems describes pathing would have to be changed, which could present practical problems depending on what scanner is used. However, the most significant challenge would be changing the way the data reconstruction process works, as the system currently requires the same acquisition time for all measured pixels. This would require all movements to be done at a speed which matches the target acquisition time, or some form of normalization or weighting that would account for the variations in acquisition time. Chopp, on the other hand, would be somewhat simpler, as the approach uses more traditional raster movements. Since the method already can account for maximum and minimum dwell times through iterative optimization, a way to implement this would be to selectively optimize the resulting acquisition time maps along the primary scanning direction in such a way that would minimize changes in scanning speed. This would definitely introduce hysteresis problems, but such issues are already present and addressed in dynamic raster scanning, so it is likely they could be solved for dynamic Chopp scans as well.

6.3. MULTI-MODAL MA-XRF/RIS DATA PROCESSING AND ACQUISITION

The study of objects through combined MA-XRF/RIS analysis was the original topic of this research project. Though the previously mentioned administrative problems with the MA-XRF scanner required a shift in focus, mixed MA-XRF/RIS is still believed to be a promising avenue to address the limitations of both methods.

In terms of data processing, the complementary nature of MA-XRF and RIS is well known. Many existing works already make use of this complementary nature,[2–9] so its value is certainly appreciated by the wider field. However, most of these works do not process the data together, but instead process the data separately and only manually compare the outputs during the interpretation phase. Only a few examples, like those by Alfeld et al.[10] and Butler et al.,[11] actually process the data jointly. In both these cases, the data is processed through unsupervised ML methods, which are particularly well suited for handling such complex multi-modal data. However, the former example fuses the data first and then process it jointly, whilst the latter example process the data separately and then fuses the data for another, simpler

processing step. Both approaches have their advantages and disadvantages, but share the challenge of actually fusing the data. Since the two imaging methods present different spatial patterns, aligning the datasets to each other is a challenge. Usually, the alignment of the datasets is done manually or semi-automatically through the use of feature detection algorithms, like scale-invariant feature transform (SIFT).[12] Work has been done for the automated alignment of these types of datasets[13, 14] but no solution has been widely adopted.

A potential way around the issue of data registration is the use of a multi-modal scanner, which inherently provides aligned datasets. Already several such scanners have been described and proven to provide valuable complementary information,[15] some even covering other imaging methods like LIS.[16] A commercially available scanner has even been released in the market,[17, 18] pointing towards wider adoption of this technology. As such, the development of multi-modal data processing methods will only become increasingly relevant and should be a priority in future research in the field.

BIBLIOGRAPHY

[1] F. Preda, A. Perri, and D. Polli. "A New 'Hera' in Hyperspectral Imaging". In: *PhotonicsViews* 18.1 (2021), pp. 45–49. ISSN: 2626-1294. DOI: 10.1002/phvs.202100020.

[2] G. van der Snickt, K. A. Dooley, J. Sanyova, H. Dubois, J. K. Delaney, E. Melanie Gifford, S. Legrand, N. Laquiere, and K. Janssens. "Dual mode standoff imaging spectroscopy documents the painting process of the Lamb of God in the Ghent Altarpiece by J. And H. Van Eyck". In: *Science Advances* 6.31 (2020). ISSN: 23752548. DOI: 10.1126/sciadv.abb3379.

[3] S. D. Meyer, F. Vanmeert, R. Vertongen, A. V. Loon, V. Gonzalez, J. Delaney, K. Dooley, J. Dik, G. V. der Snickt, A. Vandivere, and K. Janssens. "Macroscopic x-ray powder diffraction imaging reveals Vermeer's discriminating use of lead white pigments in Girl with a Pearl Earring". In: *Science Advances* 5 (8 Aug. 2019). ISSN: 2375-2548. DOI: 10.1126/sciadv.aax1975. URL: https://www.science.org/doi/10.1126/sciadv.aax1975.

[4] N. De Keyser, F. T. Broers, F. Vanmeert, A. van Loon, F. Gabrieli, S. De Meyer, A. Gestels, V. Gonzalez, E. Hermens, P. Noble, F. Meirer, K. Janssens, and K. Keune. "Discovery of pararealgar and semi-amorphous pararealgar in Rembrandt's The Night Watch: analytical study and historical contextualization". In: *Heritage Science* 12.1 (2024), pp. 1–20. ISSN: 20507445. DOI: 10.1186/s40494-024-01350-x. URL: https://doi.org/10.1186/s40494-024-01350-x.

[5] J. K. Delaney, K. A. Dooley, A. van Loon, and A. Vandivere. "Mapping the pigment distribution of Vermeer's Girl with a Pearl Earring". In: *Heritage Science* 8.1 (2020), pp. 1–16. ISSN: 20507445. DOI: 10.1186/s40494-019-0348-9. URL: https://doi.org/10.1186/s40494-019-0348-9.

[6] K. A. Dooley, D. M. Conover, L. D. Glinsman, and J. K. Delaney. "Complementary standoff chemical imaging to map and identify artist materials in an early italian renaissance panel painting". In: *Angewandte Chemie - International Edition* 53 (50 2014), pp. 13775–13779. ISSN: 15213773. DOI: 10.1002/anie.201407893.

[7] N. D. Keyser, A. van Loon, F. Gabrieli, F. Vanmeert, F. T. Broers, P. Noble, S. D. Meyer, A. Gestels, V. Gonzalez, M. Almasian, I. van der Werf, E. Hermens, K. Janssens, and K. Keune. "Illuminating Rembrandt's Chiaroscuro in The Night Watch: the painting process of Van Ruytenburch's costume". In: *npj Heritage Science* 13 (1 Dec. 2025). ISSN: 30593220. DOI: 10.1038/s40494-025-01874-w.

[8] N. D. Keyser, F. Broers, F. Vanmeert, S. D. Meyer, F. Gabrieli, E. Hermens, G. V. der Snickt, K. Janssens, and K. Keune. “Reviving degraded colors of yellow flowers in 17th century still life paintings with macro- and microscale chemical imaging”. In: *Science Advances* 8 (23 2022). ISSN: 23752548. DOI: 10.1126/sciadv.abn6344.

[9] M. Alfeld, M. Mulliez, J. Devogelaere, L. de Viguerie, P. Jockey, and P. Walter. “MA-XRF and hyperspectral reflectance imaging for visualizing traces of antique polychromy on the Frieze of the Siphnian Treasury”. In: *Microchemical Journal* 141.April (2018), pp. 395–403. ISSN: 0026265X. DOI: 10.1016/j.microc.2018.05.050. URL: https://doi.org/10.1016/j.microc.2018.05.050.

[10] M. Alfeld, S. Pedetti, P. Martinez, and P. Walter. “Joint data treatment for Vis–NIR reflectance imaging spectroscopy and XRF imaging acquired in the Theban Necropolis in Egypt by data fusion and t-SNE”. In: *Comptes Rendus Physique* 19 (7 2018), pp. 625–635. ISSN: 16310705. DOI: 10.1016/j.crhy.2018.08.004. URL: https://doi.org/10.1016/j.crhy.2018.08.004.

[11] L. Butler, S. Kogou, A. Hogg, Y. Li, A. Vichi, A. Gallop, and H. Liang. “Machine learning analysis of complementary multimodal spectral imaging data from a large manuscript collection”. In: *Proc.SPIE*. Vol. 11784. June 2021, p. 1178405. DOI: 10.1117/12.2593918. URL: https://doi.org/10.1117/12.2593918.

[12] D. G. Lowe. “Object recognition from local scale-invariant features”. In: *Proceedings of the Seventh IEEE International Conference on Computer Vision*. Vol. 2. 1999, 1150–1157 vol.2. DOI: 10.1109/ICCV.1999.790410.

[13] F. Gabrieli, J. K. Delaney, R. G. Erdmann, V. Gonzalez, A. van Loon, P. Smulders, R. Berkeveld, R. van Langh, and K. Keune. “Reflectance imaging spectroscopy (RIS) for Operation Night Watch: Challenges and achievements of imaging Rembrandt’s masterpiece in the glass chamber at the Rijksmuseum”. In: *Sensors* 21 (20 2021), pp. 1–18. ISSN: 14248220. DOI: 10.3390/s21206855.

[14] M. E. Villafane, N. Daly, C. Kimbriel, C. Higgitt, and P. L. Dragotti. “Multimodal image registration and mosaicking of artworks: an approach based on mutual information”. In: *Proc.SPIE*. Vol. 12620. Aug. 2023, p. 1262004. DOI: 10.1117/12.2673427. URL: https://doi.org/10.1117/12.2673427.

[15] J. K. Delaney, D. M. Conover, K. A. Dooley, L. Glinsman, K. Janssens, and M. Loew. “Integrated X-ray fluorescence and diffuse visible-to-near-infrared reflectance scanner for standoff elemental and molecular spectroscopic imaging of paints and works on paper”. In: *Heritage Science* 6 (1 2018), pp. 1–12. ISSN: 20507445. DOI: 10.1186/s40494-018-0197-y. URL: https://doi.org/10.1186/s40494-018-0197-y.

[16] R. Moreau, T. Calligaro, L. Pichon, B. Moignard, S. Hermon, and I. Reiche. “A multimodal scanner coupling XRF, UV–Vis–NIR photoluminescence and Vis–NIR–SWIR reflectance imaging spectroscopy for cultural heritage studies”. In: *X-Ray Spectrometry* 53.4 (2024), pp. 271–281. ISSN: 10974539. DOI: 10.1002/xrs.3364.

[17] M. Occhipinti, R. Alberti, T. Parsani, C. Dicorato, P. Tirelli, M. Gironda, A. Tocchio, and T. Frizzi. "IRIS: A novel integrated instrument for co-registered MA-XRF mapping and VNIR-SWIR hyperspectral imaging". In: *X-Ray Spectrometry* January 2023 (2023), pp. 520–530. ISSN: 10974539. DOI: 10.1002/xrs.3405.

[18] E. Catelli, Z. Li, G. Sciutto, P. Oliveri, S. Prati, M. Occhipinti, A. Tocchio, R. Alberti, T. Frizzi, C. Malegori, and R. Mazzeo. "Towards the non-destructive analysis of multilayered samples: A novel XRF-VNIR-SWIR hyperspectral imaging system combined with multiblock data processing". In: *Analytica Chimica Acta* 1239.September 2022 (2023), p. 340710. ISSN: 18734324. DOI: 10.1016/j.aca.2022.340710. URL: https://doi.org/10.1016/j.aca.2022.340710.

A

Appendix A: Supplementary information for chapter 2

A

A.1. SAMPLE PIGMENT CHARACTERIZATION

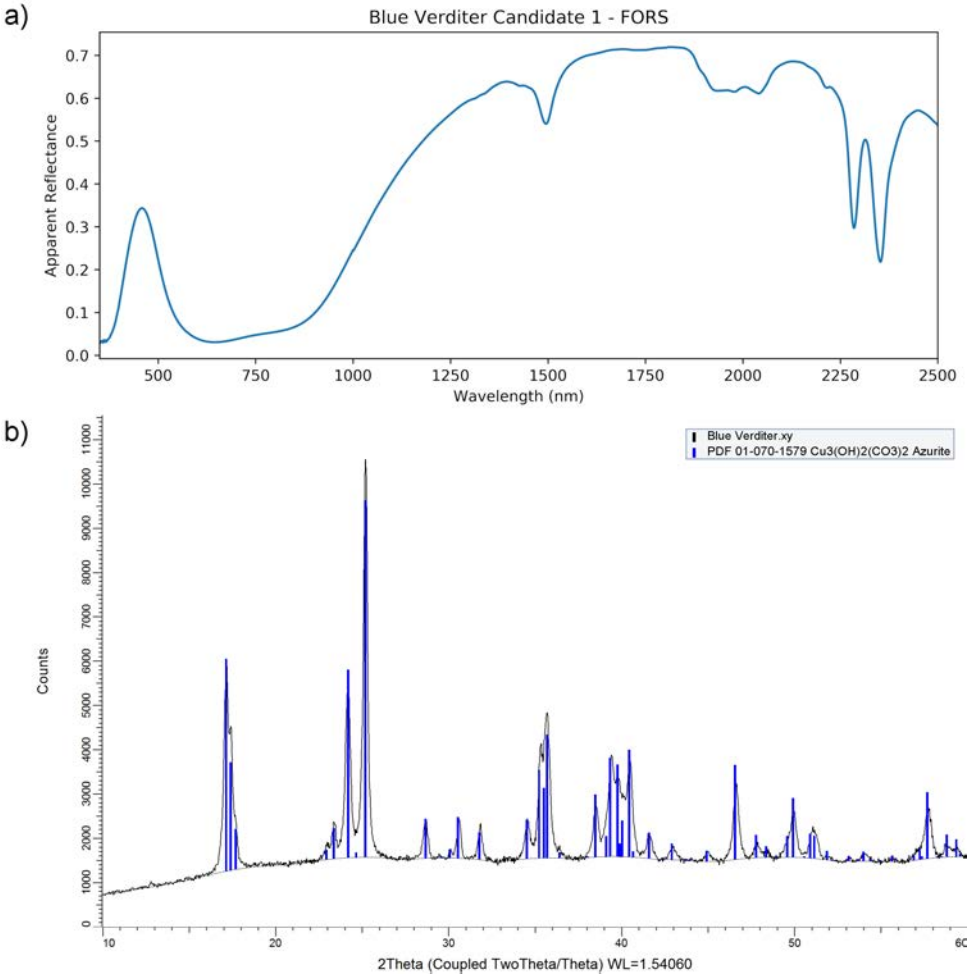

Figure A.1.: Blue Verditer (Rublev Colours Blue Verditer Pigment) Analysis. a) FORS Spectrum. b) XRD spectrum.

Table A.1.: Blue Verditer (Rublev Colours Blue Verditer Pigment) Analysis quantitative XRD results.

Compound	Formula	Weight percentage (%)
Azurite	$Cu_3(CO_3)_2(OH)_2$	100

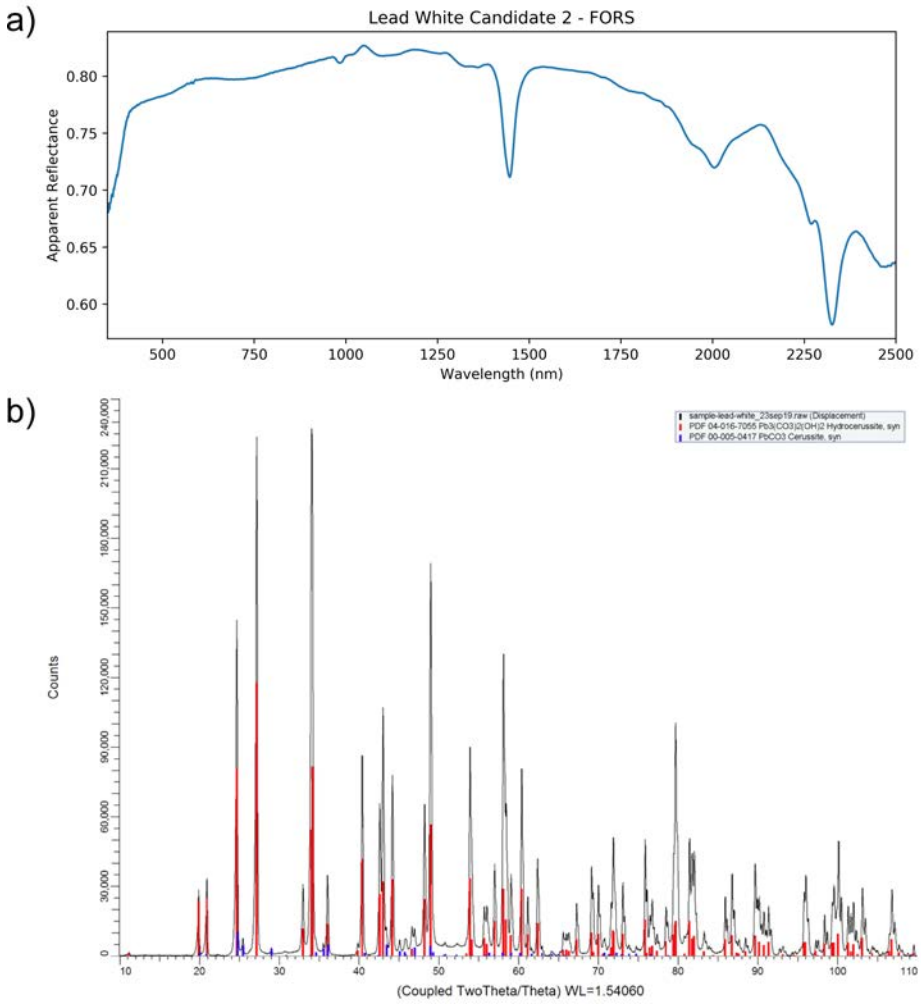

Figure A.2.: Lead White (Rublev Colours Stack Flake White Pigment) Analysis.

Table A.2.: Lead White (Rublev Colours Stack Flake White Pigment) Analysis quantitative XRD results.

Compound	Formula	Weight percentage (%)
Hydrocerussite	$Pb_3(CO_3)_2(OH)_2$	98± 1
Cerussite	$PbCO_3$	2± 1

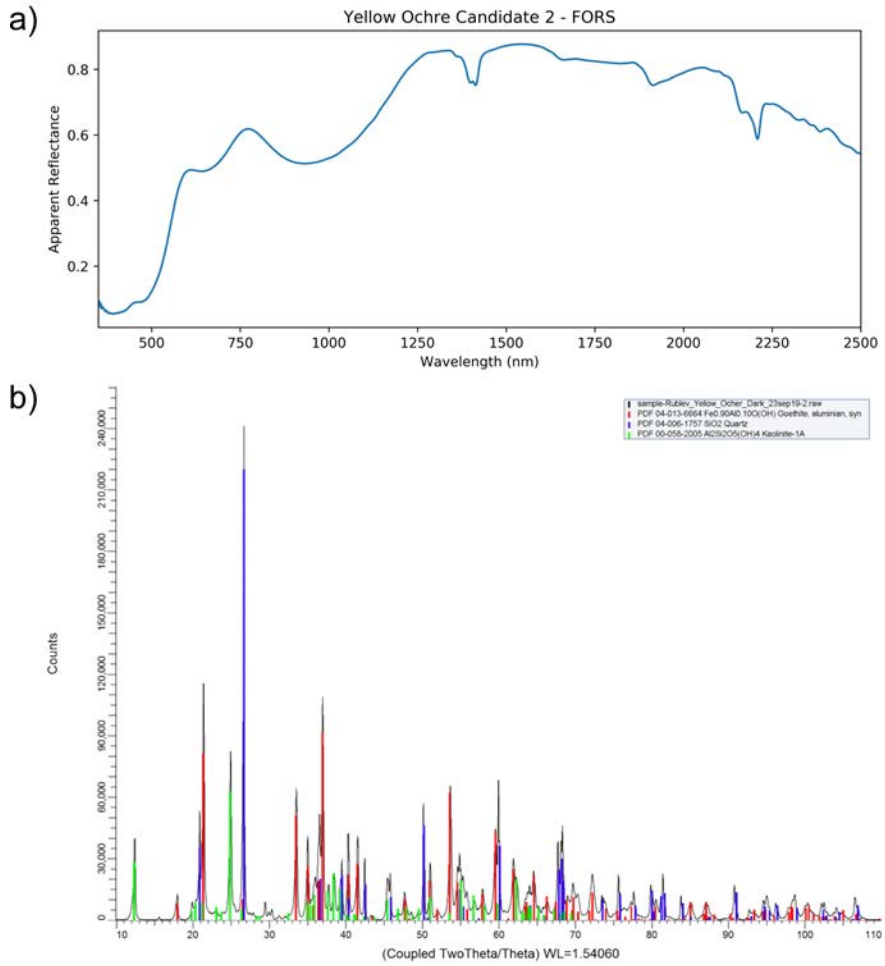

Figure A.3.: Yellow Ochre (Rublev Colours Yellow Ochre Dark Pigment) Analysis.

Table A.3.: Yellow Ochre (Rublev Colours Yellow Ochre Dark Pigment) Analysis quantitative XRD results.

Compound	Formula	Weight percentage (%)
Quartz	SiO_2	37±2
Goethite-Aluminian	$Fe_{0.9}Al_{0.1}O(OH)$	33±2
Kaolinite-1A	$Al_2(OH)_4Si_2O_5$	30±2

A.2. SAMPLE SUPPORT MATERIAL CHARACTERIZATION

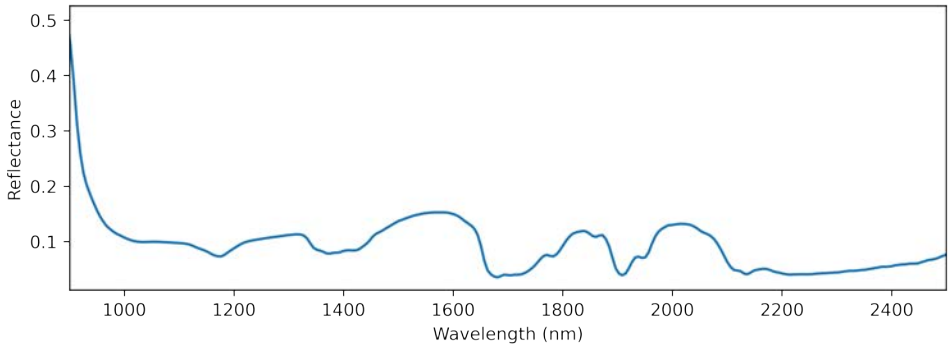

Figure A.4.: Average reflectance spectrum of paint sample background (50 µm Melinex + 3 mm plexiglass).

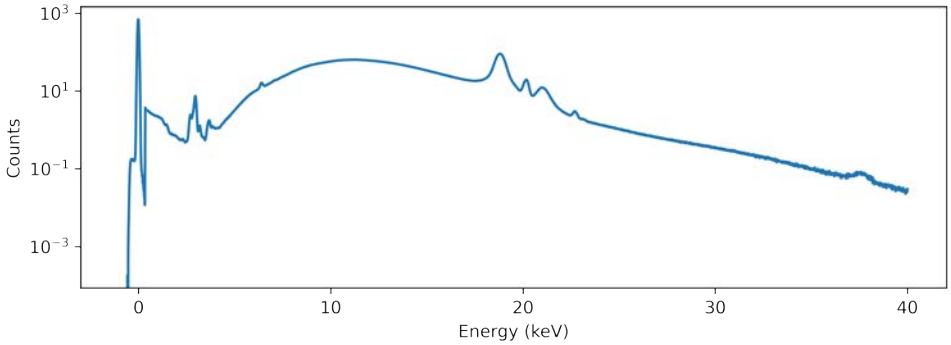

Figure A.5.: Average XRF spectrum of paint sample background (50 µm Melinex + 3 mm plexiglass).

Table A.4.: Average signal intensities of paint sample background (50 µm Melinex + 3 mm plexiglass) acquired with 400 ms dwell time per pixel.

X-ray fluorescence line	Signal intensity
Al-K	-1.319
Si-K	-3.242
Ar-K	84.866
K-K	-6.486
Ca-K	12.068
Ti-K	-8.000
V-K	-5.502
Cr-K	1.569
Fe-Kα	49.215
Fe-Kβ	5.715
Cu-Kα	1.874
Cu-Kβ	68.052
Zn-K	44.702
Rh-L	34.981
Pb-Lα	151.908
Pb-Lβ	-59.371
Pb-Lγ	-106.335
Pb-M	-22.744

A.3. MIXTURE SAMPLES DENSITIES

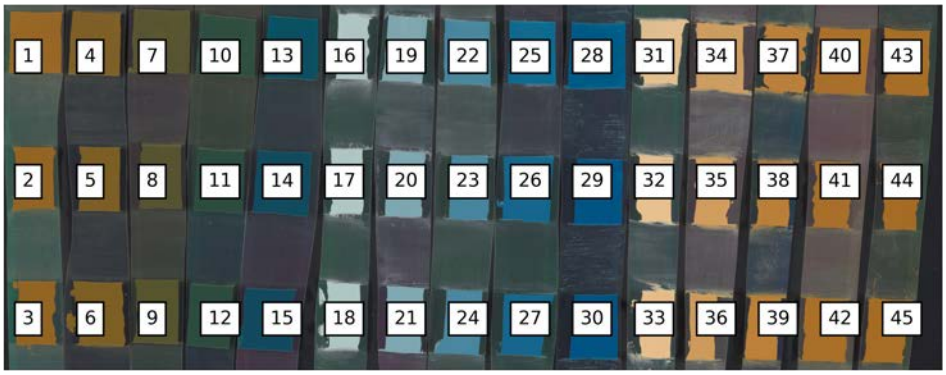

Figure A.6.: Mixture samples legend for table A.5.

Table A.5.: Mixture samples areal density composition.

Sample	Layer thickness (μm)	Lead white (g/cm^2)	Blue verditer (g/cm^2)	Yellow ochre (g/cm^2)	Linseed oil (g/cm^2)
1	50	0	0.0851	0.0040	0.0253
2	100	0	0.1701	0.0081	0.0506
3	150	0	0.2552	0.0121	0.0759
4	50	0	0.0706	0.0160	0.0262
5	100	0	0.1413	0.0319	0.0524
6	150	0	0.2119	0.0479	0.0786
7	50	0	0.0430	0.0388	0.0280
8	100	0	0.0859	0.0777	0.0560
9	150	0	0.1289	0.1165	0.0840
10	50	0	0.0167	0.0605	0.0297
11	100	0	0.0335	0.1210	0.0593
12	150	0	0.0502	0.1815	0.0890
13	50	0	0.0041	0.0709	0.0305
14	100	0	0.0083	0.1418	0.0610
15	150	0	0.0124	0.2128	0.0914
16	50	0.1397	0.0068	0	0.0261
17	100	0.2794	0.0135	0	0.0522
18	150	0.4191	0.0203	0	0.0782
19	50	0.1089	0.0249	0	0.0259
20	100	0.2179	0.0498	0	0.0518

Table A.6.: Mixture samples areal density composition.

Sample	Layer thickness (μm)	Lead white (g/cm^2)	Blue verditer (g/cm^2)	Yellow ochre (g/cm^2)	Linseed oil (g/cm^2)
21	150	0.3268	0.0747	0	0.0776
22	50	0.0593	0.0542	0	0.0256
23	100	0.1185	0.1084	0	0.0511
24	150	0.1778	0.1627	0	0.0767
25	50	0.0210	0.0768	0	0.0253
26	100	0.0420	0.1536	0	0.0506
27	150	0.0630	0.2304	0	0.0759
28	50	0.0050	0.0862	0	0.0252
29	100	0.0099	0.1725	0	0.0504
30	150	0.0149	0.2588	0	0.0756
31	50	0.1399	0	0.0061	0.0264
32	100	0.2798	0	0.0122	0.0528
33	150	0.4197	0	0.0183	0.0791
34	50	0.1070	0	0.0222	0.0274
35	100	0.2140	0	0.0443	0.0548
36	150	0.3210	0	0.0665	0.0822
37	50	0.0565	0	0.0468	0.0290
38	100	0.1130	0	0.0936	0.0579
39	150	0.1695	0	0.1404	0.0869
40	50	0.0196	0	0.0648	0.0301
41	100	0.0391	0	0.1297	0.0602
42	150	0.0587	0	0.1945	0.0904
43	50	0.0046	0	0.0722	0.0306
44	100	0.0092	0	0.1443	0.0612
45	150	0.0137	0	0.2165	0.0917

A.4. LAYER SAMPLES DENSITIES

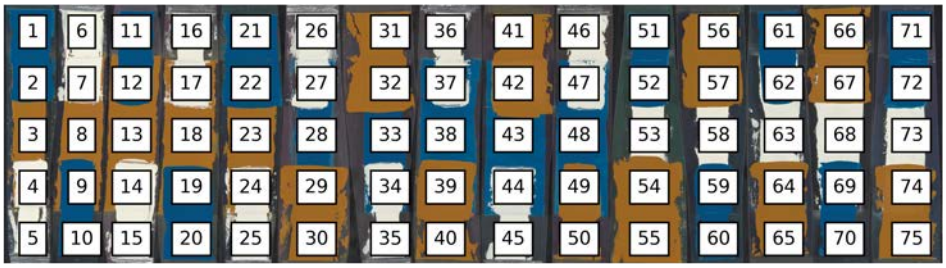

Figure A.7.: Layer samples legend for table A.7.

Table A.7.: Layer samples 1-20 areal density composition.

Sample	Layer 1 thickness (μm)	Layer 2 thickness (μm)	Lead white (g/cm^2)	Blue verditer (g/cm^2)	Yellow ochre (g/cm^2)	Linseed oil (g/cm^2)
1	-	150	0	0.2672	0	0.0756
2	100	50	0	0.0891	0.1496	0.0865
3	100	-	0	0	0.1496	0.0613
4	100	50	0.1547	0	0.1496	0.0869
5	-	150	0.4640	0	0	0.0770
6	-	150	0.4640	0	0	0.0770
7	100	50	0.1547	0	0.1496	0.0869
8	100	-	0	0	0.1496	0.0613
9	100	50	0	0.0891	0.1496	0.0865
10	-	150	0	0.2672	0	0.0756
11	-	150	0	0.2672	0	0.0756
12	50	100	0	0.1782	0.0748	0.0810
13	50	-	0	0	0.0748	0.0306
14	50	100	0.3093	0	0.0748	0.0820
15	-	150	0.4640	0	0	0.0770
16	-	100	0.3093	0	0	0.0513
17	50	50	0.1547	0	0.0748	0.0563
18	50	-	0	0	0.0748	0.0306
19	50	50	0	0.0891	0.0748	0.0558
20	-	100	0	0.1782	0	0.0504

Table A.8.: Layer samples 21-58 areal density composition.

Sample	Layer thickness (μm)	Lead white (g/cm^2)	Blue verditer (g/cm^2)	Yellow ochre (g/cm^2)	Linseed oil (g/cm^2)	
21	-	100	0	0.1782	0	0.0504
22	50	50	0	0.0891	0.0748	0.0558
23	50	-	0	0	0.0748	0.0306
24	50	50	0.1547	0	0.0748	0.0563
25	-	100	0.3093	0	0	0.0513
26	-	150	0.4640	0	0	0.0770
27	100	50	0.1547	0.1760	0	0.0766
28	100	-	0	0.1760	0	0.0510
29	100	50	0	0.1760	0.0754	0.0814
30	-	150	0	0	0.2263	0.0915
31	-	150	0	0	0.2263	0.0915
32	100	50	0	0.1760	0.0754	0.0814
33	100	-	0	0.1760	0	0.0510
34	100	50	0.1547	0.1760	0	0.0766
35	-	150	0.4640	0	0	0.0770
36	-	150	0.4640	0	0	0.0770
37	50	100	0.3093	0.0880	0	0.0768
38	50	-	0	0.0880	0	0.0255
39	50	100	0	0.0880	0.1508	0.0865
40	-	150	0	0	0.2263	0.0915
41	-	100	0	0	0.1508	0.0610
42	50	50	0	0.0880	0.0754	0.0560
43	50	-	0	0.0880	0	0.0255
44	50	50	0.1547	0.0880	0	0.0511
45	-	100	0.3093	0	0	0.0513
46	-	100	0.3093	0	0	0.0513
47	50	50	0.1547	0.0880	0	0.0511
48	50	-	0	0.0880	0	0.0255
49	50	50	0	0.0880	0.0754	0.0560
50	-	100	0	0	0.1508	0.0610
51	-	150	0	0.2672	0	0.0756
52	100	50	0.3008	0.0891	0	0.0777
53	100	-	0.3008	0	0	0.0525
54	100	50	0.3008	0	0.0754	0.0830
55	-	150	0	0	0.2263	0.0915
56	-	150	0	0	0.2263	0.0915
57	100	50	0.3008	0	0.0754	0.0830
58	100	-	0.3008	0	0	0.0525

Table A.9.: Layer samples 59-75 areal density composition.

Sample	Layer 1 thickness (μm)	Layer 2 thickness (μm)	Lead white (g/cm^2)	Blue verditer (g/cm^2)	Yellow ochre (g/cm^2)	Linseed oil (g/cm^2)
59	100	50	0.3008	0.0891	0	0.0777
60	-	150	0	0.2672	0	0.0756
61	-	150	0	0.2672	0	0.0756
62	50	100	0.1504	0.1782	0	0.0766
63	50	-	0.1504	0	0	0.0263
64	50	100	0.1504	0	0.1508	0.0872
65	-	150	0	0	0.2263	0.0915
66	-	100	0	0	0.1508	0.0610
67	50	50	0.1504	0	0.0754	0.0568
68	50	-	0.1504	0	0	0.0263
69	50	50	0.1504	0.0891	0	0.0515
70	-	100	0	0.1782	0	0.0504
71	-	100	0	0.1782	0	0.0504
72	50	50	0.1504	0.0891	0	0.0515
73	50	-	0.1504	0	0	0.0263
74	50	50	0.1504	0	0.0754	0.0568
75	-	100	0	0	0.1508	0.0610

A.5. MIXTURE SAMPLES MA-XRF MAPS

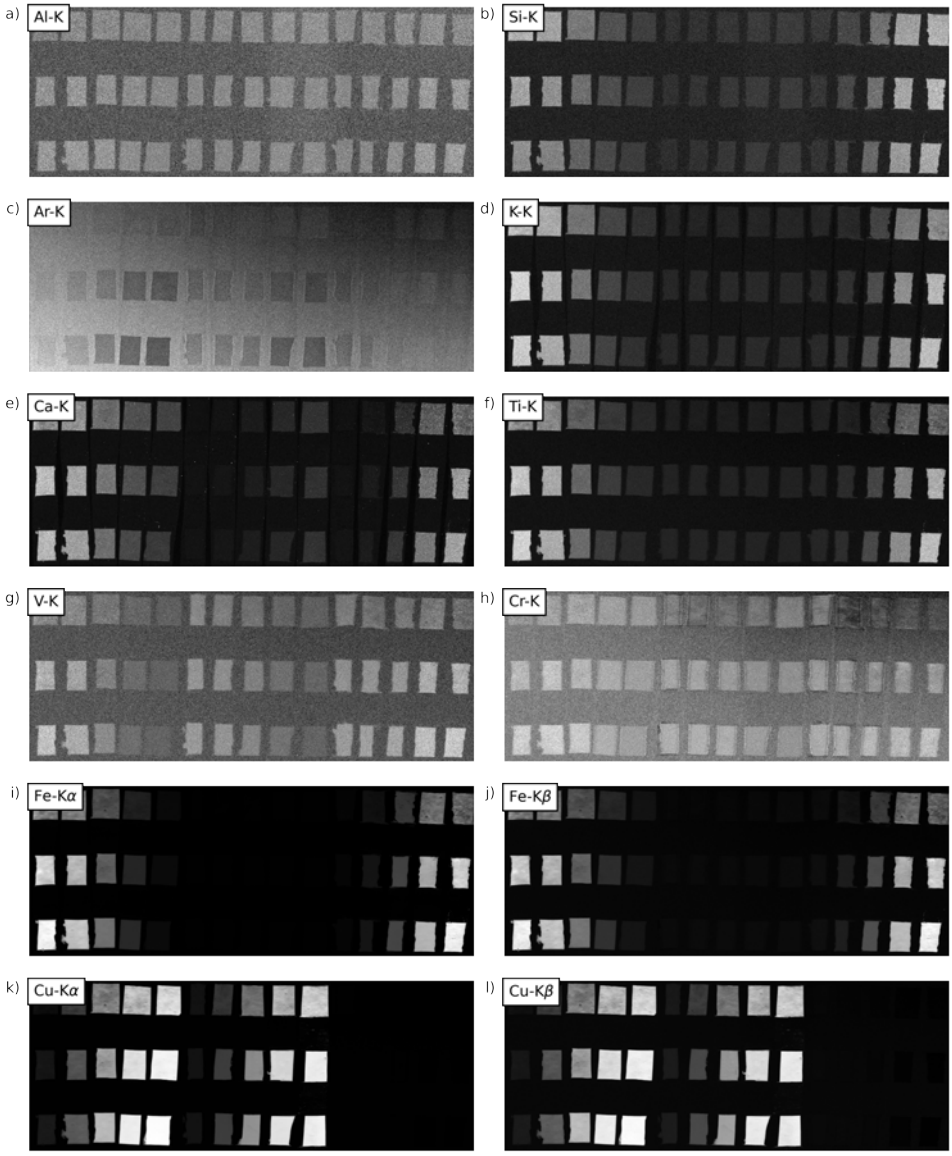

Figure A.8.: Mixture Samples MA-XRF maps. White is higher signal and black is lower signal.

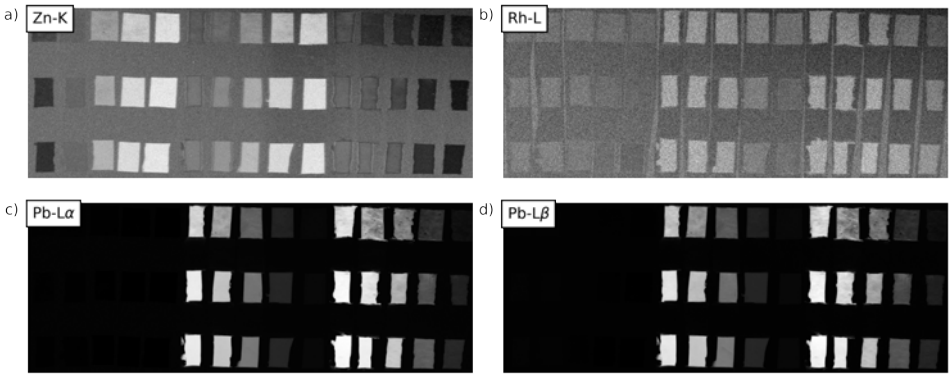

Figure A.9.: Mixture Samples MA-XRF maps. White is higher signal and black is lower signal.

A.6. LAYER SAMPLES MA-XRF MAPS

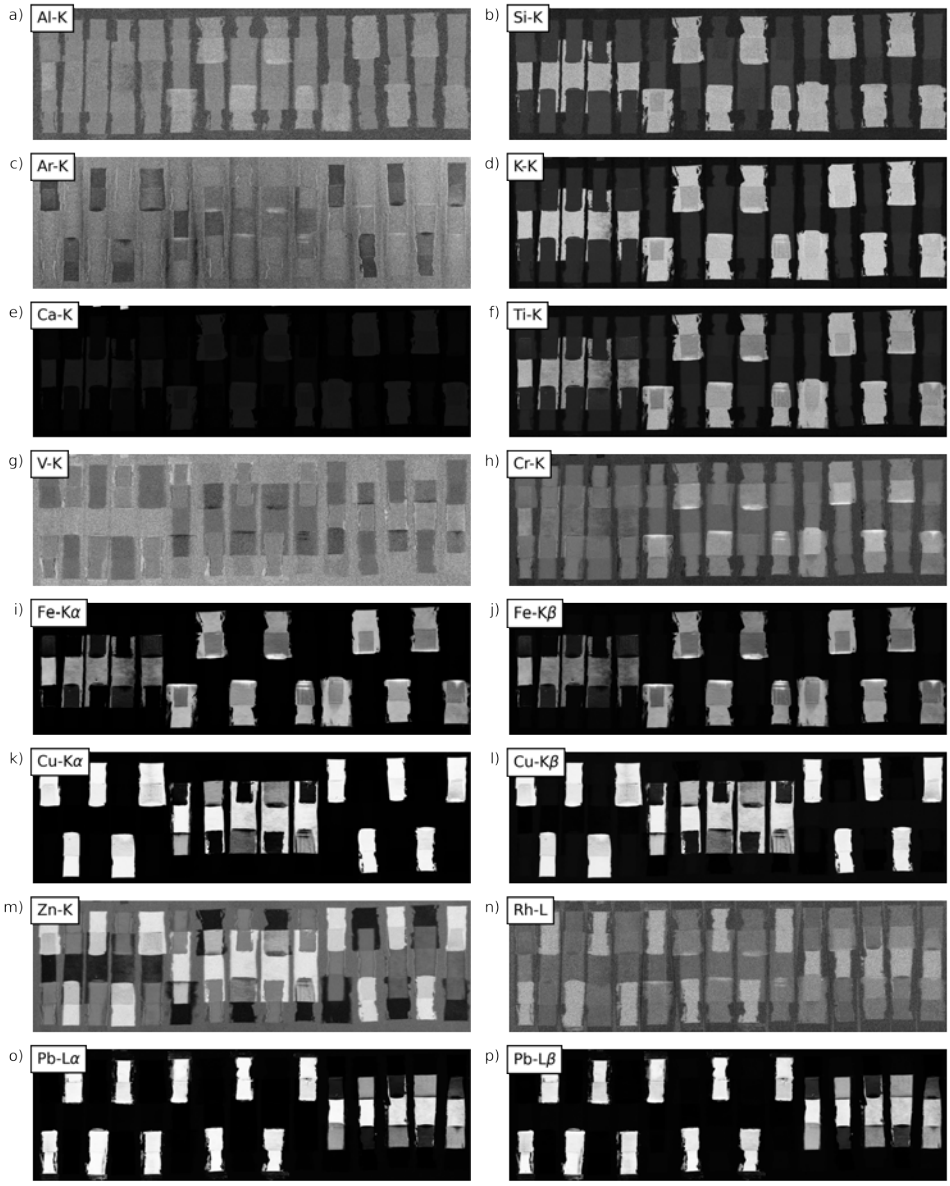

Figure A.10.: Layer Samples MA-XRF maps. White is higher signal and black is lower signal.

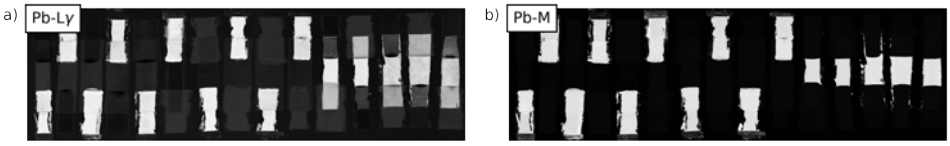

Figure A.11.: Layer Samples MA-XRF maps. White is higher signal and black is lower signal.

A.7. PIGMENT ATTENUATION AND TRANSMISSION VALUES

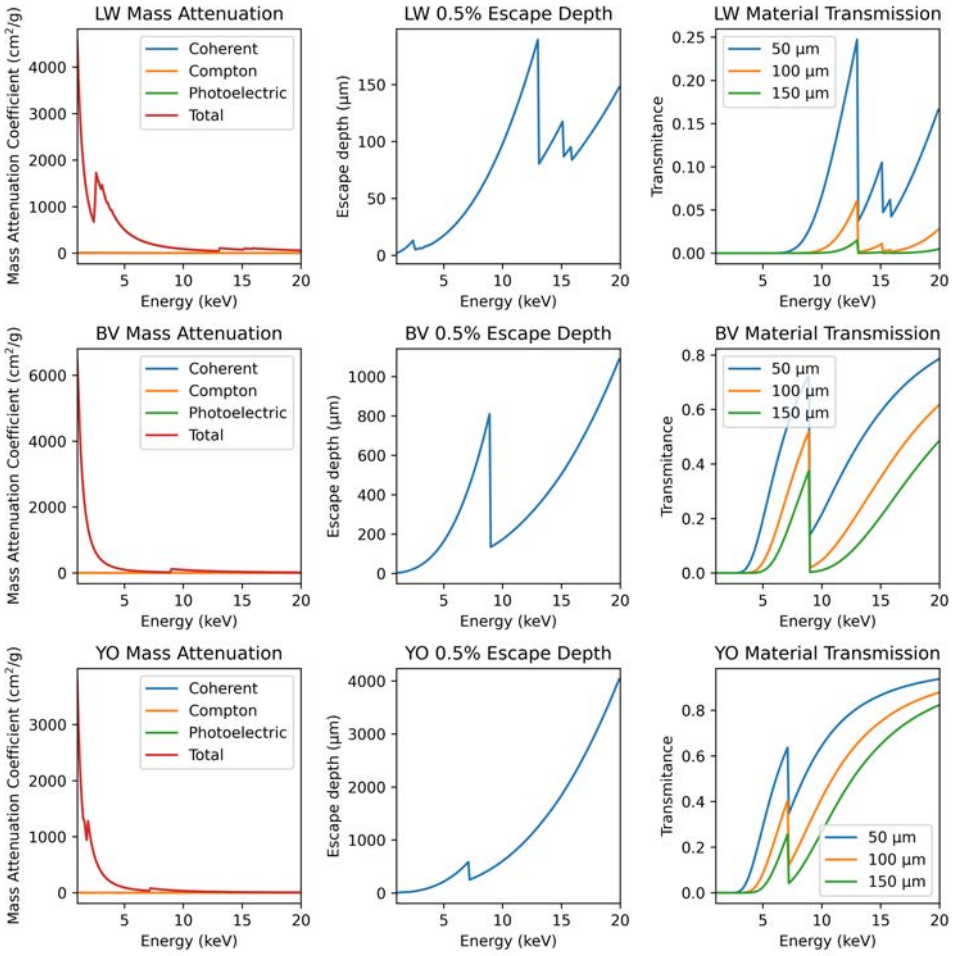

Figure A.12.: Mass attenuation, 0.5% escape depth and material transmission information for lead white (LW), blue verditer (BV) and yellow ochre (YO). The 0.5% escape depth is the depth at which only 0.5% of the radiation at each energy value is able to escape the sample (99.5% of the radiation is absorbed within the sample), providing an idea of the information depth of MA-XRF.

A.8. SAMPLE PAINTING DISTRIBUTION MAPS

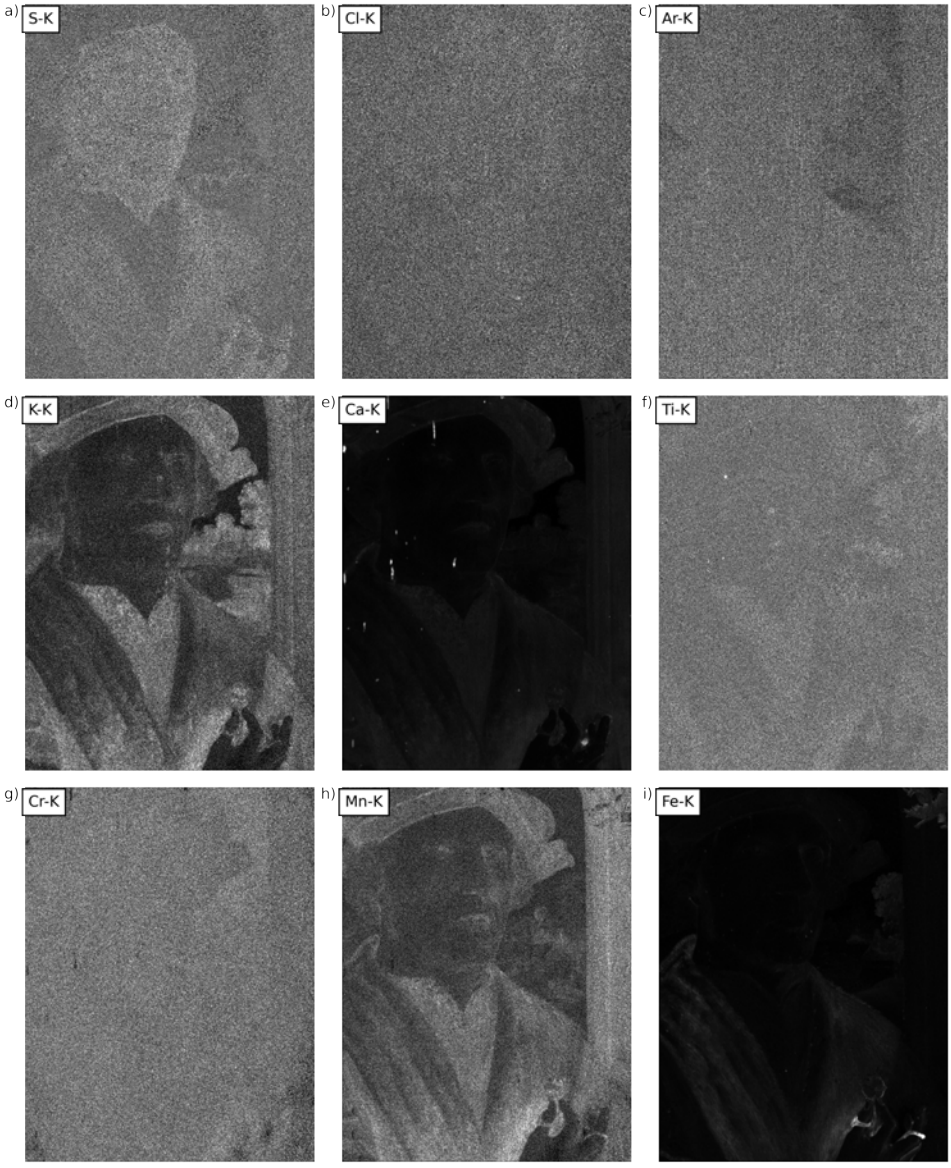

Figure A.13.: Painting MA-XRF maps. White is higher signal and black is lower signal.

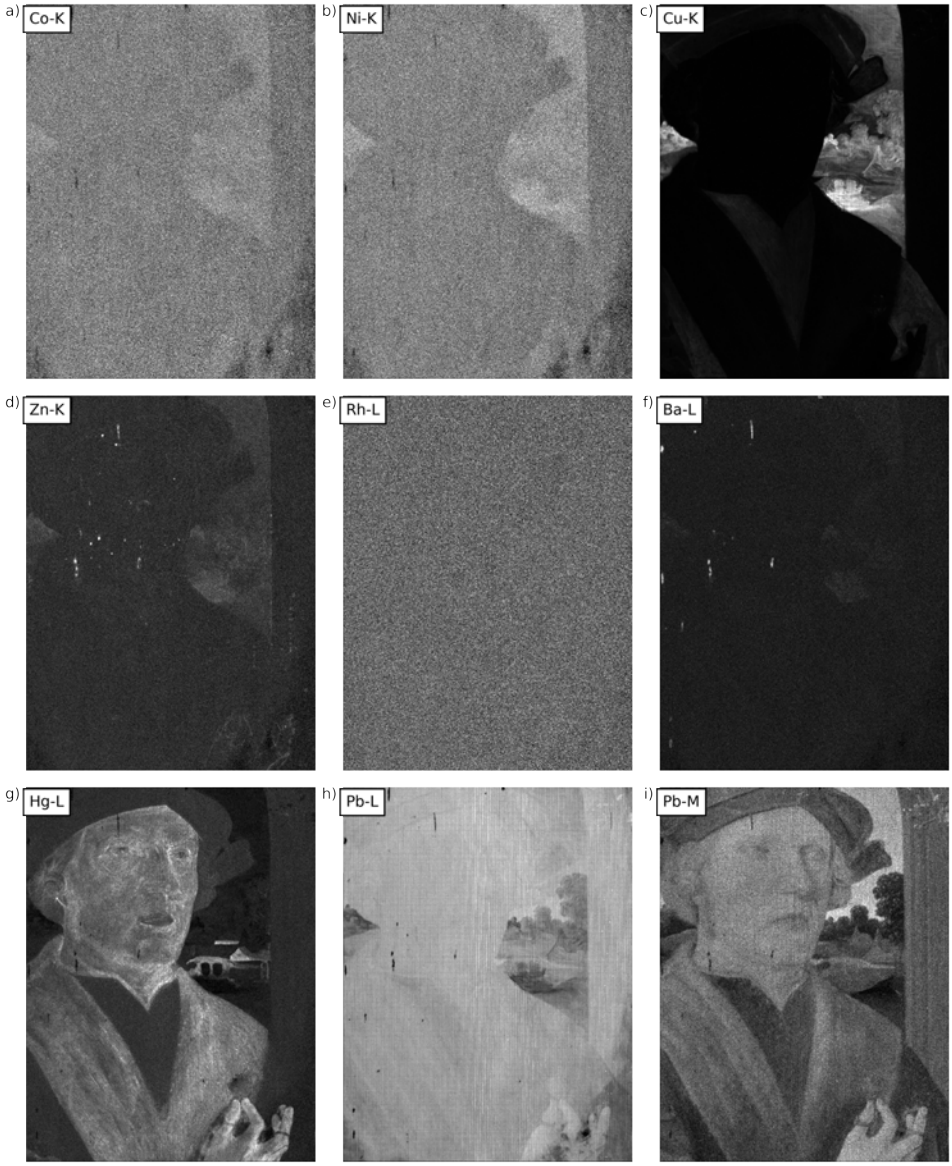

Figure A.14.: Painting MA-XRF maps. White is higher signal and black is lower signal.

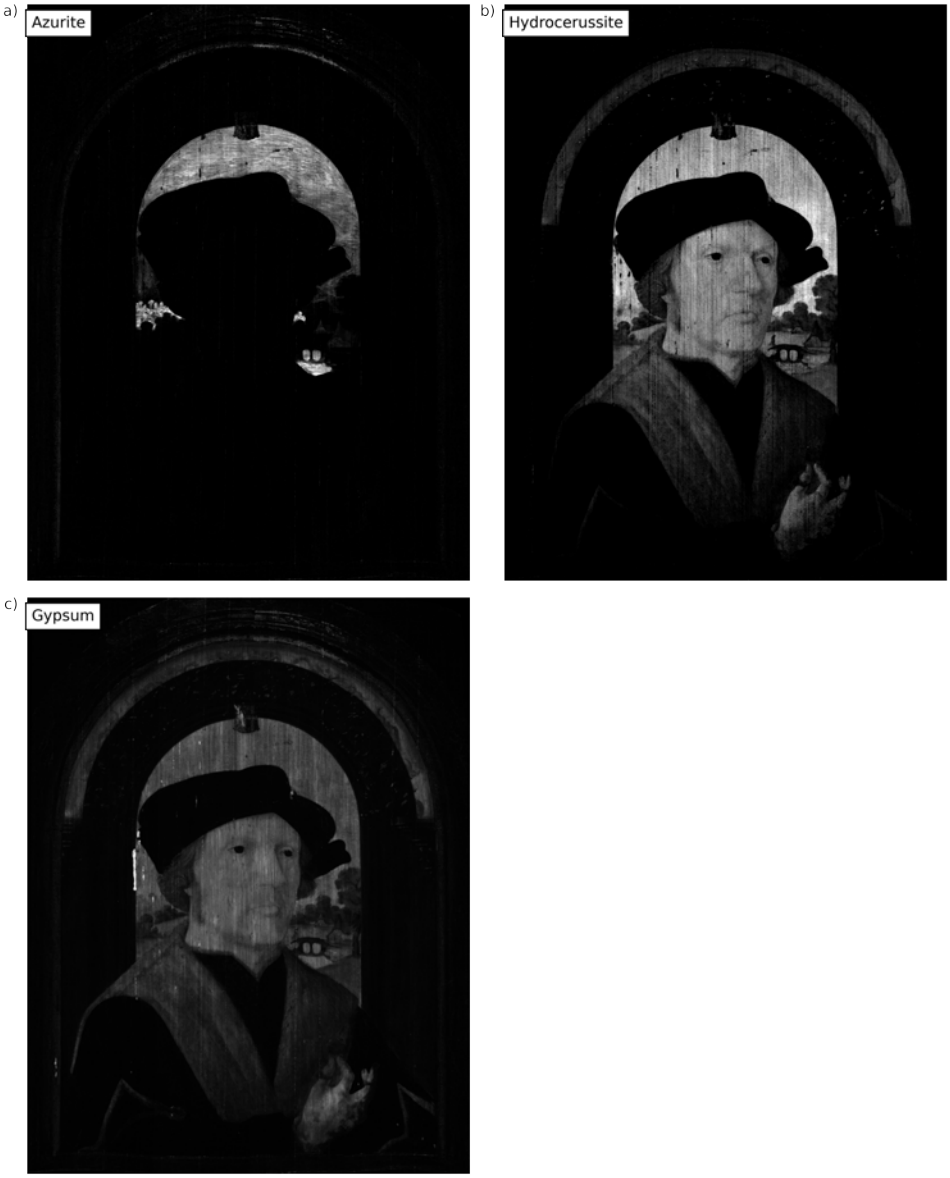

Figure A.15.: Painting RIS maps. White is higher signal and black is lower signal.

B

Appendix B: Supplementary information for chapter 3

B.1. XGBOOST SETTINGS

Table B.1.: Settings for Leiden Riddle classifier.

Setting	Value
Objective	binary:logistic
eval_metric	logloss
learning_rate	0.3
max_depth	6
subsample	0.8
colsample_bynode	0.8
reg_lambda	1
reg_alpha	1
seed	1, 3, 7, 10, 15, 22, 37, 42, 59 and 69

Table B.2.: Settings for Locke Constitution classifiers.

Setting	Value
Objective	binary:logistic
eval_metric	logloss
learning_rate	0.01
max_depth	4
subsample	0.8
colsample_bynode	0.8
reg_lambda	5
reg_alpha	5
seed	1, 3, 7, 10, 15, 22, 37, 42, 59 and 69

B.2. CLASSIFIER METRICS

Table B.3.: Metrics of Leiden Riddle Riddle Ink vs. Non-riddle-ink Classifier.

Value	Train	Test
Accuracy	0.99400	0.97170
Balanced Accuracy	0.98922	0.94863
Recall	0.98922	0.94863
Precision	0.99173	0.96070
F1	0.99400	0.97151

Table B.4.: Metrics of Locke Constitution Ink vs. Non-Ink Classifier.

Value	Train	Test
Accuracy	0.97786	0.96693
Balanced Accuracy	0.97487	0.96253
Recall	0.97487	0.96253
Precision	0.97522	0.96325
F1	0.97786	0.96692

Table B.5.: Metrics of Locke Constitution Original Ink vs. Edit Ink Classifier.

Value	Train	Test
Accuracy	0.76538	0.71402
Balanced Accuracy	0.76537	0.71411
Recall	0.76537	0.71411
Precision	0.76992	0.71862
F1	0.76436	0.71251

B.3. LEIDEN RIDDLE AREAS OF INTEREST

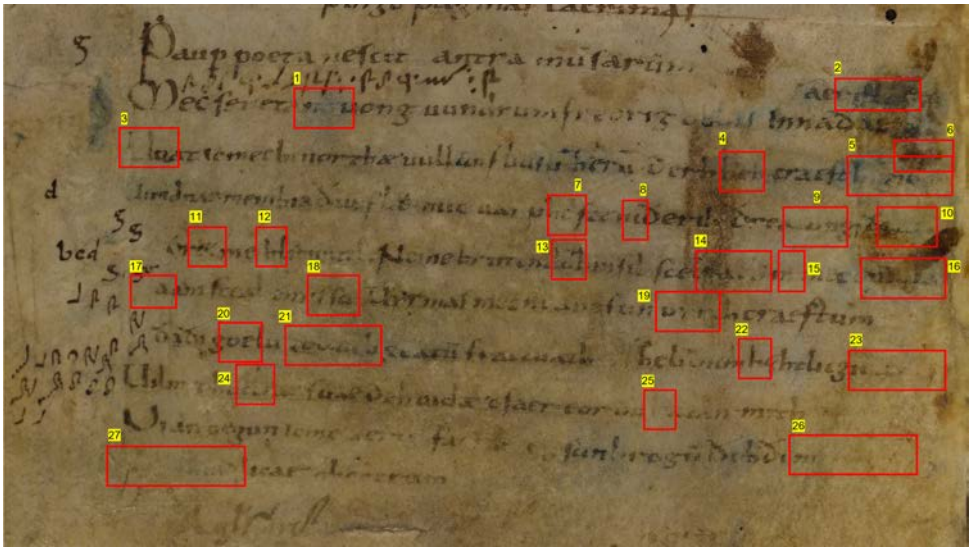

Figure B.1.: Areas of interest of the Leiden Riddle.

B.4. LEIDEN RIDDLE SAMPLING MASKS

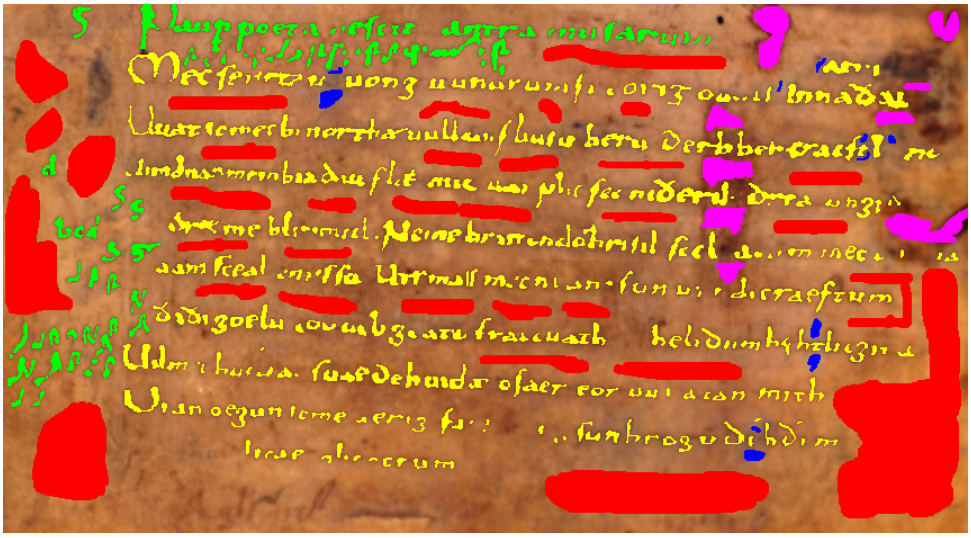

Figure B.2.: Leiden Riddle Sampling Mask 1.

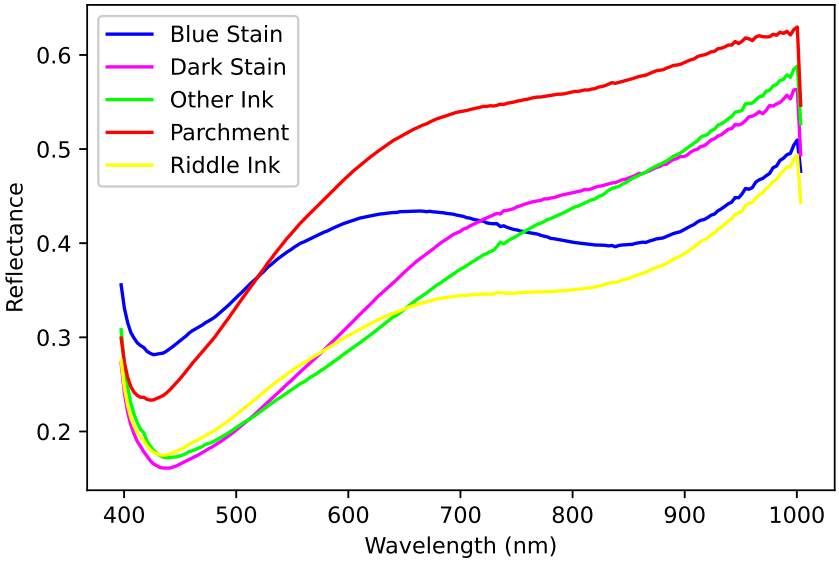

Figure B.3.: Leiden Riddle Sampling Mask 1 Class Average Spectra.

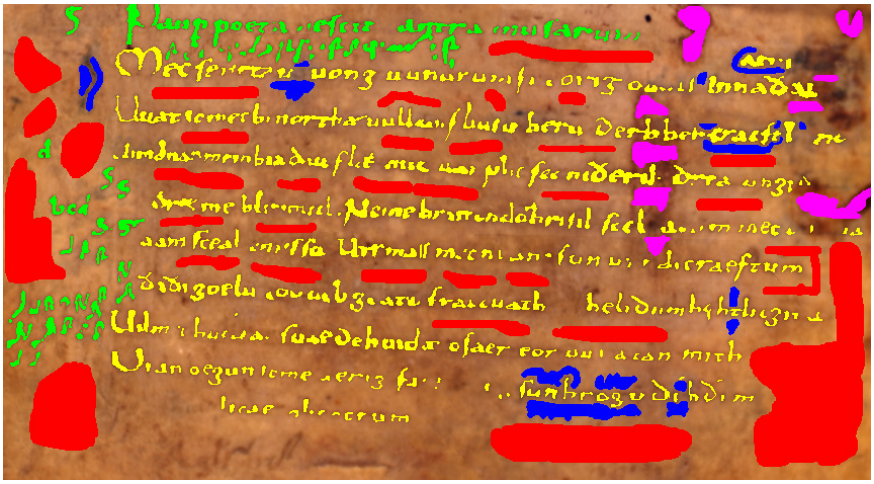

Figure B.4.: Leiden Riddle Sampling Mask 2.

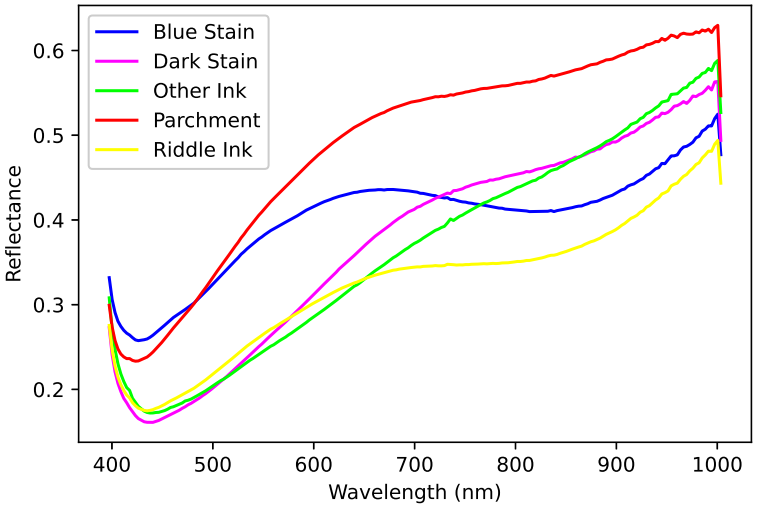

Figure B.5.: Leiden Riddle Sampling Mask 2 Class Average Spectra.

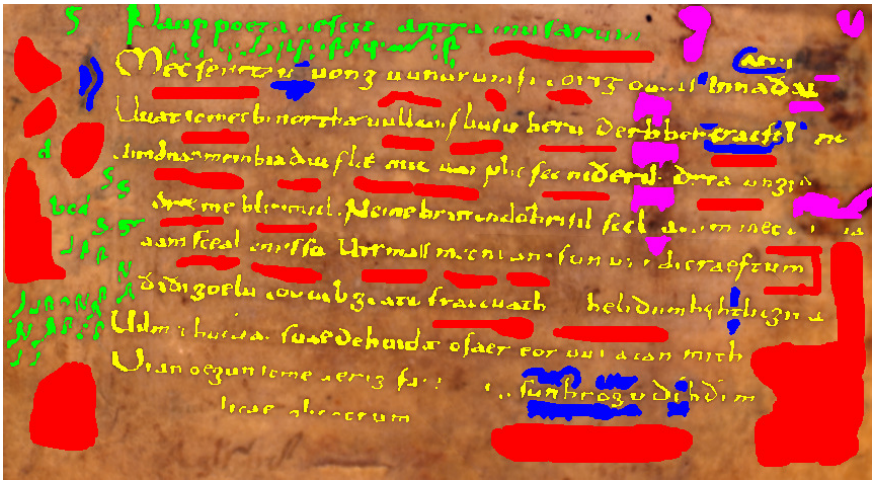

Figure B.6.: Leiden Riddle Sampling Mask 3.

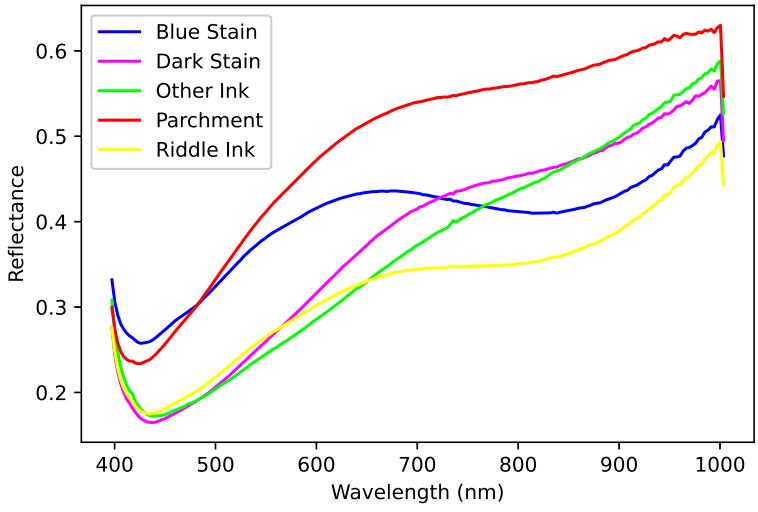

Figure B.7.: Leiden Riddle Sampling Mask 3 Class Average Spectra.

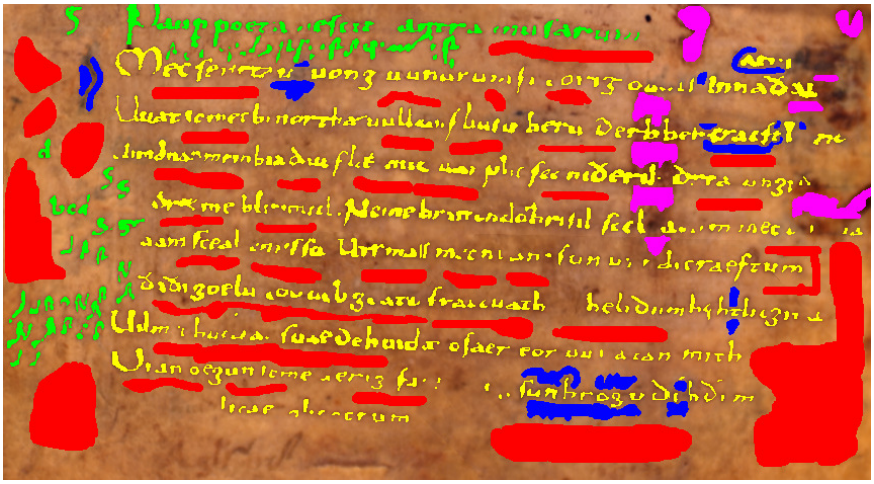

Figure B.8.: Leiden Riddle Sampling Mask 4.

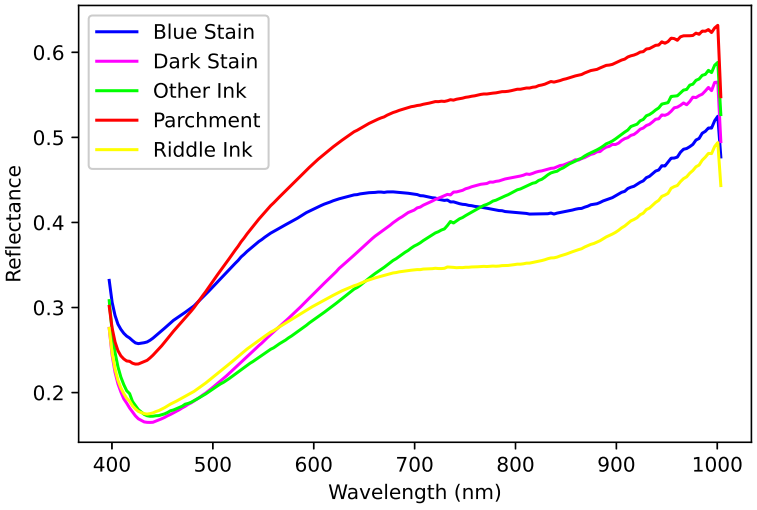

Figure B.9.: Leiden Riddle Sampling Mask 4 Class Average Spectra.

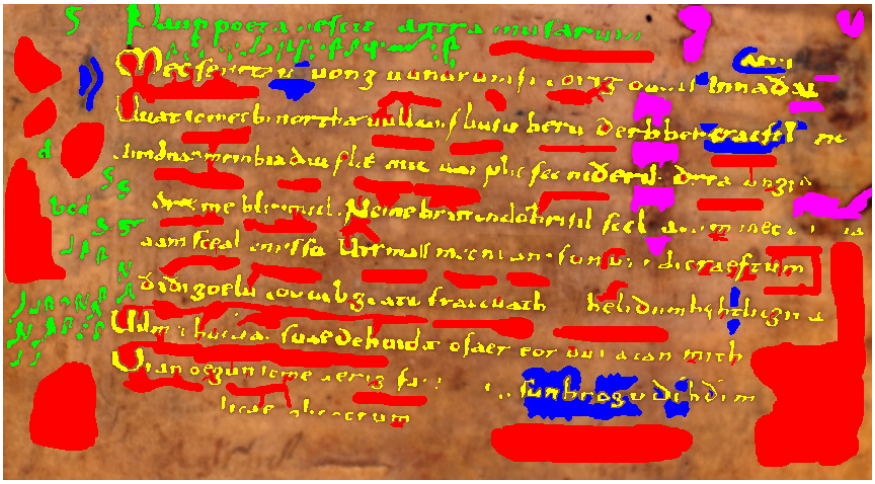

Figure B.10.: Leiden Riddle Sampling Mask 5.

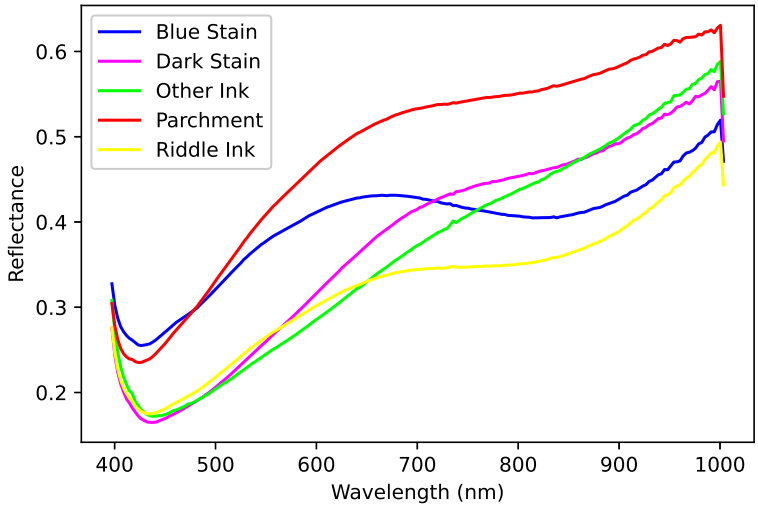

Figure B.11.: Leiden Riddle Sampling Mask 5 Class Average Spectra.

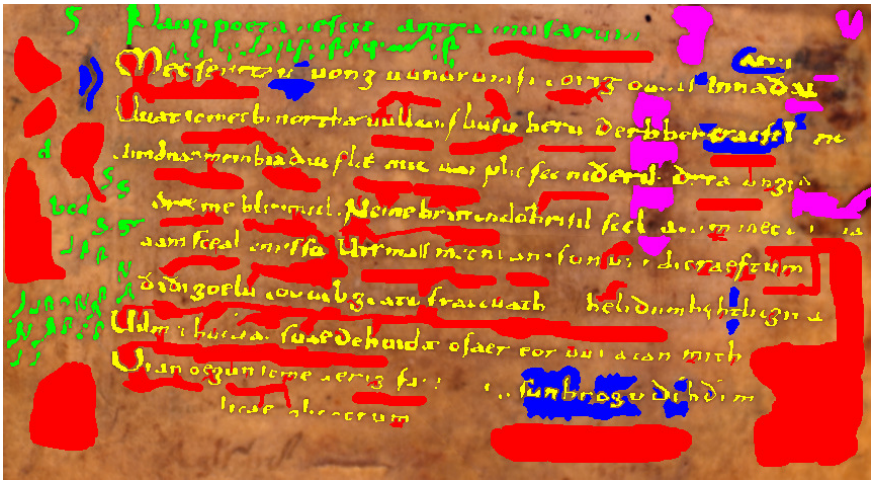

Figure B.12.: Leiden Riddle Sampling Mask 6.

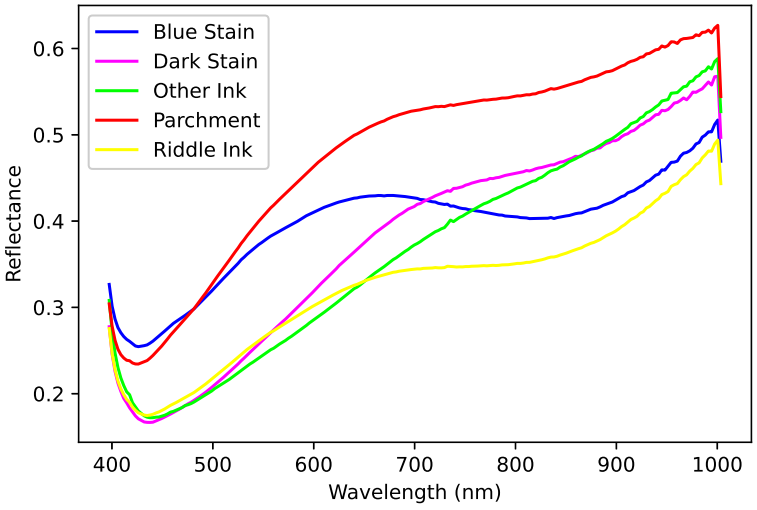

Figure B.13.: Leiden Riddle Sampling Mask 6 Class Average Spectra.

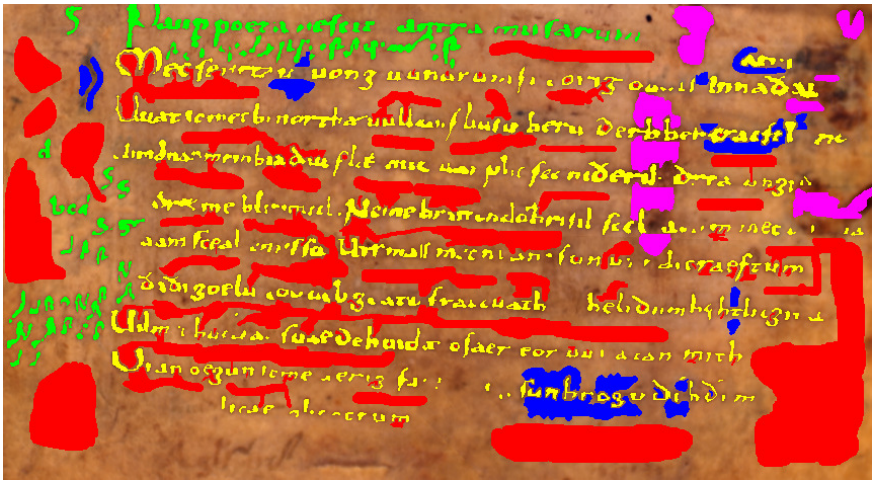

Figure B.14.: Leiden Riddle Sampling Mask 7.

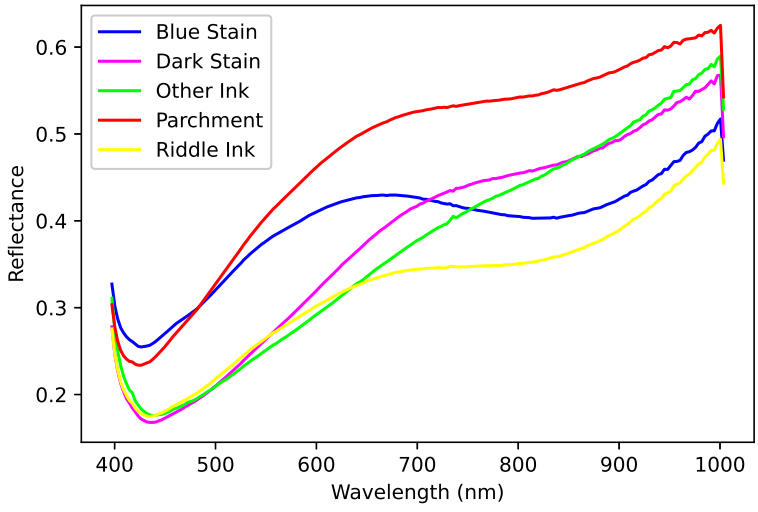

Figure B.15.: Leiden Riddle Sampling Mask 7 Class Average Spectra.

B.5. LEIDEN RIDDLE LOCAL SHAP MAPS

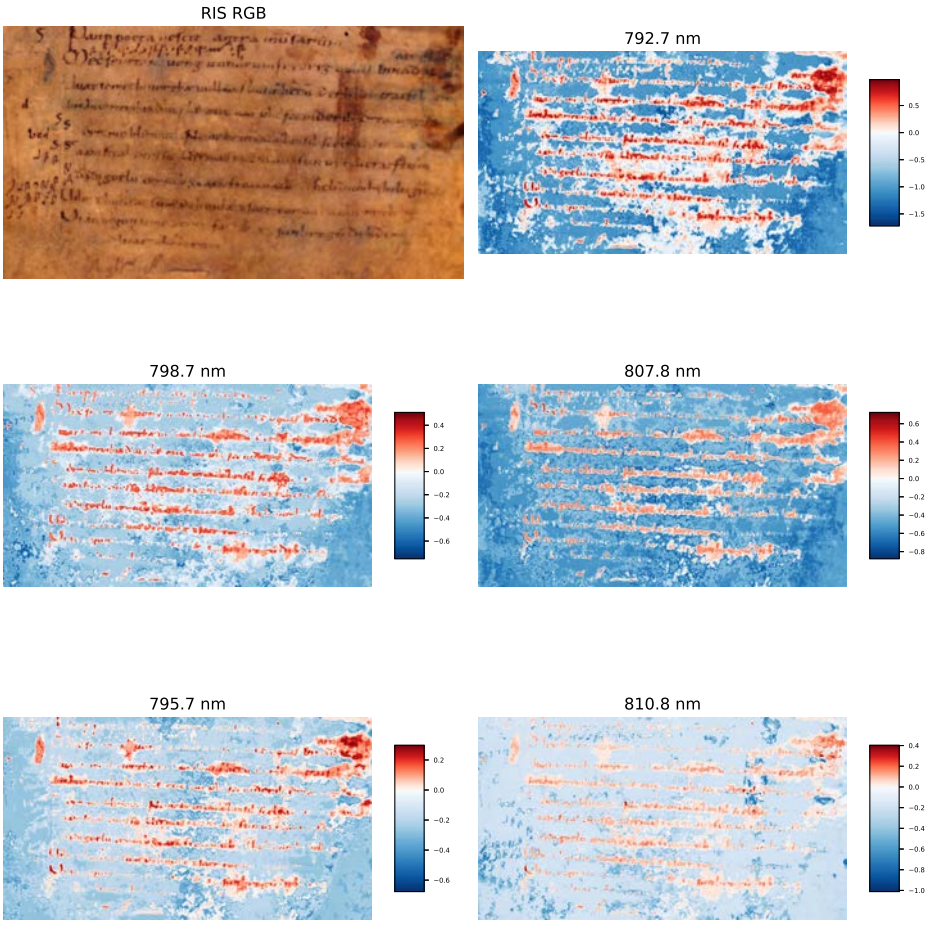

Figure B.16.: Lieden Riddle Local SHAP Maps 1-5.

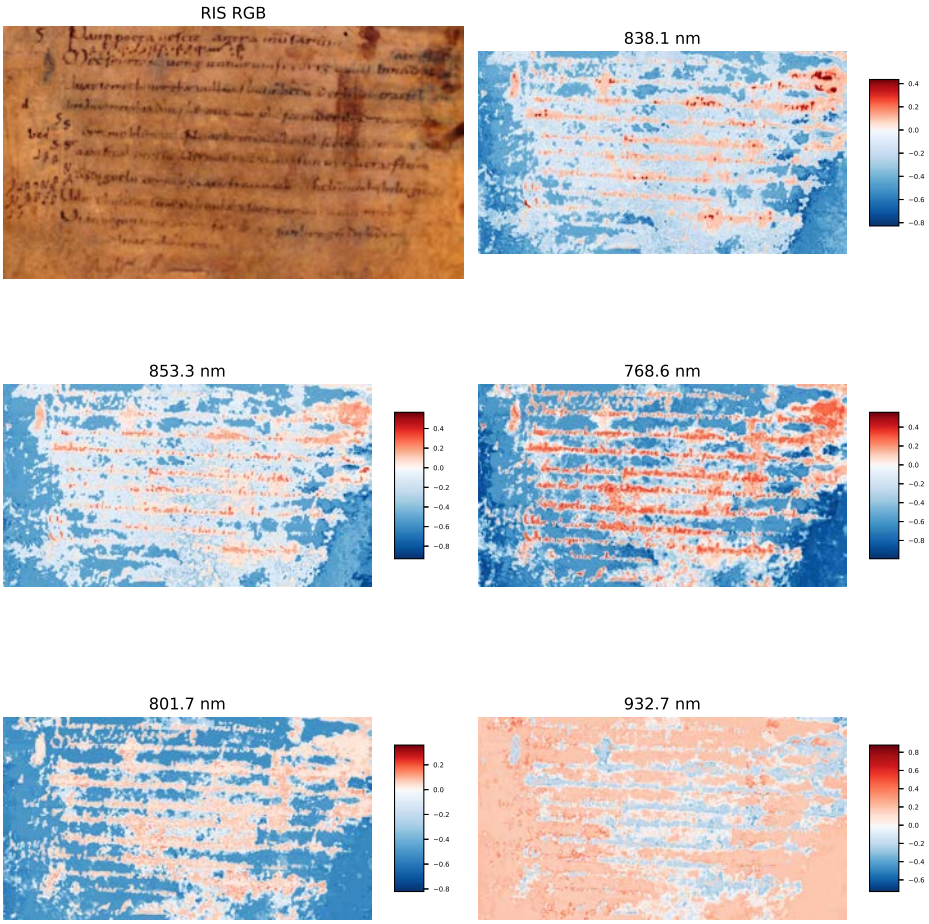

Figure B.17.: Lieden Riddle Local SHAP Maps 6-10.

B.6. LOCKE CONSTITUTION SAMPLING MASKS

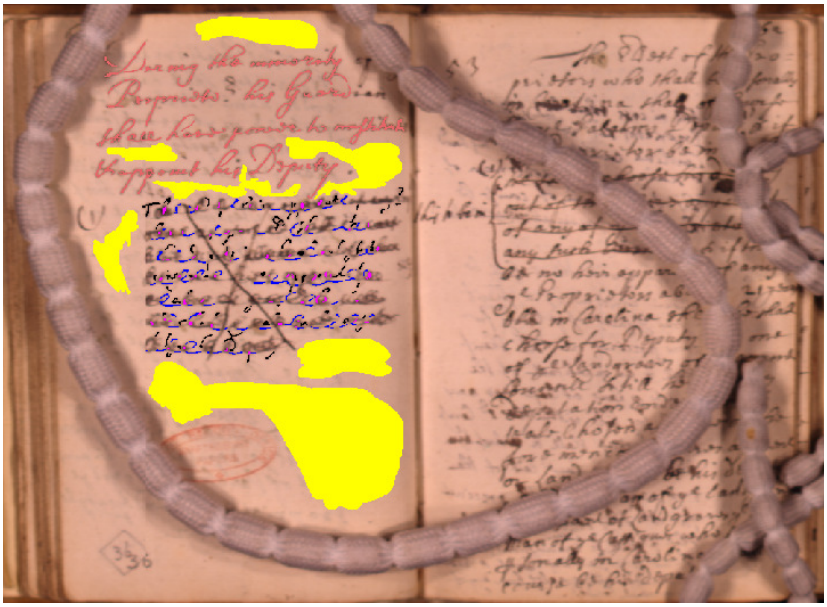

Figure B.18.: Locke Constitution Sampling Mask 1.

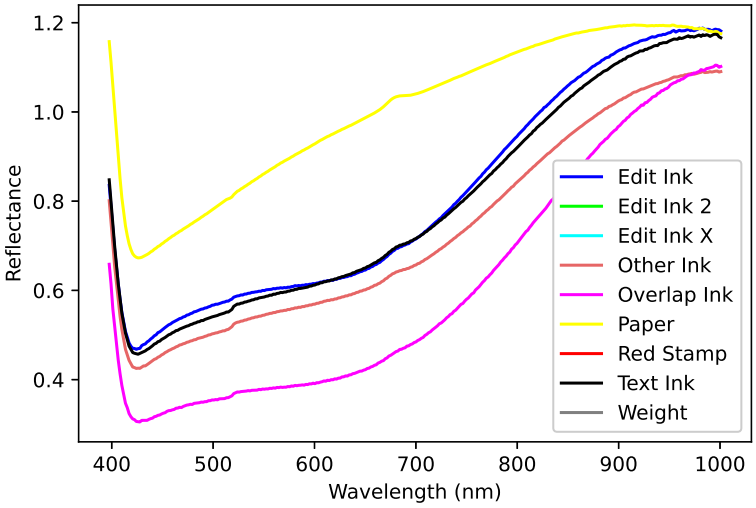

Figure B.19.: Locke Constitution Sampling Mask 1 Class Average Spectra.

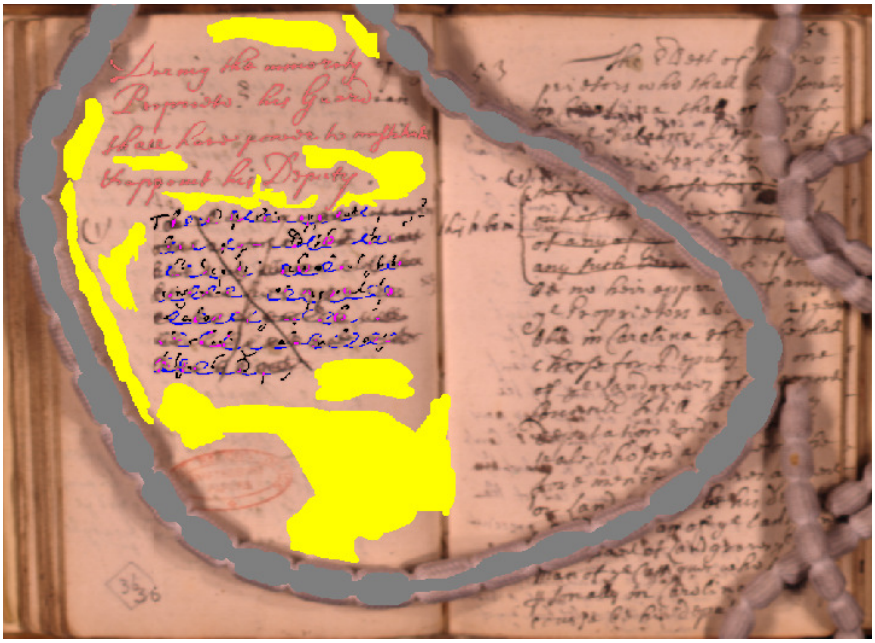

Figure B.20.: Locke Constitution Sampling Mask 2.

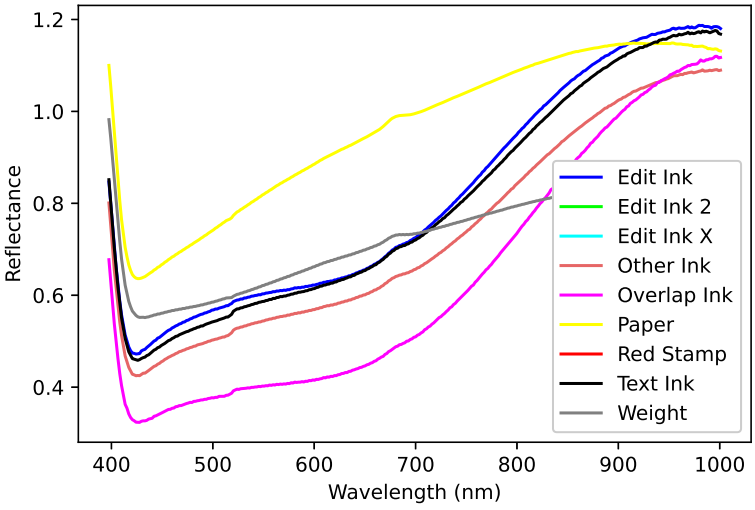

Figure B.21.: Locke Constitution Sampling Mask 2 Class Average Spectra.

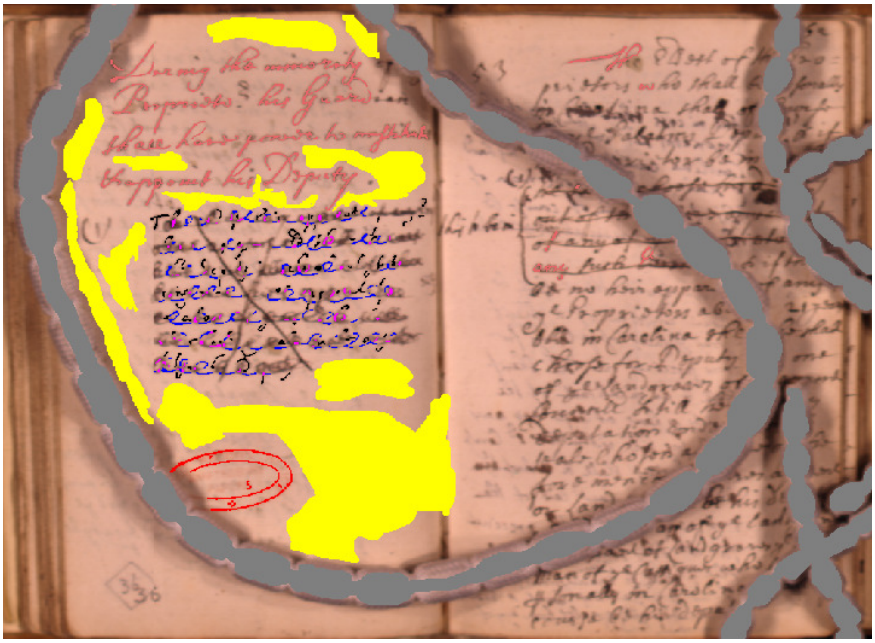

Figure B.22.: Locke Constitution Sampling Mask 3.

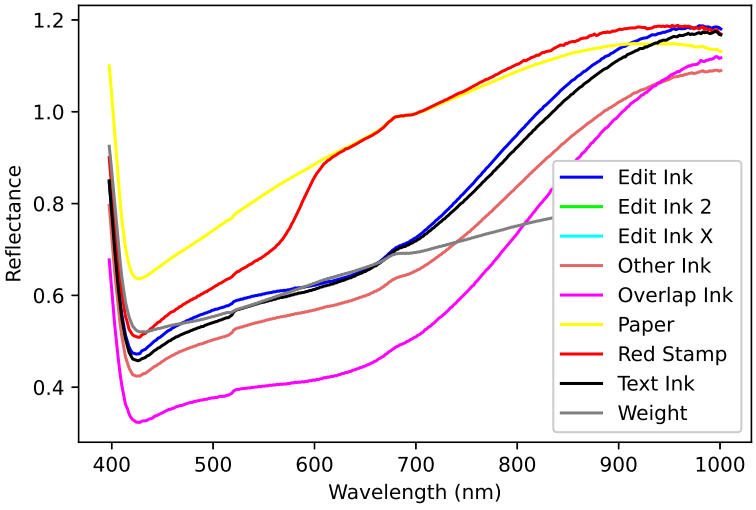

Figure B.23.: Locke Constitution Sampling Mask 3 Class Average Spectra.

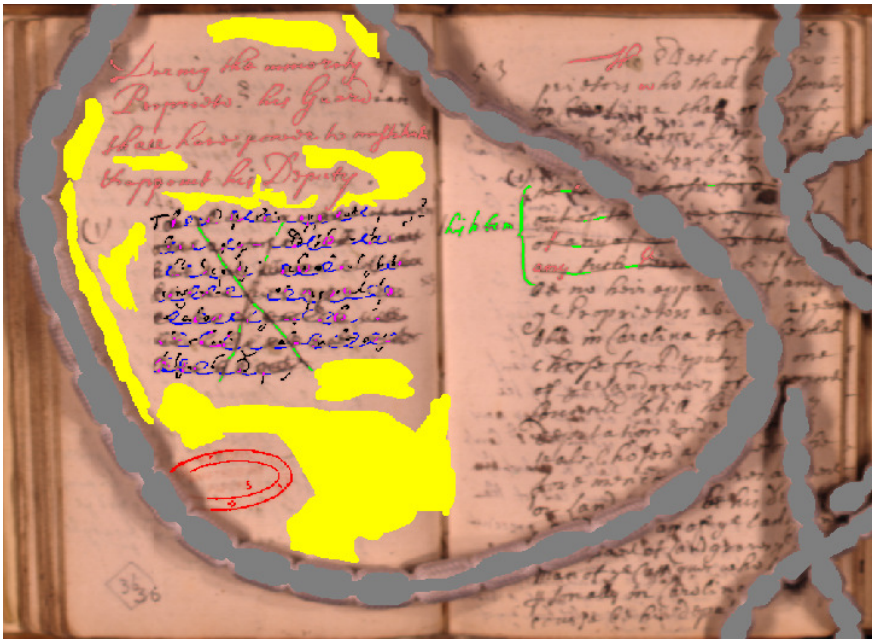

Figure B.24.: Locke Constitution Sampling Mask 4.

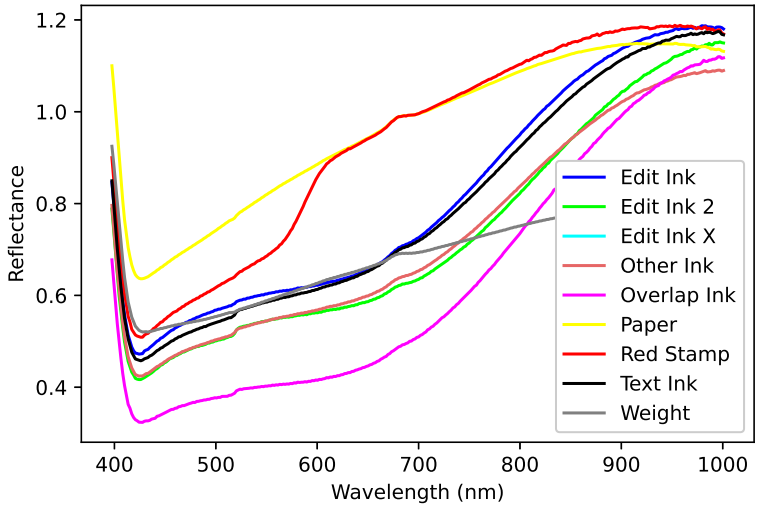

Figure B.25.: Locke Constitution Sampling Mask 4 Class Average Spectra.

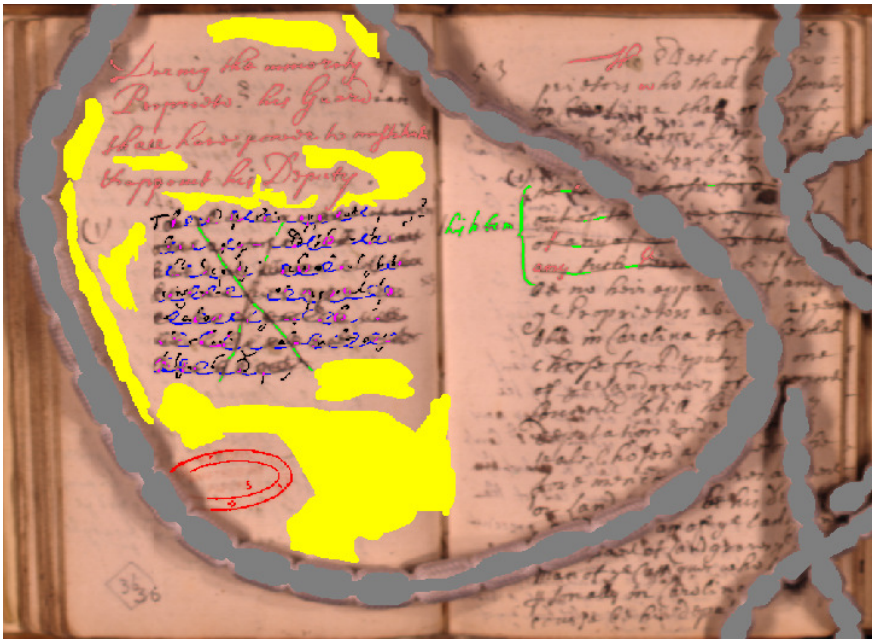

Figure B.26.: Locke Constitution Sampling Mask 5.

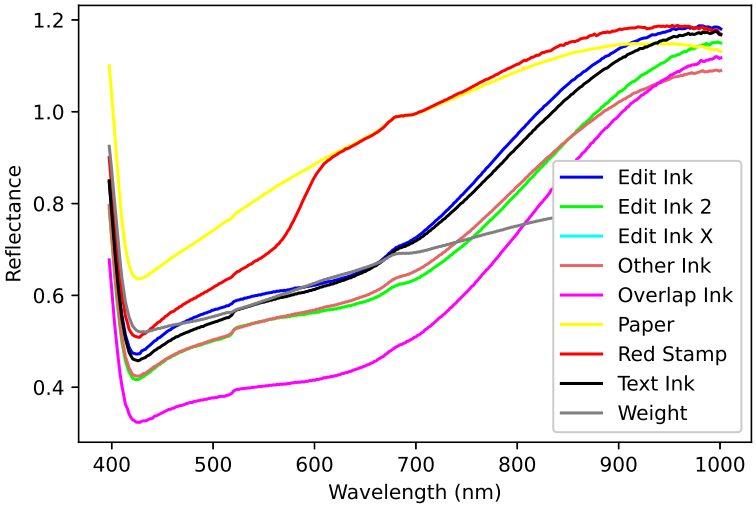

Figure B.27.: Locke Constitution Sampling Mask 5 Class Average Spectra.

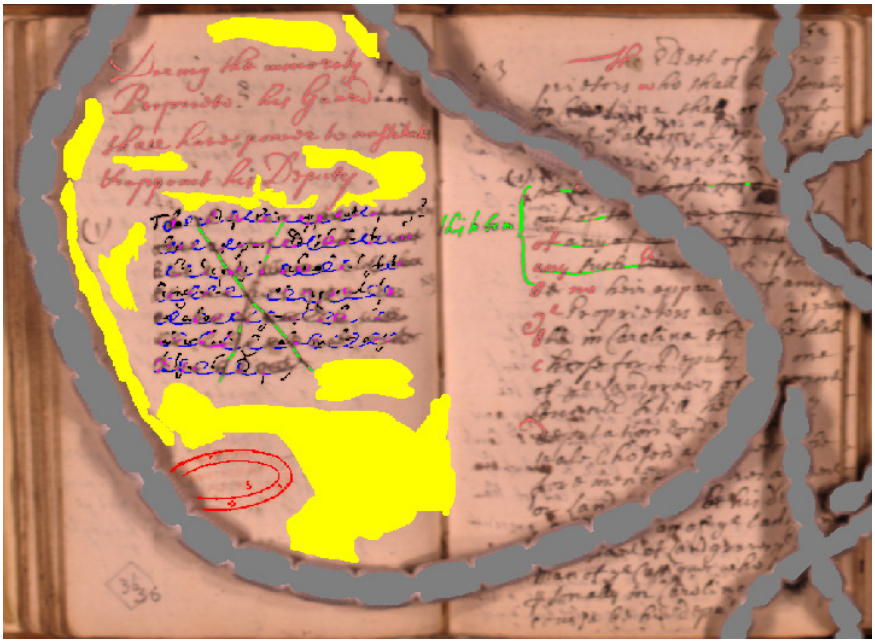

Figure B.28.: Locke Constitution Sampling Mask 6.

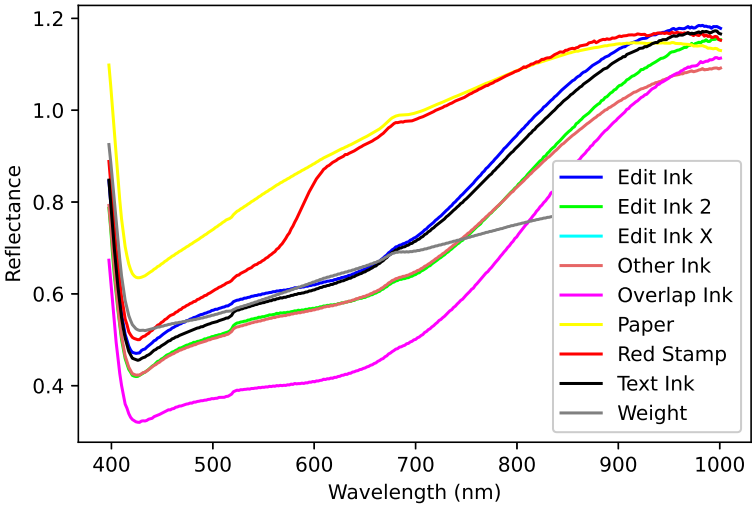

Figure B.29.: Locke Constitution Sampling Mask 6 Class Average Spectra.

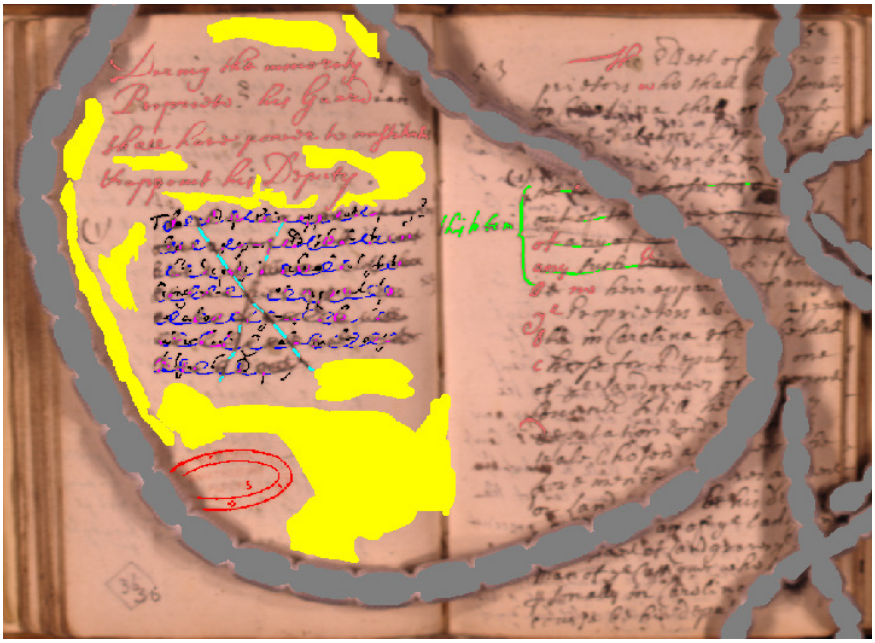

Figure B.30.: Locke Constitution Sampling Mask 7.

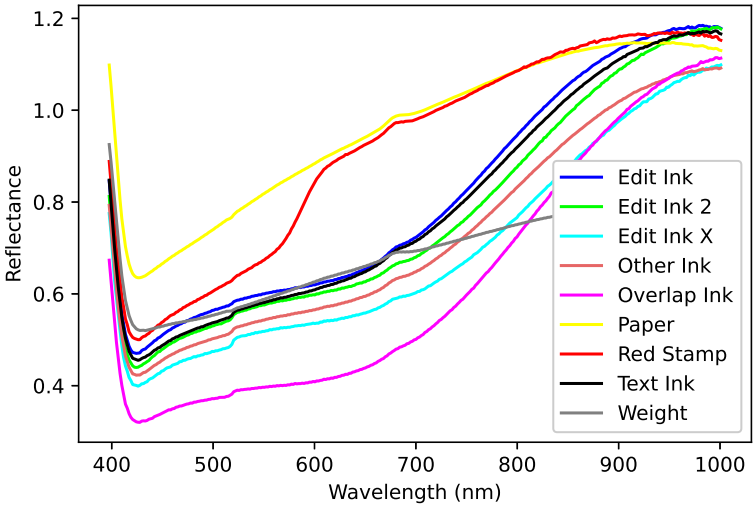

Figure B.31.: Locke Constitution Sampling Mask 7 Class Average Spectra.

B.7. LOCKE CONSTITUTION LOCAL SHAP MAPS

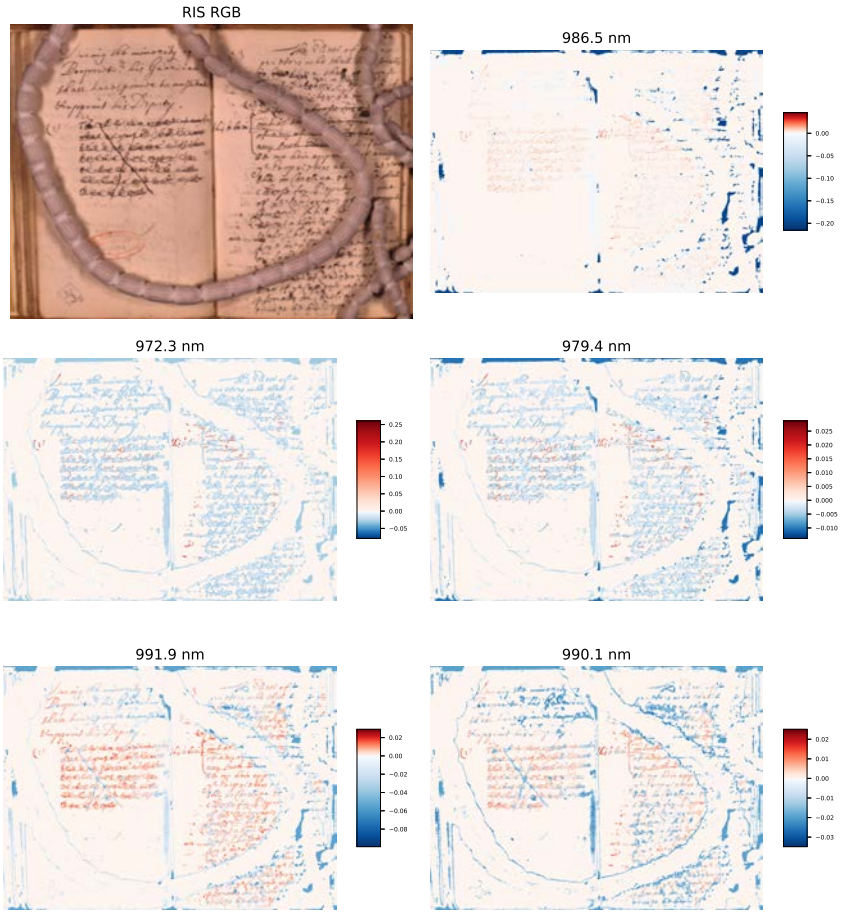

Figure B.32.: Locke Constitution Local SHAP Maps 1-5.

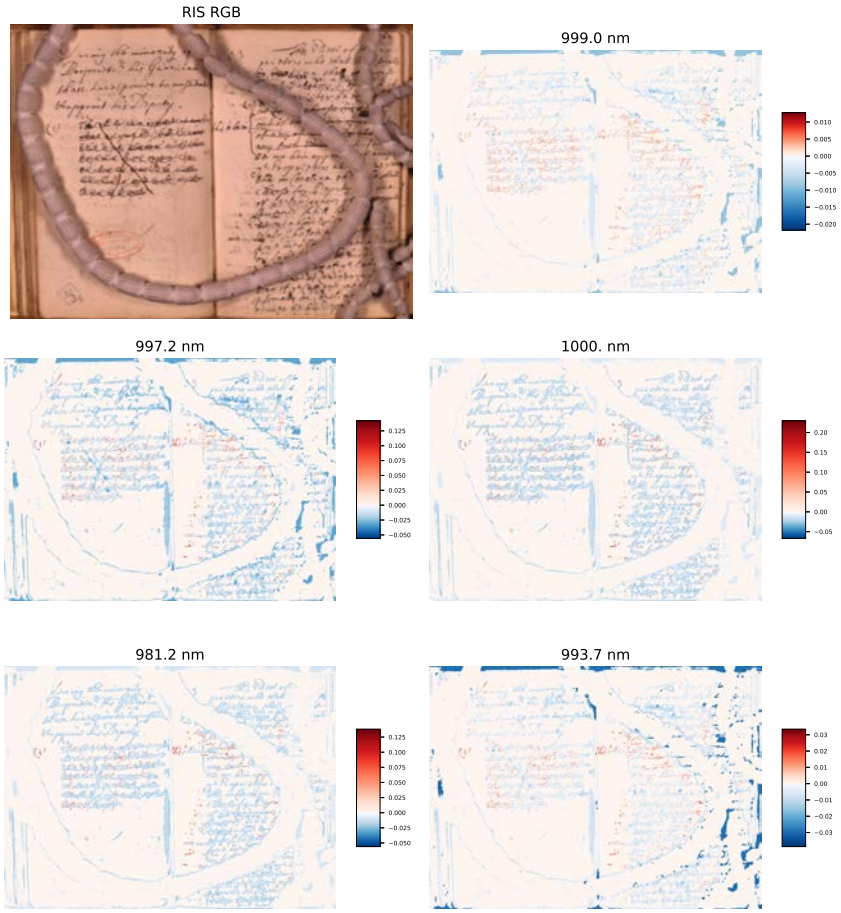

Figure B.33.: Locke Constitution Local SHAP Maps 6-10.

B.8. LOCKE CONSTITUTION SHAP SPECTRA

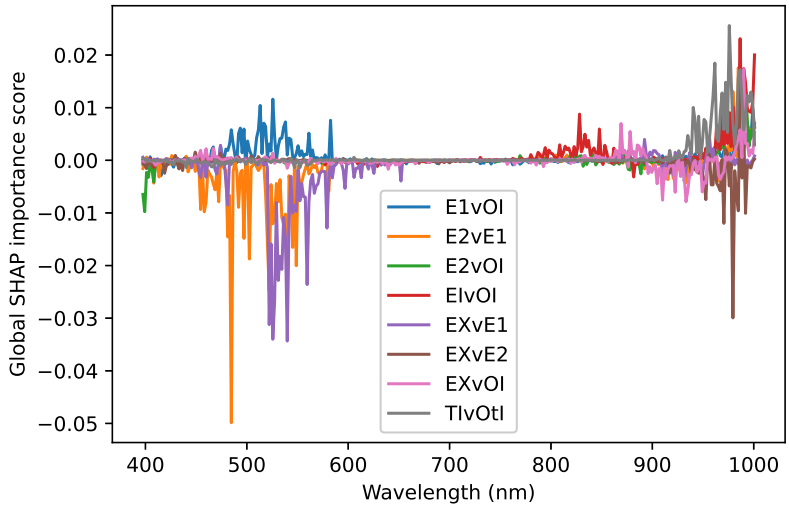

Figure B.34.: SHAP spectra for classifiers distinguishing between the different ink classes of the Locke Constitution: Edit Ink 1 (E1), Edit Ink 2 (E2), Edit Ink X (EX), Original Ink (OI), Edit Inks (EI), Text Inks (TI), and Other Inks (OtI).

C

Appendix C: Supplementary information for chapter 5

C.1. MA-XRF SIMULATION MAPS

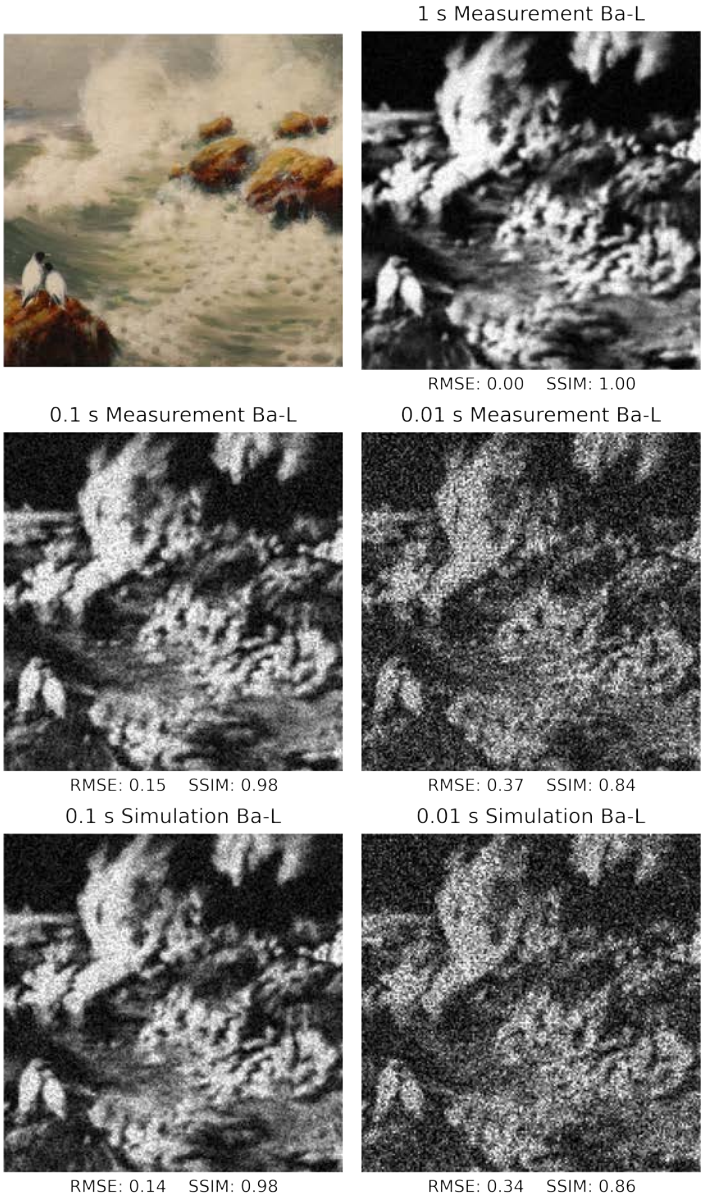

Figure C.1.: Comparison of Ba-L maps from real MA-XRF scans and simulated MA-XRF scans and the calculated RMSE and SSIM values.

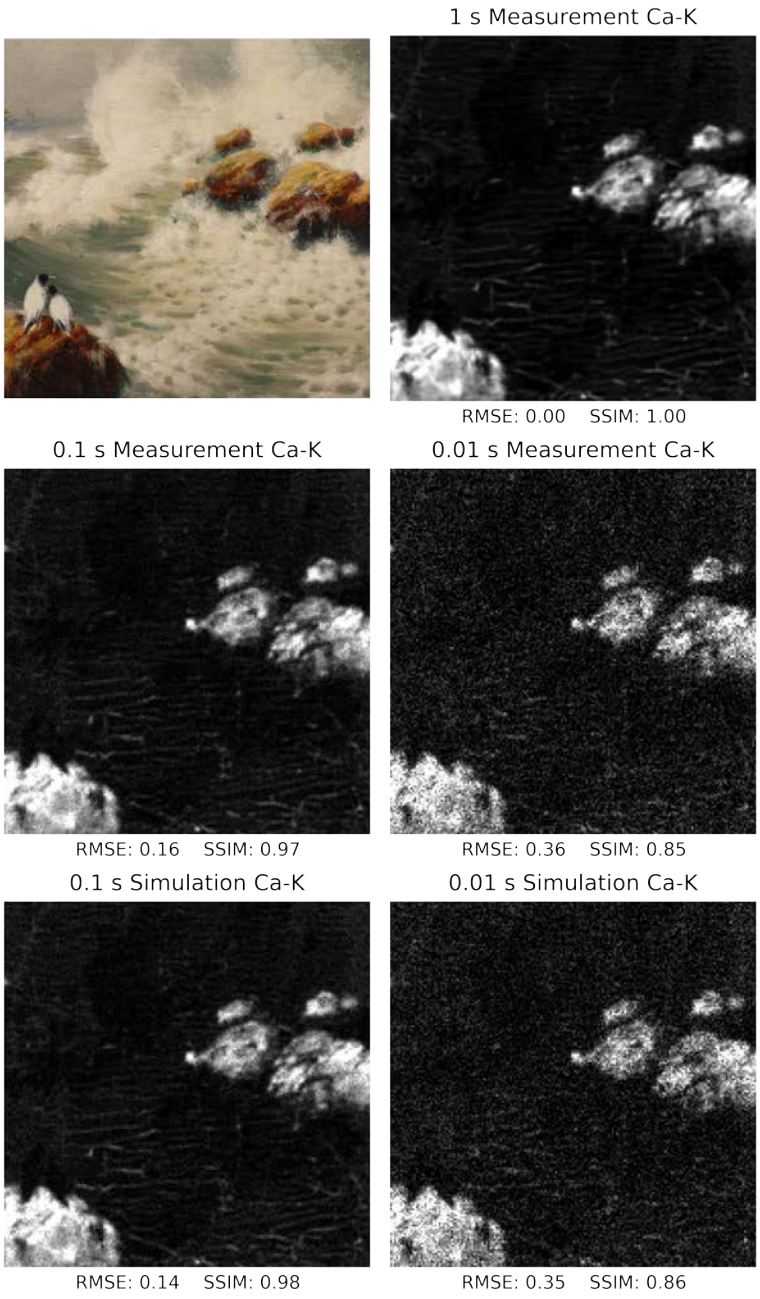

Figure C.2.: Comparison of Ca-K maps from real MA-XRF scans and simulated MA-XRF scans and the calculated RMSE and SSIM values.

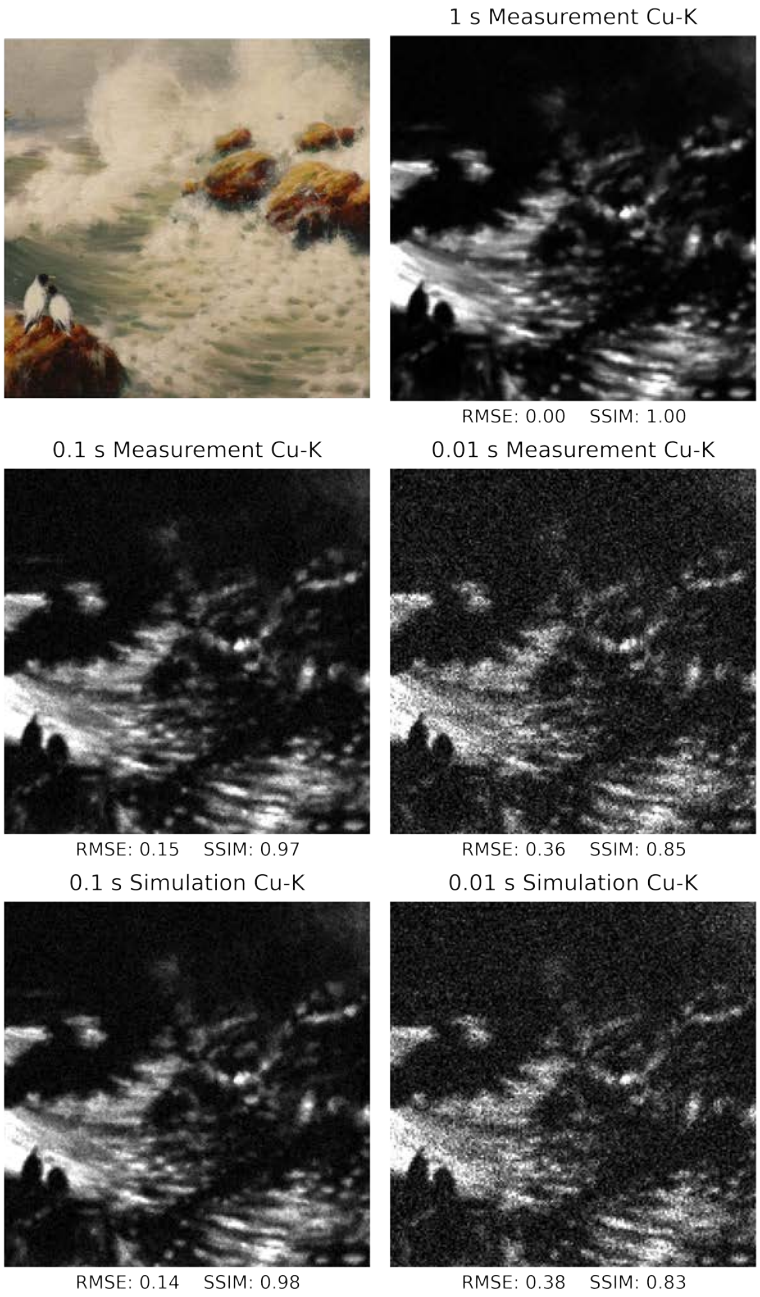

Figure C.3.: Comparison of Cu-K maps from real MA-XRF scans and simulated MA-XRF scans and the calculated RMSE and SSIM values.

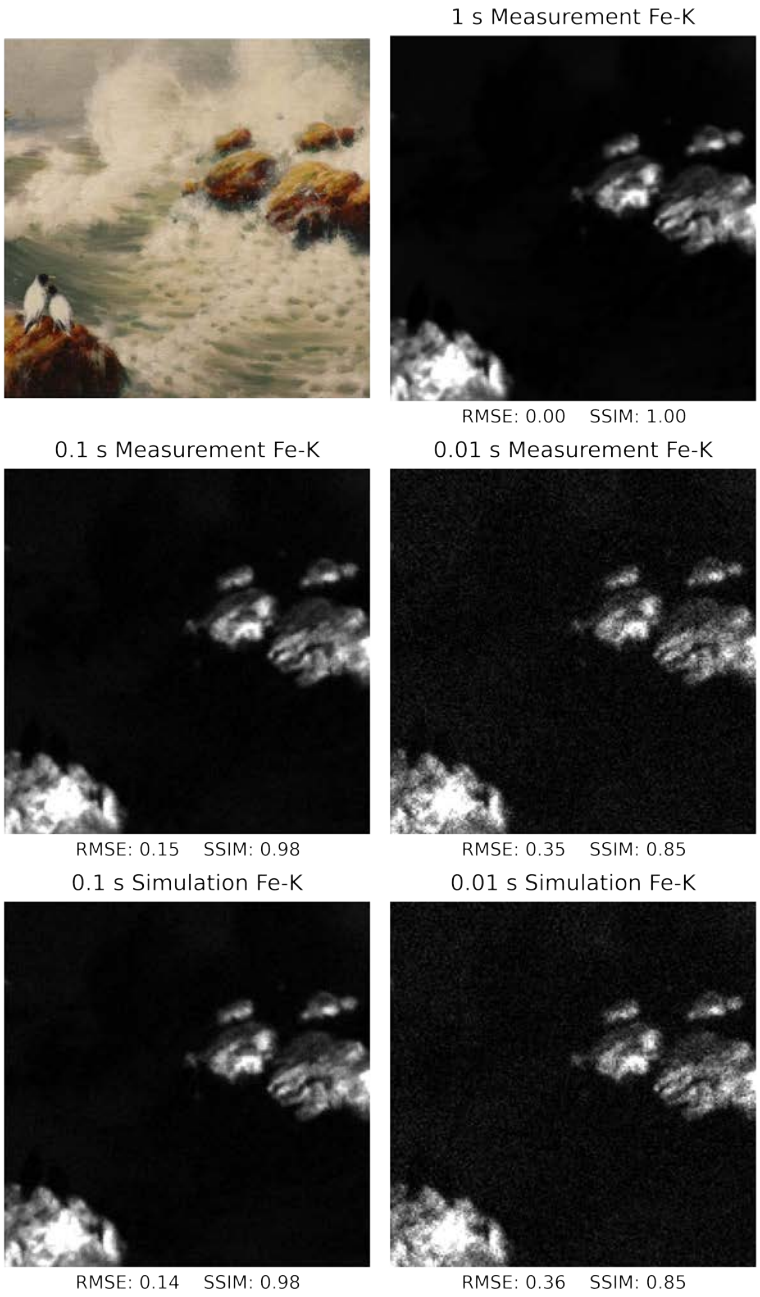

Figure C.4.: Comparison of Fe-K maps from real MA-XRF scans and simulated MA-XRF scans and the calculated RMSE and SSIM values.

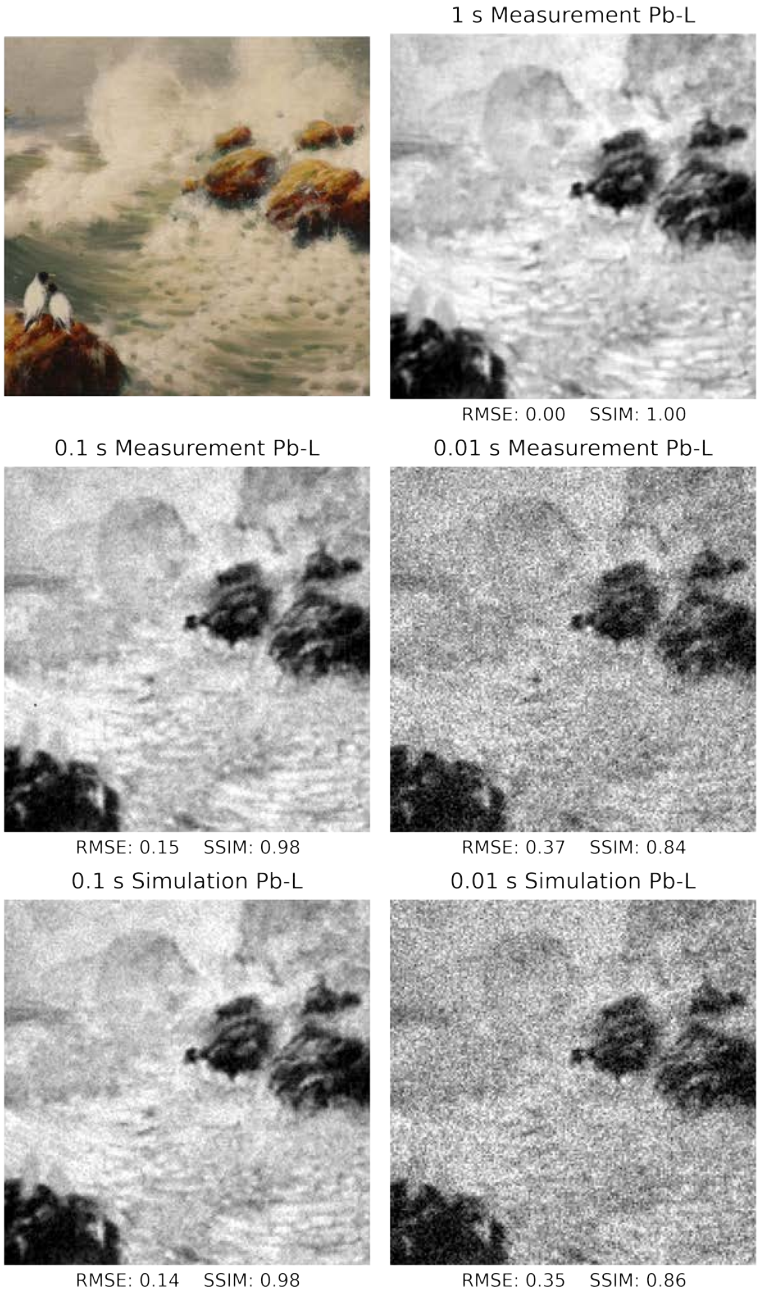

Figure C.5.: Comparison of Pb-L maps from real MA-XRF scans and simulated MA-XRF scans and the calculated RMSE and SSIM values.

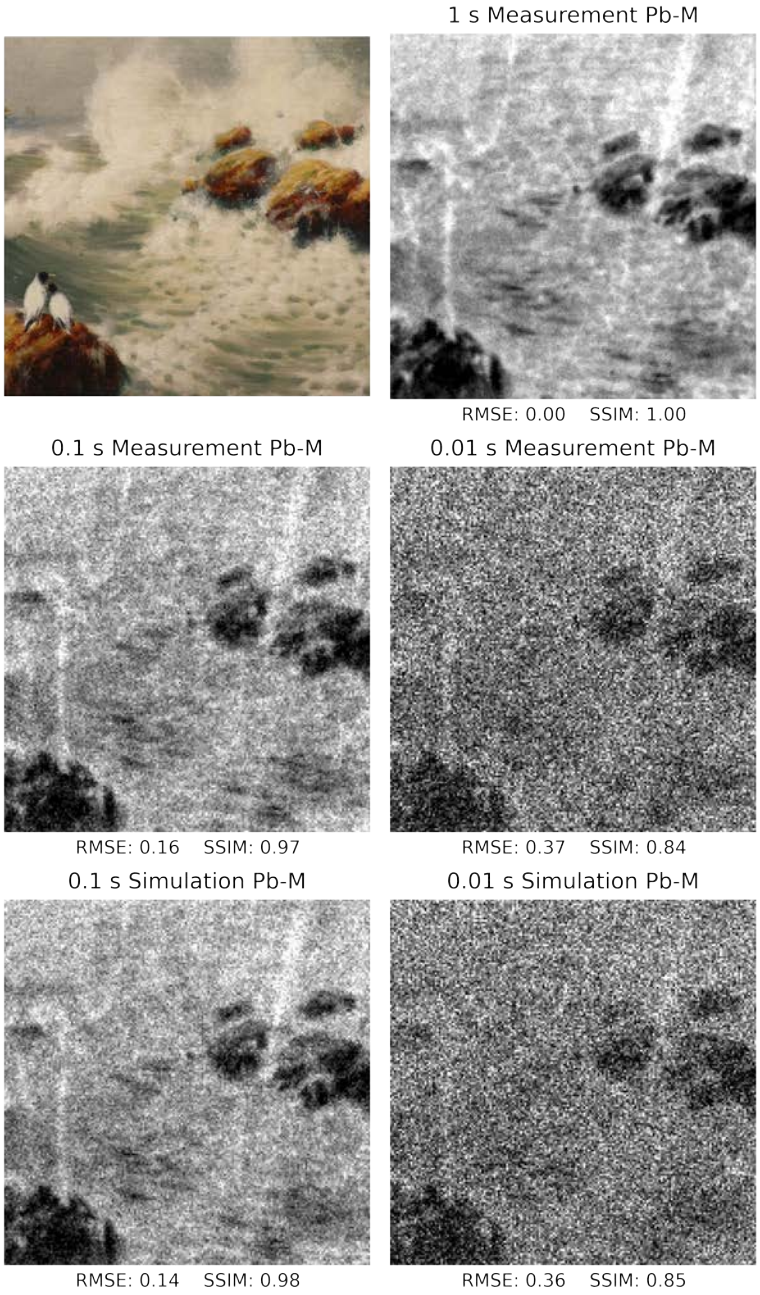

Figure C.6.: Comparison of Pb-M maps from real MA-XRF scans and simulated MA-XRF scans and the calculated RMSE and SSIM values.

C.2. FAST SIMULATION PARAMETERS

Table C.1.: FAST hyperparameters tested in simulations. All combinations between all values within each row were tested.

b	b_0	T_{a0}	Element fluorescence line selection
200 400	200 400	0.05 0.1	1 (Ca-K, Fe-K, Cu-K, Zn-K, Ba-L, Pb-L, Pb-M) 2 (Ca-K, Fe-K, Cu-K, Zn-K, Ba-L, Pb-L) 3 (Ca-K, Fe-K, Cu-K, Zn-K, Ba-L, Pb-M) 4 (Ca-K, Cu-K, Zn-K, Ba-L, Pb-L, Pb-M) 5 (Fe-K, Cu-K, Zn-K, Ba-L, Pb-L, Pb-M) 6 (Ca-K, Cu-K, Zn-K, Ba-L, Pb-L, Pb-M) 7 (Ca-K, Fe-K, Cu-K, Zn-K, Pb-L) 8 (Fe-K, Cu-K, Zn-K, Ba-L, Pb-L) 9 (Fe-K, Cu-K, Zn-K, Pb-L)
300 350 400 450 500 550	400	0.01 0.05 0.1 0.2 0.3	1 (Ca-K, Fe-K, Cu-K, Zn-K, Ba-L, Pb-L, Pb-M)

C.3. CHOPP SIMULATION PARAMETERS

Table C.2.: Chopp hyperparameters tested in simulations. All combinations between all values within each row were tested.

T_{a0}	τ	Element fluorescence line selection
0.001 0.003	100 500 1000	1 (Ca-K, Fe-K, Cu-K, Zn-K, Ba-L, Pb-L, Pb-M) 2 (Ca-K, Fe-K, Cu-K, Zn-K, Ba-L, Pb-L) 3 (Ca-K, Fe-K, Cu-K, Zn-K, Ba-L, Pb-M) 4 (Ca-K, Cu-K, Zn-K, Ba-L, Pb-L, Pb-M) 5 (Fe-K, Cu-K, Zn-K, Ba-L, Pb-L, Pb-M) 6 (Ca-K, Cu-K, Zn-K, Ba-L, Pb-L, Pb-M) 7 (Ca-K, Fe-K, Cu-K, Zn-K, Pb-L) 8 (Fe-K, Cu-K, Zn-K, Ba-L, Pb-L) 9 (Fe-K, Cu-K, Zn-K, Pb-L)
0.001 0.003 0.005 0.01	500	1 (Ca-K, Fe-K, Cu-K, Zn-K, Ba-L, Pb-L, Pb-M)
0.001 0.003 0.005 0.008 0.01 0.03	1640	1 (Ca-K, Fe-K, Cu-K, Zn-K, Ba-L, Pb-L, Pb-M)
0.001 0.003	100	1 (Ca-K, Fe-K, Cu-K, Zn-K, Ba-L, Pb-L, Pb-M)
0.001 0.003 0.005	200 300 400 500 600 700 800 900 1000 1100 1200	1 (Ca-K, Fe-K, Cu-K, Zn-K, Ba-L, Pb-L, Pb-M)

Table C.3.: cont. Chopp hyperparameters tested in simulations. All combinations between all values within each row were tested.

T_{a0}	τ	Element fluorescence line selection
0.001 0.003 0.005	1300 1400 1500 1600 1700 1800	1 (Ca-K, Fe-K, Cu-K, Zn-K, Ba-L, Pb-L, Pb-M)
0.003	2000 2500 3000 4000 5000 8000 10000 12000 15000 18000 20000 25000 30000 35000	1 (Ca-K, Fe-K, Cu-K, Zn-K, Ba-L, Pb-L, Pb-M)

C.4. ACCELERATED MA-XRF MAPS

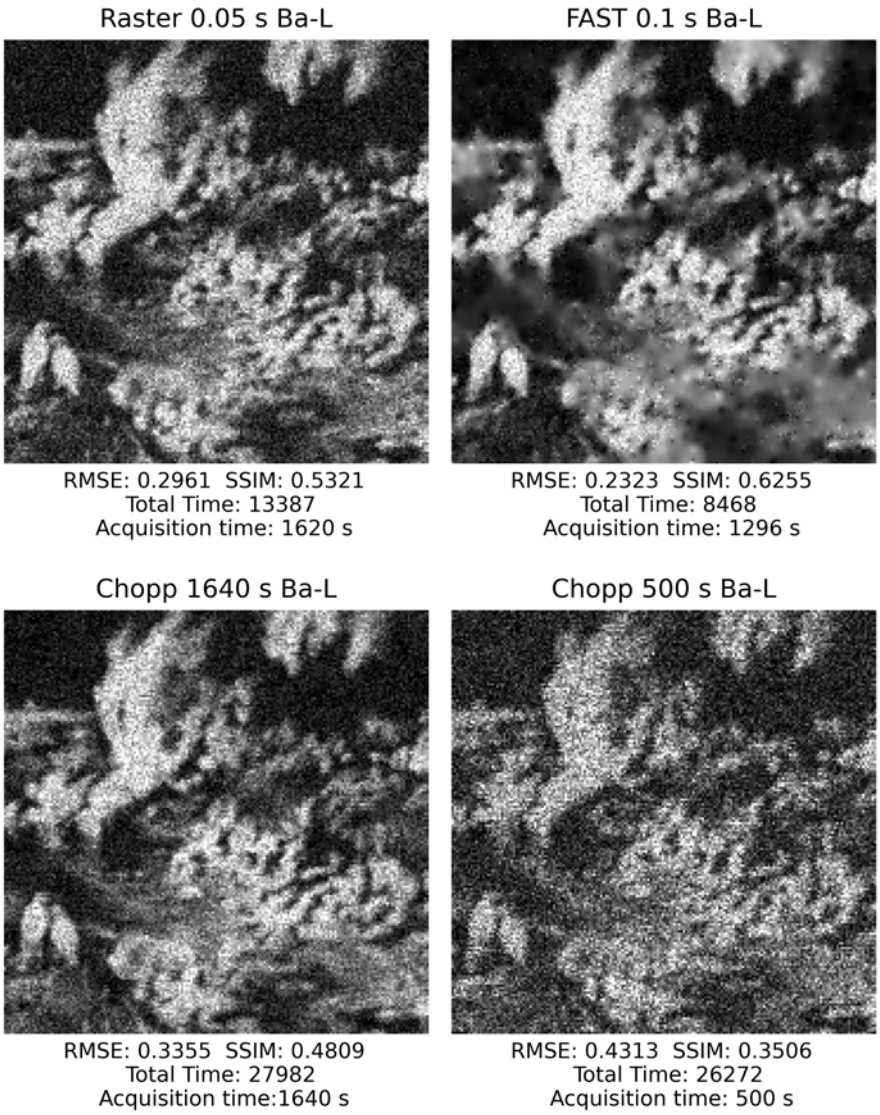

Figure C.7.: Resulting Ba-L maps of a t_a =50 ms uniform raster scan, a τ =1640 s Chopp scan, a τ =500 s Chopp scan and a FAST scan, and the achieved RMSE and SSIM values for each.

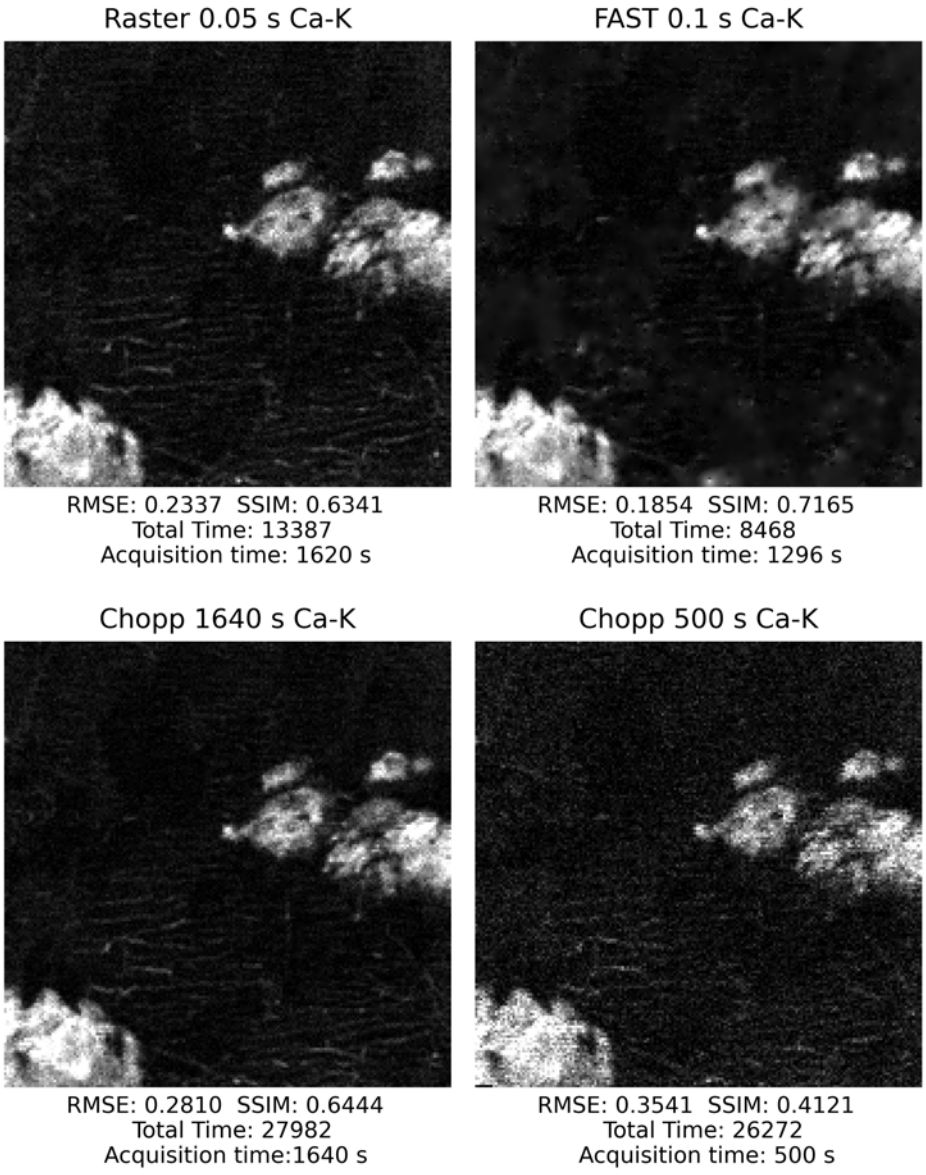

Figure C.8.: Resulting Ca-K maps of a t_a =50 ms uniform raster scan, a τ =1640 s Chopp scan, a τ =500 s Chopp scan and a FAST scan, and the achieved RMSE and SSIM values for each.

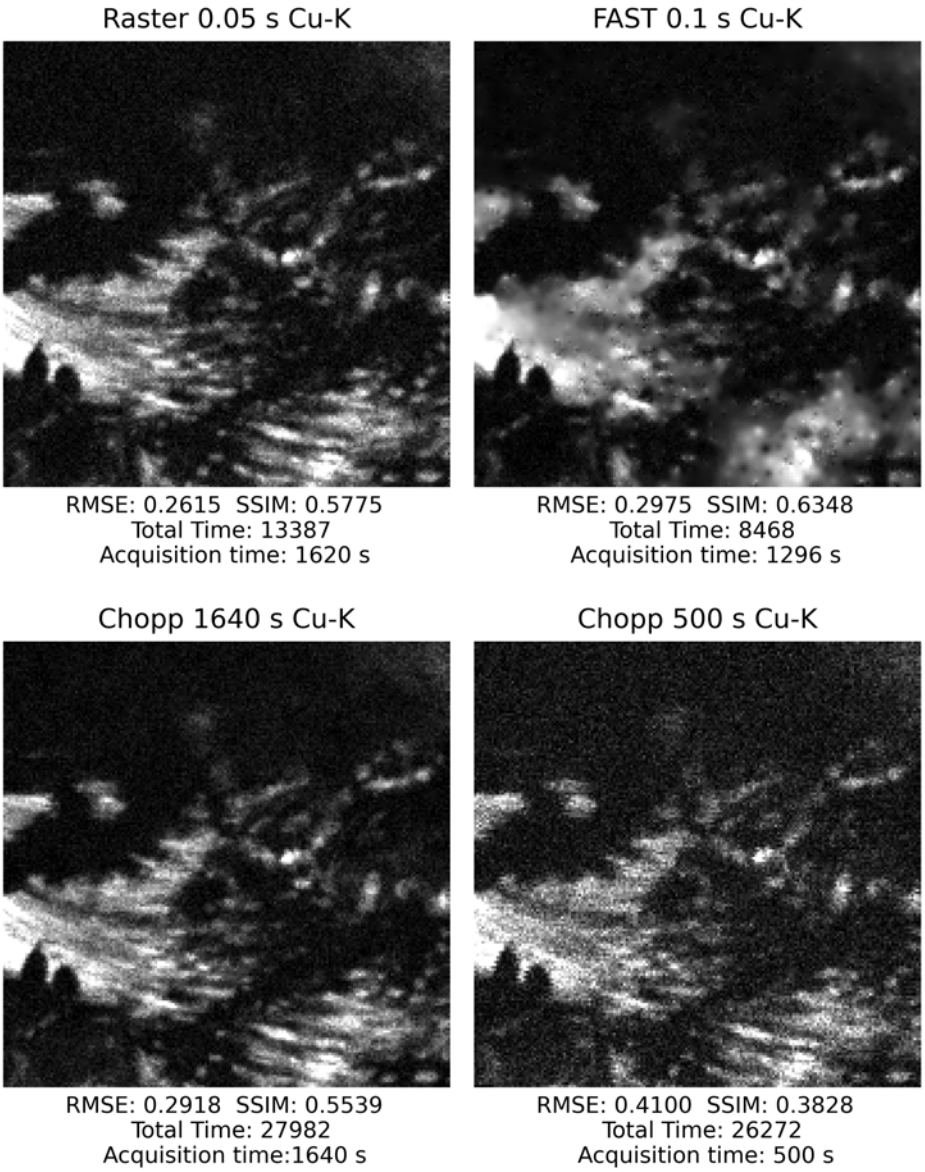

Figure C.9.: Resulting Cu-K maps of a t_a =50 ms uniform raster scan, a τ =1640 s Chopp scan, a τ =500 s Chopp scan and a FAST scan, and the achieved RMSE and SSIM values for each.

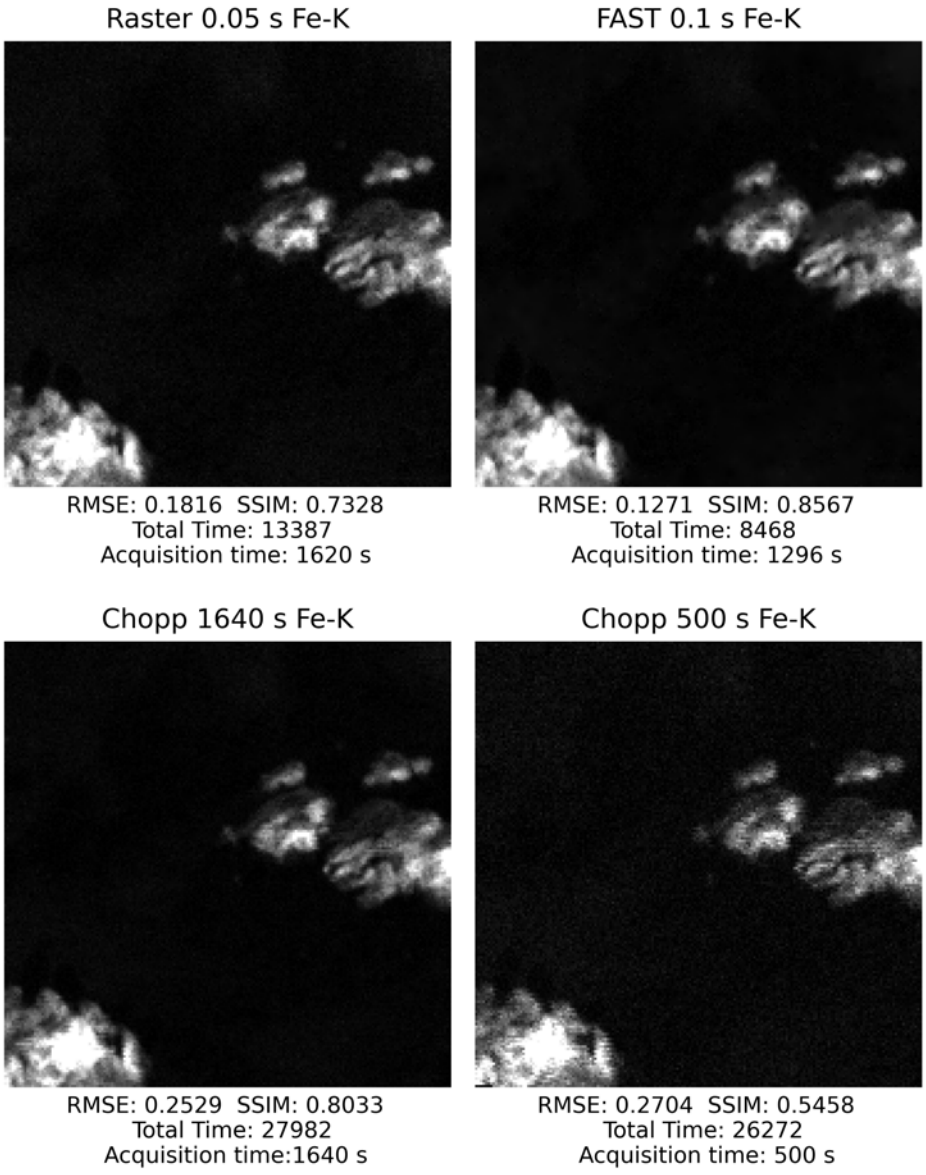

Figure C.10.: Resulting Fe-K maps of a t_a =50 ms uniform raster scan, a τ =1640 s Chopp scan, a τ =500 s Chopp scan and a FAST scan, and the achieved RMSE and SSIM values for each.

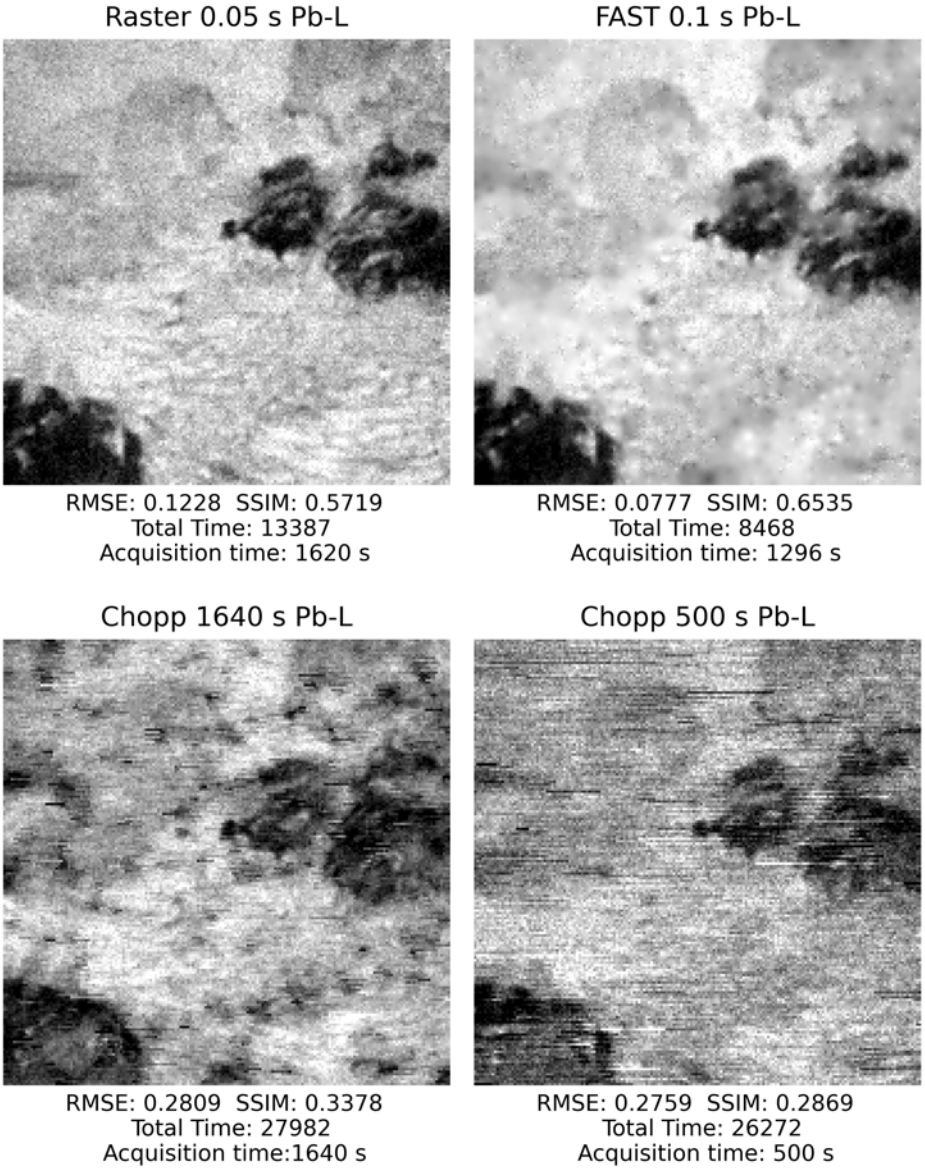

Figure C.11.: Resulting Pb-L maps of a t_a =50 ms uniform raster scan, a τ =1640 s Chopp scan, a τ =500 s Chopp scan and a FAST scan, and the achieved RMSE and SSIM values for each.

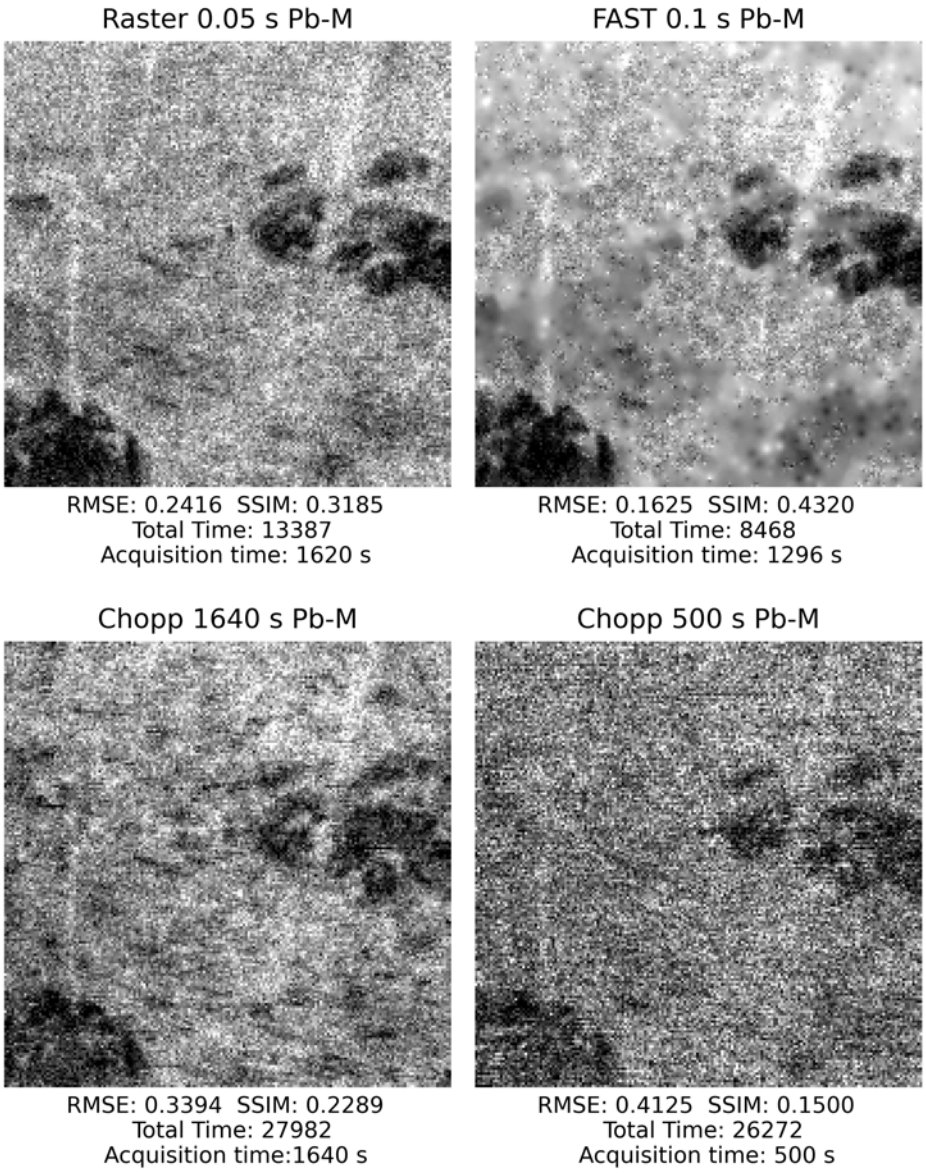

Figure C.12.: Resulting Pb-M maps of a t_a =50 ms uniform raster scan, a τ =1640 s Chopp scan, a τ =500 s Chopp scan and a FAST scan, and the achieved RMSE and SSIM values for each.

ACKNOWLEDGEMENTS

They say it takes a village to raise a child. Whilst I cannot personally attest to the accuracy of this, I can state in no uncertain terms that it certainly took a village to get through this PhD. So many people have contributed to this endeavour, in ways large or small, that it is difficult for me to remember them all. I must, however, still attempt to appropriately acknowledge all of them and can only apologize for those that may have slipped my mind when trying to recall the five years that it took to finish this project.

Firstly, I would like to thank my supervisors, in a completely arbitrary order, without whom I would have never been able to start, much less finish, this PhD. Dr. Matthias Alfeld has been a constant guide and inspiration for me since I started in this field. His flexibility when dealing with my somewhat chaotic way of thinking was, and is, greatly appreciated. Our many conversations on a diverse range of topics were always a welcome reminder that there is life beyond the PhD and that things are often not as bad as I may think. Dr. Raf Van de Plas' insight and advice was always pointed and valuable. Your easygoing and humorous approach always provided levity to what were, for me, at times difficult meetings. Prof. Joris Dik was the one who first introduced me to the field of cultural heritage science through what I know consider a very funny story. A vague course name, me forgetting to send Joris an e-mail, and a broken down car set me on a path to what I hope will be a lengthy academic career. For this I am extremely grateful. His jovial attitude and strong will has been a boon, not only for me and this project, but to the MSE department as a whole, which has been lucky to have him as department head for the last few years.

Beyond my supervisors, no one played a more significant role in the success of this project than my collaborator, mentor, and friend, Dr. Francesca Gabrieli. Not only was she the main collaborator for my first publication, but she has guided me since my first RIS measurements during my master's and I owe most of my knowledge on the topic to her. Her unwavering support and encouragement helped me through tough times and her self-assuredness (backed with extensive knowledge) is a constant source of inspiration.

Further, the people with the most significant contributions to the completion of this PhD were my collaborators: Dr. Victor Gonzalez, Dr. Annelies van Loon, Dr. Lukasz G. Migas, Dr. Marc Vermeulen, and Dr. Henry Chopp. This dissertation would certainly have been worse if not for their valuable contributions. Although not included in this dissertation, I must thank my collaborator, Alessia di Benedetto, for giving me two publications to add to my rather short list of academic outputs.

I was fortunate enough to be part of two research groups during this PhD project, the Alfeld lab and the Van de Plas lab. The members of both these labs provided valuable insight to the project. From the Alfeld lab I would like to thank Daniel, Gesa, Janneke, Marijn, Paulina, Tiffany, and Yousef. From the Van de Plas lab I would like to thank Léonore,

Maartje, Meenakshi, Paul-Louis, and Roger.

Given that I was the only PhD working in the Alfeld lab through most of my PhD, it could have been very lonely endeavour. Luckily, I was constantly surrounded by the great people of the MSE department, with whom I could share laughs and sorrows in equal measure. My thanks to my colleagues, Alice, Amir, Arjun, Arthur, Camila, Can, Daniel, Devi, Elsa, Eszter, Fabian, Gaojie, Gautham, Hannah, Jasper, Jithin, Joep, John, José, Julia, Konstantina, Marco, Milou, Mohammed, Philipp, Radhey, Robert, Sean, Soroush, Virgínia, Vitória, and Yeli. Further thanks are due to the technical and administrative staff working within MSE, who are the ones that keep the department running, in particular Agnieszka, Elise, Hans, Jurian, Kees, Minouska, Nico, Olaf, Patrick, Remko, Richard, Ruud, and Ton. Special thanks are due to Sander van Asperen and Saskia van der Meer, who played a significant role during my master's.

However, even when surrounded with amazing researchers at MSE, my research was very different than that conducted by the rest of my colleagues, which meant I did not have anyone I could really discuss my research with. Luckily, Prof. Katrien Keune, the head of the Rijksmuseum science department, allowed me to join her group as a guest researcher, for which I am very grateful. This allowed me to stay in direct contact with fellow cultural heritage scientists, conservators and curators at the Rijksmuseum, RCE, and UvA. I would like to thank Alba, Alessandra, Amelia, Anna, Apas, Aurora, Benjamin, Bianca, Carola, Catarina, Dagmar, Danielle, Elizabeth, Fabiana, Francien, Frederik, Fréderique, Giulia, Gwen, Han, Hannah, Henk, Hoa, Idelette, Ilse, Joen, Jorien, Julia, Karin, Kirill, Leila, Lucy, Marie-Noëlle, Mathijs, Mitra, Momoko, Nouchka, Petria, Rika, Rob, Robert, Sander, Sanne, Susan, Tamar, Theo, Tracy, and Victoria.

Outside of all these great people I worked alongside, there were many friends who helped keep me sane through these very tumultuous five years. My Wales friendos (Bryony, Clown, Frankie, Jordan, Lucy, Nic, and Seb), my Germany friends (Aleks, Johanna, Maurice, Mehran, and Will), my friends from the open studio (Amber, Anant, Elise, Esmée, Gabi, Giulia, Imara, and Koen), my Britnis (Bermu, Diego, Giraldo, Lucas, Pablo, Pablo, Ponchis, and Sergio), my Netherlands friends (Archana, Artemis, Ai-Yu, Chaandi, Emma, Ide, Indra, Ines, Jelmer, Jennifer, Jesper, Katja, Kathi, Kelsey, Linda, Maria, Meysa, Nanditha, Nic, Ragnheiður, Rie, Robin, Rohan, Sana, Sienna, Stratos, Tamara, Vivetta, and Xiao), the pickle jar (Alice, Dani, Jack, Lewis, Louise, Maddie, Marcus, Maria, and Mitch), my fellow TACHies (Aura, Danny, Ember, Lekk, Owen, Ram, and Tzahr), and the Big Man Echo Chamber (Cass and Viki).

I was very fortunate to travel quite a bit during the PhD, both for work and for leisure, and the highlight of these trips were the great people I got to meet and spend time with. I am thankful to have met and been able to share time with Arthur, Asami, Brynn, Caroline, Clare, Edith, Prof. Erich Uffelman, Julia, Dr. Lucia Burgio, Prof. Manako Tanaka, Maria Eugenia, Ria, Roxanne, Sawako, and Tomás.

I would also like to thank the professors who supported and inspired me during my higher education: Prof. Achim Kehrein, Prof. Eduardo Mendes, Prof. Marcel Sluiter, Prof. Niels Østergaard, Prof. Peter Kisters, and Prof. Roland Schmetz.

Ultimately, none of my career (and life more generally) would have been possible without the love and support of my family. My parents, Manuel and Lorena; my siblings, Ariana, Gustavo, Josh, and Valeria; my beloved nephew, Luca; my aunts and uncles, Sofi,

Titi, Brent, Kako, and Veronica; my grandparents, Guabu, Gustavo, Irene and Manuel; and my godparents, Luigi, Sarita, and Tote. I would not be who I am today without their willingness to deal with all my shenanigans for the last 30 years.

And last but not least I would like to thank five people who have been particularly important to me being able to finish this dissertation. Firstly, my psychologist, Naheed, who quite literally kept me sane and helped me better understand myself. The best friend I could ever ask for, Iantra, who read through this entire dissertation and corrected my very many mistakes. My Delft paranymph, Tim, who has stood with me since the first day of our masters all the way through our PhDs, sharing our victories and defeats, our joys and our sorrows. My Rijks paranymph, Ida, whose empathy, care and drive are a constant inspiration for me. My beloved spouse, Jun, who made sure I did not waste away as I lost myself in this dissertation. And finally, Qiao, who sat alongside me for hours on end as we both struggled to finish our respective theses. I look forward to many more hours sitting beside you.

Curriculum Vitæ

Luís Manuel de Almeida Nieto

20-09-1995 Born in Caracas, Venezuela.

Education

2013 - 2017 BSc Mechanical Engineering
Rhine-Waal University of Applied Science, Germany
Thesis: Controller development for pump synchronization for an additive manufacturing process

2017 - 2020 MSc Materials Science and Engineering
TU Delft, The Netherlands
Thesis: XRF and RIS for semi-quantitative sub-surface layer detection and composition analysis of easel paintings

2021 - 2026 PhD Materials Science and Engineering
TU Delft, The Netherlands
Thesis: Chemical imaging methods for cultural heritage: Advanced data acquisition and processing

Professional Experience

2013 - 2016 Teaching Assistant
Rhine-Waal University of Applied Science, Germany

2016 - 2017 Additive Manufacturing Engineer
Melos GmbH, Germany

2018 - 2020 Assistant Lab Technician and Teaching Assistant
TU Delft, The Netherlands

2019 - 2020 Imaging and Analysis of Paintings Intern
Rijksmuseum, The Netherlands

2025 Research Scientist
Rijksmuseum, The Netherlands

VOLUNTEER WORK

2014 - 2016 Chairman
Board of Student Representatives (Fachschaftsrat),
Faculty of Technology and Bionics,
Rhein-Waal University of Applied Sciences, Germany

2017 - 2019 President and Education Committee Member
Het Gezelschap Tubalkaïn Student Association,
Materials Science and Engineering Department,
TU Delft, The Netherlands

2019 - 2020 Student Representative
Board of Studies,
Materials Science and Engineering Department,
TU Delft, The Netherlands

2023 - 2025 Departmental Council Representative and PhD Liaison
Het Gezelschap Tubalkaïn Student Association,
Materials Science and Engineering Department,
TU Delft, The Netherlands

2025 - 2026 Administrator
DEIK Open Art Studio, The Netherlands

LIST OF PUBLICATIONS

5. L. M. de Almeida Nieto, H. Chopp, J. Dik, R. Van de Plas, and M. Alfeld. "Accelerating MA-XRF through advanced scanning strategies". In preparation

4. L. M. de Almeida Nieto, L. G. Migas, M. Vermeulen, J. Dik, M. Alfeld, and R. Van de Plas. "Advance analysis of historical manuscripts through interpretable machine learning of reflectance imaging spectroscopy". In preparation

3. A. D. Benedetto, L. M. de Almieda Nieto, D. Marsh, J. Zwetsloot, R. Janssen, A. T. Popkema, H. de Vries, D. Comelli, and M. Alfeld. "Unveiling hidden text in Frisian historic manuscripts by fused reflectance and transmittance imaging spectroscopy". In: *npj Heritage Science* 13 (1 Dec. 2025). ISSN: 30593220. DOI: 10.1038/s40494-025-02001-5

2. A. Di Benedetto, L. M. de Almieda Nieto, A. Candeo, G. Valentini, D. Comelli, and M. Alfeld. "Multivariate analysis on fused hyperspectral datasets within Cultural Heritage field". In: *EPJ Web of Conferences* 309 (2024), pp. 1–2. ISSN: 2100014X. DOI: 10.1051/epjconf/202430914007

1. L. M. de Almeida Nieto, F. Gabrieli, A. van Loon, V. Gonzalez, J. Dik, R. Van de Plas, and M. Alfeld. "Comparison of macro x-ray fluorescence and reflectance imaging spectroscopy for the semi-quantitative analysis of pigments in easel paintings: A study on lead white and blue verditer". In: *X-Ray Spectrometry* August (2023). ISSN: 10974539. DOI: 10.1002/xrs.3394